NASA TM X- 66034

SIGNIFICANT

ACCOMPLISHMENTS

IN SCIENCES

GODDARD SPACE FLIGHT CENTER, 1971

JUNE 1972
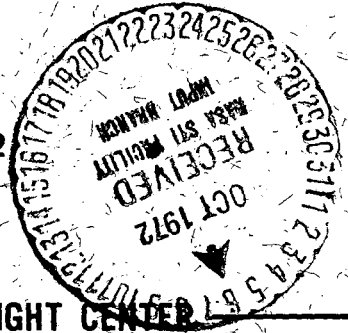
GODDARD SPACE FLIGHT CENTER

GREENBELT, MARYLAND

SIGNIFICANT

ACCOMPLISHMENTS

IN SCIENCES

GODDARD SPACE FLIGHT CENTER, 1971

The proceedings of a symposium held at the NASA
Goddard Space Flight Center, November 10, 1971

Prepared by Goddard Space Flight Center
Greenbelt, Maryland

FOREWORD

This is an almost-verbatim transcript of a symposium held at Goddard Space Flight Center, Greenbelt, Maryland, on November 10, 1971. No attempt has been made to introduce editorial or stylistic uniformity in the talks; on the contrary, an effort has been made to retain the informality of the proceedings.

The sole major change results from NASA policy, which now requires in all formal publications the use of international metric units according to the Systeme International d'Unites (SI). However, in certain cases, utility requires the retention of other systems of units in addition to the SI units. The conventional units stated in parenthesis following the computed SI equivalents are the basis of the measurements and calculations reported here.

Preceding page blank

CONTENTS

vii

OPENING REMARKS

Donald P. Hearth
Deputy Director of Goddard Space Flight Center

I want to welcome you to Goddard's annual review of its technical accomplishments. I particularly want to welcome our visitors from Headquarters and the other field centers. There are many familiar faces in the audience. We are glad Homer Newell, NASA Associate Administrator, Len Jaffe, Deputy for Applications, Dave Johnson from the National Oceanographic and Atmospheric Agency, to name a few, are with us. We are certainly glad to see all of you.

In the next 2 days, we will be presenting approximately 90 individual papers that will cover a number of Goddard accomplishments over the past year. This work is funded by OART, OSSA, OMSF, and OTDA. It includes some advanced studies work, although it is largely in the ART/SRT area.

This work comprises approximately 7 percent of the Goddard R&D budget, some $30 to $35 million a year. We apply a large fraction of our manpower to this effort, approximately 700 to 750 man-years.

As you would imagine, there are some changing trends within this area. The OART work is decreasing whereas the work in applications and advance studies is increasing.

You will be hearing about many accomplishments of which we are very proud. However, because we are limited in what we can present in 2 days, you will not be able to hear about many of which we are equally proud.

Today we will be covering generally the disciplines in space sciences and applications, although some of the application disciplines will carry over into tomorrow. Today's session will be chaired by Les Meredith, who is Deputy Director of Earth and Space Sciences and is serving as Acting Director while George Pieper is away on a well-deserved sabbatical.

Tomorrow we will be covering generally spacecraft technology as well as OTDA work, launch vehicle work, and so forth. That session will be chaired by Dan Mazur. At this point let me introduce today's chairman, Dr. Les Meredith.

1

REMARKS

Dr. Leslie H. Meredith, Chairman

Most of you have been to these presentations in previous years and, as you know, we have individual talks that are not more than 5 minutes; generally the speakers stay within that limit. From your program, you can see how long it is going to take to present all the talks. The length of the program means that the number of questions after each of the talks has to be somewhat limited. However, I think that it will be possible to have questions after the talks, so please feel free to ask. If the question period is becoming too long, I will terminate it.

SOIL MOISTURE MEASUREMENTS WITH
MICROWAVE RADIOMETERS

Dr. Thomas J. Schmugge

There is considerable interest in the measurement of the moisture content of soils. For example, meteorologists are interested in monitoring moisture content of soils over large areas to learn more about the energy exchange of the air/soil interface.

One technique of measuring moisture content that appears promising is that of microwave radiometry. In the microwave region of the spectrum, the emissivity of water is approximately 0.4, whereas that of dry soil is approximately 0.9. Therefore, the emissivity of the soil can range from about 0.6 to 0.9 as the soil changes from a wet to a dry condition. Recent ground base measurements have demonstrated emissivity changes of this magnitude.

To test the use of this approach for remote sensing of soil moisture, the NASA Convair 990 was flown over agricultural test sites in the vicinity of Phoenix, Ariz., during late February 1971. On the same day, soil moisture measurements were made on the ground for 200 fields. On board the aircraft were six microwave radiometers, ranging in wavelength from 21 cm to 8 mm. The results of one of these radiometers is shown in Figure 1.

This is a false-color image produced by the 1.55-cm mapping microwave radiometer similar to that scheduled for Nimbus E. The flightpath was from south to north along a line about 8 km west of Phoenix.

The rectangular pattern of the fields is quite apparent, and we are clearly able to distinguish between a wet field A, which in this case has about 35 percent water content (expressed as weight percent) and, for example, the dry field B, which has a moisture content of approximately 6 percent.

The other radiometers were nonscanning and looked at the fields along the aircraft's flightpath, that is, those directly along the center of the map shown in Figure 1.

Figure 2 is an example of the results from these radiometers. It is the plot of the microwave brightness temperature versus the soil moisture for the 21-cm-wavelength radiometer, and the straight line is a linear regression fit of the data; the fit is reasonably good.

3
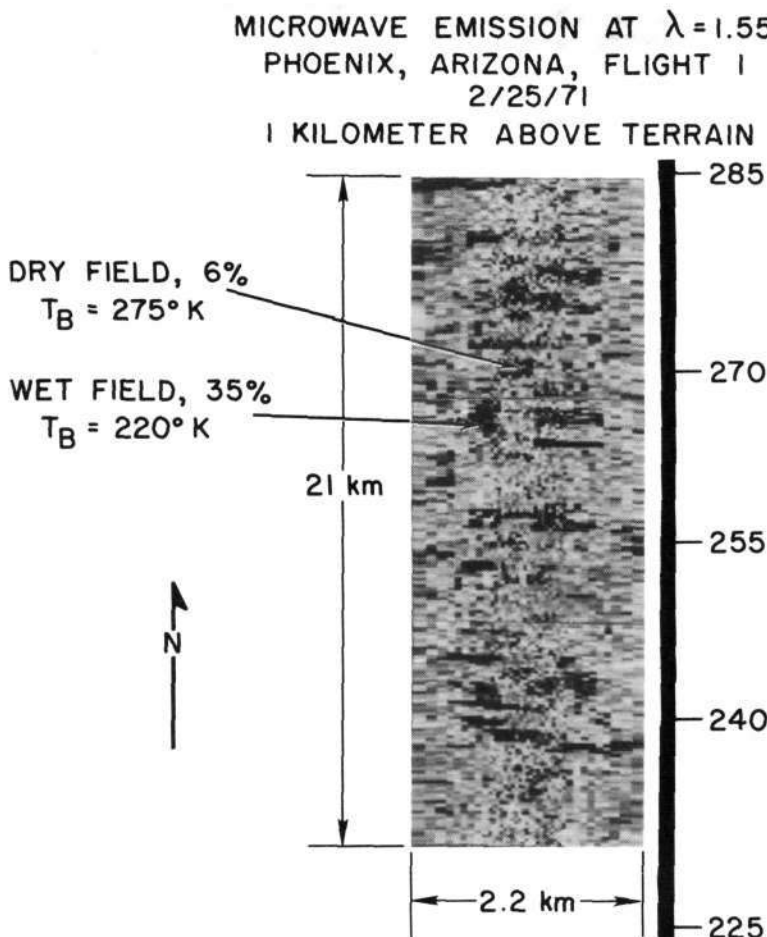
Figure 1–Microwave emission at 1.55-cm wavelength, 1 km above the terrain; flight 1, February 25, 1971, at Phoenix, Ariz. Field *A* is a wet field with a moisture content of 35 percent and microwave brightness temperature of 220 K. Field *B* is dry with 6 percent moisture content and microwave brightness temperature of 275 K.

We have considerable amount of scatter in the low moisture content area, but we attribute this scatter to variations in such quantities as the temperature and moisture profiles in the soil, the soil type, the surface roughness, and the vegetative cover, all of which will affect the microwave emission and had not been taken into account in this plot.

It is interesting to note that some of the fields with vegetation cover lie reasonably close to the curve for the bare fields, indicating that it may be possible to measure the moisture content even with vegetation present.
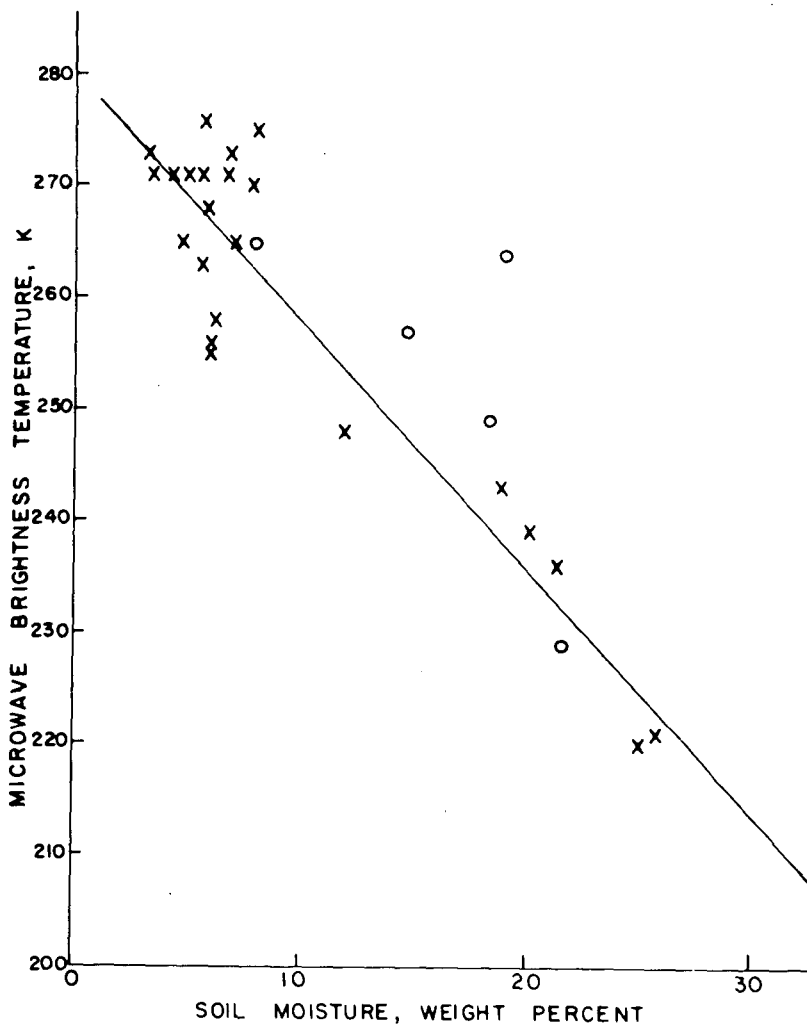
Figure 2–Plot of the microwave brightness temperature versus the soil moisture for the 21-cm wavelength radiometer, flight 1 over Phoenix, Ariz., February 25, 1971. X indicates the bare fields; o, the vegetated fields.

The results from three other radiometers are given in Table I, which is a table of regression results indicating the intercept of the curve, the slope of the curve, and the rms deviation of the data from the straight line. The results were calculated from the same 23 bare fields as were used in Figure 2. For

TABLE 1—Linear Regression Results of Microwave Brightness
Temperature Versus Soil Moisture Content

Wavelength, cm	Intercept	Slope	Standard Error of estimate
21	280	-2.22	6.22
6	307	-1.65	5.46
1.55	281	-1.44	4.34
.8	292	-1.16	5.50

the scanning radiometer, which is the 1.55-cm radiometer, only those fields
that were directly along the aircraft's flightpath were used. There is a general
decrease in the negative slope of the curve with decreasing wavelength. This
is to be expected because the difference between the emissivity of the water
and the dry soil decreases with decreases in wavelength. This effect plus the
fact that the longer wavelengths provide greater penetration depth in the
soil and better atmospheric transmission characteristics indicate that they
would be best for soil moisture sensing.

These results are encouraging and lead us to believe that it should be possible
to remotely monitor soil moisture changes with the microwave radiometers.

MINERAL EXPLORATION FROM
HIGH-ALTITUDE IMAGERY

Herbert W. Blodget

There is still considerable debate within the geologic community as to what types of remote sensing can best be done from spacecraft and what types can best be done from aircraft. To help resolve this problem, we selected five geologically distinctive areas in northwestern Saudi Arabia for detailed study. The areas were mapped as thoroughly as possible on each of several different types of imagery. The final objective was to identify those classes of geologic problems that can best be resolved using satellite data and then to identify areas where orbital imagery might profitably be used to extend existing knowledge, with emphasis placed on mineral exploration.

I have selected the Harrat volcanic area to illustrate some of the imagery used in this study and will point out a few of the advantages and shortcomings of each type. (See Figure 1.)

Standard aircraft photographs yield by far the greatest detail. At 1:60 000 scale, resolution of 6 m (20 ft) is adequate to define features as small as cooling fractures and collapse depressions on individual lava flows. The small area covered by individual photographs, however, makes it impossible to recognize the significance of the area in the regional context.

Photomosaics are constructed by reducing overlapping aircraft photographs to a convenient scale. We can readily see that they have an inherent patchwork pattern that results from the different photometric density of adjacent photographs; this can mask important but subtle linear and tonal features. At the 1:250 000 scale of this mosaic, resolution is reduced to 34.5 m (115 ft), but the subject area appears in context as part of a total volcanic field.

Resolution of the Gemini 11 photograph (Figure 1) is approximately 195 m (650 ft) in the area covered by the mosaic. This compares with 90 m (300 ft) expected of ERTS. Toward the horizon, however, the resolution degrades to more than 900 m (3000 ft) because of photographic obliquity. Although the resolution is low, the scene provides a useful overview for the study of regional tectonics and generalized lithology distribution. The subparallelism of the coasts is easily recognized and we can see finer structural detail, such as fracture patterns on both sides of the Red Sea. Based on textural and tonal differences, we can identify at least four generalized rock types on this picture; but even this gross classification can be subject to local interpretive error if not validated by field checking.

7
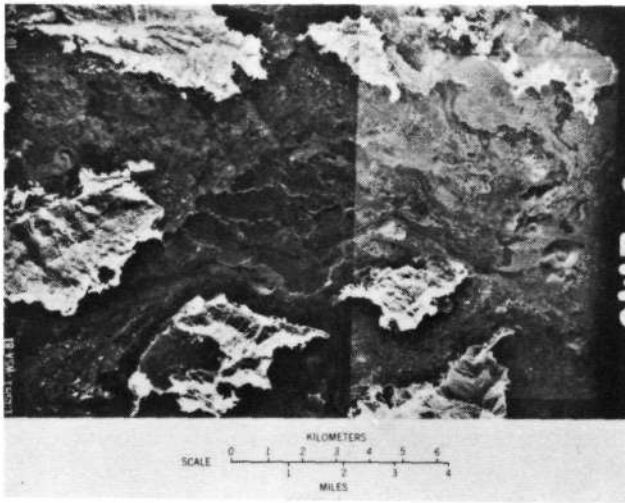
(a) Aircraft photograph, altitude 9.1 km (30 000 ft).

(b) Aircraft photomosaic.

Figure 1–Earth observations from spacecraft and aircraft.

(c) **Gemini 11 photograph, alti-
tude 410 km (220 n. m.).**

(d) **Nimbus 3 high-resolution in-
frared radiometer photograph,
orbit 711, altitude 1110 km (600
n. m.).**

Figure 1 (Cont.)—Earth observations from spacecraft and aircraft.

Nimbus imagery has about 8-km (5-mile) resolution. We find that this is too
low for most geologic research, but it does provide a framework for inter-
relating major structural units within systems of intercontinental magnitude.

It is obvious, even from this comparative glimpse, that the synoptic view
(such as the Gemini 11 photograph), despite its low resolution, is the best
type of imagery for regional investigations. We determined that the mapping
of the distribution and alinement of major structural fracture systems can be
done particularly well from synoptic imagery, and such studies may yield
important information for extending known mineral provinces.

After considering the geologic history of the Red Sea and noting the similar
structural and stratigraphic relationships between a described mineral de-
posit in Saudi Arabia and mineral occurrences near the coast of Egypt, we
have concluded that northwestern Saudi Arabia is particularly well suited
for synoptic mapping designed to locate prospective areas for the occurrence
of ore deposits.

The rationale for this conclusion is that, geologically, western Arabia was part of the Egyptian shield until it was separated by rifting of the Red Sea during Miocene time. The nature of the rifting mechanism is still conjectural; but, with the recent developments of Plate Tectonics concepts, the Red Sea is now generally considered to be an area of incipient continental drift. This means that, as indicated on the schematic, in Figure 2, the present coastlines were once contiguous, and of course implies that the pre-Miocene rock types near the present coasts should be very similar.
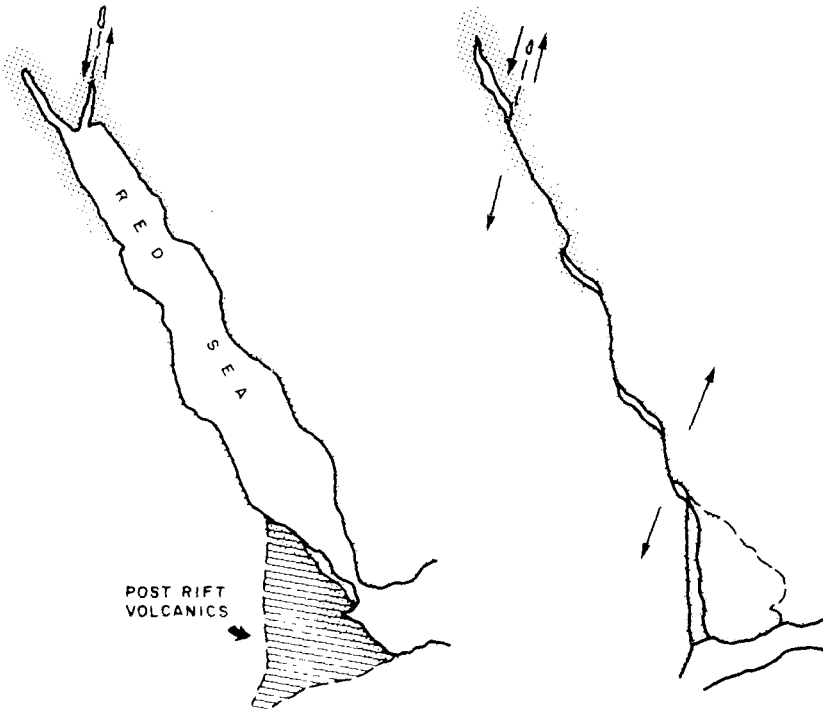
Figure 2–Schematic drawing of the Red Sea, present position (left) and reconstructed pre-Miocene position (right).

The map in Figure 3 shows locations of Miocene and older mineral deposits worked in historic time. Most of these are controlled by geologic structures such as fault zones. In contrast to Egypt, practically no mining has been done in the corresponding part of Saudi Arabia. Thus, locating ore deposits

in Saudi Arabia might be possible if geologic structures there could be correlated with the Egyptian mineral-bearing structures; synoptic imagery with its uniform photometric geometry can provide the means for such regional correlation.
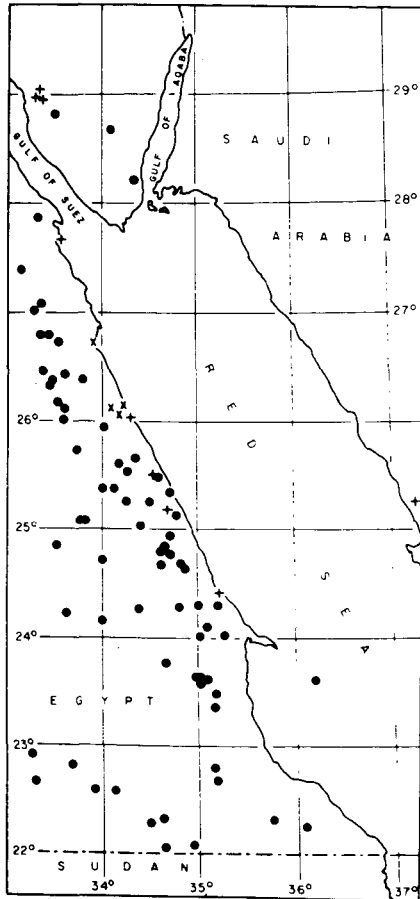
Figure 3—Map of Egypt showing locations of economic mineral deposits (from Ref. 1). ●: pre-Cambrian mineral deposits; x: Cretaceous mineral deposits; +: Miocene mineral deposits.

Present investigations are restricted by limited coverage and the obliquity of available orbital photography. The availability of overlapping, vertical, high-resolution imagery from ERTS should permit systematic mapping of major structural trends on both sides of the Red Sea. Correlation of these trends then should provide the means of isolating the more prospective mineral-bearing fractures from the total structural system of western Arabia.

REFERENCE

1. Said, Rushdi: The Geology of Egypt, Delsevier Pub. Co. (Amsterdam-New York), 1962.

ARCTIC ICE MEASUREMENTS WITH
MICROWAVE RADIOMETERS

Dr. Per Gloersen

We have continued our program of airborne passive microwave experiments in support of the upcoming missions to be flown on the Nimbus E and F and EOS satellites. I would like to report some of the highlights of our most recent expedition with the NASA remote-sensing aircraft to the Arctic polar region. The mission took place during March 1971. The flights were in conjunction with the Arctic Ice Dynamics Joint Experiment (AIDJEX), which is a cooperative interagency effort involving several U.S. and Canadian organizations.

The AIDJEX group established and operated a base camp, Camp 200, on the Arctic polar ice canopy at a location approximately 74° N and 131° W, which is just inside the limits of the permanent polar ice pack off Banks Island. They were, therefore, in an excellent position to supply us with detailed surface truth information in a limited region of the polar ice canopy that could be used to interpret the microwave signatures of the sea ice that we had obtained at seven different wavelengths while flying over Camp 200.

Figure 1 is a map of the region in which these activities took place. This map, which covers an area of about 76 by 95 km (40 by 50 n. m.), was produced from data obtained with the 1.55-cm mapping microwave radiometer. What you see is an enormous multiyear ice floe about 48 by 29 km (25 by 15 n. m.) in extent surrounded by first-year ice. Camp 200 was located at about 74°07'N, 131°24'W on the edge of this ice floe. It is interesting to note that although the members of the expedition knew the camp was located near the edge of the multiyear ice floe, they had no idea of the vastness of this particular floe until this image was formed after the expedition. This image is, of course, a false color representation of the radiometric brightness temperatures of the ice. The temperature scale in kelvins appears on the right of the figure.

The experiment I am describing represents a first. It is the first time that Arctic ice data have been obtained simultaneously on the surface with conventional instrumentation and remotely with microwave and infrared radiometers, photography, and a laser geodolite.

13

Figure 1–Passive microwave image of Arctic sea ice ($\lambda = 1.55$ cm) taken on a clear day from a NASA aircraft, March 15, 1971.

The mosaic in Figure 1 was produced by flying five equally spaced parallel tracks at an altitude of 11 km and using a computer to arrange the digital radiometer and positional data in map format, much in the same way as the microwave data to be obtained from the Nimbus E and F radiometers will be formated.

According to the AIDJEX surface truth data, the temperature at Camp 200 was 256 K, which was within 2 K of the value recorded by the onboard infrared radiometer. Another observation of the ground crew was that there were no substantial differences in the surface temperatures of the multiyear ice and the first-year ice. This again was substantiated by the onboard infrared radiometer. Thus, in this mosaic, the radiometric temperature differences are due almost entirely to emissivity differences between the two kinds of sea ice.

I would like now to show you some of the multichannel data obtained from a low-altitude pass over this area and on the return leg to Eielson Air Force Base.

Our pass started at about 74°20'N, 131°W in a southwesterly direction, passed over the northeastern boundary of the multiyear ice floe, over the region of multiple refrozen leads and on across the southern boundary of the multiyear floe again to first-year ice.

Figure 2 shows the response of seven different microwave radiometers to the two kinds of sea ice near the AIDJEX camp. We can see clearly the boundaries of the large ice floe at the highest frequencies; the multiple refrozen leads appear as spikes between the boundaries of the ice floe.

With the exception of the 94-GHz radiometer, we have confidence in the sensitivity shown at the left of each record. The radiometric temperature of the first-year ice is approximately 250 K in all cases. Thus, as we had noted from earlier studies, the emissivity difference between multiyear and first-year ice increases with frequency up to about 38 GHz. We can just begin to see this contrast at 10.69 GHz. If our 4.99-GHz radiometer had been less noisy, it is conceivable that the phenomenon might have been observable at that frequency also.

In conclusion, since we were fortunate in having ground truth available to us from the ice canopy, we can now ascertain the relationship between the various microwave radiometric temperatures and ice type.
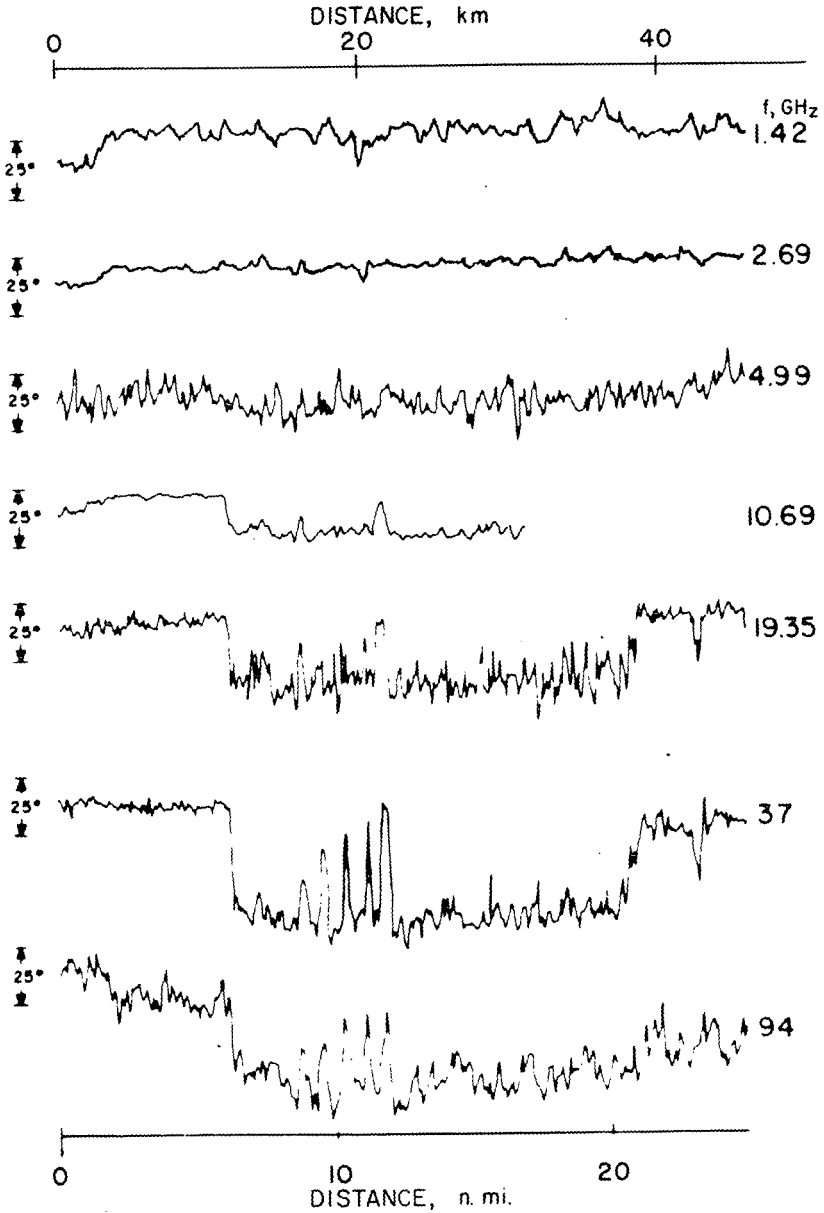
Figure 2—Multifrequency view of large multiyear ice floe.

CHAIRMAN:

Are there any questions?

MEMBER OF THE AUDIENCE:

What happens on a cloudy day?

DR. GLOERSEN:

I can show you the results of such conditions in Figure 3. This was taken on the following day when there was a complete undercast over the AIDJEX campsite. There seems to be a net 8-K upward shift of temperatures, both over the multiyear ice and the first-year ice, so there is some slight effect. As you can see, the features still appear the same.

MEMBER OF THE AUDIENCE:

What are the spikes that appear in Figure 2?

DR. GLOERSEN:

The large spikes between the ice floe boundaries are the refrozen leads in the large ice floe. The cracks are filled with first-year ice. They did not show at the high altitude in that much detail. Only about two of them appeared at high altitude, but these data were obtained at low altitude.

MEMBER OF THE AUDIENCE:

How do you account for the difference in emissivities?

DR. GLOERSEN:

At this point, we have only a qualitative idea. We think that it is strongly connected with skin depth. In first-year ice, the salinity of the ice is a function of its age. Brand new ice is highly saline, about half the salinity of ocean water, and the salinity decreases — I hestitate to say exponentially, but let us say expotentially — with age. The saline ice is a lossy substance, and it has a rather high emissivity. The skin depth in multiyear ice, which is practically pure water ice, is rather large in terms of wavelengths. There-fore, the opportunity for volume scattering exists; and when there is good volume scattering, you are really looking at the sky, which has a very low brightness temperature, because you are looking in a diffused reflector. That is one way of accounting for the difference. We are exploring it actively in more detail.
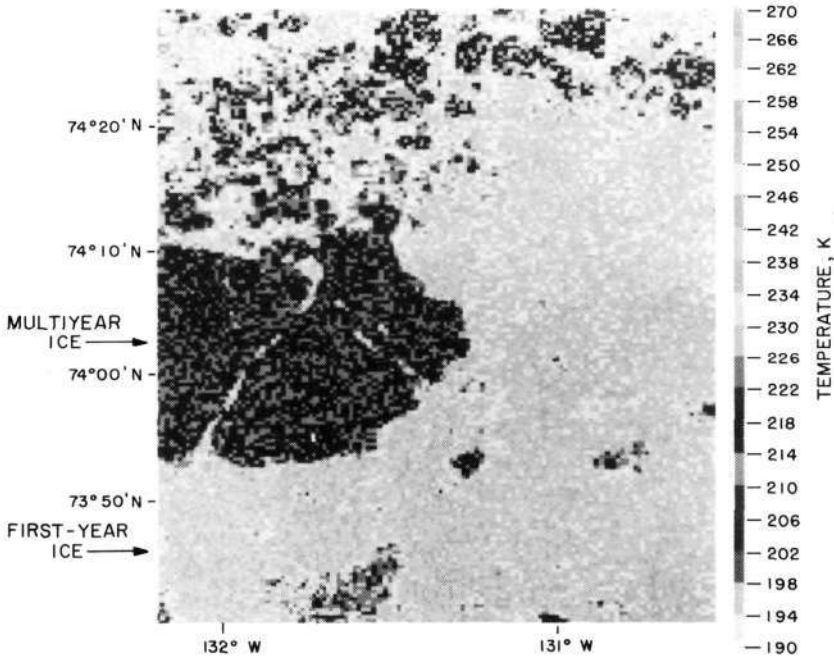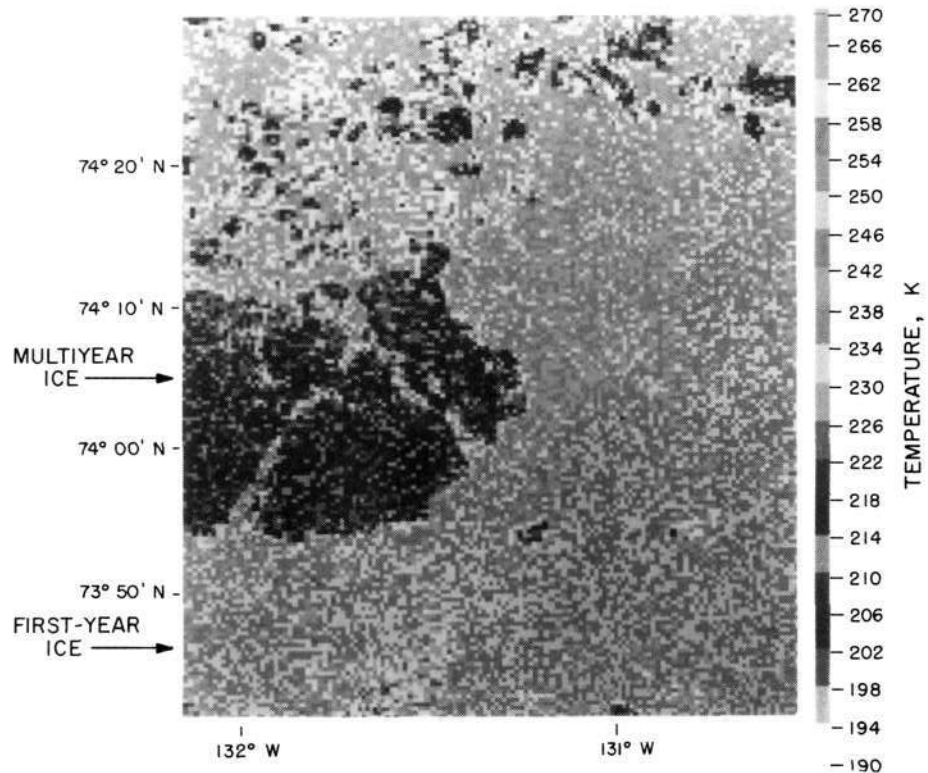
Figure 3–Passive microwave image of Arctic sea ice ($\lambda = 1.55$ cm) taken on a cloudy day from a NASA aircraft, March 16, 1971.

A MULTISPECTRAL METHOD OF DETERMINING
SEA SURFACE TEMPERATURES

William E. Shenk

There are two basic problems in remotely measuring sea surface temperature. The first and perhaps most important problem is establishing that you have a cloud-free line of sight, and the second problem is determining the effects of the atmosphere on the emission in an infrared atmospheric window.

In this investigation, three channels of the Nimbus 2 medium resolution infrared radiometer (MRIR) were used. The first channel measured the 10- to 11-μm emission. This channel, in the absence of clouds, sensed the radiance from the sea surface and the intervening atmosphere, and the other two channels tested for the presence of clouds. The other two channels were a broadband reflectance channel from 0.2 to 4.0 μm, and another channel sensitive to water vapor emission from 6.4 to 6.9 μm. If the reflectivity over the ocean was low, cloudiness would either be absent or confined to thin cirrus. Therefore, it was necessary to consider the 6.4- to 6.9- μm measurements that indicated if the upper troposphere was dry. If it was, then the probability of cirrus was low. Thus, when the thresholds of these two channels were met, the registered window measurement that was concurrently made was accepted as coming from the sea surface and the intervening atmosphere.

Figure 1 shows the establishment of the reflectance threshold for which the data were taken on four relatively clear days over the western North Atlantic during a 1-month period from mid-June to mid-July 1966. Normalized reflectances are plotted along the abscissa and frequency of observation is shown along the ordinate. The maximum frequency was associated with a spectral albedo of 6; and, considering the magnitude of instrument noise, a threshold of 9 was accepted as being associated with cloud-free conditions. A similar procedure was used to establish the thresholds for the 6.4- to 6.9- μm channel.

For results that were not corrected for the effects of the atmosphere, there is a difference between the sea surface temperatures as observed by ships and the equivalent blackbody temperature as determined by the radiometer. These differences are depicted in Figure 2 for four different latitude bands. The band nearest the tropics indicates a mean difference of about 8 K. To the north, the effects of a lower atmospheric water vapor content and the lower sea surface temperatures resulted in a smaller mean difference between the measurements of 4 to 5 K.
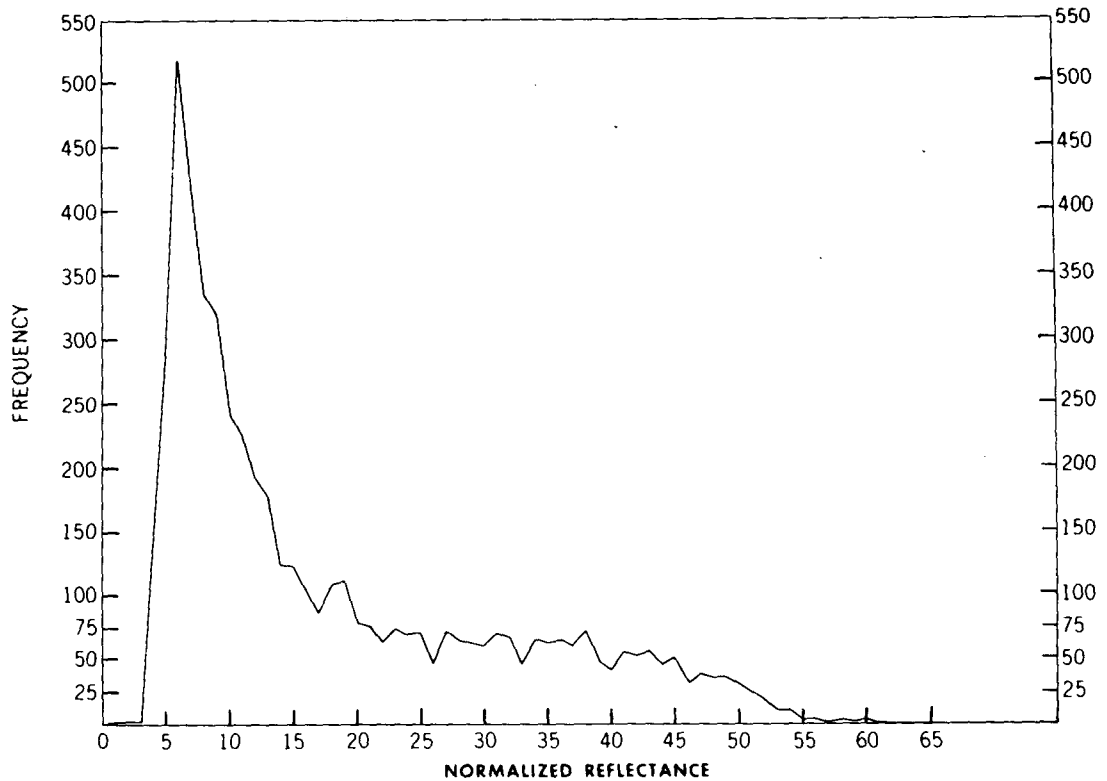
Figure 1–Reflectance threshold over the western North Atlantic.
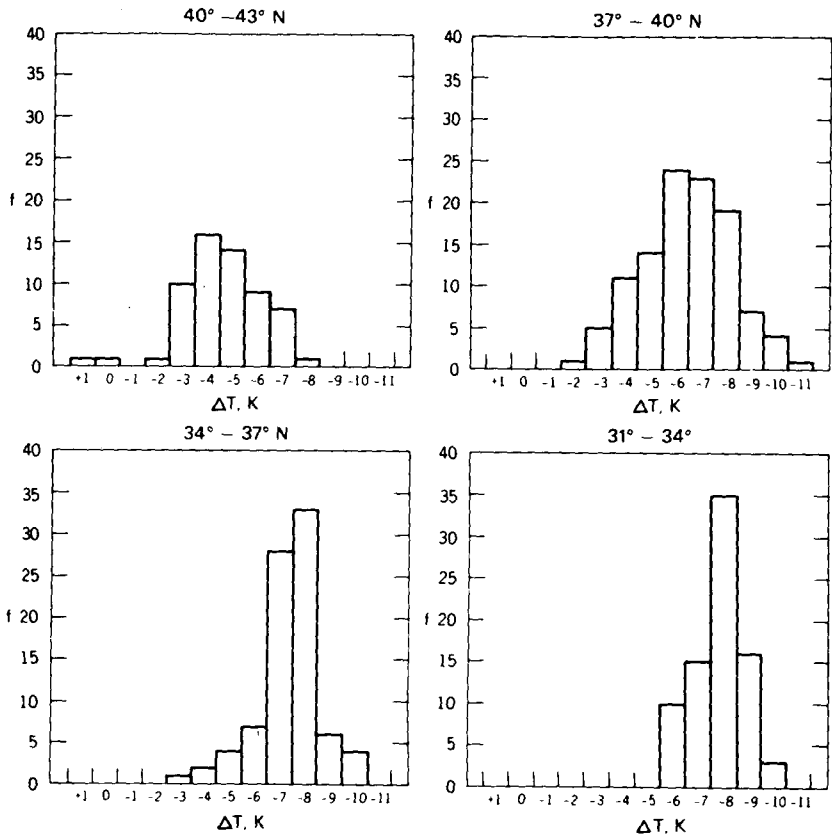
Figure 2–Differences between the actual sea surface temperatures and the equivalent blackbody temperatures as determined by the radiometer.

An important feature of the diagram is the small amount of scatter about the means. In the latitude band nearest the tropics there is a total scatter of $2°$ on either side of the mean. The scatter becomes slightly larger further north. This most likely occurred because the MRIR measurements had to be acquired over a 1-month period, for which the variability of sea surface temperature is greater. The 1-month period was necessary because of the low spatial resolution of the sensor which meant that relatively few cloud-free measurements could be acquired. A statistical method for correcting for the atmosphere was employed where a regression equation was developed between the radiances and the ship temperatures. The regression equation considered the effects of viewing angle, water vapor (the 6.4- to 6.9-μm measurements were used to provide information on atmospheric water vapor content), and any possible clouds (with the reflectance channel).

Figure 3 shows a sea surface temperature map constructed over the western North Atlantic for the same 1-month period; the results have been corrected by the regression equation for the effects caused by the atmosphere. The continent of North America is shown as a dark area. The warm tongue of the Gulf Stream is seen sweeping northeastward off the U.S. coast and the north wall of the Gulf Stream is clearly visible. This temperature gradient is less than it generally would be on an individual day because of the 1-month averaging period of observation and the spatial resolution of the sensor (55 km). Also, the Sargasso Sea is seen below the Gulf Stream as an area with small temperature gradients.

The accuracy we have achieved is about 1- to 1.5 K. The best results were achieved nearest the tropics. With improved information on water vapor content and with higher spatial resolution, even better results can be anticipated. This technique has the advantage of providing an independent test for the presence of clouds and using every measurement.
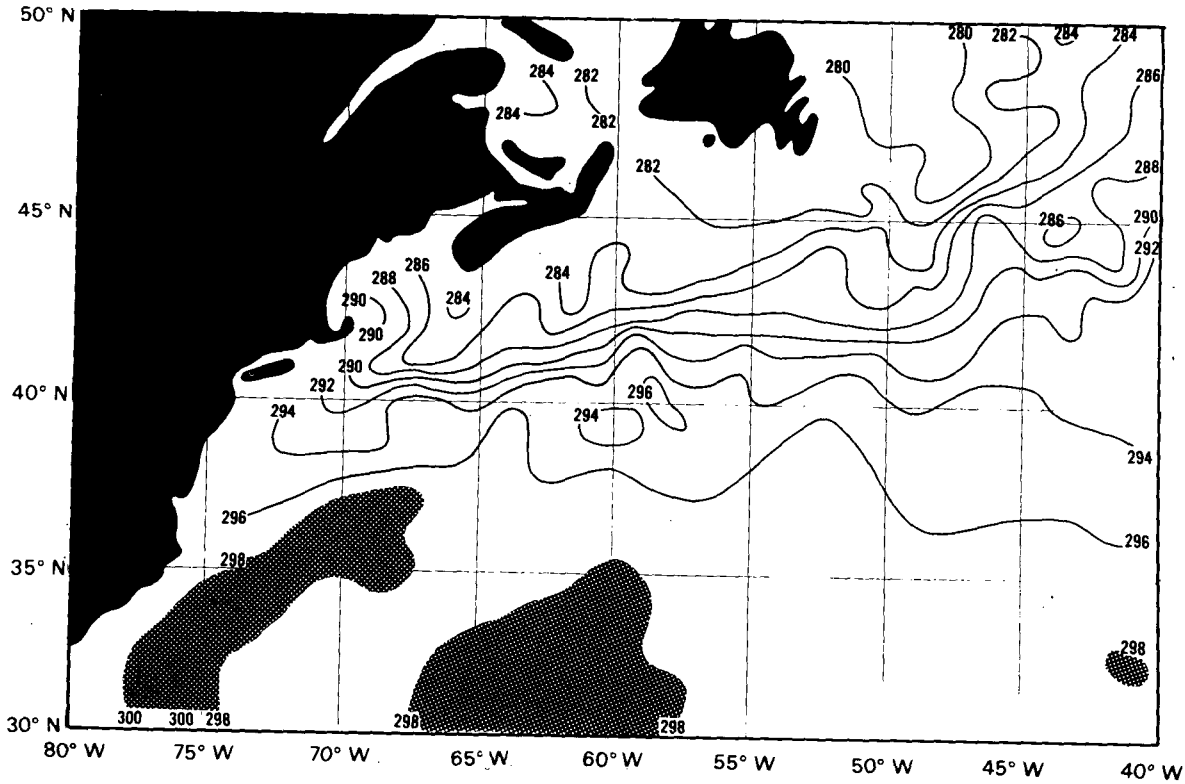
Figure 3–Sea surface temperature map.

MEASUREMENTS OF OCEAN COLOR

Dr. Warren A. Hovis

Studies of ocean color are of interest because the color of the ocean indicates the concentration of phytoplankton in the water. Plankton are at the bottom of the food chain; thus a high concentration of plankton indicates an area where one would expect to find a high concentration of other organisms, with fish of principal interest.

Phytoplankton can be sensed by remote-sensing systems because they contain chlorophyll. Chlorophyll has two strong absorption bands in the visible spectrum as shown in Figure 1. The laboratory-measured reflectance of the algae *Chlorella* shows the strongest absorptions at 450 and 675 nm. If we could use this absorption to make a quantitative global map for the plankton concentration from a spacecraft, we could then indicate areas of potential productivity in the ocean.

Measurements have been made from aircraft at low altitudes over various water masses, and a clear relationship between chlorophyll concentration and color has been shown. Unfortunately, because of limited equipment, atmospheric effects were not considered in these measurements because low-altitude aircraft were used.

In August of this year, using a NASA-leased jet, we were able to make high-altitude measurements for the first time over areas of varying ocean color at up to 16 000 km (50 000 ft), which is above about 95 percent of the molecular scattering atmosphere of Earth.

Figure 2 shows the measured spectrum between 400 and 700 nm at two altitudes, 0.91 and 14.9 km (3000 and 48 900 ft). As you can see, at the lower altitude there is much less energy than at the higher altitude. The sharp spikes in the spectra are the Fraunhofer lines of the solar spectrum and have nothing to do with the ocean color.

At the higher altitude, we observe approximately five times as much energy at the sensor as we do at the lower altitude. This is principally due to the addition of energy scattered by the atmosphere. Unfortunately, the energy that does leave the ocean, that we see at low altitude, does not reach the high altitude undiminished. If it did, one would expect that the contrast would be reduced by this increase in energy by a factor of 5.
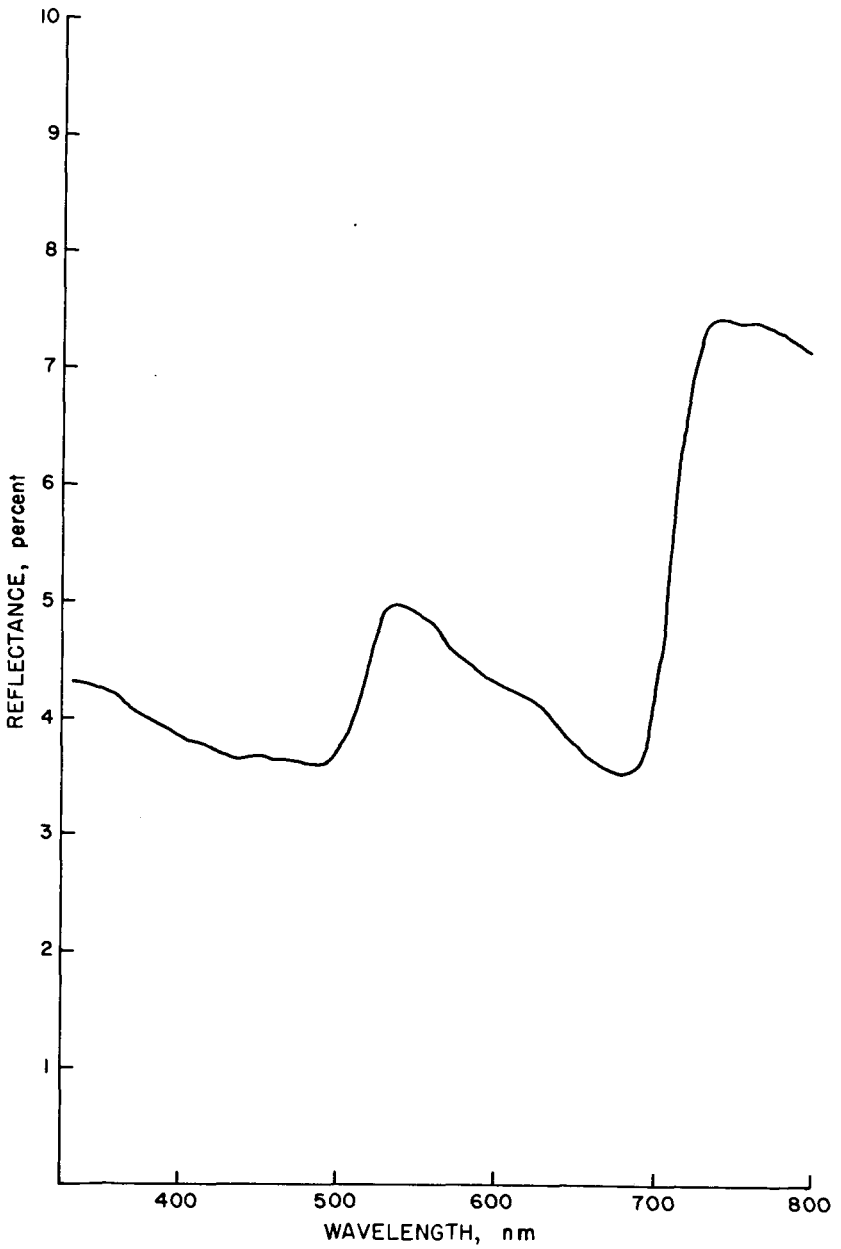
Figure 1—Laboratory-measured reflectance of *Chlorella*.
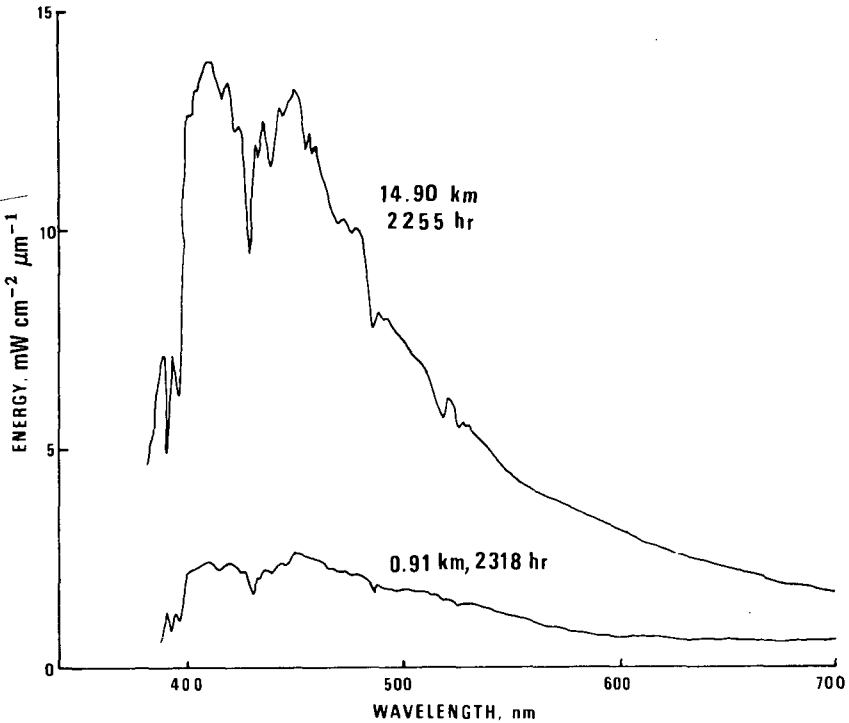
Figure 2—Measured spectrum of ocean color at low and high altitudes.

As shown in Figure 3, we have multiplied the radiance seen at the lower altitude by a factor of 5 to facilitate comparison and plotted it along a track of about 80 km (43 n. m.) as we flew from the shoreline out over a ship.

The dashed line shows the contrast observed at the low altitude. The solid line shows the contrast observed at the high altitude, and the straight line is there to facilitate comparison.

As we progress over reasonably clear water near shore to the richer water out around 65 to 68 km (35 to 37 n. m.), a decrease is seen in the reflected energy but, more important, the contrast is reduced by a factor of about 10 and not 5. This indicates that of the energy reflected off the ocean, only 10 percent was transmitted unattenuated to 14.9 km.
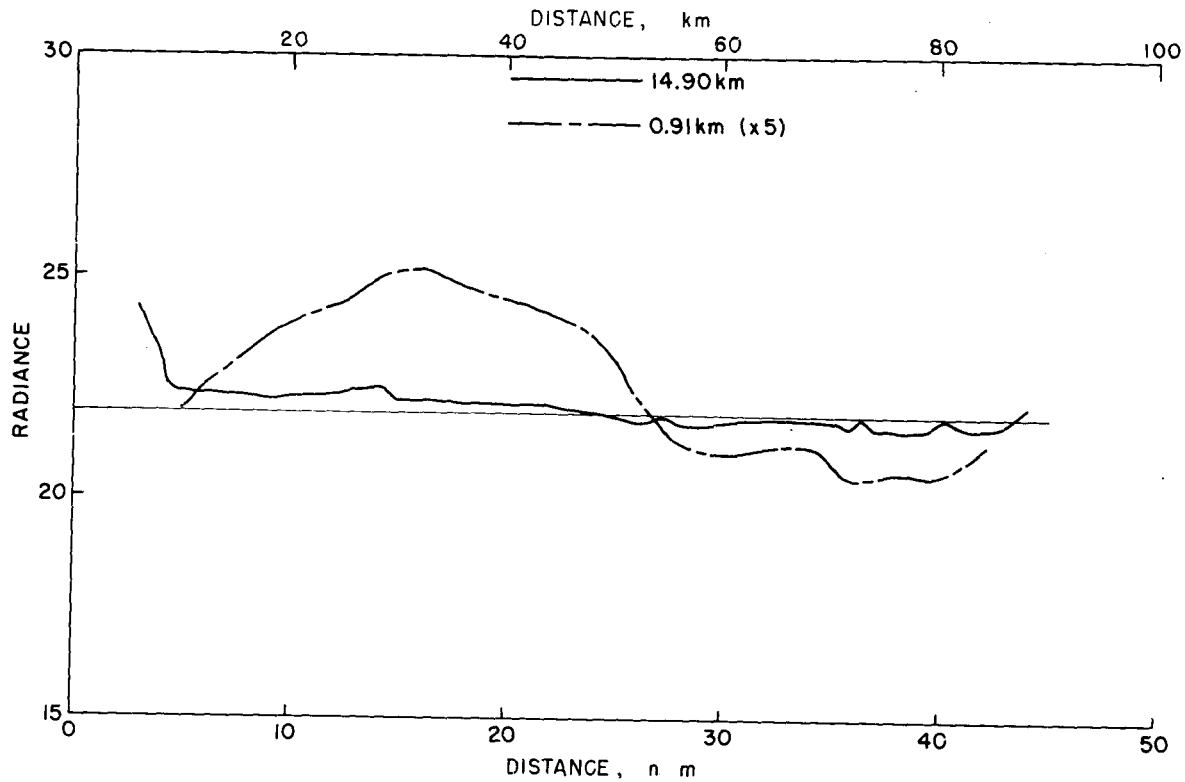
Figure 3--Comparison of low- and high-altitude observations.

Obviously, if we are going to make any quantitative measurement of ocean color on a global basis, we must have some indication of what the atmosphere below us is doing, because our information is contained in small changes within that 10 percent of the total signal. Fortunately, the data not only show the magnitude of the problem but also point to a possible solution.

At wavelengths shorter than 400 nm in the ultraviolet, the energy observed by the sensor is almost exclusively due to the atmosphere and to Rayleigh scattering because of the strength of that scattering.

If we can measure the Rayleigh scattering component at the short wavelengths, we can then extrapolate it to the longer wavelengths through the well-known Rayleigh formula for scattering as a function of wavelength.

At longer wavelengths, around 800 nm, the ocean water becomes for all practical purposes black, so any energy observed by the sensor is due entirely to scattering by the atmosphere. If we know the Rayleigh scattering component by extrapolation from the shorter wavelengths, any difference must then be due to Mie scattering caused by the particulants in the atmosphere. We then hope to extrapolate the Mie scattering measurement back into the shorter wavelengths and eliminate that effect from ocean color measurements.

Future aircraft tests will be conducted to determine the accuracy of this technique before an ocean color sensor that is to fly on the EOS satellite is designed.

CHAIRMAN:

Thank you. Are there any questions on this paper?

MEMBER OF THE AUDIENCE:

Do you not feel that surface measurements by laser telemetry are necessary in conjunction with these flights?

DR. HOVIS:

I agree that a ground crew is absolutely necessary. I should have mentioned that under these flights the U. S. National Marine Fisheries Service was making measurements of chlorophyll both at the surface and at 3 m below the surface and all of these were in accord with our aircraft measurements.

The technique of measuring chlorophyll is still open to question because the oceanographers themselves do not agree on which is the best technique. Laser telemetry is promising because it gives a very quick realtime measurement and, in fact, was used by the ground crew in conjunction with other techniques under our aircraft flights.

ATMOSPHERIC WIND FIELDS DERIVED FROM
NIMBUS OZONE MEASUREMENTS

Dr. Cuddapah Prabhakara

Atmospheric ozone is known to be a good tracer of circulation in the upper troposphere and lower stratosphere. A knowledge of circulation in these upper layers can aid the meteorologists in understanding and predicting the behavior of the lower atmospheric circulation.

Because the ozone layer is well above the tropospheric clouds, it is ideally suited for remote sensing from satellites orbiting around the globe. Two independent experiments on board the Nimbus 4 satellite, namely the infrared interferometer spectrometer (IRIS) and the backscatter ultraviolet spectrometer (BUV), can measure ozone content in the atmosphere. The two sets of measurements are in good agreement and thereby conclusively prove our ability to measure the global distribution of this gas.

In this study the global ozone measurements made by the Nimbus 3 IRIS were used to trace the circulation in the upper troposphere. This was possible because the atmospheric ozone content is closely related to the geopotential heights in the upper troposphere. In Figure 1, we show that there is a linear relationship between 20-kN-m^{-2} (200 mbar) geopotential heights and the total ozone measured by Nimbus 3. With the help of the geostrophic law, atmospheric winds can be derived from the horizontal gradient of the geopotential heights. So, utilizing the linear relationship shown in Figure 1, we can deduce winds from our satellite measurements of total ozone.

A map of the global winds at the 20-kN-m^{-2} (200-mbar) level, for the month of July 1969, derived from the Nimbus 3 IRIS ozone measurements is shown in Figure 2. The solid lines are the stream lines and the isotachs are shown by dashed lines.

These ozone-derived winds bear a good agreement with the conventional maps of 20-kN-m^{-2} (200-mbar) flow over the Northern Hemisphere. However, over the Southern Hemisphere there are no such conventional maps readily available. Thus, the winds derived from our ozone data in the Southern Hemisphere can furnish the missing information.

From these 20-kN-m^{-2} (200-mbar) winds, we can also determine the strength and position of the jetstreams in both the hemispheres. The regions delineated by black shading are locations of the strongest winds or,
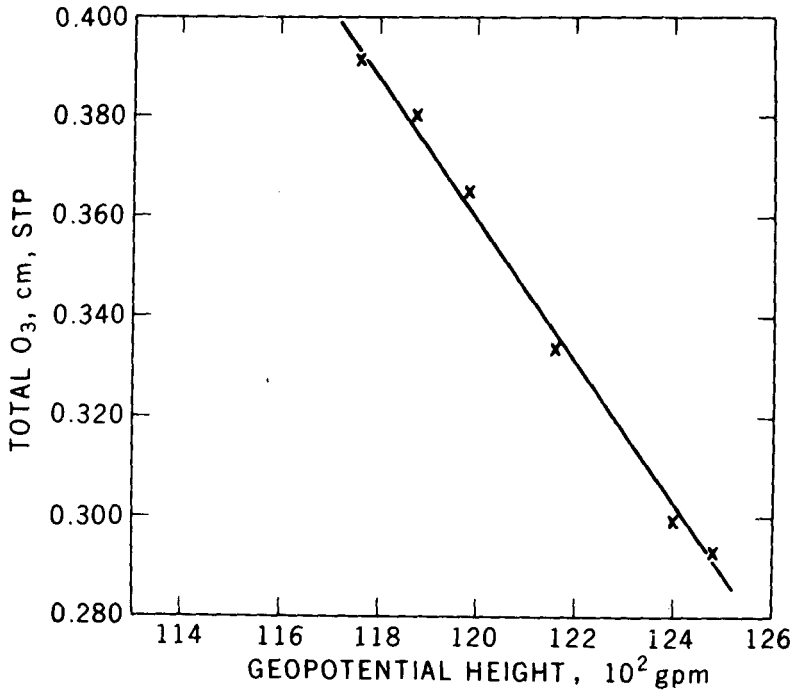
Figure 1—Total ozone versus 20-kN-m^{-2} (200-mbar) geopotential heights.

in other words, jetstreams. This information about the jetstreams can aid the meteorologists in their efforts to understand and predict the weather.

In addition to the subtropical and polar jetstreams that are shown in Figure 2, we have been able to observe the tropical easterly jetstream over Southeast Asia and Africa during the month of July 1969 from Nimbus 3 ozone measurements. The tropical easterly jetstream has a profound influence on the onset and progress of the southwest monsoon rains over southeastern Asia. However, the sparse upper-air conventional data over the tropics does not help the meteorologist to observe this jet well. In this regard the satellite measurements of ozone can be useful.

The total ozone distribution derived from Nimbus 3 over Asia and Africa during the period of July 1969 is shown in Figure 3. The heavy dashed lines define the axis of ozone maximum. This axis corresponds well with the course of the tropical easterly jet. The meteorologists can take advantage of such observations to predict the monsoon rainfalls.
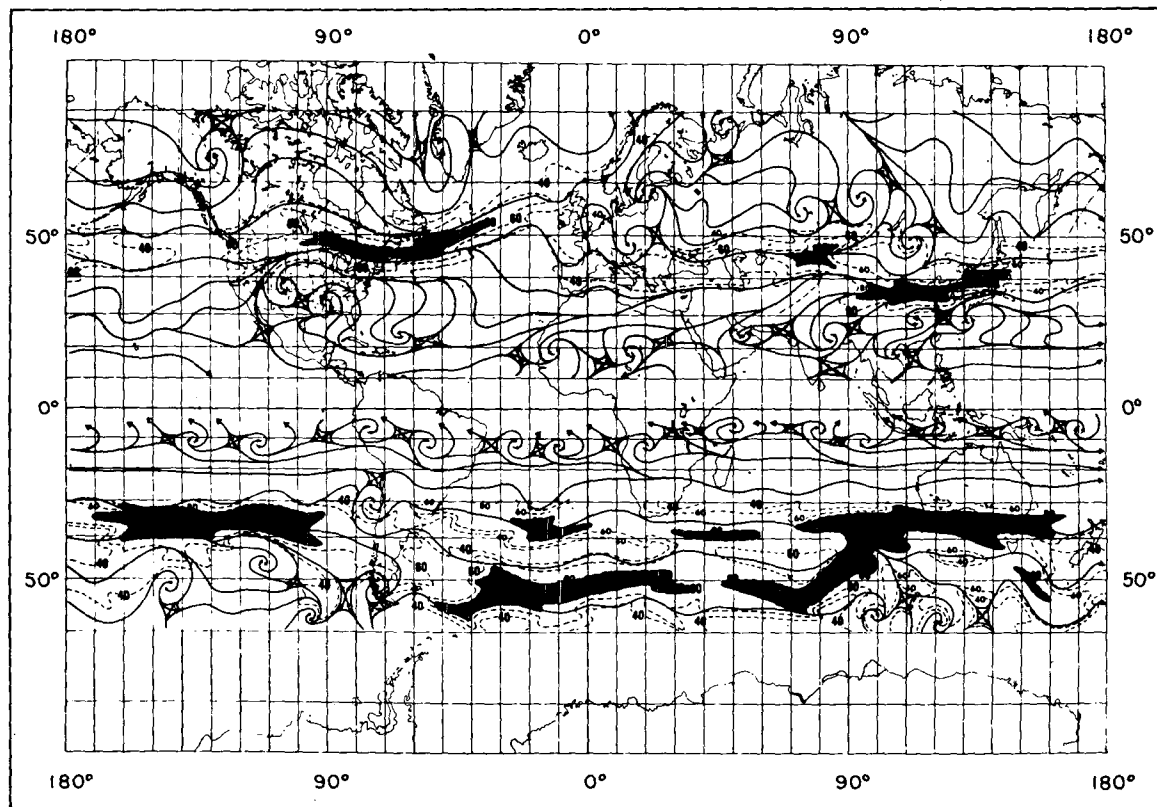
Figure 2—Geostrophic winds for 20-kN-m^{-2} (200-mbar), derived from total ozone data, IRIS, July 1969.
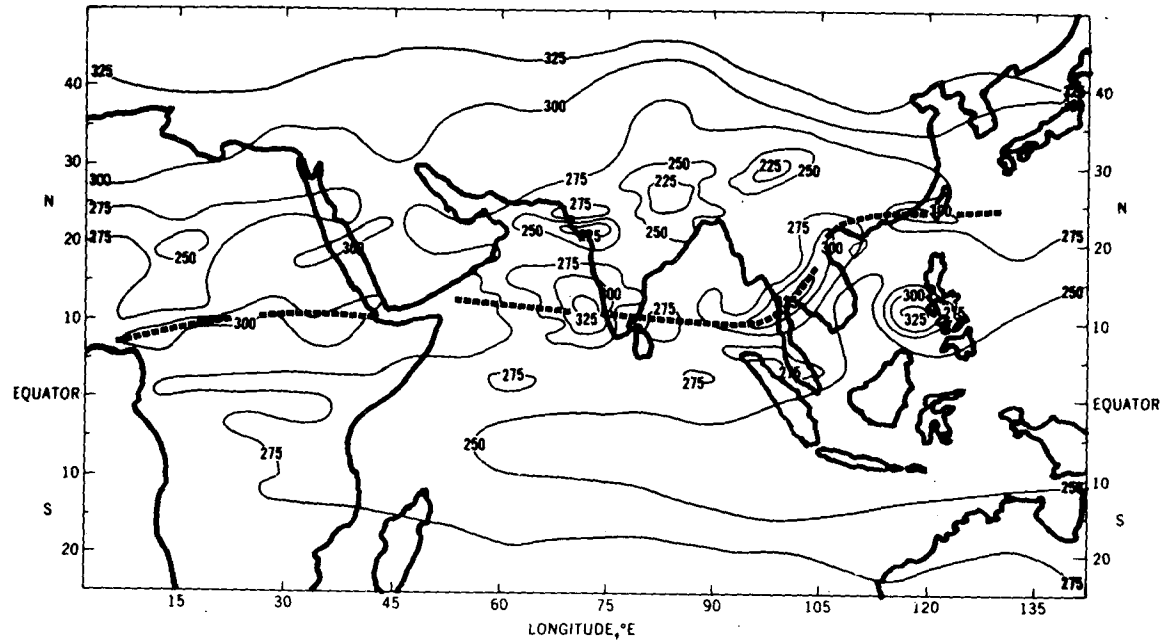
Figure 3–Total ozone data (10^{-3} cm, STP), July 5 to 22, 1969.

STRATOSPHERIC OZONE

Dr. Richard W. Stewart

For several years, some of my colleagues and I have been engaged in studies of the photochemistry and thermal structure of the atmospheres of Mars and Venus as part of the program for interpreting data returned by the various Mariner spacecraft.

In the past several months, we have begun to apply the techniques developed in this work to a study of the photochemical and transport processes in the Earth's stratosphere. We are especially concerned with the effects of certain trace constituents such as water vapor and oxides of nitrogen on the stratospheric ozone distribution.

This study has been motivated in part by recent discussions of pollutants associated with engine exhaust from high-altitude aircraft. We have been encouraged to pursue this program by Dr. Tepper, and we expect initial results from a combined photochemical and vertical transport study in February 1972.

The work has thus far yielded two results, which I will describe shortly. The major goal of this study is to determine the changes in the surface ultraviolet radiation levels which result from changes in the chemical composition in the stratosphere. The problem consists of three related studies that are being carried out by Dr. Hansen and Dr. Hogan, in collaboration with myself: first, the study of the photochemistry of ozone and various trace constituents in the stratosphere, which involves roughly 60 chemical reactions among about 20 constituents; second, a study of the vertical and horizontal transport of these constituents by diffusion and large-scale atmospheric motions; and third, a study of the transmission of ultraviolet radiation through the atmosphere, which requires a multiple-scattering calculation for an inhomogeneous, partially absorbing medium.

To some extent, the absorption and scattering of ultraviolet radiation influences the thermal structure of the stratosphere. Study of the full problem involving all three of these related studies has not been attempted previously.

We have two preliminary results from the third part of this study. Figure 1 shows an increase in the surface radiation levels for various assumed ozone reductions. One of the next steps is to calculate the ozone reductions for a given level of pollution in the stratosphere. This calculation takes into
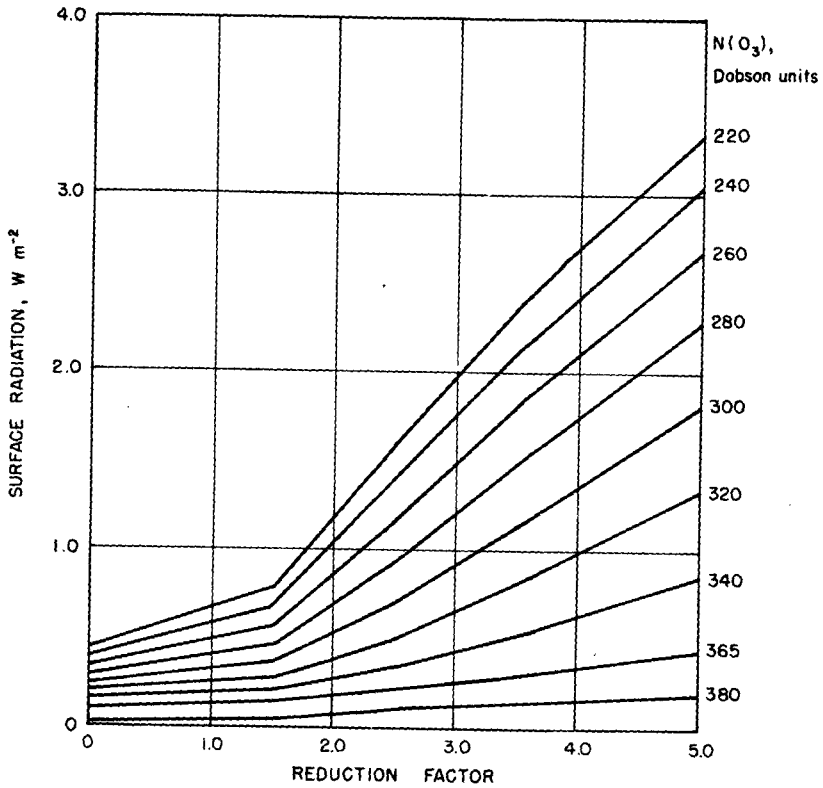
Figure 1—Surface radiation levels for various assumed ozone reductions.

account only the absorption by ozone. The top curve is for the Equator and the successive curves below that are for 10° increments in latitude. The bottom curve represents the increase in flux levels at 80° latitude. Longitude is 0.0°. The ozone amounts are listed to the right of each curve.

For a factor of 2 reduction in ozone, as postulated in a recent paper by Johnson (Ref. 1), these calculations would indicate about, or close to, a threefold increase in radiation levels. This radiation, by the way, is in the biologically significant range from 290 to 300 nm.

As I have said, this graph is an overestimate because it does not take into account the effects of aerosol and molecular scattering. Dr. Hansen has completed calculations of the transmission of the atmosphere at 290 nm,

assuming the complete absence of ozone. He finds that even if all the ozone were to be removed from the atmosphere, the transmission of the atmosphere would still be about 30 percent. You would not get the solar constant down on your head if all the ozone were gone because radiation scattering would become of increasing relative importance as the ozone was reduced.

The essence of Hansen's calculation is the multiple scattering of photons by molecules and atmospheric aerosols, and he states that as a result the back-scattering is far greater than if the problem was done as a superposition of single scatterings.

To our knowledge, the effect of scattering in diminishing the ultraviolet intensity has not been fully appreciated in previous studies of this problem.

CHAIRMAN:

Are there any questions for Dr. Stewart?

MEMBER OF THE AUDIENCE:

What is the process in the atmosphere that will reduce ozone? Is there any process that will reconvert molecular oxygen to ozone?

DR. STEWART:

Speculation seems to center about the effect of oxides of nitrogen. That is a catalytic process. You start with nitrogen dioxide and the effect is to destroy odd oxygen. It converts both oxygen and ozone to O_2. So if you put these oxides into the atmosphere, you will destroy ozone and produce O_2. Of course, ozone is created in the first place because there is molecular oxygen in the atmosphere. This dissociates and the atomic oxygen reacts. It is certainly true that if you destroy ozone and get back more oxygen, some of that oxygen is going to produce ozone. We always have a balance between production and loss; but if you take the present equilibrium and put in constituents that rapidly convert oxygen and ozone to molecular oxygen, it seems to me you can only go in that direction. That is, you will shift the equilibrium toward more molecular oxygen and less ozone.

REFERENCE

1. Johnson, Harold: Catalytic Reduction of Stratospheric Ozone by Nitrogen Oxides. UCRL-20568, Univ. of California, 1971.

VERTICAL MOTIONS INFERRED FROM
SATELLITE RADIOMETRY

Dr. Vincent V. Salomonson

Medium resolution radiometer measurements on Nimbus 2 and 3 and
relatively high resolution measurements on Nimbus 4 have been made in
6.4- to 6.9- and 20- to 23-μm water vapor absorption regions where the
weighted means in the observed radiation occur in the troposphere near the
40- and 60-kN-m^{-2} (400- and 600-mbar) levels, respectively. An illustrative
example of the imagery obtained from the Nimbus 4 temperature-humidity
infrared radiometer (THIR) is shown in Figure 1. This example demon-
strates clearly that there is a distinct pattern difference between the 6.7-μm
observations coming from the midtroposphere and the more common 11.5-
μm "atmospheric window" observations showing the emitted radiation
associated with opaque surfaces such as the ground or optically thick clouds.
The water vapor observations show considerable detail that is not well
understood along areas where jetstreams and pressure troughs are occurring.
We know that the darker areas in the 6.7-μm imagery are associated with
relatively dry air and the lighter areas are associated with relatively moist
or cloudy regions. Some qualitative explanations have been given in the
past to explain how these observed features occur but very little definitive
and quantitative work has been published that describes in detail the
dynamic conditions such as vertical velocity and mass divergence that are
associated with water vapor patterns such as those shown in the figure.

Over the past year this task of deriving dynamic parameters from conven-
tional meteorological data and explaining the satellite observations has
been undertaken using a 10-level diagnostic numerical model that pro-
vides relatively reliable, but otherwise difficult to obtain computations of
vertical motion. A typical meteorological situation involving a well-
defined pressure trough occurring over the United States October 17,
1969, was selected for study. At this time Nimbus 3 observations were
available in both the 6.4- to 6.9- and 20- to 23-μm spectral regions at
approximately 0600 Greenwich meridian time (GMT). The synoptic
situation as represented by the flow at 50 kN m^{-2} (500 mbar) (5 km) for
this time is shown in Figure 2. The trough in the pressure field extending
from Hudson's Bay southward to the Great Lakes can be seen along the
movement of this trough over the 12-hr period between 0000 and 1200
GMT on October 17. Vertical motions and other dynamic parameters
were computed for both the standard 0000 and 1200 observation times.
The 50-kN-m^{-2} (500-mbar) vertical-motion results, as interpolated to the
satellite observation times of 0600 GMT, are shown in Figure 3.

Figure 1—Imagery obtained from the Nimbus 4 THIR, May 14, 1970. (a) 6.7-μm wavelength observations.
(b) 11.5-μm wavelength observations.
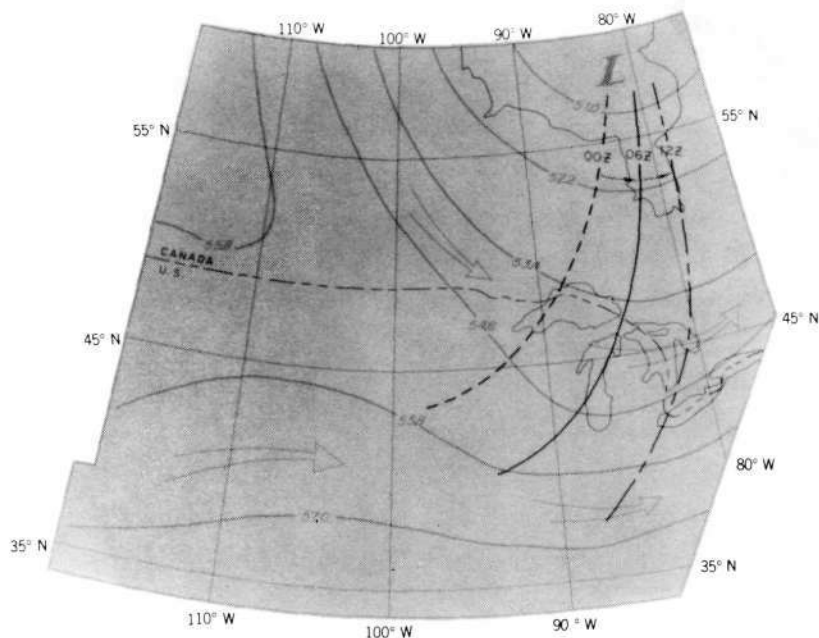
Figure 2—Motion of 50-kN-m^{-2} (500-mbar) flow at 0600 GMT, October 17, 1969.

All areas of sinking motion are within the area outlined with heavy black; are outside this area. The areas with more pronounced sinking or rising motions are in darker tones. Superimposed on the vertical motion field are the observed 20- to 23-μm brightness temperature patterns as represented by the 245, 251, and 258 K isotherms. One can easily note the general correspondence between the areas of sinking motion and the brightness temperatures greater than 251 K. In particular, note the correspondence between the area of maximum sinking motion and the 258 K isotherm. In the case of rising motions versus brightness temperature patterns, some ambiguity is introduced by clouds, and as a result the agreement is not quite so good. The same overall agreements shown in Figure 3 is also found in the 6.4- to 6.9-μm results when the fact that these observations occur at a higher level is taken into consideration. In conducting this research it has also been found that the radiometric observations of water vapor are very useful in providing more representative spatial detail in the analysis of point measurements of water vapor made by standard meteorological radiosonde networks.
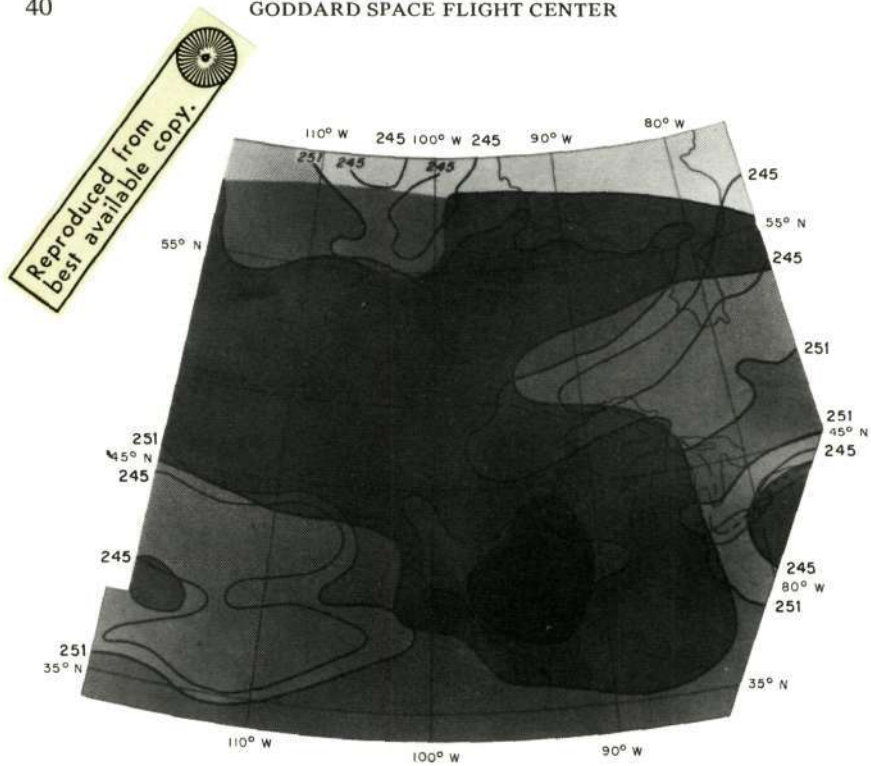
Figure 3—Vertical-motion results as interpolated to the satellite
observation times of 0600 GMT.

In this study it is felt that quantitative verification has been provided that
shows that Nimbus radiometric water vapor observations are reflecting im-
portant dynamic processes in the middle and upper troposphere and that
these observations can be reliably used to delineate areas of vertical motion,
particularly areas of strong subsidence or downward vertical motion. Cer-
tainly one can now proceed with a higher degree of confidence in applying
these satellite observations to the study of weather systems in the tropics
and large oceanic regions such as those in the Southern Hemisphere, where
conventional meteorological data are sparse or nonexistent.

CHAIRMAN:

Are there any questions?

MEMBER OF THE AUDIENCE:

Why is it that one should expect warmer brightness temperatures with downward motion?

DR. SALOMONSON:

Observations made in the 6.4- to 6.9-μm and 20- to 23-μm spectral regions are sensitive to water vapor. When downward motion occurs, moisture at a given height is normally replaced by drier air and moved downward to a region of warmer atmospheric temperature. This causes the weighted mean associated with the observed brightness temperature of the two spectral regions to occur at a lower altitude and, as a result, to appear warmer.

STUDIES WITH SATELLITE RADIOMETER DATA

Dr. Milton Halem

Our work with satellite radiometer data has been concentrated on preparing for the data we expect to receive from ITOS D next spring and Nimbus E next fall. The vertical temperature profile radiometer (VTPR) on ITOS D will provide temperature data with sufficient coverage to test the results of the simulation studies that were carried out earlier. These studies indicated that global winds could be derived from the temperature data with sufficient accuracy to allow forecasts of improved quality. We are preparing to experiment with the ITOS speed data on a near realtime basis through a data link to Suitland. In preparing for the ITOS D data, we have obtained two important results which we would like to report on today.

The main limitation in our earlier work was the crudeness of the Mintz-Arakawa model which GISS borrowed from UCLA to use in these earlier simulation studies. The model was especially poor in its use of only two vertical levels for determining the entire vertical structure of the atmosphere. We have therefore rebuilt the model with an arbitrary number of vertical levels. We have also rebuilt the physics in the areas of radiative transfer and cloud effects.

We thought that the five-level model would be sufficient, but we recently discovered at the meeting of the Joint Organizing Committee — which is the scientific body for planning at the international level under the Global Atmospheric Research Program — that five levels may not be adequate and nine levels appear to be required. We now have our model working with both five and nine levels and have tested it and have proved that it works well under the shocks of inserted temperature data and as a model for generating forecasts. Although we are not in the forecasting business, we need to run forecasts on occasion because accuracy is our principal means of judging the quality of the winds that we obtain from the temperature data.

Figure 1 shows the comparison between the old UCLA two-level model, the improved GISS five-level model, and the observations obtained from the National Meteorological Center (NMC) for the period of July 1 to 3, 1970. Both models were started from NMC observations for the Northern Hemisphere for July 1 as the initial states. The figure shows that after 48 hr, the agreement between the GISS five-level model and the observations are appreciably better than the UCLA two-level model.

F
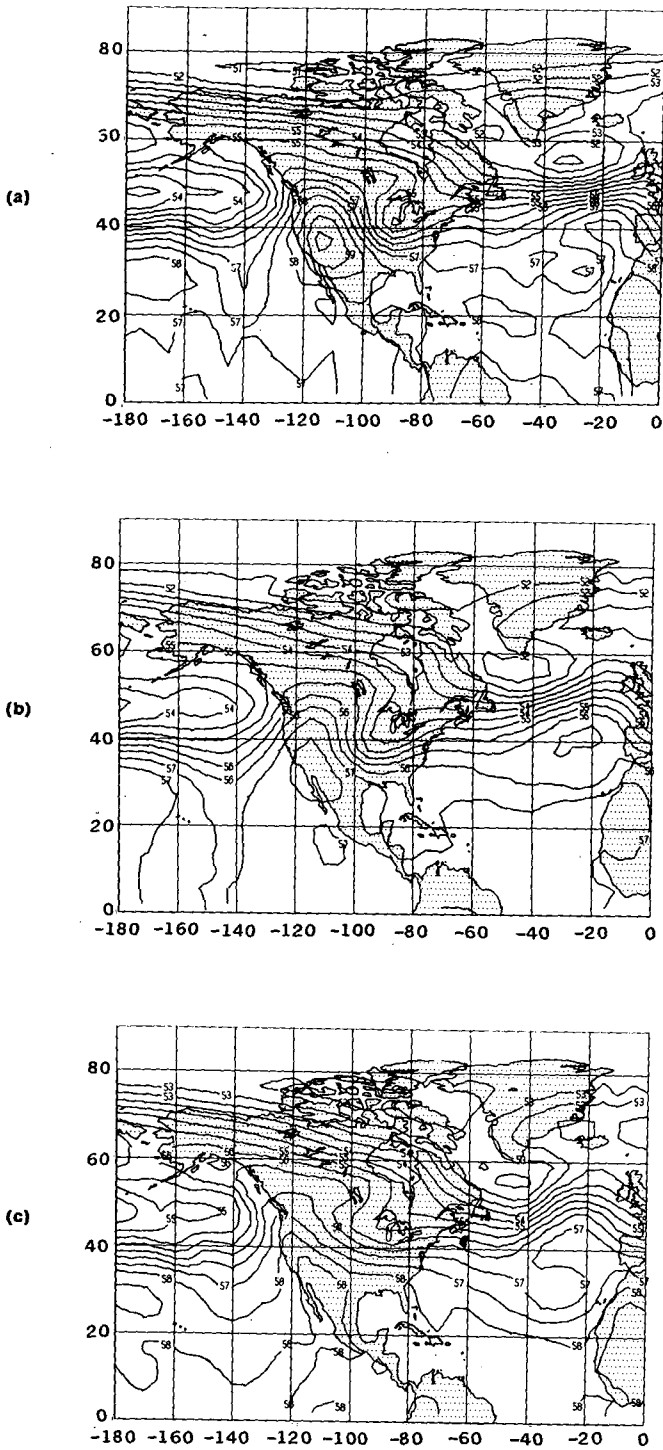
Figure 1—Comparison of 50-kN-m^{-2} (500-mbar) geopotential height analyses: (a) NMC observation; (b) Five-level GISS model; (c) Two-level UCLA model.

I would like to draw your attention in particular to the intensity and axis of the trough centered below the Great Lakes and to the high centered off the coast of California. Figure 1(a) represents the actual NMC 50-kN-m⁻² (500-mbar) geopotential height analysis for the same period 2 days after the initial study. Figure 1(c) indicates what we obtained from the two-level UCLA model. The axis of this trough did not change sufficiently in two days, nor did the high develop in the California region.

These results encourage us to continue the numerical modeling research in which the efforts will now be concentrated on the physics of the moist convection and the treatment of the planetary boundary layer.

As our second point of preparation for ITOS D, we developed methods for the four-dimensional assimilation of satellite radiometer data and tested these schemes with the currently available satellite infrared spectrometer (SIRS) radiance data. The results are shown in Figure 2.
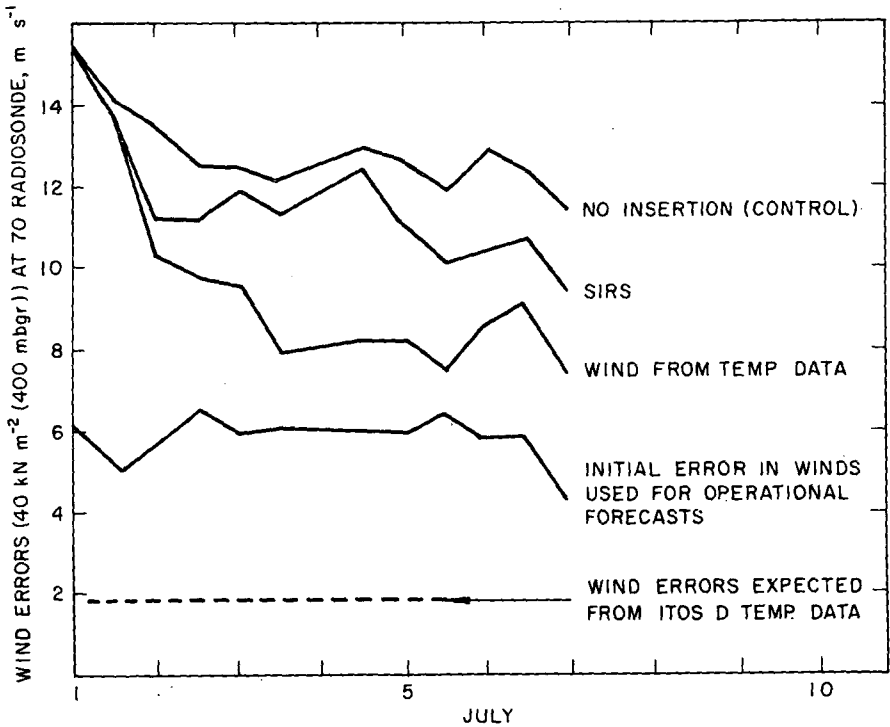
Figure 2—July 1970 experiment.

The average wind error plotted on the vertical axis is the difference between the observed winds obtained at 70 radiosonde stations in the Northern Hemisphere and the winds calculated from the model and interpolated to these stations. At the start of the experiment, the model was evolving along lines completely unrelated to the actual stage of the atmosphere on July 1, 1970. Our aim was to see whether the repeated insertion of the temperatures derived from satellite radiometer data would drive the winds into better agreement with the observations, as the simulation studies had indicated. The temperature inversion program was supplied by the Smith group at the National Environmental Satellite Service and was directly coupled to the atmospheric equations of the model; that is, the radiances were inserted as inputs and the temperatures were calculated internally.

The second graph from the top shows the effect of the SIRS temperature data. The effect is immediate, starting out at about 14 m s^{-1}, which is the normal value for two completely unrelated flows, dropping steadily to about 9 or 8 m s^{-1}. However, these wind errors are only about as good as the wind errors NMC obtains at the end of a 24-hr forecast. The third graph shows the effect of inserting real temperature data as obtained from NMC analysis, that is, a mass of ground-based data as well as SIRS satellite data. The temperatures were inserted at intervals corresponding to the amount of temperature data available for a single polar-orbiting satellite. The mean wind error for these data is about 6 m s^{-1}. At this level of wind errors, most of the major pressure features found in the Northern Hemisphere are correctly given. The bottom graph shows the expected wind errors from the VTPR obtained by performing simulation studies for this instrument. Serving as initial states, these should generate very good forecasts.

We have also completed major programs for imbedded grids designed to be used in conjunction with GATE and for high-resolution short-range forecast experiments utilizing dense data from geostationary sounders. We have completed modification of Dr. Shuman's six-level operational model to run on the GISS 360/95 computer. We will test the model dependence of our results by running the experiments on these two different models, GISS and NMC.

CHAIRMAN:

Are there any questions for Dr. Halem?

MEMBER OF THE AUDIENCE:

I would like to ask whether the improvement in error in going from the Nimbus SIRS radiometer to the future VTPR radiometer on ITOS is due to

the improved field of the instrument or to the scanning of the instrument or due to the accuracies. Do you know what the source of the improvement is?

DR. HALEM:

The source is precisely all three of the factors you mentioned. The SIRS has a field of resolution of about 250 km. The VTPR is expected to have a field of resolution of about 60 km. The SIRS did not have what we call true side-scan coverage, having what was really a side stepping along the vertical path. The VTPR will provide us with the side-scanning coverage so that we will have almost contiguous coverage of the Earth in 12 hr. And, finally, with this improved vertical resolution, we do expect to get better accuracy in the retrievals, mainly because we expect to see through more clouds.

THE "NONEFFECT" OF SOLAR ECLIPSES ON THE ATMOSPHERE

John S. Theon

Solar radiation, of course, provides not only the long-term driving force for the entire circulation of the atmosphere but is also responsible for the thermodynamic structure of the upper atmosphere. Absorption of solar ultraviolet radiation by ozone near 50 km provides the heat necessary to sustain the warm feature known as the stratopause, and absorption of extreme ultraviolet radiation at levels above 80 km gives rise to the structure known as the thermosphere. Thus, a solar eclipse presents an opportunity to examine the effect that a sudden removal of solar radiation would have on this structure. The effects of the eclipse that occurred on March 7, 1970, were explored with three pitot probe rocket soundings launched from Wallops Island, Va., at times during a 42-min period corresponding to 40, 80, and 100 percent totality.

Figure 1, which is a plot of the temperature profiles obtained during the course of the eclipse, indicates that the atmosphere was indeed disturbed. There were many small-scale features that appear to have persisted from one sounding to the next, especially below 90 km. At levels above 100 km, the changes were very large. At many levels, the progressive removal of solar energy was accompanied by warming, which eliminates the simplistic direct-heating viewpoint as an explanation of the changes.

Because radiative considerations alone could not account for these variations, dynamic explanations were sought. Figure 2 shows the temperature changes observed during the eclipse as a function of time for altitudes of 60, 80, 100, and 120 km. Note that at 60 km there was a 2 to 4 K continuous cooling as the eclipse progressed. At 80 km, cooling also occurred between the first two soundings, but a warming trend had begun at the time of the third sounding, when the eclipse was total. At 100 km, initial cooling was followed by a substantial 16 K warming at totality. The temperature history at 120 km indicates that a sharp warming of 65 K at 80 percent totality was followed by a temperature drop of 100 K during the final 15 min. preceding totality.

There was great temptation to attribute these large changes solely to the eclipse; however, it was recognized that soundings with this type of time and altitude resolution had never before been obtained at this latitude and time of year, so another series of soundings was conducted on a day about 1 yr later at the same place and at times identical to those of the eclipse day. The results of the second series are shown in Figure 3. Initially
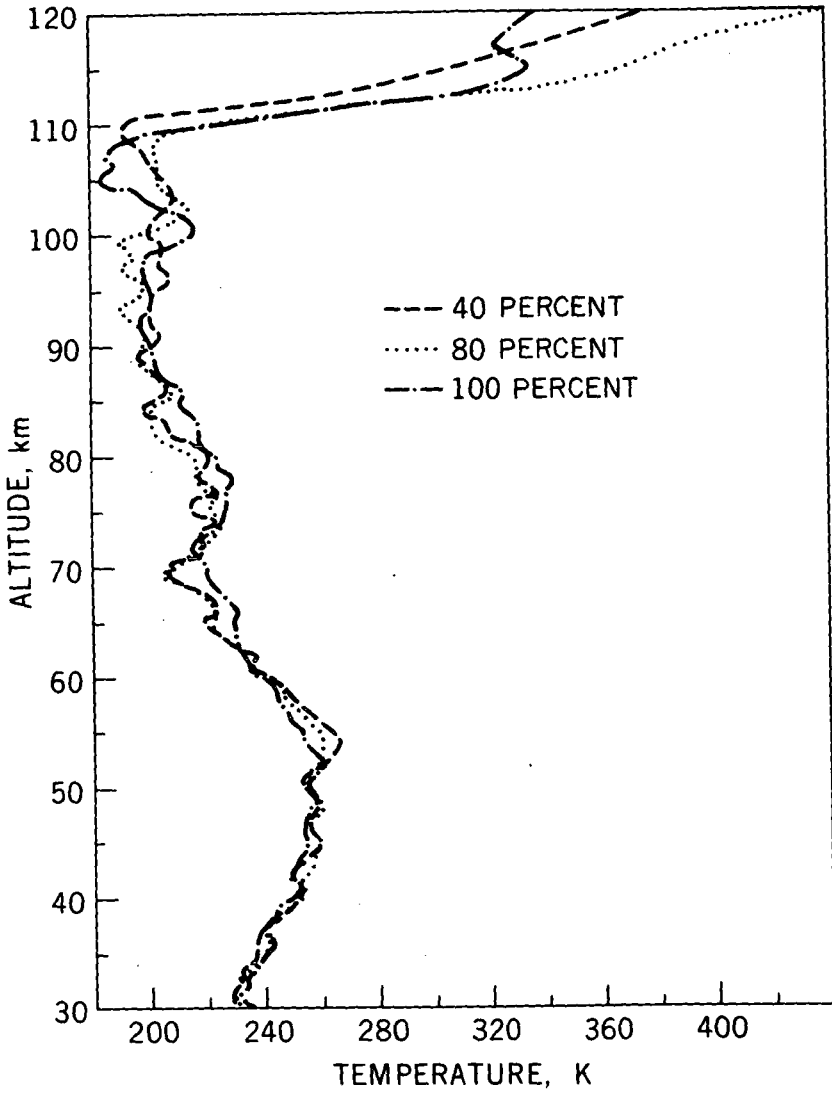
Figure 1–Temperature profiles of upper atmosphere obtained during the solar eclipse.
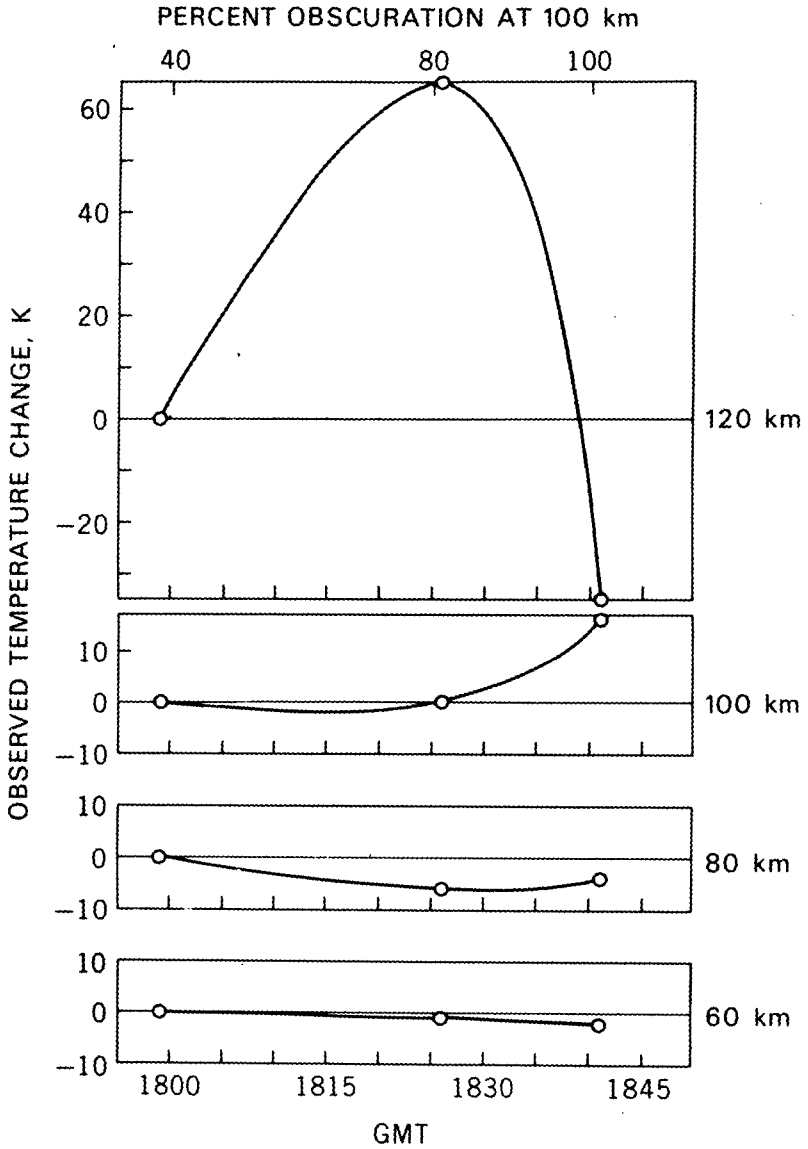
Figure 2—Temperature changes of upper atmosphere as a function of time during the solar eclipse.
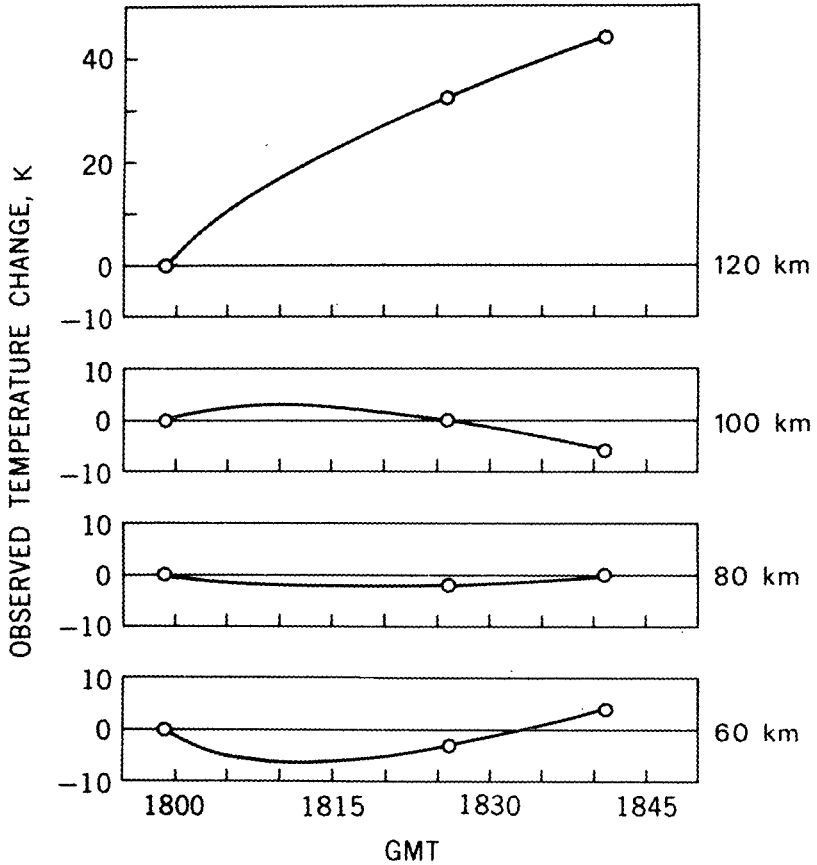
Figure 3–Temperature changes of upper atmosphere as a function of time under normal solar conditions.

there was cooling at 60 km, larger in magnitude than that observed during the eclipse, followed by a warming of about 10 K. At 80 km, the eclipse day and the normal day were almost identical. At 100 km, there was first warming, then cooling similar in amplitude, but opposite in phase to the changes observed on the eclipse day. At 120 km, a continuous warming of approximately 45 K occurred during the 42-min period, demonstrating that the thermosphere was in a disturbed state during both series of soundings. At 120 km, the 45 K warming on the normal day is comparable to the 65 K warming observed during the eclipse, and it is not possible to determine

whether cooling comparable to that observed on eclipse day occurred on the normal day. These two series of soundings clearly demonstrate that there are large and rapid variations in the structure of the upper atmosphere which must be of dynamic origin, but that these phenomena, be they tides or gravity waves, are not uniquely generated by a solar eclipse as some theoreticians had predicted. Therefore, caution should be exercised when interpreting measurements made during an eclipse unless measurements made under normal conditions are available for comparison.

THE GLOBAL HYDROGEN BUDGET

Henry C. Brinton

Atomic hydrogen is one of the most important, and at the same time least understood, constituents of the Earth's atmosphere. Because of difficulties associated with the measurement of hydrogen, neither its absolute density nor its complex temporal variations are known with certainty. Today I would like to report on a study, based on Explorer 32 data, that has produced unique experimental results bearing on the atomic hydrogen question.

Figure 1 depicts the major processes governing the distribution of hydrogen. It is produced by photodissociation of water vapor in the mesosphere, and diffuses upward into the thermosphere. Because of its low mass, hydrogen is subject to thermal planetary escape, and its concentration and global distribution are therefore largely governed by the atmospheric temperature T_g.
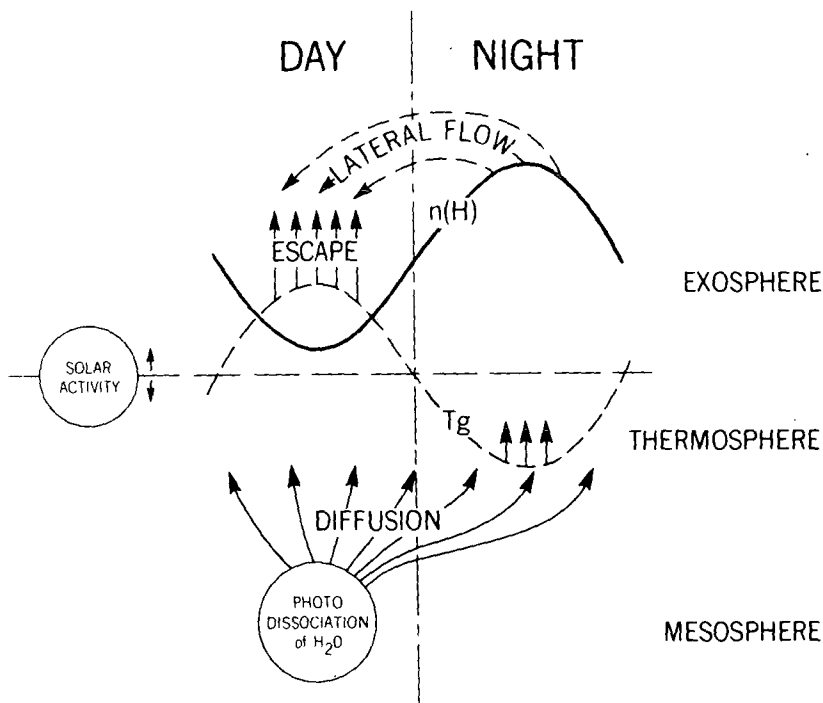
Figure 1—The major processes governing the distribution of hydrogen.

Since T_g is higher on the dayside of the Earth than on the nightside, the escape rate is higher during the day and the dayside hydrogen density $n(H)$ is consequently lower.

The process referred to as lateral flow, in which hydrogen is transported around the Earth from the region of high concentration to the region of lower concentration, reduces the magnitude of the diurnal variation which would result from escape alone.

Adding to the complexity of the daily variation is the fact that the range of T_g rides up and down with long-term variations of solar activity.

The upper graph of Figure 2 shows the observed variation of hydrogen concentration at 350-km altitude above the continental United States during the period June 1966 to January 1967. The hydrogen densities were derived from the chemical equilibrium relationship shown at the left of the graph, which holds at thermospheric heights. The H^+ to O^+ ratio was obtained directly from Explorer 32 measurements; the $n(O)$ values by which the ratio is multiplied to obtain the hydrogen densities were obtained from an atmospheric model, the accuracy of which was verified by Explorer 32 pressure gage results.

During the period of measurement, the satellite orbit phased through two diurnal cycles; the local time scale is shown at the top of the graph. Note that periods of higher concentration correspond to nighttime hours and periods of lower concentration correspond to daytime hours. This behavior is evidence of the diurnal variation that I described earlier. The general decrease in hydrogen concentration during the measurement period resulted from an increase in solar activity, and hence atmospheric temperature and thermal escape, during the 8-month interval.

Analysis has resolved the observed hydrogen temporal variation into a number of density components, each associated with a primary factor affecting the atmospheric temperature. The solid line in the lower graph represents the diurnal density component, and indicates that the thermospheric hydrogen concentration increases by about a factor of 2 between day and night. This diurnal component is shown superimposed on the observed hydrogen densities in the top graph. The scatter of points about the diurnal curve is caused by the presence of other components in the hydrogen temporal variation, one of the most important being the solar activity component, shown by the dashed line in the bottom graph. Note the long-term density decrease due to rising solar activity and the 27-day variation in this component associated with solar rotation.
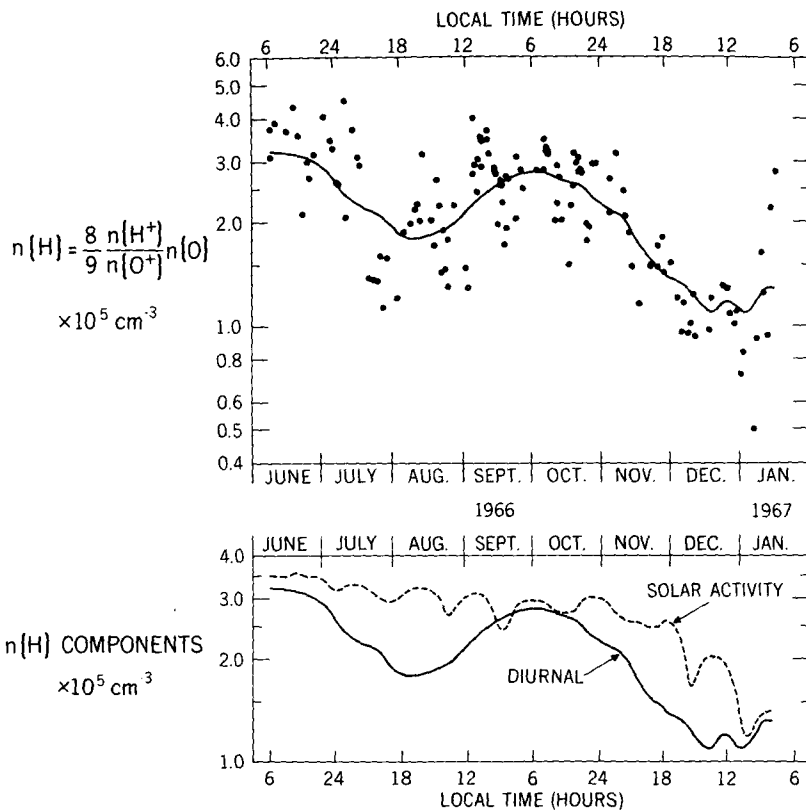
Figure 2—The observed hydrogen temporal variation and two of its components.

In conclusion, I would like to speak about the significance of these results. As shown in Table I, our observations differ markedly from the hydrogen behavior given by several model atmospheres currently in use, both in the amplitude of the diurnal variation and in absolute hydrogen density. Our factor of 2 for the night-to-day density ratio clearly disagrees with both the CIRA (Ref. 1) and Jacchia (Ref. 2) empirical models. It tends to confirm, instead, the theoretical hydrogen models of McAfee (Ref. 3) and Patterson (Ref. 4), both of which include the effects of lateral flow.

The last column in this table shows that our observed hydrogen density at 350-km altitude exceeds previous estimates by a factor of 3 to 10. This new information on the thermospheric hydrogen content could have important implications, and I will mention two.

TABLE I. Atomic Hydrogen in the Thermosphere

		$\dfrac{n(H)_{NIGHT}}{n(H)_{DAY}}$	$\overline{n(H)}$ at 350 km
MODEL ATMOSPHERES	CIRA	~1.1	4×10^4
	JACCHIA	~4	1×10^5
THEORETICAL HYDROGEN MODELS (INCLUDING LATERAL FLOW)	McAFEE	~2	
	PATTERSON	~2	
EXPLORER 32 IN SITU OBSERVATIONS		~2	3×10^5

First, the interpretation of airglow observations of the hydrogen geocorona is dependent on an assumed global hydrogen distribution at thermospheric heights; a spherically symmetric distribution (that is, one with no day-to-night difference), which is frequently assumed, is not correct according to our results.

Second, a revised hydrogen distribution could have important implications for our understanding of the ionosphere because the protonosphere is populated during the day by hydrogen ions created at lower altitudes by charge transfer between atomic hydrogen and O^+. At night this process reverses, and the protonosphere contributes to the maintenance of the nighttime F region. A full evaluation of these processes is clearly dependent upon knowledge of the atmospheric hydrogen density and its variation with time.

CHAIRMAN:

Questions?

MEMBER OF THE AUDIENCE:

You have shown that some of your measurements deviate somewhat from the standard models, but they do not reflect the knowledge of the atomic oxygen concentrations based on the same models. What reason do you have to believe that oxygen does not vary just as much as your deduced hydrogen content?

MR. BRINTON:

As I mentioned, we verified the model which we use for oxygen by means of pressure gage results from the same satellite, Explorer 32. Now, in the altitude range of these observations, the composition of the atmosphere is almost pure oxygen; and in the very limited range of latitude and longitude covered by these observations, George Newton's pressure gage results (Ref. 5) are in essentially perfect agreement with the model that we use.

I think that it is the latitude limit on the observations that makes the model good; that is, we confine ourselves to midlatitudes above the continental United States.

CHAIRMAN:

Are there other questions?

MEMBER OF THE AUDIENCE:

There is another comment to that. The reason why I think the model is incorrect as far as hydrogen is concerned is that it assumes diffusive control. You have to include thermal escape; this has not been taken care of in the hydrogen models.

MEMBER OF THE AUDIENCE:

Would your higher hydrogen densities say something about the rate of escape of water from the atmosphere?

MR. BRINTON:

They may. Since hydrogen is formed by dissociation of water vapor, and the hydrogen escape rate is proportional to its density, and since we are obtaining densities a factor of 3 to 10 times higher than previous estimates, it would be implied that the loss of water vapor from the Earth's lower atmosphere is proceeding at a greater rate than heretofore thought. Most of the water vapor, of course, does not reach high enough altitudes because of the cold-trap effect.

MEMBER OF THE AUDIENCE:

I was wondering if you had compared your new results with the results that Keating and some of his associates had come up with.

MR. BRINTON:

Yes, we have. I think you are speaking of his drag results at very high altitude, 2000 km or so (Ref. 6). His results also indicate higher hydrogen densities by about a factor of 3 than predicted by the models.

REFERENCES

1. COSPAR Working Group IV: COSPAR International Reference Atmosphere, 1965 (CIRA, 1965). North-Holland Pub. Co. (Amsterdam), 1965.

2. Jacchia, L. G.: Static Diffusion Models of the Upper Atmosphere With Empirical Temperature Profiles. Smithson. Astrophys. Observ. Spec. Rep. 170, Dec. 1964.

3. McAfee, J. R.: Lateral Flow in the Exosphere. Planet. Space Sci., Vol. 15, 1967, p. 599.

4. Patterson, T. N. L.: The Diurnal Variation of the Atomic Hydrogen Concentration at the Base of the Exosphere. Planet. Space Sci., Vol. 14, 1966, p. 425.

5. Newton, G. P.: Latitudinal Dependence of the Diurnal Density Variation. J. Geophys. Res., Vol. 75, 1970, p. 5510.

6. Prior, E. J.: Hydrogen Drag Deduced from Simultaneous Measurements Near 2300 km and 2800 km. Paper presented at Spring Meeting, Amer. Geophys. Union, (Washington, D.C.), 1971.

MAGNETIC CONTROL OF THE HIGH-LATITUDE THERMOSPHERE

Dr. Alan E. Hedin

I am going to describe observations of composition and density made with the neutral mass spectrometer on the polar-orbiting OGO-6 satellite. The observations were made during a quiet magnetic period in late August and early September 1969 when the satellite perigee was near the South Pole.

The observations show that there are marked cyclic variations in density and composition which have a 24-hr period, and these are interpreted to indicate a significant heat input into the polar thermosphere, possibly due to particle precipitation.

Figure 1 shows the variations of helium, nitrogen, and oxygen density as a function of time at constant altitude. Note the cyclic variation in both N_2 and helium, with N_2 and helium being out of phase. Oxygen shows no particular strong effect. (This is atomic oxygen; we could not measure O_2.)

To interpret these measurements, we should keep in mind that the plane of the satellite orbit was essentially fixed with respect to the Sun, so that these observations are essentially at uniform local time; but as Greenwich time progresses and the Earth turns underneath the orbit, we see a succession of longitudes. In other words, longitude is perfectly correlated with universal time.

Figure 2 shows the latitude distribution of this phenomenon. We have contours of constant nitrogen and helium densities plotted on a geographical latitude-longitude grid. We note a maximum in nitrogen at approximately $160°$ W longitude and $70°$ S latitude and at the same time there is a minimum of helium.

Now, upon examining individual orbits of the satellite, we found that nitrogen densities actually tend to maximize at close approach to the magnetic pole; but the orbits which occurred near 8 hr Greenwich mean time, which corresponds to $160°$ W longitude, indicated the highest overall densities, and these dominate the picture.

To understand these unique observations of composition, when nitrogen is increasing at a time when helium is decreasing, we can refer to a theory proposed by Hans Mayr of our laboratory. This theory indicates that the effect

58
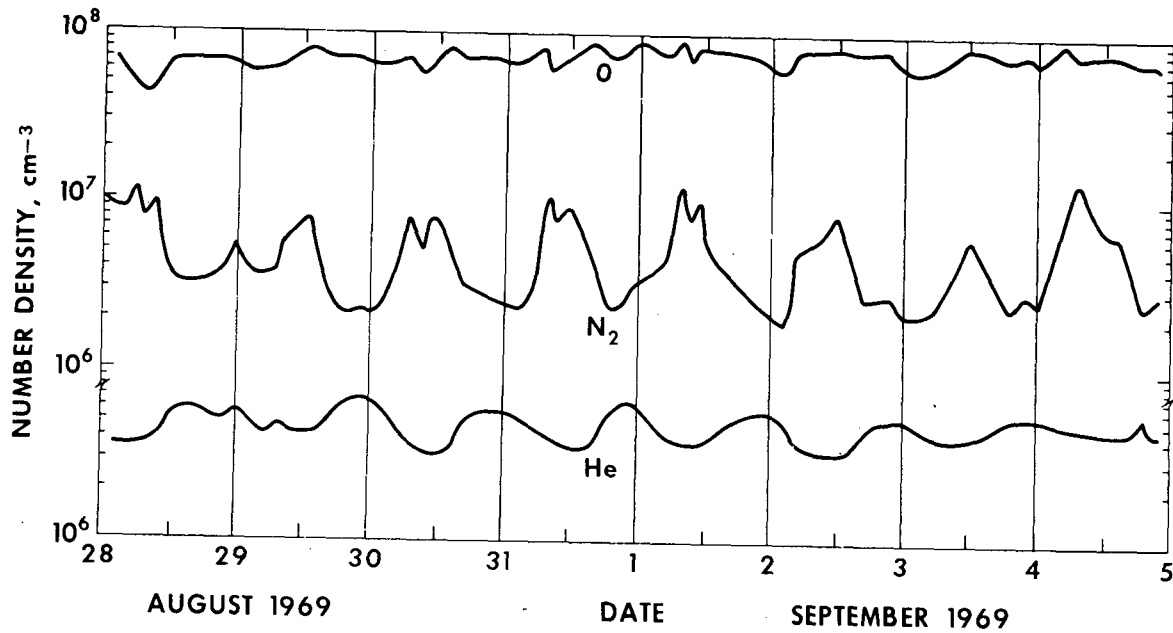
Figure 1 – Gas densities at 430-km altitude as observed by the OGO 6 satellite near the South Pole.
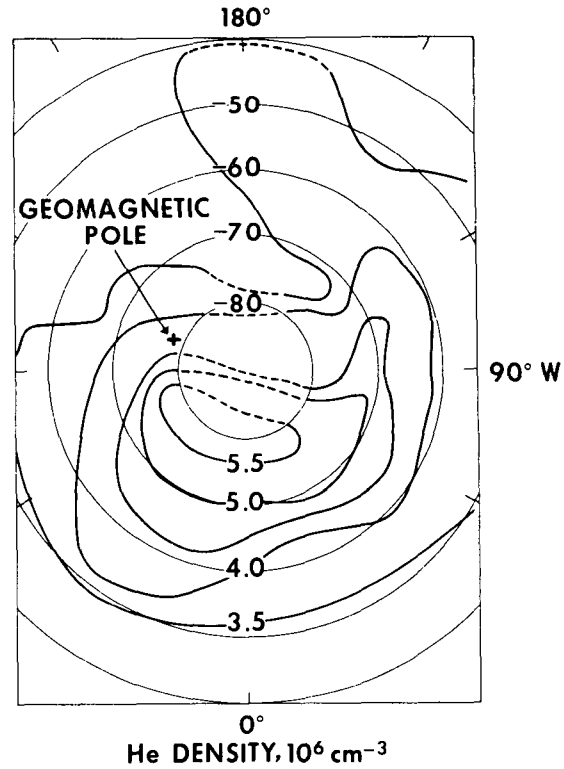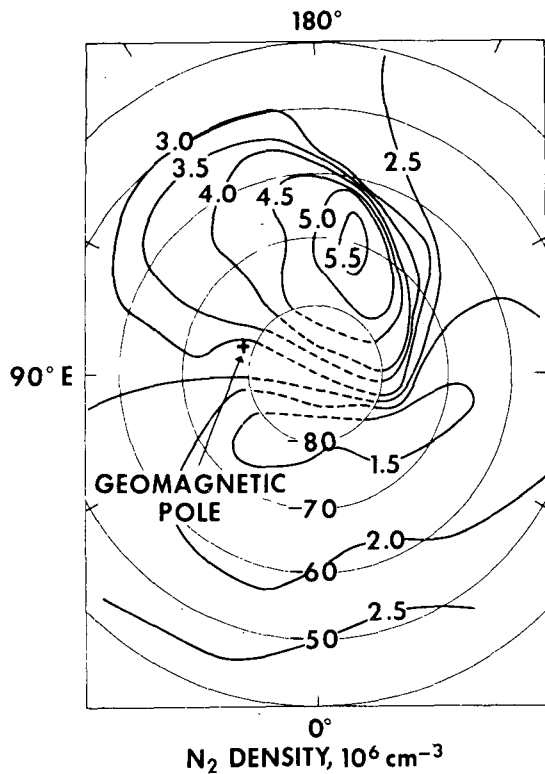
Figure 2–Contours of observed constant N_2 and helium densities plotted on a geographical latitude-longitude grid. Densities are extrapolated to 450 km.

of heat input into the thermosphere would, through increased temperature and establishment of a circulation pattern, result in just the types of composition changes observed. The heavier gases, such as nitrogen, would tend to increase at the time of energy input; and light gases, like helium, would tend to decrease at certain altitudes.

If we take into account the fact that observations of electron density made simultaneously on the OGO satellite also have strong variations and correlate very strongly with the nitrogen densities, this suggests that particle precipitation would be a likely explanation for this heat input.

It is known from measurements that the poleward boundary of auroral electron precipitation shows periodic variations that are consistent with these observations. We would expect that particle precipitation would have a periodic variation because the Earth's magnetic dipole is going through a 24-hr period with respect to the Sun.

In summary this suggests that there is a modulation in the magnetosphere causing a modulation of electron precipitation. This precipitation heats the atmosphere directly or through joule heating, and this increased joule heating causes a change in the composition of the atmosphere.

CHAIRMAN:

Are there any questions?

MEMBER OF THE AUDIENCE:

How much did the temperature increase at this time and have you attempted to correlate the temperature measurement in the atmosphere with the Blamont red line measurement?

MR. HEDIN:

We have been trying to get his measurements. We just do not have the exact thing to compare with ours. There are difficulties in that he does not measure at the satellite position or altitude and so it is not easy to correlate his data with ours. He also measures only in sunlight and these particular data were mostly obtained in darkness. The temperature change was on the order of a 200 K increase, I believe.

A NEW VIEW OF THE RING CURRENT

Dr. Masahisa Sugiura

The concept of the ring current was originally introduced about 40 yr ago to explain the worldwide field decrease observed during magnetic storms. Evidence for such a ring current has been found by satellite observations of particles and magnetic field. The idea that a ring current exists even at quiettimes has developed in recent years because it takes many days for a stormtime ring current to decay and because protons having energies similar to those of the particles considered to be responsible for the storm-time ring current are observed even during quiet periods.

OGO 3 and 5 observations have provided the first reliable magnetic field survey in the inner magnetosphere. The observations showed that both the intensity and distribution of the quiettime ring current are very much different from what has been usually thought. Figure 1(a) shows a contour map in the noon-midnight meridian plane of average ΔB observed during quiet periods by the Rb magnetometers on OGO's 3 and 5, where ΔB is defined as the observed scalar field minus the magnitude of a reference field calculated from a spherical harmonic expansion of the main field. The existence of a negative ΔB region near the dipole equator is clearly indicated. The minimum ΔB under average quiet conditions is about -40 nT (-40 γ). An example of a ΔB contour map for a theoretical ring current model is shown in Figure 1(b) (From Ref. 1). Important differences between the two ΔB distributions can be seen, for example, in the variations of ΔB on the dipole equator as a function of radial distance, as shown below the contour maps. The observed ΔB continues to decrease with decreasing distance; whereas ΔB in the theoretical model has a minimum at the center of a toroidal belt and recovers substantially toward the Earth. This indicates that the distribution of particles responsible for the equatorial -ΔB is different from that assumed in the model.

The problem of the quiettime ring current was once regarded as being settled when a belt of low-energy protons was observed by Frank (Ref. 2) and was identified as the quiettime ring current belt of the type shown in the model. That this was a case of misidentification becomes clear in Figure 2, where examples of OGO 3 and 5 observations along individual orbits are presented. Figure 2(a) shows the ΔB observed on OGO 3 and the plasma parameter β determined from Frank's observations of protons and electrons made on the same satellite, where β is the ratio of the plasma energy density to the

62
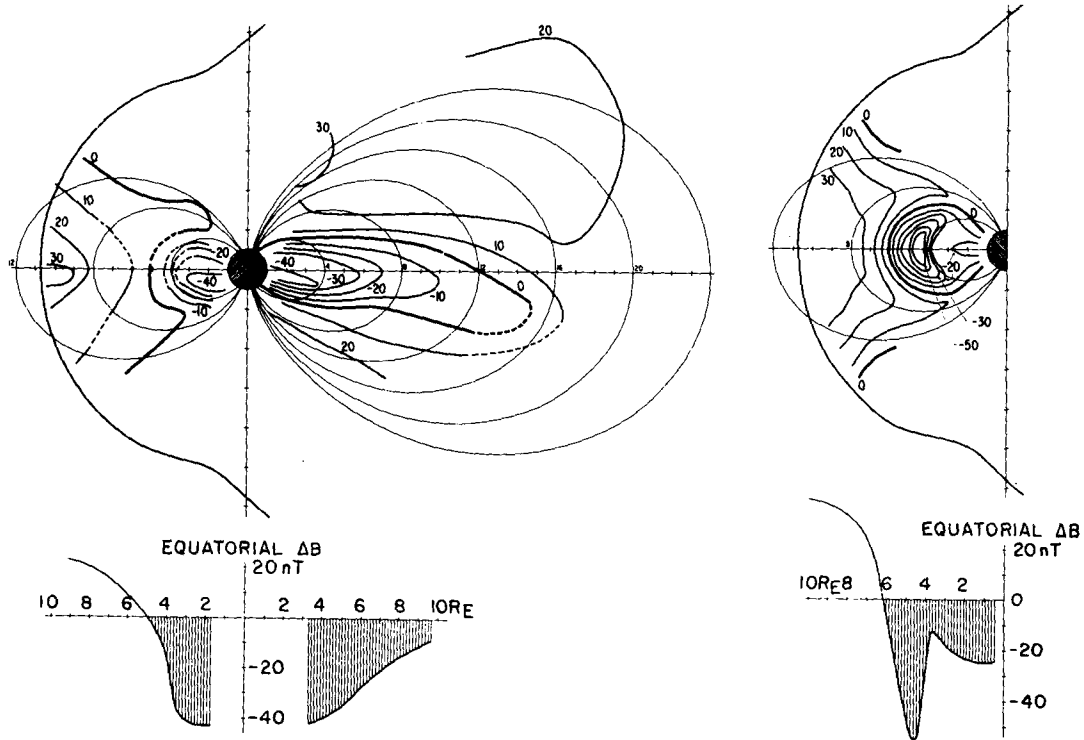
(a) Observed by OGO's 3 and 5, noon-midnight sectors, Kp = o to 1.

(b) Hoffman-Bracken (Ref. 1) quiettime ring current model.

Figure 1—Equal ΔB contours.
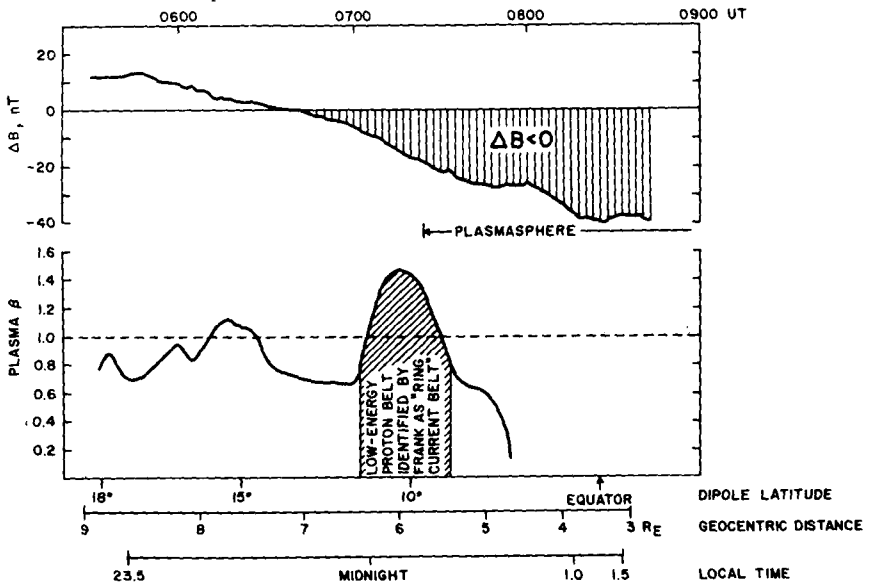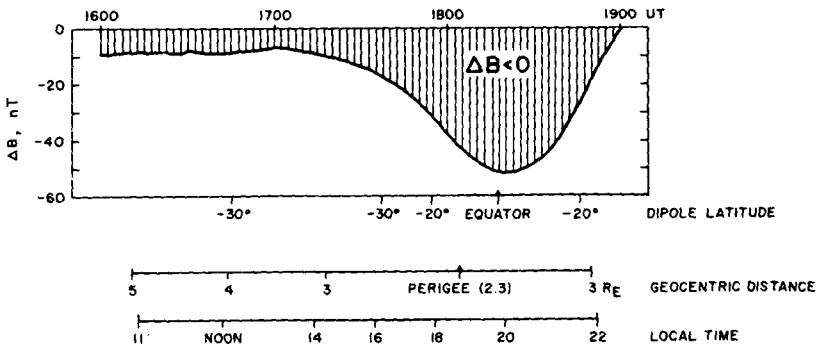
Figure 2—Satellite ΔB observations along individual orbits. (a) ΔB near midnight equator observed by OGO 3 Rb magnetometer. (b) ΔB near perigee observed by OGO 5 Rb magnetometer.

magnetic field energy density. The graph covers geocentric distances approximately from $9R_E$ to $3R_E$ (Earth radii) near midnight and from geomagnetic latitude 18° to a little below the dipole equator. It is clear that the high β belt near $6R_E$, which was called the "terrestrial ring current," cannot be responsible for the -ΔB observed well inside the plasmasphere. Figure 2(b) shows an example of the ΔB distribution obtained during a relatively quiet period (of Kp = 1+) by OGO 5 near perigee at 2.3 R_E; ΔB is about -50 nT (-50) near the dipole equator, which was crossed shortly after perigee.

Figure 3 summarizes the differences between the old view of the quiettime ring current (Fig. 3(a)) and the new view based on the OGO observations (Fig. 3(b)). In the old model a toroidal proton belt of doughnut shape was considered the cause of the field decrease in the near-Earth region. The OGO observations imply that the plasma responsible for this field decrease resides in an equatorial disklike region inside the plasmasphere.

The field energy density associated with the minimum ΔB (of about -40 nT) is greater than the plasma energy density estimated from the available thermal plasma observations by a factor of 10 or more. On the other hand, Frank claims that there are no significant fluxes of protons in the energy range 0.08 to 8.0 fJ (0.5 to 50 kEV) in the region in question. Thus, the identification of particles constituting the quiettime ring current is still left for future investigation.

REFERENCES

1. Hoffan, R. A.; and Bracken, P.A.: Magnetic Effects of the Quiet-Time Proton Belt. J. Geophys. Res., Vol. 70, 1965, p. 3541-3556.

2. Frank, L. A.: Relationship of Plasma Sheet Ring Current, Trapping Boundary, and Plasmapause Near the Magnetic Equator and Local Midnight. J. Geophys. Res., Vol. 76, 1971, p. 2265-2275.

C
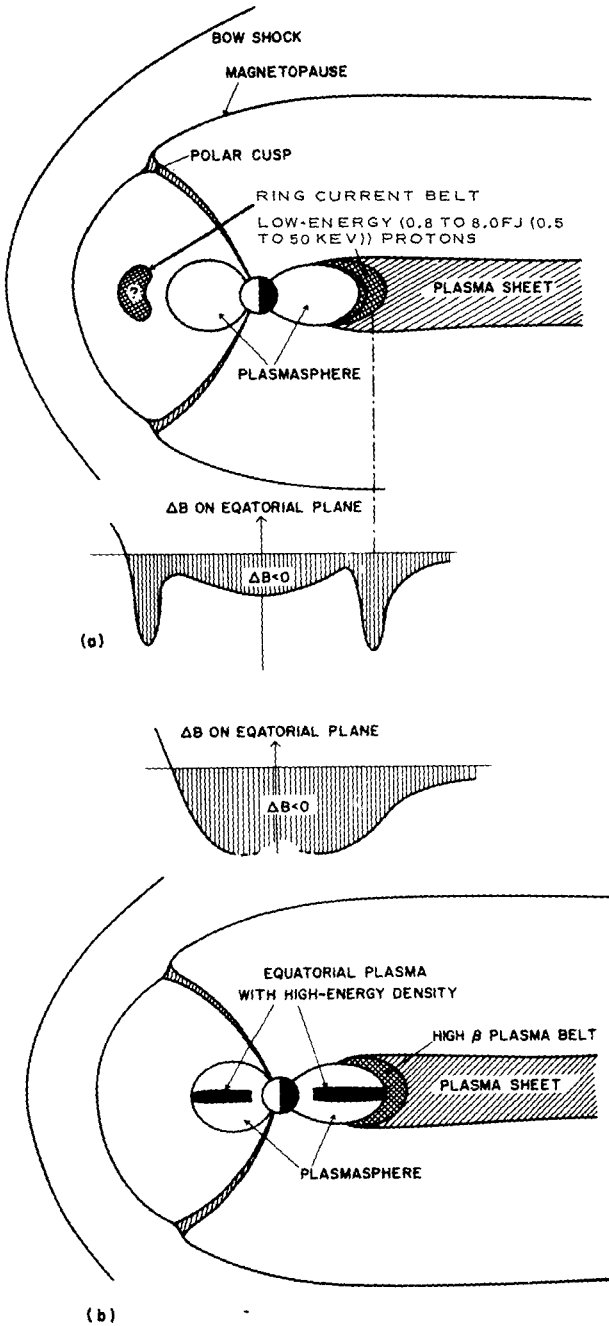
Figure 3–Quiettime ring current. (*a*) Conventional view based on old models.
(*b*) New view based on OGO observations.

THE MAGNETOSPHERIC PLASMA TAIL

Dr. Joseph M. Grebowsky

The dynamic state of the Earth's plasma environment is most evident during the onset and early recovery phases of intense magnetic storms. By observing the time delays between storm-induced plasma changes it is possible to delineate structural relationships that always exist but are not readily apparent under moderate activity. For this reason, thermal proton density measurements by the rf ion mass spectrometer on the low-altitude polar-orbiting satellite OGO 4 were compared on five consecutive nightside passes during the early recovery stage of an intense storm occurring in September 1967. These observations revealed a new feature of the Earth's plasmasphere.

The storm considered is shown in Figure 1, which depicts the Kp variation for September. The Kp index reaches values higher than 7 just before our measurements. The five consecutive nightside passes studied immediately followed the peak of the storm.
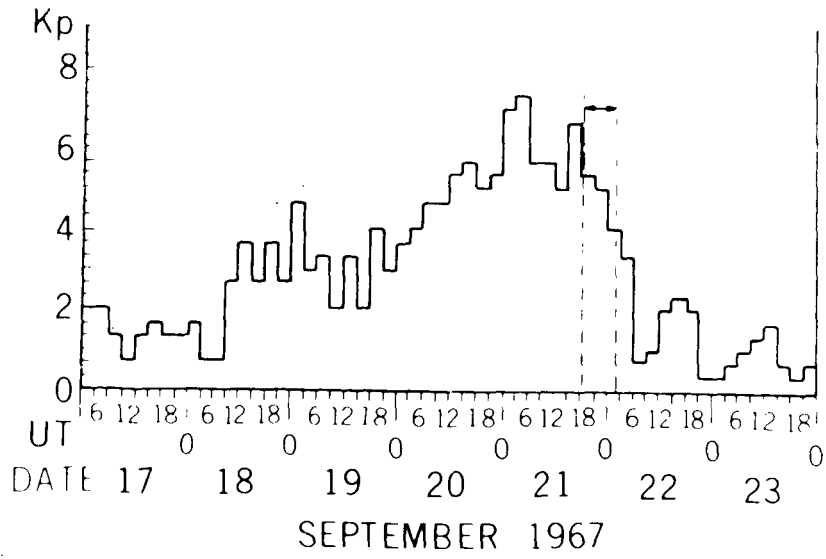
Figure 1—Magnetic storm depicted by the Kp variations. OGO 4 thermal proton observations were made during the period enclosed by the dashed lines.

Since the spectrometer was in a short sweep mode during this period, high
spatial resolution of the H$^+$ density along the OGO 4 trajectory was obtainable.
Figure 2 shows the proton density measured from north to south on each
of the five consecutive nightside passes near midnight. The L coordinate
denotes the equatorial geocentric distance of the magnetic field line passing
through the satellite; increasing L values correspond to increasing magnetic
latitudes.
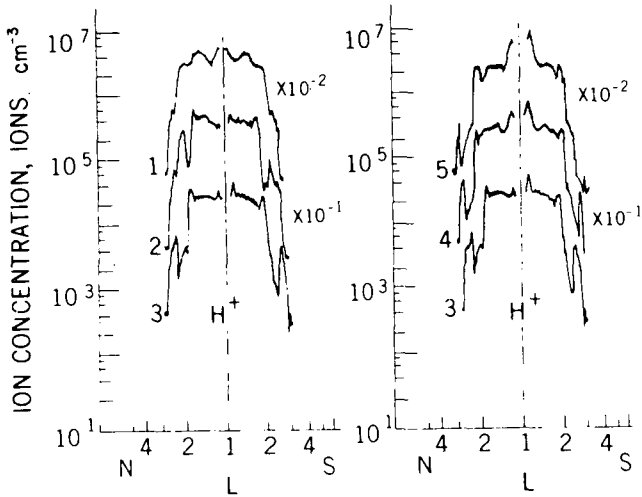
Figure 2–Proton density measured from north to south on each
of five consecutive passes by OGO 4.

The first pass after the peak of the storm shows the characteristic termina-
tion of the dense plasmasphere. This boundary, known as the plasmapause,
exists because plasma in the depleted region outside of the plasmasphere
drifts onto magnetic field lines which connect to the interplanetary field,
thus allowing a direct path by which the light ions can readily escape from
the Earth's environment. The plasmapause is alined along magnetic field
lines, as is readily apparent by the symmetry of its position about the
equatorial plane.

On the second nightside pass, 1.5 hr later, a new feature appears – a secondary
enhancement of the ion density poleward of the first abrupt plasmapause.
On successive passes this enhancement region moves to higher L values, cor-
responding to higher latitudes. At the same time the thickness of this region
of enhancement tends to decrease; after the fifth midnight pass, we could no
longer detect the enhancement.
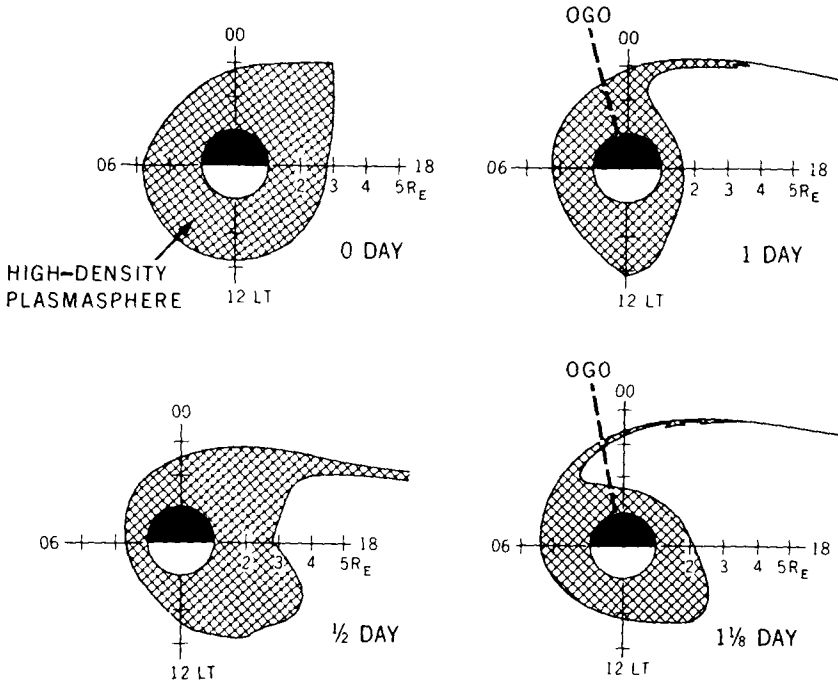
Figure 3—Model calculation of the high-density plasmasphere.

To give better perspective to the observations, a simple calculation is shown in Figure 3.

One day before the measurements the plasmapause variation with local time was taken as that typical of the average steady-state configuration with a bulge occurring in the dusk-midnight sector. Since the drift motion of magnetosphere plasma is a superposition of corotation with the Earth and a solar-wind-induced flow from the magnetosphere tail, the evolution of the plasmapause was computed by varying the magnitude of the tailwind in step with the Kp index as depicted in Figure 1. As shown, the September storm variation produced an elongated plasma tail attachment to the plasmasphere. The cusp of the streamer tends to rotate during the recovery phase of the storm through the satellite trajectory near midnight.

Along the orbit of OGO 4 this characteristic tail would produce an enhanced region of ion density poleward of the bulk of the plasmasphere. This second-ary peak of ion density would move to higher latitudes as the tail sweeps by the

trajectory of the satellite and at the same time the thickness of the enhancement region would decrease, as was observed by the satellite.

Hence the OGO measurements can be accounted for by the existence of an elongated plasma tail during the recovery phase of this storm.

Although considered here after an intense storm when tail development is pronounced, such a structure or even multiple tails of this type should also exist during relatively quiet magnetic conditions. Such extremely thin plasmasphere extensions would account for the irregularities often observed near or outside the body of the plasmasphere and could explain the origin of discrete elf emissions often observed in the depleted region known as the trough.

CHAIRMAN:

Any questions?

MEMBER OF THE AUDIENCE:

Was the OGO 5 operating at the same time as these measurements?

DR. GREBOWSKY:

No, it was not.

MAGNETIC FIELD OBSERVATIONS OF THE DAYSIDE POLAR CUSP

Dr. Donald H. Fairfield

Important information on the entry of particles into the magnetosphere was obtained by the IMP 5 spacecraft which made the first systematic measurements of the polar or dayside cusp. This region is illustrated in Figure 1, which is a view of the magnetosphere in the noon-meridian plane. The Sun is toward the left. Various boundaries and regions are labeled appropriately. The dashed lines represent magnetic dipole lines force and the solid lines represent more realistic distorted lines of force. The IMP 5 spacecraft makes passes through the region labeled "polar cusp," which separates the lines that close on the dayside of the Earth from those that go back over the polar cap.

The plasma instrument of Dr. Frank observes magnetosheath-like plasma in the polar cusp region down to altitudes of about 4 Earth radii. Low-altitude polar-orbiting spacecraft also detect magnetosheath-like plasma just above the ionosphere; apparently this magnetosheath-type plasma has access to the magnetosphere through the polar cusp region.

Today I would like to talk about the magnetic field measurements in this region. A very important subject that has been discussed for many years is the question of whether magnetosphere magnetic field lines become connected to the magnetosheath lines at a neutral point or is the magneto-pause tangential discontinuity such that the field lines in the magnetosheath are completely isolated from the field lines of the magnetosphere. If any connection were found to occur it would provide an easy explanation for the entry of plasma to the cusp region and also provide insight into the question of how energy is put into the magnetosphere. IMP 5 passes through the polar cusp in just the region where we would hope to be able to answer this question.

Figure 2 represents 4 hr of magnetic field data beginning outside the bow shock at about 12 Earth radii and continuing to about 6 Earth radii where the instrument becomes saturated. The top trace indicates the magnitude of the field on a logarithmic scale. Below this is ΔB, which is defined as the measured magnetic field minus the value of an internal reference field extrapolated from surface measurements. The inclination I and declination D are defined in the conventional sense and they indicate the direction of the field. The bottom trace is a standard deviation δ, which is a measure of the higher frequency fluctuations that are occurring at this time.

71
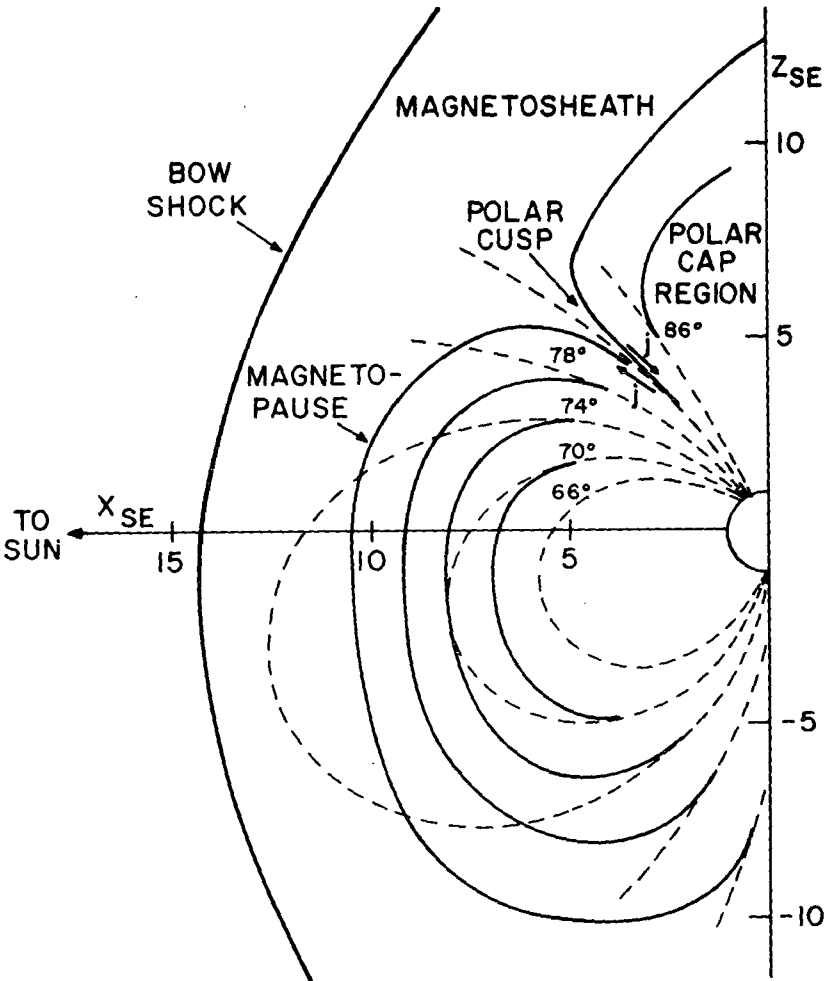
Figure 1—The magnetosphere in the noon-meridian plane.

The vertical dashed lines represent the boundaries of the polar cusp as defined by Dr. Frank's plasma experiment (Ref. 1). The primary characteristic of the magnetic field is the depressed nature of the field in this region. Field strengths are as much as 130 nT (130 γ) below the reference field in this region centered on the polar cusp. This means that field lines that certainly must connect to the Earth have field strengths that are only 30 to 40 percent of the dipole value.
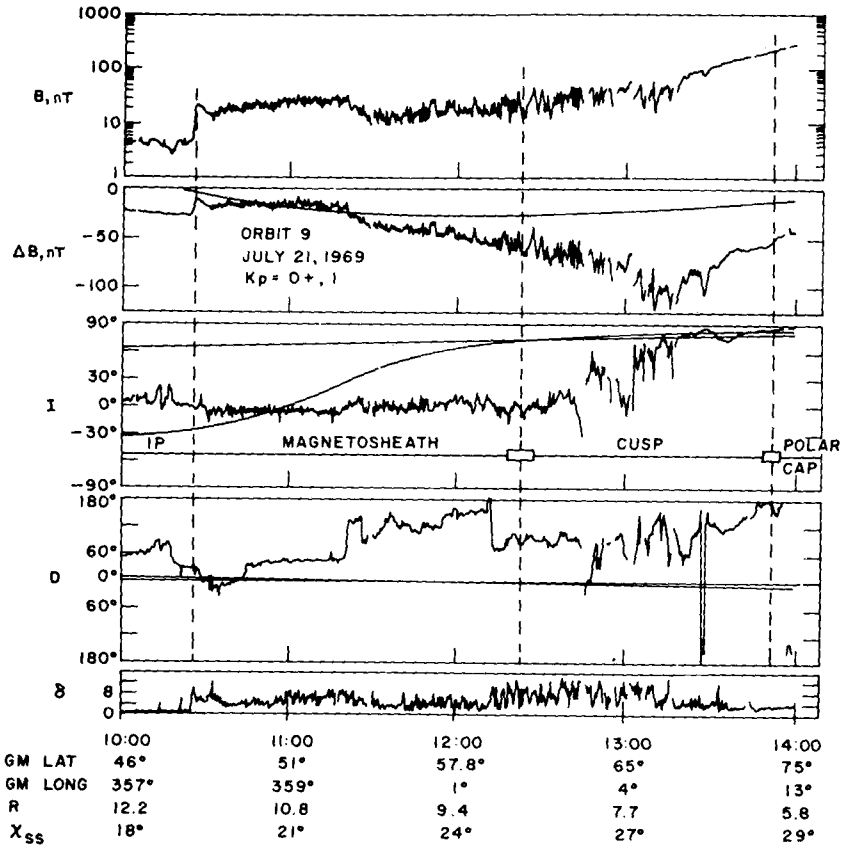
Figure 2—Magnetic field data obtained by IMP 5.

The second characteristic is the absence of a well-defined magnetopause on this pass. On the left portion of the magnetosheath, the field direction is determined by whatever the interplanetary field happens to be and on the right the direction is determined by the Earth's dipole. The transition between these two regions is gradual and many large fluctuations in direction are observed.

A third characteristic of the polar cusp is the presence of very large amplitude higher frequency fluctuations as are indicated by higher values of δ. Power spectra computed for this interval indicate more power than had been found on more than 70 similar intervals at lower latitudes in the magnetosheath.

The question of interconnection of field lines is usually approached by searching for a field component normal to a magnetopause boundary. Since a magnetopause boundary cannot even be found in this case, such an analysis obviously cannot be carried out. The question being asked is "what is the path of a field line in this region?" One must remember that a magnetometer makes a vector measurement at a given point in space. Therefore, only if the field retains this direction over a distance scale of many thousands of kilometers can anything be said about the path of the field line. In the case of the polar cusp the field is fluctuating rapidly with large amplitudes, so it is not easy to determine where the field line goes.

In summary, the magnetic field measurements in the polar cusp are characterized by unusually low magnitudes and large fluctuations. The low magnitudes can probably be explained by currents on the magnetopause and the diamagnetic effect of the plasma. The transition between the magnetosheath and the cusp portion of the magnetosphere is not characterized by a well-defined magnetopause as at low latitudes. The fact that there is no well-defined discontinuity is consistent with the interconnection of magnetosheath and magnetosphere magnetic fields, but there is no definitive proof that such reconnection does occur.

REFERENCE

1. Frank, L.: Plasma in the Earth's Polar Magnetosphere. J. Geophys. Res., Vol. 76, 1971, p. 5202.

RECENT PROBE MEASUREMENTS OF dc ELECTRIC FIELDS FROM IMP I

Dr. Thomas L. Aggson

Figure 1 shows the IMP I satellite. This was launched this spring into a rather eccentric orbit about the Earth. The electric field sensors are the long stem antennas. One pair was extended 91.5 m (300 ft) tip to tip and one pair extended to 45.7 m (150 ft) tip to tip. These antennas were used by many different experiments and were actually shared with some five other ac electric field experiments which monitored frequencies up to 10 MHz. But for the dc electric field measurements, these antennas were used as double floating probes. The inner portions of the antennas had an insulative coating to remove the active areas away from the plasma sheath of the spacecraft.
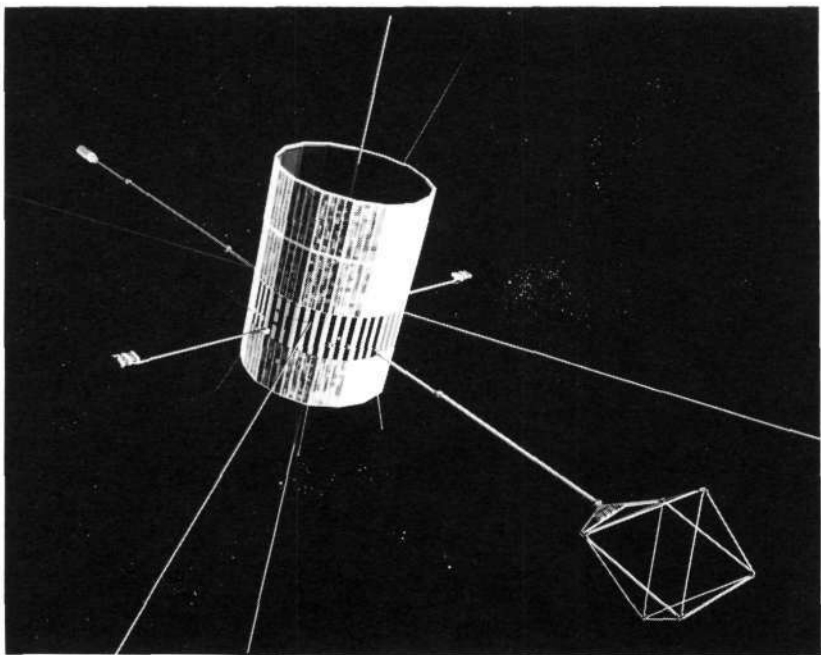
Figure 1–IMP I satellite.

We had tried this technique earlier on the OGO satellites with 9.2-m (30-ft) probes. They worked fine in the ionosphere, but they were not long enough to overcome the contaminating electric field of the spacecraft in the outer magnetosphere.

One point I would like to make here today is that we have tried this technique again in the outer magnetosphere on IMP I with much longer probes, and these longer probes were successful this time.

The data I want to show you are from a satellite crossing of the magneto-sphere. Figure 2 shows the location of this crossing, the 25 min of data were gathered at point 2 on an outbound crossing. The experiment data are shown in Figure 3, in which two quantities are plotted. The lower graph is simply a plot of the ac electric field noise in the frequency band of 54 to 100 Hz. The units are microvolts per meter. The upper graph shows the γ component of the dc electric field as the satellite rotates with a spin period of some 2 min. I have plotted the dc electric field in the spinning coordinate system of the spacecraft to emphasize the vector component nature of the dc measurements.

The magnetopause occurs at about 12 Earth radii. The noise enhancement which occurs at the magnetopause is not completely understood, but it is not surprising. This phenomenon probably represents the excitation of one of several universal or two stream instabilities.

The first interpretation of the dc probe data is also somewhat straightfor-ward. Considering the plasma from the point of view of magnetohydro-dynamics, a change in electric field is equivalent to a change in the average plasma velocity. The electric field is related to the plasma velocity, of course, by the Lorentz invariants $\mathbf{E} + \mathbf{V} \times \mathbf{B}$.

Thus, what we are seeing in the upper graph is a transition from what appears to be a turbulent region of plasma in the magnetosphere into the uniforming streaming plasma in the interplanetary region where the electric field is some 10 mV m^{-1}.

This is what we should have expected. If we go back to Figure 2, the data show the satellite passing out into this streaming interplanetary region.

The magnetic field on this crossing was some 60 nT (60 γ); dividing that into the electric field 10 mV m^{-1} yields about 200 km s^{-1}, a reasonable value for the plasma flow in this region of the magnetosheath.
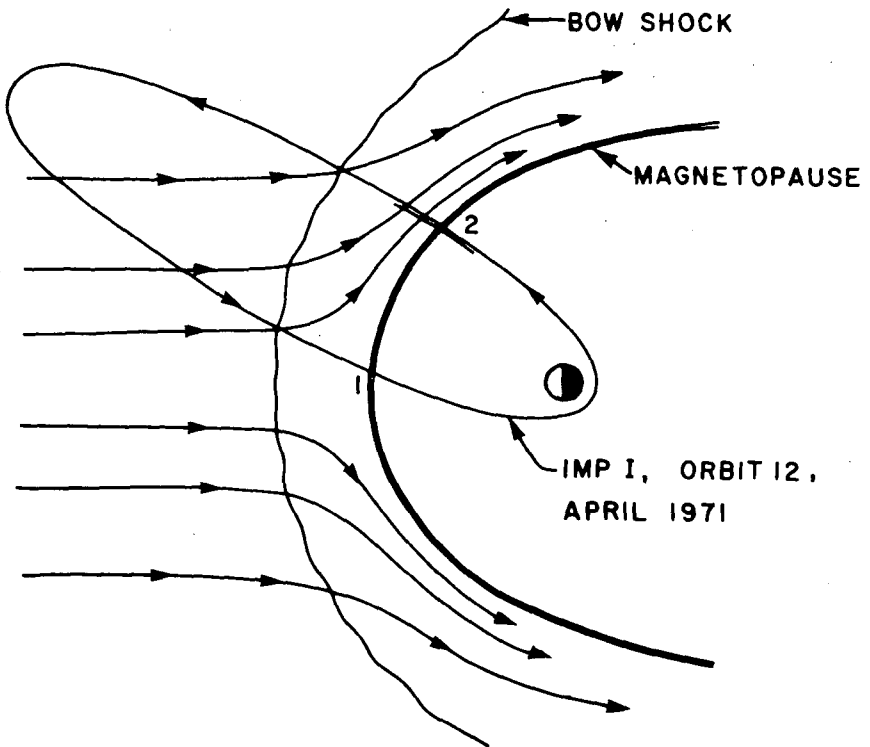
Figure 2–Satellite crossing of the magnetosphere.

I do not have time to show the measured electric field we observed on the inbound crossing of the magnetopause at point 1; it was much smaller, less than 1 mV m^{-1} in the magnetosheath. This is consistent with our understanding of the flow at the subsolar point; the flow becomes quite stagnant like a pilot tube.

In general, we observe fields of the order of 1 mV m^{-1} in the solar wind, with about a 40 percent jump at the bow shock. As the plasma becomes magnetized and the electric field is built up to several millivolts per meter in the magnetosheath, there is a large discontinuity at the magnetopause. Inside, the electric field varies from about 1 mV m^{-1} to tens of millivolts per meter in the auroral ionosphere.
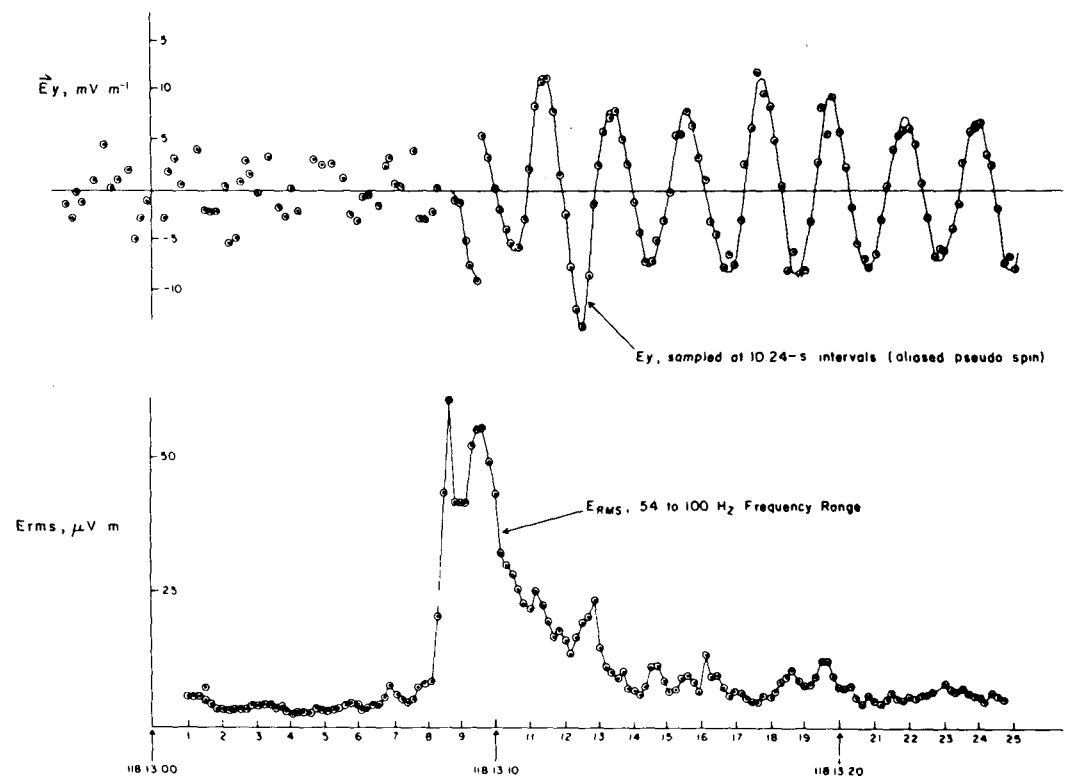
Figure 3–Electric field data. Lower graph is the ac electric field noise. Upper graph is the γ component of the dc electric field as the outbound satellite crosses the magnetopause; day 118, year 1971.

SOLAR-WIND MAINTENANCE OF THE NIGHTTIME
VENUS IONOSPHERE

Dr. Richard E. Hartle

In this talk we propose a possible ionization source which can reproduce the observed features of the nighttime Venus ionosphere.

Let us first consider the observed electron density profiles inferred from the two-frequency occultation experiment on Mariner 5, which are shown in Figure 1. The electron density is shown as a function of altitude for both dayside and nightside. The dayside ionosphere is understood reasonably well from models in which the ionization layer, with a peak at 140 km, corresponds to essentially pure CO_2 in photochemical equilibrium. The topside ionosphere, indicated by the large scale height above about 200 km, is composed of light ions, hydrogen and helium, in diffusive equilibrium. The sharp density cutoff at about 500 km corresponds to the interface between the ionosphere and the solar wind and is termed the ionopause. On the nightside, the ionization peak also occurs at 140 km with a density of about 20 000 cm^{-3}. We also note the appearance of a light ion tail.

The maintenance of the nightside ionosphere is more difficult to explain primarily because the rotation period of the planet is about 225 days whereas the relaxation time of a CO_2 ionosphere is on the order of 100 s. Several mechanisms have been proposed that seem unrealistic to us. The mechanism we suggest is that of corpuscular ionization and heating due to the penetration of solar-wind plasma into the nightside ionosphere.

To make this possibility more conspicuous, let us consider the solar-wind interaction model illustrated in Figure 2. We have adopted this interaction model because it is consistent with Mariner 5 and Venera observations. In this model the magnetic field, carried along by the solar wind, is forced to pile up on the dayside of the highly conducting ionosphere, forming a magnetic obstacle in the solar wind which diverts the wind around the planet and results in the formation of a bow shock. This interaction results in hot 10^6 K solar-wind plasma surrounding the cold 10^3 K ionospheric plasma. A small fraction of the hot solar-wind plasma is expected to leak across the unstable ionopause and into the ionosphere. Upon entering the ionosphere, a solar-wind proton charge exchanges with the dense CO_2 gas to produce a hot neutral hydrogen atom which then penetrates deeper, scattering and ionizing CO_2 on its way. A hot hydrogen atom so produced typically suffers 20 such collisions before thermalizing, efficiently heating and ionizing the atmosphere in the process.
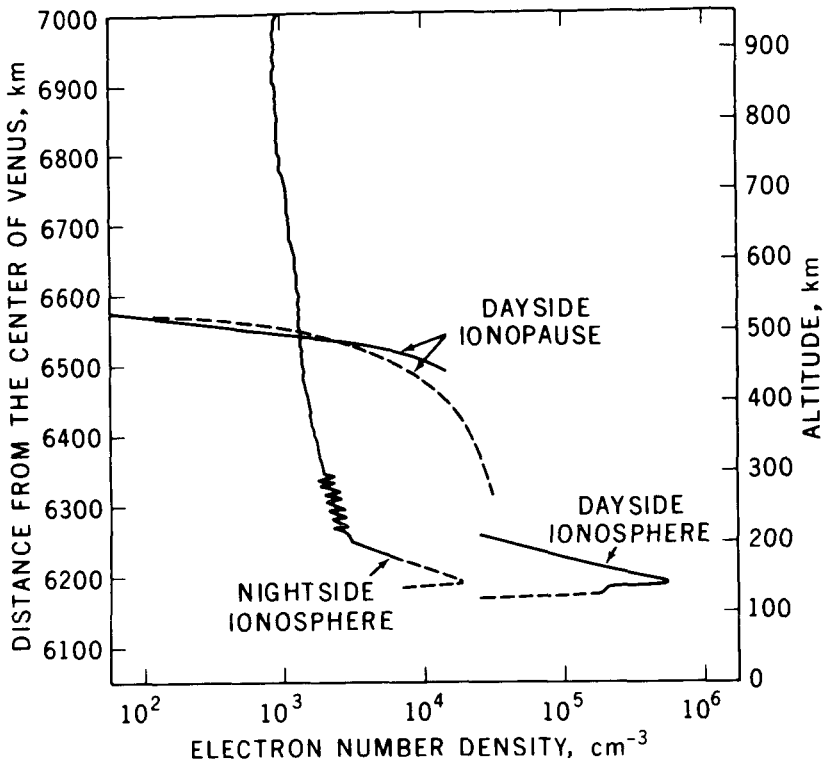
Figure 1—Observed electron density profiles (from Ref. 1).

We have evaluated the significance of this ionization and heat source in the context of our previously developed Venus ionosphere model which is based on a self-consistent solution of the continuity, momentum, and heat transport equations. We obtain the spatial and energy distributions of the incoming solar-wind flux by an appropriate multienergy group transport theory. On applying this new source to the dayside, we find that both the ionization and heating caused by this flux are ignorable relative to that due to extreme solar ultraviolet light. On the nightside, however, where the solar-wind flux is the primary ionization source, we find that only as little as 2 percent of the solar-wind energy flux is required to produce the observed ionization peak. The results of this model are shown in Figure 3.
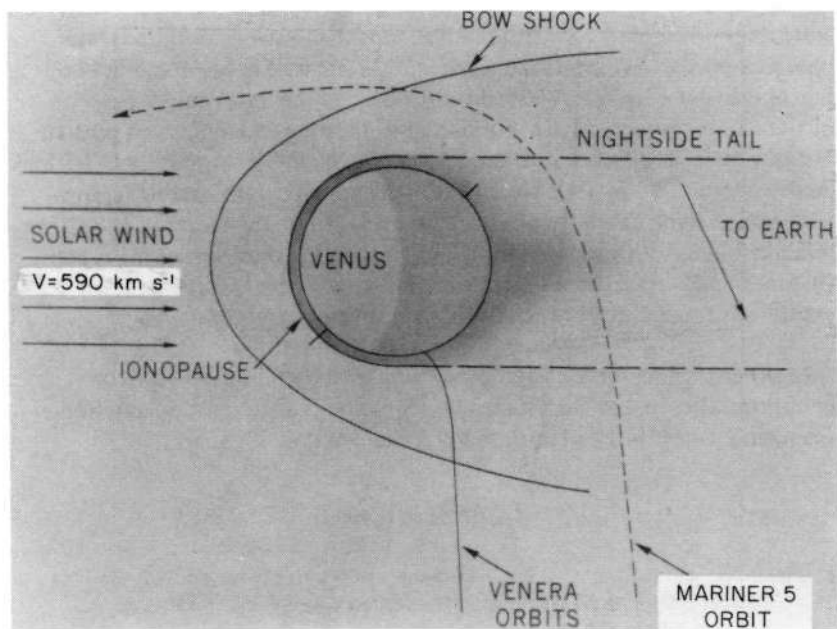
Figure 2–Solar-wind interaction model.
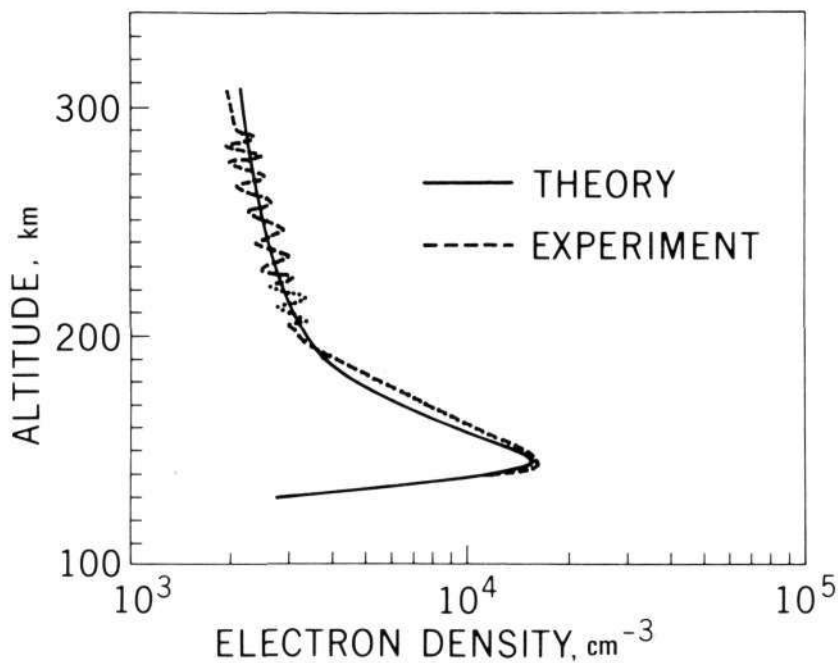
Figure 3–Nightside ionosphere model.

In Figure 3, the electron density is given as a function of altitude, where the solid line corresponds to the theoretical model and the dashed line is the observed profile. We see that the theoretical model can be placed in excellent agreement with the observed profile and, in this case, only 2 percent of the solar-wind energy flux is required to produce the ionization peak of 20000 cm^{-3}. The lower ionization layer corresponds to primarily CO_2^+ ions. Above about 200 km we have outward-streaming H^+ ions producing the large-scale height. These light ions flow upward rapidly because of the large polarization electric field present which propels H^+ outward with a force 21 times that of gravity. In fact, if the tail is sufficiently extended, we expect a strong tailwind which may reach supersonic speeds.

Altogether then, from our good agreement with the observed electron density profile, we conclude that the solar-wind is a strong candidate for the maintenance of the nighttime Venus ionosphere.

REFERENCE

1. Fjeldo, G., and Eshleman, V.R.: Atmosphere of Venus as Studied With the Mariner 5 Dual Radio Frequency Occultation Experiment. Radio Sci., Vol. 4, 1969, p. 879.

ION CLUSTERS AND THE VENUS ULTRAVIOLET HAZE LAYER

Dr. Arthur C. Aikin

The daytime ionosphere of Venus is observed between 100- and 500-km altitude with a peak electron concentration of 5×10^5 cm^{-3} at 140 km (Ref. 1). Below 200 km, CO_2^+ is thought to be the principal ion (Refs. 2 and 3) unless oxygen is present. We suggest that at altitudes less than 130 km the ion $CO_2^+ \cdot CO_2$ is an important ionic constituent of the Venus ionosphere. Below 100 km, ion clustering processes combine with the low temperature at the mesopause to form coagulates giving rise to the ultraviolet haze layer which has frequently been observed.

For clustering of neutrals to ions, Keller and Beyer (Ref. 4) have shown the dependence of clustering rate on the polarizability of the neutral molecule and the mass of the ion. A rate of $k_1 = 5 \times 10^{-30}$ cm^6 s^{-1} and $k_{-1} = 5 \times 10^{-14}$ cm^3 s^{-1} would be predicted for the reactions

$$CO_2^+ + CO_2 + CO_2 \underset{k_{-1}}{\overset{k_1}{\rightleftharpoons}} CO_2^+ \cdot CO_2 + CO_2 \qquad (1)$$
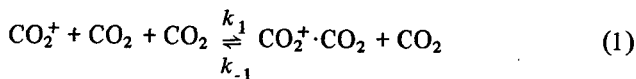
The forward reaction has been observed in the laboratory with a rate of 3×10^{-28} cm^6 s^{-1} at 0.16 aJ (1eV) (Ref. 5). In addition, dissociative ion/electron recombination is operative in the ionosphere
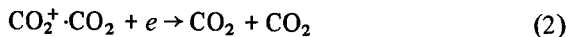
$$CO_2^+ \cdot CO_2 + e \rightarrow CO_2 + CO_2 \qquad (2)$$

Based on a measured rate of 2.3×10^{-6} cm^3 s^{-1} for O_4^+/electron recombination (Ref. 6), a rate of $a_D = 2.3 \times 10^{-6}$ (300/T) will be assumed for equation (2) where T is the temperature. The kinetic equation is

$$\frac{[CO_2^+ \cdot CO_2]}{[CO_2^+]} = \frac{k_1 [CO_2]^2}{k_{-1} [CO_2] + a_D N_e}$$

and the concentration ratio is plotted as a function of altitude in Figure 1. The atmospheric model chosen is the Goddard Space Flight Center model (Ref. 7). At altitudes below 90 km, where cosmic rays are the dominant source of ionization, the ion ratio

83
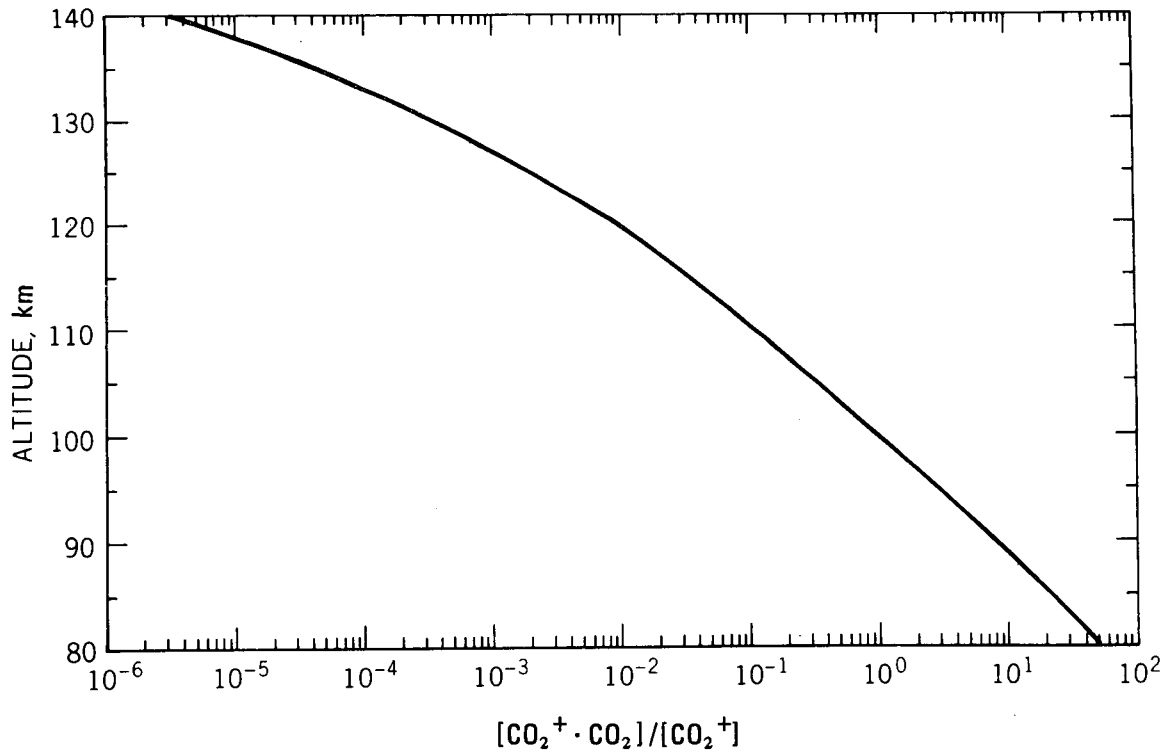
Figure 1–The ratio $[CO_2^+ . CO_2]/[CO_2^+]$ as a function of altitude.

$$\frac{[CO_2^+.CO_2]}{[CO_2^+]}$$

is greater than 1. Above 100 km the ratio is less than unity.

If N_2 and O_2 are present in the Venus atmosphere, then the processes

$$CO_2^+ + N_2 + CO_2 \rightarrow CO_2^+ \cdot N_2 + CO_2 \qquad (4)$$

and

$$CO_2^+ + O_2 + CO_2 \rightarrow CO_2^+ \cdot O_2 + CO_2 \qquad (5)$$

as well as

$$CO_2^+ + O_2 \rightarrow O_2^+ + CO_2$$
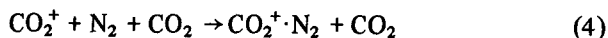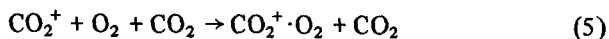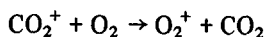
will cause loss of CO_2^+. The formation and loss processes of $O_2^+ \cdot CO_2$ have been discussed previously for the case of the Martian atmosphere (Ref. 8).

The presence of O_2 will lead to the formation of negative ions (Ref. 9) which will modify equation (3) by the addition of a loss term for $CO_2^+ \cdot CO_2$ involving ion/ion recombination.

In the event that water vapor is present above the cloud tops, reactions occur such as

$$CO_2^+ \cdot CO_2 + H_2O + CO_2 \rightarrow CO_2^+ \cdot H_2O + CO_2 \qquad (6)$$

$$CO_2^+ \cdot H_2O + H_2O \rightarrow H_3O^+ + CO_2 + OH \qquad (7)$$
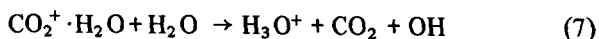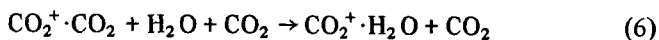
Coffey (Ref. 10) has shown that $H_3O^+ \cdot (H_2O)_n$ can react with NH_4 and HCl to form $NH_4Cl \cdot (H_2O)_n$ by the chain

$$H_3O^+ \cdot (H_2O)_n + NH_4 \rightarrow NH_4^+ \cdot (H_2O)_n + H_3O \qquad (8)$$

$$NH_4^+ \cdot (H_2O)_n + HCl \rightarrow NH_4Cl(H_2O)_m + H_3^+O(H_2O)_{(n-m)} \qquad (9)$$
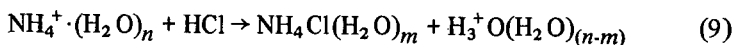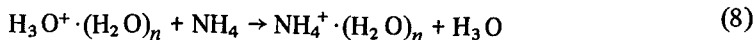
It has further been observed that the compound $NH_4Cl(H_2O)_m$ coagulates easily to form micron-sized particles.

Kuiper (Ref. 11) has suggested that the Venus ultraviolet haze layer is composed of 0.1-μm-sized particles of NH_4Cl. The location of this layer at 90 km is illustrated in Figure 2, which shows the temperature distribution for the atmospheric model employed. Also indicated are the levels of the yellow haze layer and the ratio of cluster ions relative to $[CO_2^+]$.
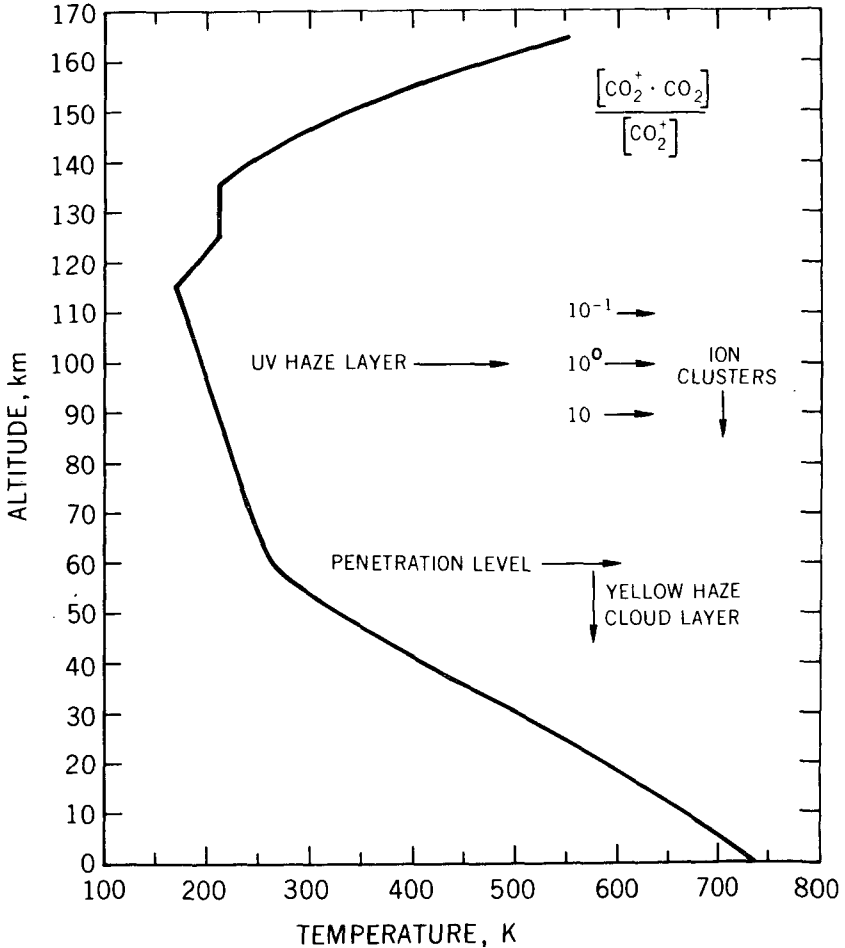
Figure 2—Altitude level of the Venus yellow cloud layer and ultraviolet haze layer in relation to the temperature distribution of the atmosphere and the ratio $[CO_2^+ \cdot CO_2]/[CO_2^+]$.

An alternate source of coagulates may be the ion $CO_2^+ \cdot H_2O$, which can attach additional water molecules as well as other neutral molecules. The complexes $CO_2^+(H_2O) \cdot XY$ can form as has been observed with NO^+, H_2O, SO_2 systems (Ref. 12). The resulting complex will further react to eliminate the ion and form coagulatable compounds. Laboratory studies at Venus atmosphere conditions will define more clearly the importance of ion clustering processes in the formation of the Venus ultraviolet haze layer.

REFERENCES

1. Fjeldbo, G.; and Eshleman, V. R.: Radio Sci., Vol. 4, 1969.

2. McElroy, M. B.: J. Geophys. Res., Vol. 74, 1969, p. 29.

3. Herman, J. R.; Hartle, R. E.; and Bauer, S. J.: Planet. Space Sci., Vol. 19, 1971, 443.

4. Beyer, R. A.; and Keller, G. E.: Trans. Amer. Geophys. Union, Vol. 52, 1970, p. 303.

5. Paulson, J. F., Dale, F.; and Mosher, R. L.: Nature, Vol. 204, 1964, p. 377.

6. Kasner, W. H.; and Biondi, M. A.: Phys. Rev., Vol. 174, 1968, p. 139.

7. Ainsworth, J. E.: NASA TMX 654-23, 1970.

8. Whitten, R. C.; Poppoff, I. G.; and Sims, J. S.: Planet. Space Sci., Vol. 1, 19, 1971, 243.

9. Aikin, A. C.: Icarus, Vol. 9, 1968, p. 487.

10. Coffey, P. C.: Bull. Amer. Phys. Soc., Vol. 16, 1971.

11. Kuiper, G.: Comm. Lunar Planet. Lab. 100-104, Vol. 6, Univ. Arizona, 1968-69, p. 229.

12. Castleman, A. W.; Tang, I. N.; and Munkelwitz, H. R.: Science, Vol. 173, 1971, p. 1025.

ON ESTIMATING THE VENUS SPIN VECTOR

Dr. Peter D. Argentiero

The Planetary Explorer (PE) mission is designed to land eight probes on Venus during the 1977 Venus opportunity. All these probes will be equipped with devices for returning range rate data to the Earth. These devices are expected to survive impact and to continue transmitting data from the planet's surface. The Venus spin vector as well as the positions of the probes on the surface are observable in these data. Thus the correct processing of these data should provide at least some improvement in our knowledge of these parameters. This prospect is an attractive one because of the considerable interest in the spin vector of Venus and because the data necessary for the estimation is obtained as a by-product of the PE mission and thus its acquisition imposes no further constraints or compromises on mission planning.

The purpose of this paper is to indicate the improvement in spin vector and probe position estimates one may reasonably expect from the processing of such data. This was done by duplicating the ensemble calculations associated with a weighted least squares with a priori estimation technique applied to range rate data that were assumed to be unbiased and uncorrelated. The weighting matrix was assumed to be the inverse of the covariance matrix of the noise on the data. Attention is focused primarily on the spin vector estimation.

PREVIOUS ESTIMATES OF VENUS SPIN VECTOR

Several radar determinations of the Venus spin vector have been reported in the literature. The technique involves the transmission of a cw signal to the planet and the analysis of the power spectrum of the return signal. If the transmitted frequency corrected for relative motion between Venus and the tracking station is used as the zero point of the spectrum, then every other frequency can be interpreted as a doppler shift, and the intensity associated with that frequency can be related to a line of constant radial velocity on the planet. These lines are easy to describe. A plane going through the tracking station and parallel to the spin axis of Venus and intersecting the planet's surface describes a circle. That segment of the circle visible to the tracking station is a member of the family of lines of constant radial velocity. A frequency at which a peak in the spectra occurs corresponds to a region on Venus that is rougher than adjacent regions. Thus a cw spectrum is a type of map of the radar brightness of

88

the surface of the planet. By obtaining such spectra at different times it should be possible to track specific surface features and from such infor-mation infer the spin vector of the planet under investigation. Carpenter (Ref. 1) reproduces several of these radar spectra and identifies several surface features as peaks in the spectra. The mathematics of how one might use such information to estimate a spin vector is given in some detail by Shapiro (Ref. 2). Basically a weighted least-squares estimation proce-dure is used with the surface features associated with peaks in the spectra treated as point sources of range rate data. This method has been applied by Carpenter (Refs. 3 and 4), Smith (Ref. 5), Goldstein (Ref. 6), and Shapiro (Ref. 2). Their various estimates of the rotation period of Venus are quite close to the so-called synodic resonance period of 243.16 days. If Venus were to have this period, it would rotate backward relative to the Earth four times between each inferior conjunction and thus present the same side of the Earth at each inferior conjunction. The uncertainties associated with present estimates are such that the hypothesis that Venus is in synodic resonance is still unsettled.

The radar determinations of the Venus spin vector are statistically incom-patible (Table 1). Clearly the standard deviations give a too optimistic representation of the accuracy of the radar determination technique. The reason is that ensemble calculations giving standard deviations of the least-squares estimation process do not reflect the impact of modeling errors. The most obvious modeling error associated with the technique is that of treating the source of a peak in a frequency spectrum as a point. Any surface feature on Venus capable of causing a significant perturbation in the return spectrum of a radar scan must be quite extensive. A more subtle though possibly less important modeling error is the assumption that the return rate data are uncorrelated. Corrections must be made to the doppler data before they can be used for least-squares estimation. These correc-tions are responsible for a portion of the noise on the data. If this portion is significant, then it is improper to model the noise on the data as an un-correlated or "white" random process. The correct procedure would then be to solve for a bias and perhaps a scale factor error in the data. If this were done the ensemble calculation would yield a more accurate though quantitatively less impressive figure for the standard deviation of the Venus spin vector estimate. Another possibility is that the cause of the peaks on the return spectra may be a complex combination of phenomena rather than a fixed surface feature.

It is not easy to obtain reasonable estimates of the quality of the radar determination technique. Carpenter (Ref. 1) suggests that the formal standard deviation numbers associated with radar determinations should be increased several times. This is quite vague, but it would be imprudent to be more precise.

TABLE I—Recent Radar Determinations and Associated Standard
Deviations of Venus Spin Vector

Determination	Rotation period, days	Right ascension, deg	Declination, deg
Carpenter (Ref. 1)	242.98 ± 0.04	94 ± 3	-71.5 ± 1
Shapiro (Ref. 7)	243.09 ± 0.18	84.7 ± 1.8	-65.8 ± 1.2
Dyce, Pettengill, and Shapiro (Ref. 8)	244.3 ± 2	90.9 ± 1	66.4 ± 1
Goldstein (Ref. 9)	242.6 ± 0.6	98 ± 5	-69 ± 2

SPIN VECTOR ESTIMATION WITH PE PROBES

The PE mission will consist of two separate launchings of multiprobe space-
craft. Each launch will land a main probe equipped with a two-way doppler
device and three miniprobes, each equipped with a one-way doppler device.
The geometric distribution of the probes is given by Figure 1. The succeed-
ing analysis rests on the following modeling assumptions:

    (1)   For the duration of their transmission of doppler data, the
          probes remain stationary relative to the Venus surface.

    (2)   For this same duration the Venus spin vector is constant.

    (3)   The noise on the range rate data transmitted by the probes is
          stationary and uncorrelated.

    (4)   Unbiased estimates of the Venus spin vector and the locations
          and effective radii of the probes are available. These estimates
          are statistically uncorrelated and their standard deviations are
          known.

Assumptions (1) and (2) should disturb no one. Assumption (3) is some-
what more troublesome. We defer discussion of this assumption to a later
stage of the analysis. Concerning assumption (4), the estimate of the Venus
spin vector and its associated uncertainty would presumably be borrowed
from a radar determination. The probe positions and associated uncertain-
ties would be obtained from extensive postflight analysis of all relevant
data gathered during the PE mission. This would include accelerometer,
temperature and pressure measurements, and range rate data.
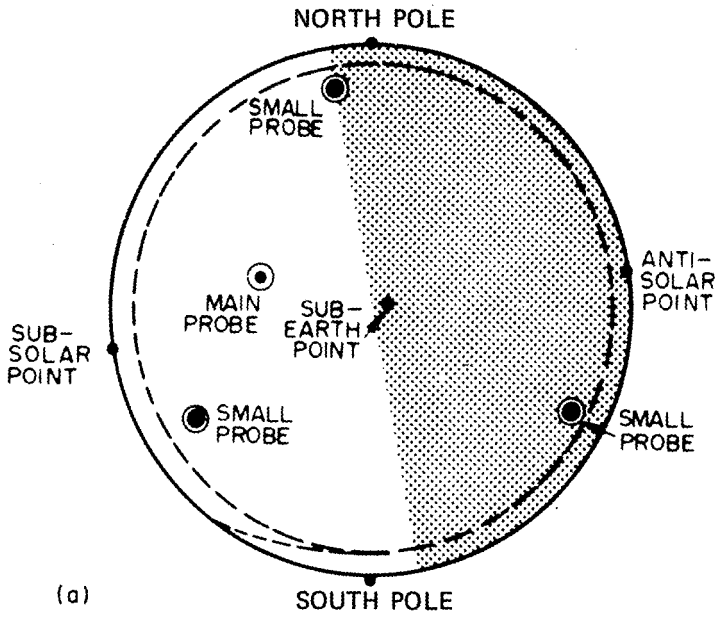
(a) First launch.
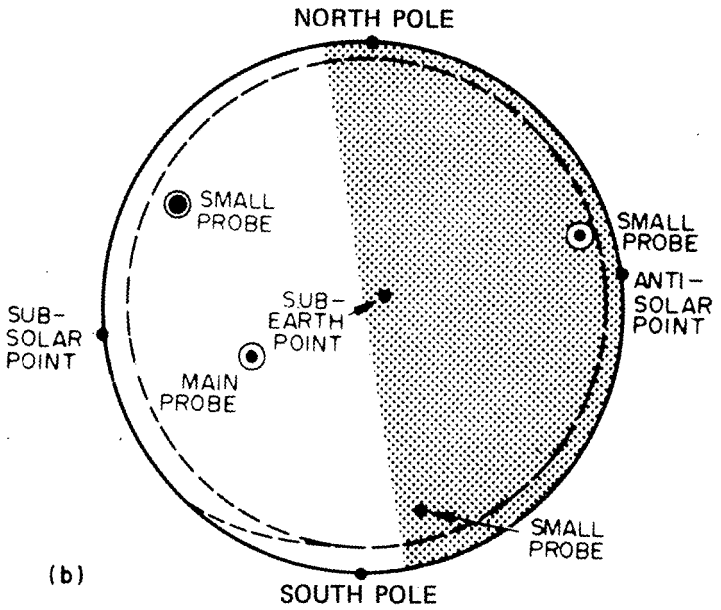
(b) Second launch.

Figure 1–Position of probes on Venus surface.

The conventional way to process the doppler data from the PE probes is to form the usual weighted least squares with a priori loss function and choose the spin vector and probe positions that minimize this loss function. To be specific, let X be a vector of dimension 27 whose elements are estimates of the spin vector and positions of each of the eight probes. Let the vector $\tilde{Y}$ be the range rate measurements, arranged in some sequence, which would be obtained in the absence of noise if X contained the true values of the parameters in question. $\tilde{Y}$ is a known function of X symbolized by

$$\tilde{Y} = f(X) \tag{1}$$

Let Q be the covariance matrix of the noise on the observations and let P be the covariance matrix of an a priori estimate X' of the parameters. Then the loss function is

$$L(X) = [Y - f(X)]^T\, Q^{-1}\, [Y - f(X)] + (X' - X)^5\, P^{-1}\, (X' - X) \tag{2}$$

where Y is the vector of measured values of range rate data obtained from the probes. Notice that by assumptions (3) and (4) the matrices Q and P are diagonal, a fact that greatly simplifies the following computations. The least-squares estimate is defined as that value of X that minimizes the loss function of equation (2). Because the data necessary to implement this procedure are not yet available, interest is focused on just the statistical properties of this estimation procedure. The covariance matrix of the least-squares estimator may be obtained if one more assumption is imposed. It must be supposed that the function of equation (1) can be accurately represented as a first-order Taylor series about X where X is the least-squares estimate. Thus we assume that equation (1) can be written as

$$Y - f(X) = A\,(X - X) \tag{3}$$

The symbol A represents the variational matrix. If N is the total number of range rate measurements, then A is an N- by 27-dimensional matrix. The element in the ith row and jth column of A is the partial derivative of the ith component of Y with respect to the jth component of X. It is relatively easy to obtain an analytical expression for A. The details are found in appendix 1 of Reference 10. If equation (3) is valid, then the covariance matrix of the least-squares estimator is given by

$$\operatorname{cov}(X) = (A^T\, Q^{-1}\, A + P^{-1})^{-1}$$

Equation (4) provides a mode for the performance of a parametric study of the accuracy attainable in the estimation of the Venus spin vector. Interest was focused primarily on the variation of this accuracy with respect to variations in the following parameters.

(1) Length of time the probes survive on the surface
(2) Quality of a priori information
(3) Size of the noise on the data.

This paper reports on the results of such a parametric study. As usual, nominal values were established for all relevant parameters. Certain parameters were then systematically varied with the other parameters fixed at their nominal values. Equation (4) is then used to obtain the corresponding standard deviations of the spin vector and probe locations. There is a certain amount of arbitrariness involved in the selection of nominal values. It is not easy, for instance, to decide what are reasonable values for the a priori uncertainties of the spin vector at some time several years in the future when the PE mission is to be executed. Also the time at which the probes land is a factor because this affects tracking sight geometry. This too is somewhat arbitrary although one would of course choose a time during which dual coverage from the DSN is possible. The date chosen for the landing is May 19, 1977. Dual coverage from Goldstone and Madrid is assumed. The nominal value of the spin vector as obtained from reference 1 is 242.982 days for the period and 94.1° and -71.4°, respectively, for the right ascension and declination of the spin vector (equator of 1950). The longitude and latitude of each probe is given in target coordinates in reference 11. The data acquisition rate is assumed to be 1 min^{-1}. It is also assumed that all biases are estimated in the least-squares procedure.

A summary of a priori standard deviations is provided in Table II.

TABLE II–A Priori Standard Deviations

Parameter	Standard deviation
Right ascension of main probes	0.115°
Declination of main probes	0.115°
Right ascension of miniprobes	0.165°
Declination of miniprobes	0.165°
Range rate from main probes	5 mm s^{-1}
Range rate from miniprobes	5 cm s^{-1}
Period of Venus rotation	1 day
Right ascension of Venus spin vector	10°
Declination of Venus spin vector	5°
Effective radius of Venus at each probe	5 km

The usual standard deviation figure for two-way range rate and for a one-per-minute sampling rate is 1 mm s^{-1}. See for instance Blackshear and Williams (Ref. 12) who use this figure for two-way range rate data in an error study similar to this one but for the Viking project. The larger figure of 5 mm s^{-1} for the two-way range rate data on the main probes was used to compensate for the fact that the data were assumed to have no time correlation. Because the various corrections that must be made to the data in fact do tend to introduce time correlations, this assumption is a questionable one. Its legitimacy can only be defended if a bias on the data is also solved for in the estimation procedure, In this error study, no provisions were made for bias estimation. Hence it was felt that to use the usual standard deviation figure for the noise on the two-way range rate data would lead to an excessively optimistic result. The use of a larger standard deviation number was an effort to compensate for this optimism. Because the presence of biases on one-way doppler data is a much more serious problem, the standard deviation of the noise on the miniprobe data was set at 10 times the corresponding figure for the noise on the main probe data.

Figures 2, 3, and 4 display the possibilities of estimating the period, right ascension, and declination of the Venus spin vector as functions of the length of time the probe range rate devices survive on the surface. Because it is not certain that all range rate devices will survive parachute openings or impact on the surface, the figures also demonstrate the deterioration in the estimation procedure if a miniprobe per launch fails to function and also if a miniprobe and a main probe on each launch fail to function. A salient feature of the figures is that most of the improvement in the estimates occurs within the first few minutes after impact. This fact suggests that the primary reason for the feasibility of this estimation procedure is the coupling provided by equation (4) between the spin vector estimate and the relatively small standard deviations of the a priori estimates of probe locations. If this were true, one would expect the quality of the estimation procedure to be far more sensitive to changes in the standard deviations of the a priori estimates of probe locations than to changes in the standard deviations of the noise on the data. This appears to be the case. For example, with regard to the nominal case with all probes lasting 30 min, the standard deviation of the rotation period is 0.28 days. When the standard deviations of the noise on the data are doubled, the number becomes 0.31 days. With the standard deviations of the noise returned to nominal values but with the standard deviations of the a priori probe location estimates doubled, the standard deviation of the estimate of the period rises to 0.4 days.
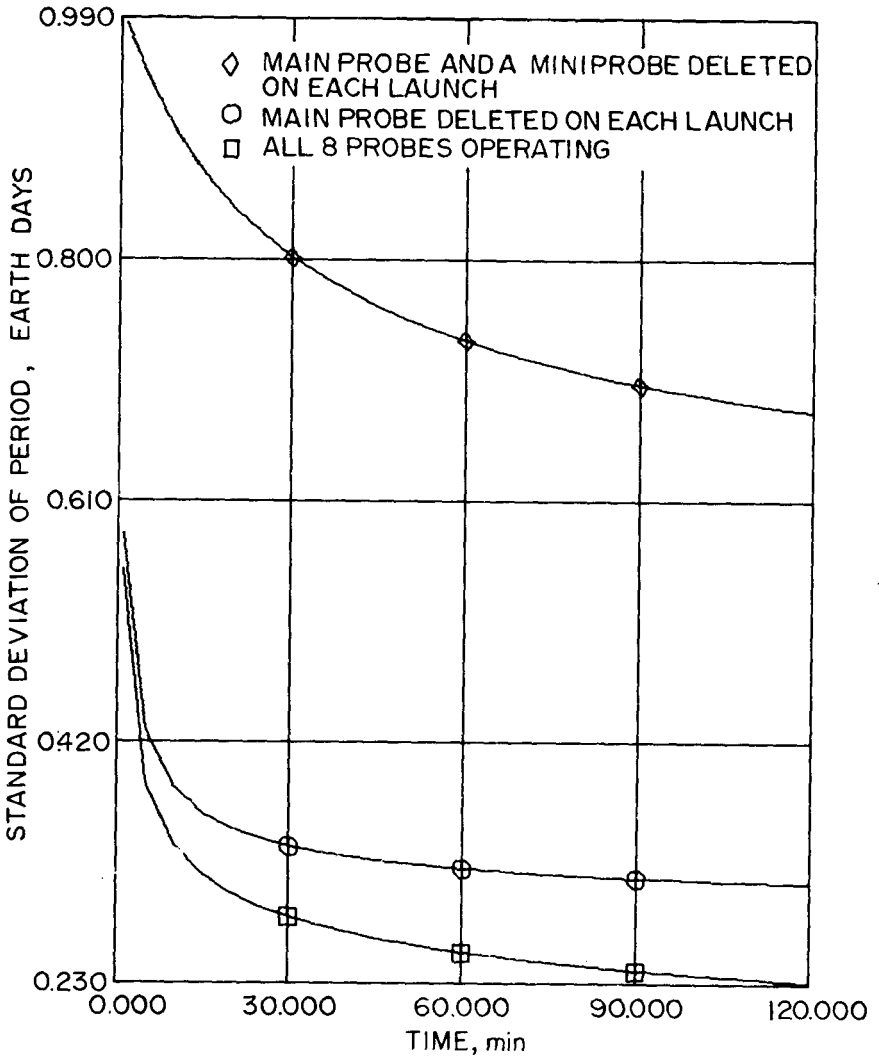
Figure 2—Standard deviation of period as a function of time. A priori
standard deviation of period is 1 Earth day.
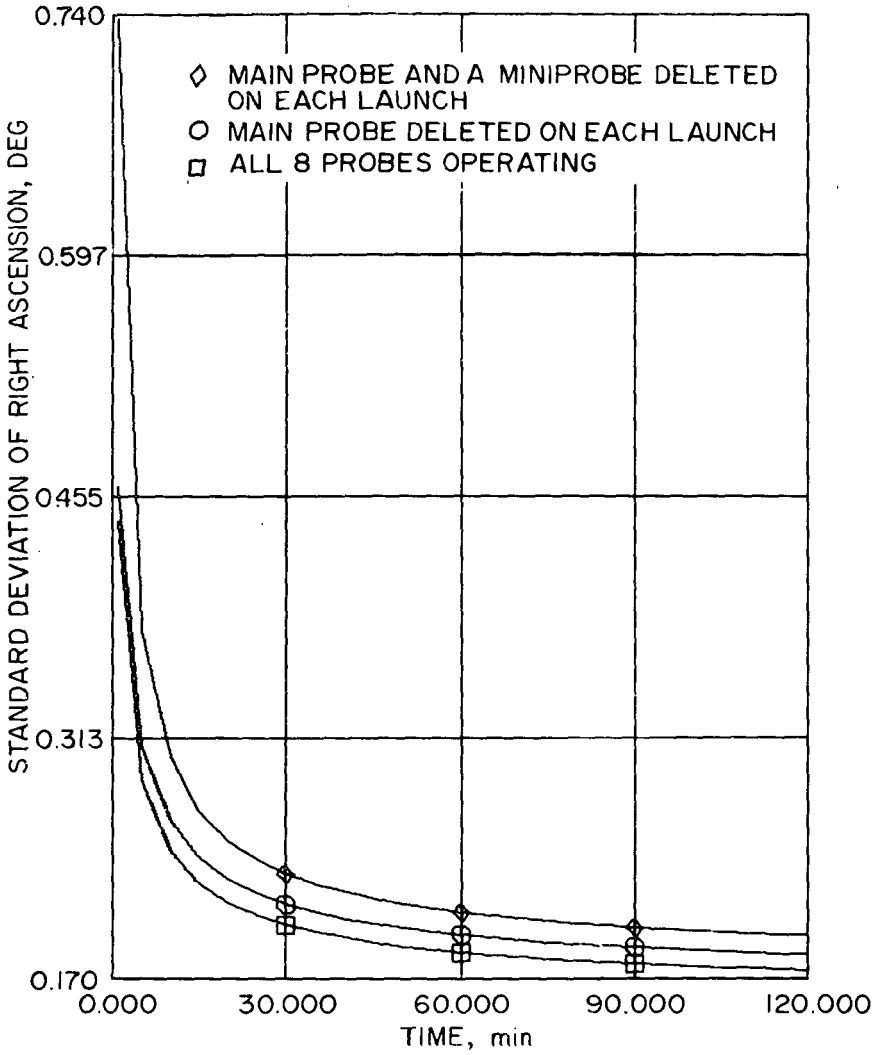
Figure 3—Standard deviation of right ascension as a function of time.
A priori standard deviation is 10°.
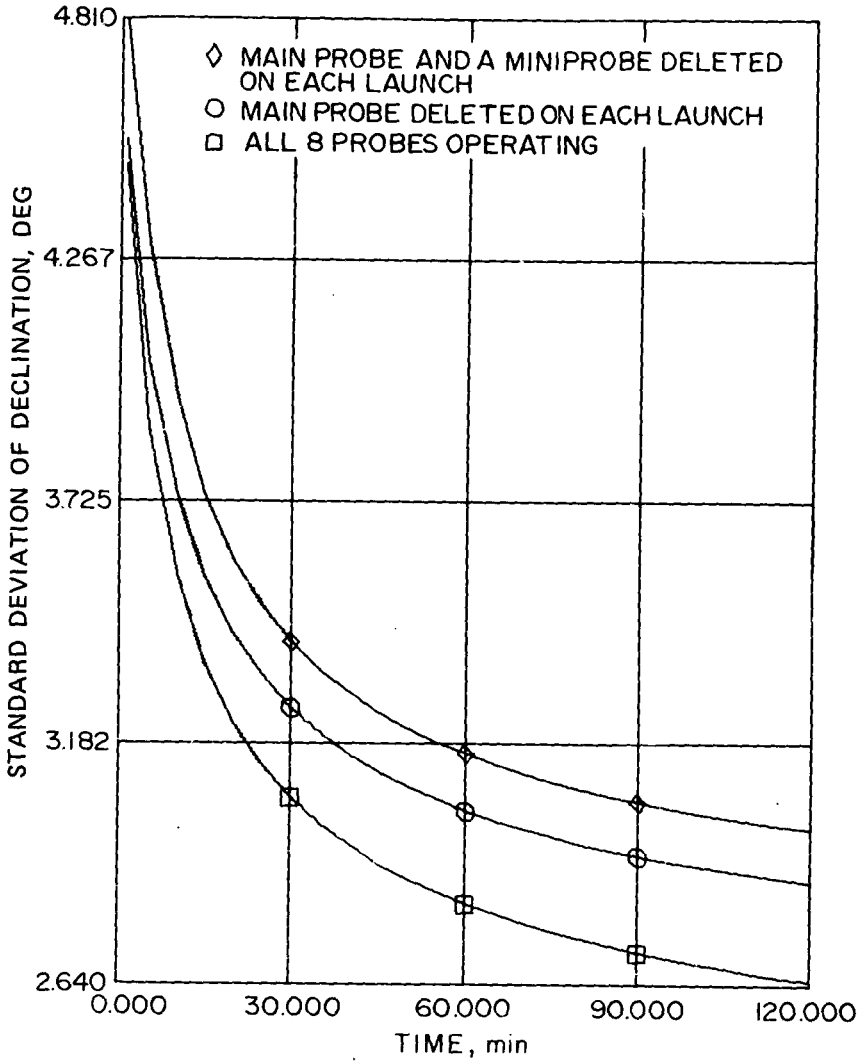
Figure 4—Standard deviation of declination as a function of time.
A priori standard deviation is 5°.

It is apparent from a comparison of Figures 3 and 4 that the right ascension of the Venus spin vector is far more observable in this experiment than the declination. A glance at Table I reveals that the situation is precisely the opposite with regard to the radar determination procedure. It is not obvious why this should be so. But in this sense, at least, the two estimation procedures should neatly complement each other.

The ability of this estimation procedure to improve knowledge of probe positions is somewhat less impressive. After 30 min of tracking, knowledge of the positions of the main probes is improved by approximately 15 percent. Knowledge of the positions of the miniprobes after the same period of tracking is improved by approximately 10 percent. After an hour of tracking these percentage improvements are, respectively, 18 and 15 percent.

CONCLUSIONS

This paper has demonstrated the feasibility of utilizing range rate data generated by PE probes to estimate the Venus spin vector. The estimation procedure is viable even if each probe transmits doppler data for just a few minutes after impact. The standard deviation figures associated with this estimation procedure are not dependent on questionable modeling assumptions for their validity. Consequently they are a true measure of the estimate's accuracy.

The right ascension of the spin vector is far more observable in the data than the declination. Fortuitously, the radar determination technique estimates the declination better than the right ascension. Thus the two estimation techniques complement each other.

The improvements in probe position uncertainty are somewhat marginal.

Finally, this proposed experiment uses data that is generated essentially as a by-product of the PE mission and hence its implementation poses no additional constraints on PE mission planning.

REFERENCES

1. Carpenter, R. L.: Astron. J., vol. 75, No. 1, 1970, p. 61.

2. Shapiro, I. I.: Science, vol. 157, 1967, p. 423.

3. Carpenter, R. L.: JPL Research Summary No. 36-14, 1962, p. 56.

4. Carpenter, R. L.: Astron. J., vol. 69, 1964, p. 2.

5. Smith, W. B.: Astron. J., vol. 68, 1963, p. 15.

6. Goldstein, R. M.: Astron. J., vol. 69, 1964, p. 12.

7. Shapiro, I. I.: J. Res. Nat. Bur. Stard. Sect. D., vol 69, 1965, p. 1932.

8. Dyce, R. B.; Pettengill, G. H.; and Shapiro, I. I.: Astron. J., vol. 72, 1967, p. 351.

9. Goldstein, R. M.: Moon and Planets, A. Dollfus, ed., North Hollad Pub. Co., (Amsterdam), 1966, p. 126.

10. Argentiero, P.; and Wyatt, G.: On Estimating the Venus Spin Vector From Data Obtained During the Planetary Explorer Mission. NASA TMX 657-28, Oct. 1971.

11. Avco Corporation: Planetary Explorer Universal Bus Study. Contract NAS5-11800, 1970.

12. Blackshear, W. T.; and Williams, J. R.: NASA TN D-6109, 1971.

INFRARED SPECTRA OF CO_2 IN THE ATMOSPHERES
OF EARTH AND VENUS

William C. Maguire

The emission and absorption of radiation within a planetary atmosphere — the Earth or Venus, say — depends on the temperature, pressure, and composition of the atmosphere. Conversely, information on atmospheric constituents, temperature, and pressure can be obtained by analyzing infrared spectra.

Flight and ground-based infrared interferometer spectrophotometers (IRIS) have yielded infrared spectra that can be used for purposes of temperature inversion. For temperature inversion of the accuracy desired, the available carbon dioxide lines were insufficient. For example, at one inversion interval in the 15-μm band, a difference of 0.4 μJ (4 ergs) between theoretical and experimental radiance has been eliminated. If this difference were systematic across the entire band, it would result in a 4 K error in the inverted temperature profile in the tropospheric region sampled by this interval, with corresponding pressure errors.

So the lack of molecular lines of weaker bands of carbon dioxide hindered reliable inversion techniques. Derived temperature profiles and surface pressures reflected imprecise knowledge of the atmospheric transmission. Consequently, theoretical calculations were made for a number of these weaker bands. These computations were made to obtain three important molecular parameters, line position, intensity, and shape, necessary to the line-by-line integrating program which yields the theoretical spectra. A good fit to several terrestrial bands of carbon dioxide, including the 15-μm band, confirms the line calculation. A knowledge of the pressure and temperature dependence of the lines allows reliable transmission calculations for Venus at other temperatures, pressures, and in other spectral ranges. The resulting theoretical spectra can be displayed as transmission versus wavelength or as radiance versus wavenumber.

Figure 1 is a plot of the Earth's radiance near Brownsville, Tex., in April 1969 as observed by the Nimbus 3 satellite. The abscissa is wavenumber increasing to the right; the ordinate is radiance. The solid curve is the present theoretical calculation. The dashed curve is the experimental value; the curve is solid where experimental and theoretical agree to within the line width. The dotted curve is the old theoretical radiance; the improved agreement is clear. Blackbody curves are given for reference

100
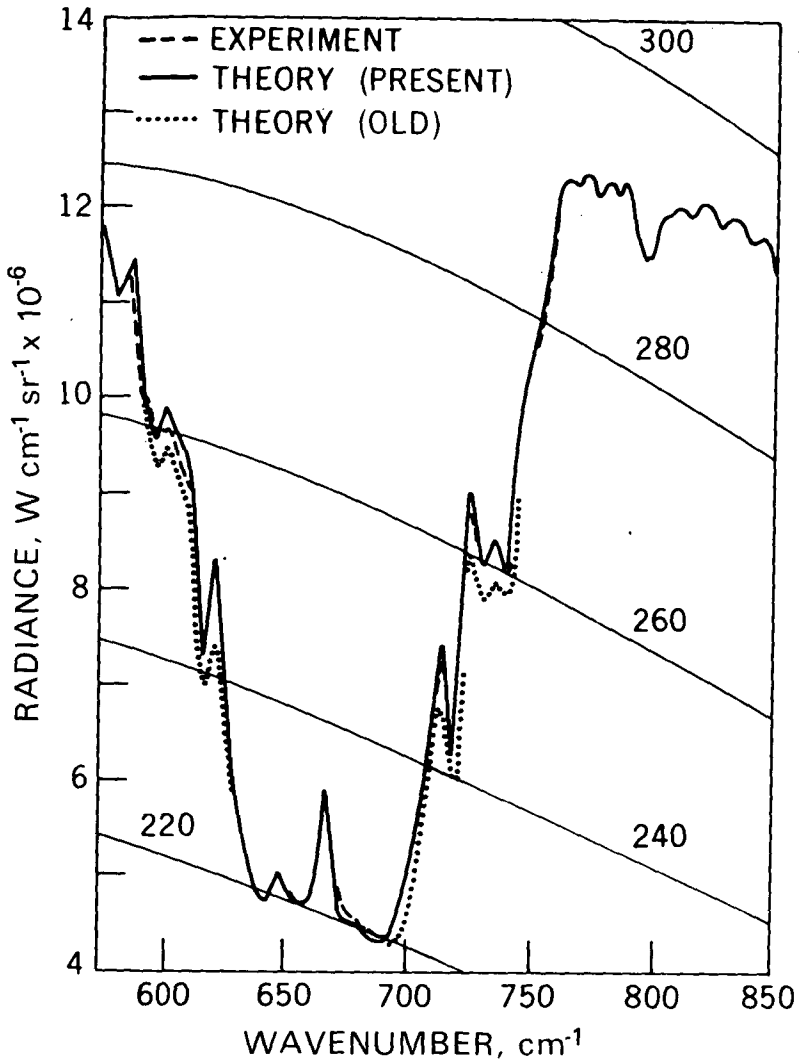
Figure 1—Earth radiance spectrum as determined by theory and as observed by the Nimbus 3 satellite over Brownsville, Tex.

purposes. The structure of the 15-μm band of carbon dioxide is shown in this plot. In the center of the band is the strongly absorbing fundamental; at this point, one is seeing high in the atmosphere. The line shape used in this calculation and the next yields an improved agreement with the observed spectra compared with the simple Lorentz line shape previously assumed. On the high- and low-wavenumber sides of the band, one is seeing lower in the atmosphere; the transmission is greater. Certain spectral intervals on the high-wavenumber side of the band are chosen for purposes of temperature inversion. Very roughly, the idea is to sample different parts of the band to yield, after some calculation, pieces of the temperature-versus-height profile. As can be seen, the agreement in general is very good. We are continuing to investigate the differences; minor constituents may be responsible for some of these.

The plot in Figure 2 is a Venus spectrum taken at McDonald Observatory in Texas. Again, the solid curve is the theoretical calculation and the dashed curve is the experimental. The abscissa is wavenumber increasing to the right; the ordinate is radiance. The smooth curves, once again, are the Planck curves. The vertical shift between experimental and theoretical is a trivial result of calculating the theoretical spectrum with a specific Venus model based on Mariner 5 data. The agreement of line positions and relative intensities is generally very good. The differences in slope reflect interesting features of the Venus atmosphere which we are continuing to elucidate. By introducing carbon dioxide lines having the same modified Lorentz shape as in the Brownsville case, the slope of the falloff in the theoretical calculation at a wavenumber of 750 has come to more nearly agree with the experimentally observed shoulder.

In conclusion, the improvement in the transmission calculation is important for interpretation of infrared measurements made from the Nimbus 3 satellite and from the ground, as well as from spacecraft such as Mariner and possibly Planetary Explorer.
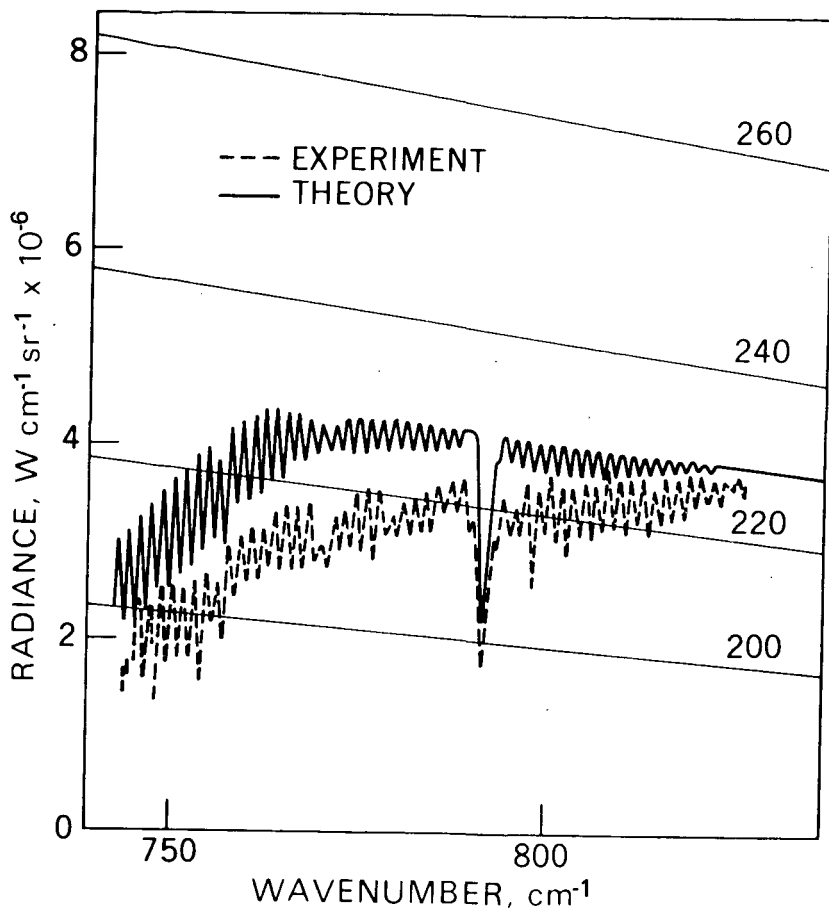
Figure 2—Venus radiance spectrum as determined by theory and as observed from McDonald Observatory.

HOT CO ON MARS

Dr. Michael J. Mumma

The Mariner 6 and 7 spacecraft, which flew by the planet Mars on July 31 and August 5, 1969, featured onboard ultraviolet scanning spectrometers. These spectrometers produced the first spectra of the dayglow of the Mars upper atmosphere over the wavelength region 100 to 400 nm. The spectra showed emissions that were characteristic of the carbon dioxide ion and neutral molecule, the carbon monoxide ion and neutral molecule, and the atomic species of hydrogen, oxygen, and carbon. The spectra between 200 and 400 nm showed emission features from each of these molecules. Between 100 and 200 nm the only observed molecular feature was the fourth positive group of CO, as shown in Figure 1 (Ref. 1). Starting at the low-wavelength end of the spectrum, we see a very prominent Lyman-alpha atomic hydrogen line, then the resonance line of atomic oxygen at 130.4 nm, the metastable oxygen line at 135.6 nm, a variety of atomic carbon lines, and then prominent features that represent the resonance band system of the CO molecule, the fourth positive group. These spectra were taken at 1-nm resolution, which is not sufficient to resolve the shape of the individual band in the fourth positive group.
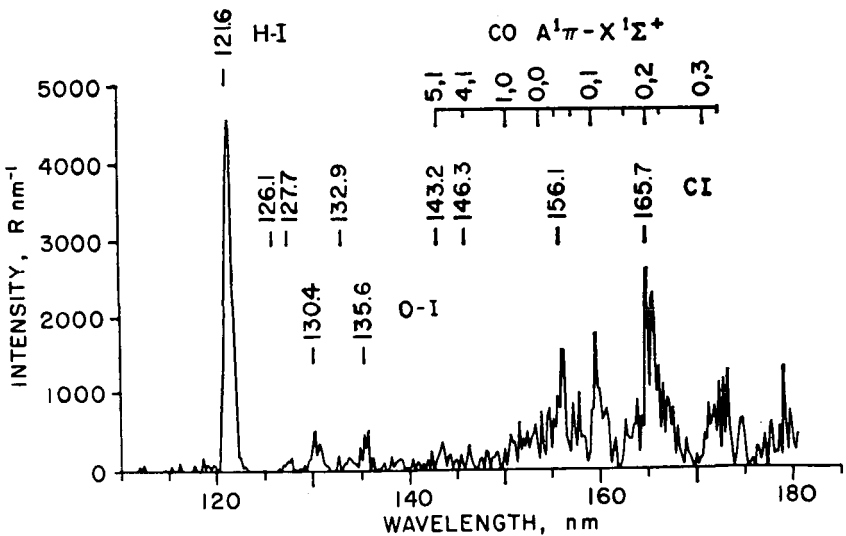
Figure 1—Ultraviolet spectrum of the upper atmosphere of Mars, 110 to 180 nm, 1-nm resolution. Spectrum was obtained by observing the atmosphere tangentially at an altitude between 140 and 160 km. This spectrum was obtained from the sum of four individual observations (from Ref. 1).

In anticipation of the Mariner 6 and 7 flybys, Mumma, Stone, Borst, and Zipf (Refs. 2 and 3) at the University of Pittsburgh and Ajello (Refs. 4 and 5) at the University of Colorado performed experimental studies of production of this band system by electron impact on CO and on CO_2. In light of these laboratory data, Barth and coworkers (Ref. 1) concluded that the fourth positive emission intensities measured by the Mariner spectrometers could be explained by photoelectron impact on CO_2 in the Mars upper atmosphere.

This presented an intriguing problem: namely, could one assign an effective rotational temperature to the excited CO fragment produced in the dissociative excitation of CO_2? If the excited CO could be characterized by an effective temperature and if the thermal distribution of the ambient CO in the Mars atmosphere were known, then the variation of emission intensity with altitude would yield the column density of CO of Mars.

The Mariner spectra were taken at too low a resolution to shown the rotational profiles. We decided to measure the rotational profiles of the fourth positive bands in the laboratory. The results of that experiment are shown in Figure 2. Here we plot the relative intensity against the wavelength for bands originating from the $v' = 1$ vibrational level of the CO $(A^1 \pi)$ state. The spectra were taken at 0.09-nm resolution and individual rotational lines are not resolved. The envelope of the lines, however, is sufficient to show that the bands are much broader in wavelength for electron impact on CO_2 than for electron impact on CO. This means that the excited CO molecule is rotating much faster when produced from CO_2 than it is when produced by electron impact on CO.

Our results show that when electrons impact on thermal CO_2 at 300 K, the rotational temperature of the CO $(A^1 \pi)$ fragment exceeds 1500 K. Furthermore, the rotational temperature is not independent of the incident electron energy but depends sensitively upon it just in the energy range at which we would expect the Mars photoelectron flux to be large, i.e., <6.4 aJ (<40 eV). In view of these results we conclude that an attempt to unfold the CO column density from the fourth positive emission intensities is presently not feasible.

We conclude that rotationally hot CO is produced on Mars by photoelectron impact on CO_2 and that the effective rotational temperature of CO $(A^1 \pi)$ is much higher than the equilibrium rotational temperature of ambient CO in the Mars upper atmosphere.
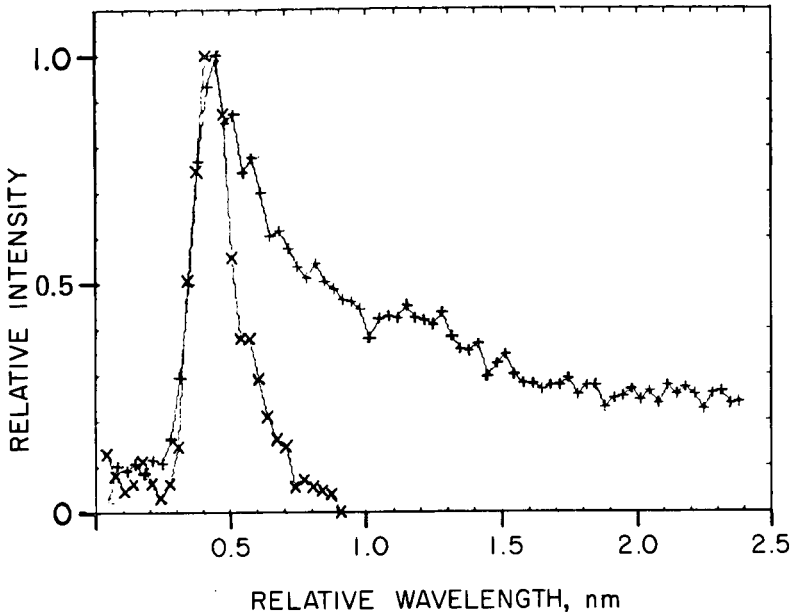
Figure 2—Emission profiles of bands of the fourth positive group. x denotes the (1, 4) band, e + CO; + denotes the (1, 0) band, e + CO_2.

We conclude further that the high effective rotational temperatures will result in reduced self-absorption of the CO fourth positive bands on Mars.

A wavelength resolution of 0.01 nm is needed for rotational band profiles to enable an unfolding of the CO column density on Mars. The present Mariner has a wavelength resolution of 0.75 nm and is therefore incapable of the required observations.

REFERENCES

1. Barth, C. A.; Hord, C. W.; Pearce, J. B.; Kelly, K. K.; Anderson, G. P.; and Stewart, A. I.: Mariner 6 and 7 Ultraviolet Spectrometer Experiment: Upper Atmosphere Data. J. Geophys. Res., vol. 76, 1971, p. 2213.

2. Mumma, M. J.; Stone, E. J.; and Zipf, E. C.: Excitation of the CO Fourth Positive Band System by Electron Impact on Carbon Monoxide and Carbon Dioxide, J. Chem. Phys., vol. 54, 1971, pp. 26-27.

3. Mumma, M. J.; Borst, W. L.; and Zipf, E. C.: Dissociative Excitation of Vacuum Ultraviolet Emission Features by Electron Impact on Molecular Gases. III. CO_2. J. Chem. Phys., vol. 57, 1972, in press.

4. Ajello, J. M.: Emission Cross Sections of CO by Electron Impact in the Interval 1260-5000 Å. I. J. Chem. Phys., vol. 55, 1971, p. 3158.

5. Ajello, J. M.: Emission Cross Sections of CO_2 by Electron Impact in the Interval 1260-4500 Å. II. J. Chem. Phys., vol. 55, 1971, p. 3169.

THEORETICAL LIMITS ON JOVIAN RADIO BELTS

Dr. Fritz M. Neubauer

The Jovian magnetosphere is a challenge to space plasma physics. As a consequence, the Jovian environment will be one of the aims of future particle-and-field missions. These missions are in great danger of being wiped out by the possibly strong Jovian radiation belts. Because only the relativistic electron population is known from observations and nothing is known about the proton population, theoretical studies are the only way to gain the information necessary for the spacecraft engineer.

The construction of a reliable, self-consistent, proton belt model would be very difficult at the present time. A more practical but more restricted approach is to derive upper limits by considering the stability of possible radiation belts. We shall consider the instability of the Jovian counterpart of geomagnetic pulsations, known as pcl's, "pearls," or hydromagnetic whistlers. The instability is driven by radiation belt protons in the disk-like region around the equatorial plane of Jupiter. This region is shown in Figure 1. The region between the field lines near Io and Europa is the region in which our theoretical model plays a significant role. We see that a wavelet of small amplitude entering the instability region is amplified by the instability. If the amplification is too strong the waves will react back on the particles, diminishing the proton number by throwing them into the ionosphere. There is therefore a flux of amplifying protons that cannot be exceeded. This is essentially the upper limit on the belts we are looking for. Figure 2 shows the results of my calculations. The energies noted on the curves denote the proton energy above which the interaction takes place at a certain planetary radial distance. The lower solid curve shows the fluxes at which the mechanism described begins to work. The upper curve gives the upper limit, which cannot be exceeded. For comparison the dashed lines show the flux of terrestrial protons above 0.56 pJ (3.5 MeV) at the position of its maximum value. We see that the proton fluxes at picojoule (megaelectron-volt) energies in the Jovian belts may be more than 100 times the terrestrial ones. By coincidence the upper curve corresponds roughly to the maximum fluxes that the magnetic field of Jupiter can trap. We cannot give limits that will reduce the concern of spacecraft engineers about possible radiation damage inside 10 radii. The virtue of the method used lies in the fact that it needs relatively few assumptions as to the nature of the Jovian magnetosphere.
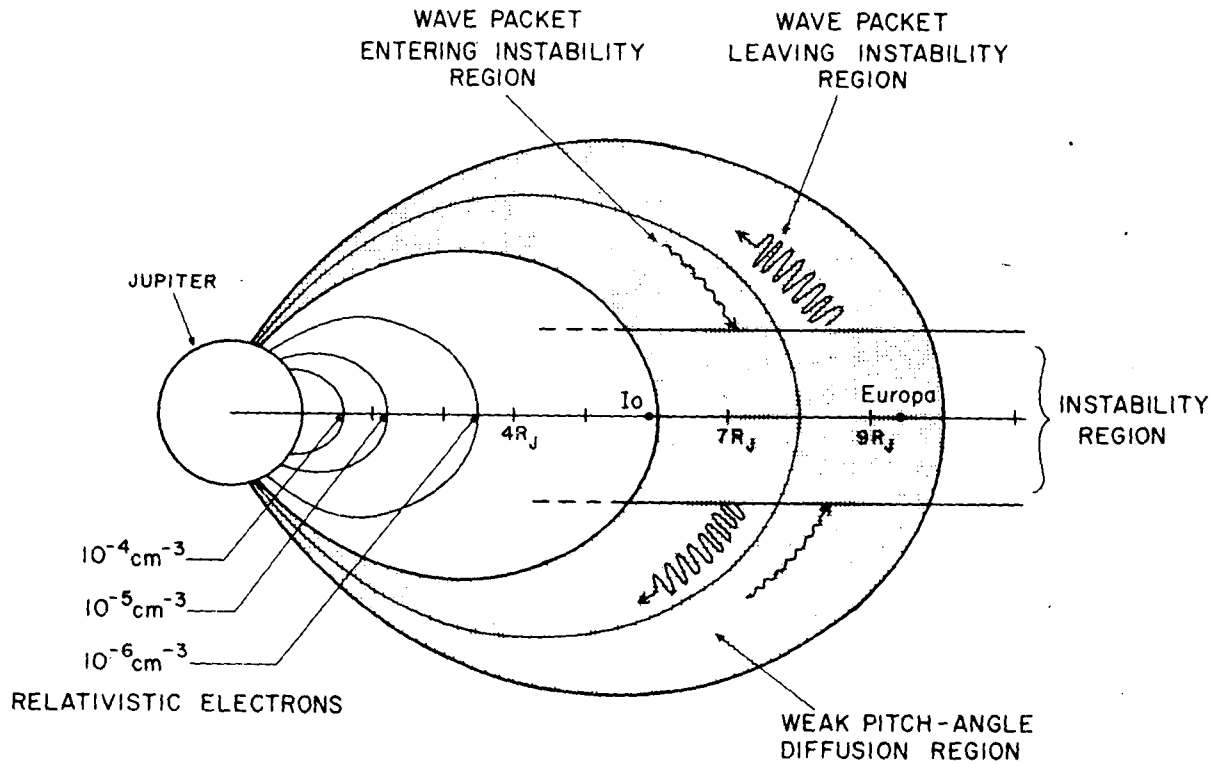
Figure 1—The environment of Jupiter showing the instability region in the radiation belts. (The positions of the relativistic electron belts are from Ref. 1.)
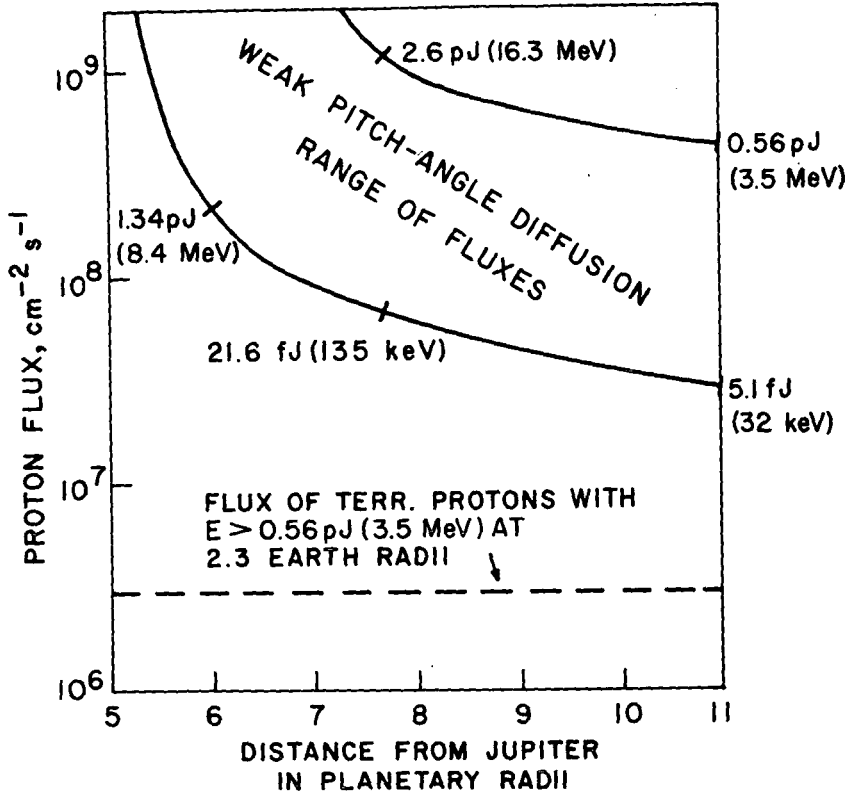
Figure 2–Calculated proton fluxes.

REFERENCE

1. Luthey, J. L.; and Beard, D. B.: Equatorial Electron Energy and Number Densities in the Jovian Magnetosphere. Proc. Jupiter Radiation Belt Workshop, Jet Propulsion Laboratory (Pasadena, Calif.), July 13-15, 1971, to be published.

RESULTS FROM THE GSFC OSO 7 SPECTROHELIOGRAPH

Dr. Werner M. Neupert

One of the prime goals of the pointed spectroheliograph on OSO 7 is to record the evolution of solar active regions and solar flares. The design philosophy of the instrument, which was successfully implemented and launched, is that it is necessary to observe each level in the solar atmosphere that might be involved in a particular solar phenomenon.

A concrete example is that to observe the evolution of a solar flare one must observe at several different heights of the solar atmosphere at which that event might occur or to which it might spread.

The solar atmosphere is a plasma existing under a wide range of physical conditions. Various levels (or components) in that atmosphere are differentiated primarily by their electron temperature and are observed by recording the radiation of ions that exist primarily at the appropriate temperature. The experiment then becomes one of observing specific spectral lines which carry the required physical information.

This brings us to the first attribute of the OSO instrument that distinguishes it from its predecessors. That is, it can record radiation over a wide range of wavelengths. The spectral range extends from the red portion of the visible spectrum (H-alpha), which is used to obtain easy comparison with ground-based observations, to soft X-ray radiation at 0.2 nm. We therefore have the capability of observing the solar atmosphere from the 10000 K level (in H-alpha, from unionized hydrogen) to short-lived flare-associated regions at 30 million K (in the radiation of 24 times ionized iron, Fe-XXV). Needless to say, the observations are far from complete. For instance, they carry no information about the magnetic field.

A second observational requirement immediately becomes obvious, and that is that the emission lines must be recorded as simultaneously as possible to obtain the complete picture at one instant in time. In the Goddard experiment there are four separate data channels giving observations simultaneously. The signals are used to build solar maps point by point by raster scanning across the surface of the Sun. Each set of four maps taken in the small raster mode required 1 min and covers an area of 5 by 5 arcmin as seen from the Earth. The separation of data points in a raster line corresponds to an angular separation of 12 arcsec, and that, together with a resolution limit of about 15 arcsec on the EUV telescope, limits the detail that we are able to resolve.

Figure 1 shows two maps of an active region on the Sun that was observed 3 hr after turning on the instrument on October 3. The two radiations recorded in Figure 1 are H-alpha, which I referred to earlier, and soft X-rays from 1.3 to 1.6 nm. The darkest region in H-alpha corresponds to a sunspot, a cooler region in the solar photosphere and chromosphere. The brighter region represents an elongated bright plage in H-alpha, corresponding perhaps to an increased magnetic field in the chromosphere. This map corresponds quite well to ground-based observations but emphasizes that two small regions are of greater intensity than the remainder of the plage. In a soft X-ray channel, we find that the X-ray source is elongated with two brighter regions. The upper bright spot in H-alpha corresponds to the tip of the upper X-ray source; the lower one is near but not coincident with the lower X-ray source. What we may be seeing here is an X-ray loop which has its feet in the solar chromosphere and has an enhancement at the two ends. The diameter of this strand of hot plasma is less than the resolution of the system and is probably only a few arcseconds (1 arcsec = 700 km on the Sun).

About 2 hours later we observed our first solar flare in this region, as shown in Figure 2. The region has moved slightly toward the left in the field of view, corresponding to the solar rotation. The solar flare emission is the highly localized and intense region to the left of center. In this figure, as in the previous figure, the actual source diameter is less than the resolution of the telescope.

An interesting comparison can be made by superimposing the first two figures as done in Figure 3. Notice that the H-alspha flare was produced primarily between the original two bright spots that existed in H-alpha. The X-ray flare source, however, is displaced toward the west from the original preflare region. This displacement is of the order of the resolution of the instrument but is obviously real and suggests that the source is not in the original region or that that region had shifted slightly in the solar corona.

These figures represent only a small amount of data — two channels for 1 min each. The observations for the event consist of four channels of data and the event lasted for on the order of 4 hr. It should be possible, by combining the OSO observations with ground-based observations, to construct a fairly complete picture of this event.

CHAIRMAN:

Are there any questions?

656.3 nm   1.3–1.6 nm

12 arcsec
(= 8400 km)

INTENSITY SCALE

>164.5	161.5–162.4	2000–2900	400–599
163.5–164.4	160.5–161.4	1000–1999	100–399
162.5–163.4	>160.5	600–999	20–100
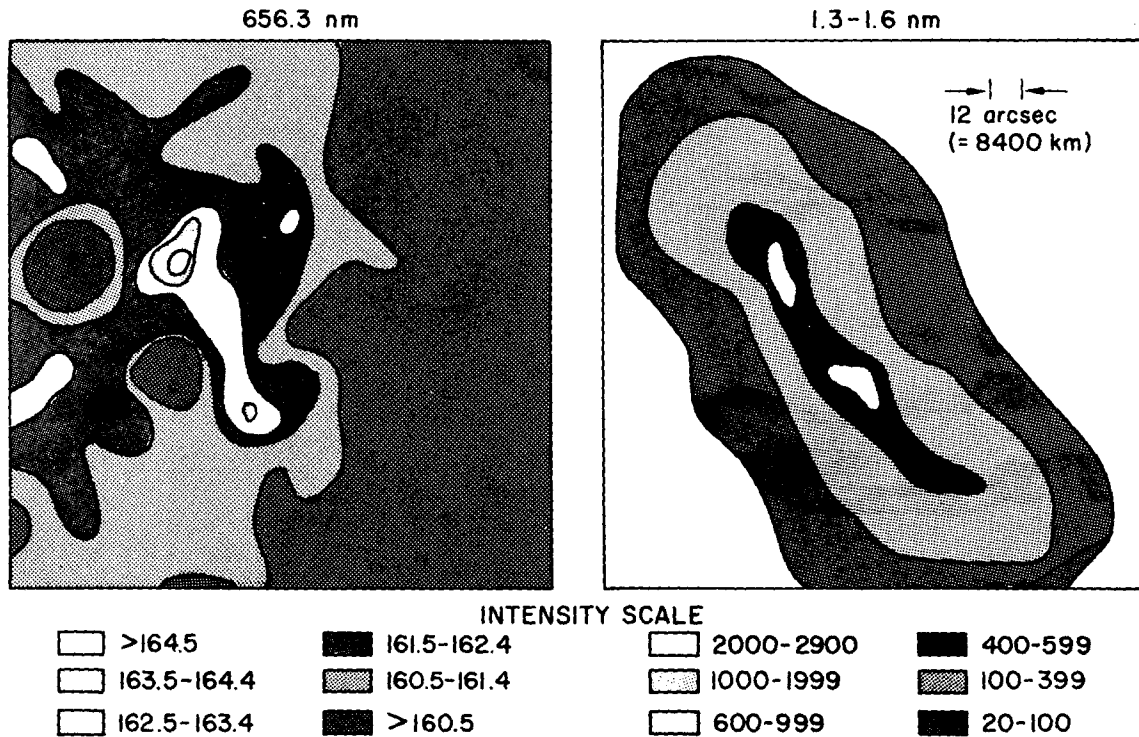
Figure 1—Observations of an active region in H-alpha and soft X-rays from OSO 7; October 3, 1971, 11:21 UT.

656.3 nm · 1.3-1.6 nm

12 arcsec (≈8400 km)

INTENSITY SCALE

>162.5	150.5-154.4
158.5-162.4	146.5-150.4
154.5-158.4	<146.5

2000-2900	400-599
1000-1999	100-399
600-999	20-100
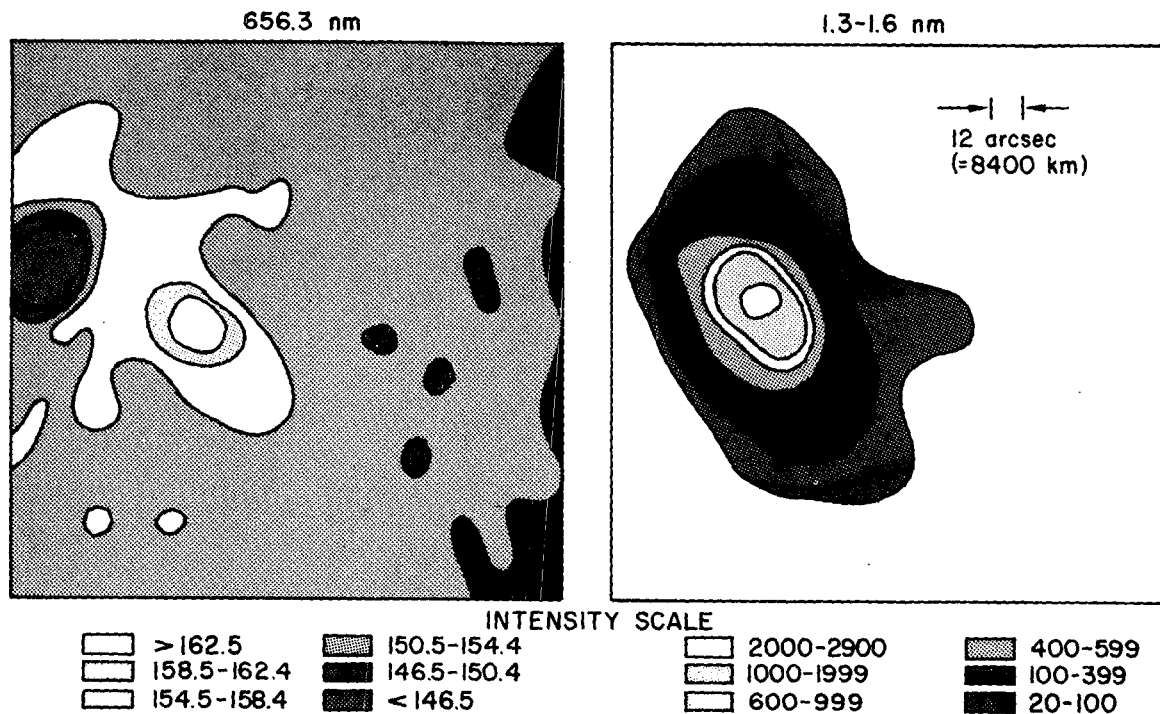
Figure 2—Observations of a solar flare in H-alpha and soft X-rays from OSO 7; October 3, 1971, 13:52 UT.
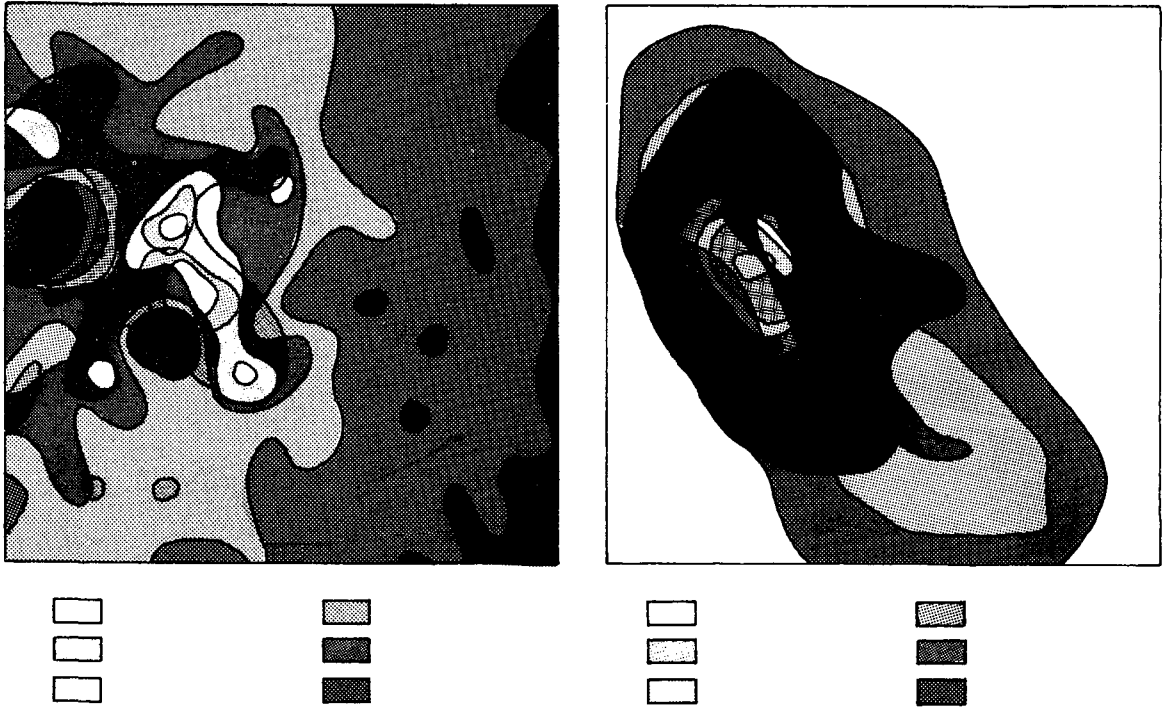
Figure 3–Superimposition of Figures 1 and 2.

MEMBER OF THE AUDIENCE:

The displacement of the X-ray source in relation to the H-alpha source might have been due to the height of the emission, if this was a limb flare; was that the case?

DR. NEUPERT:

This flare was very close to the meridian.

MEMBER OF THE AUDIENCE:

The big problem about solar flares is what triggers them. How will these observations help you to answer that question?

DR. NEUPERT:

For this flare we probably will be able to (in a very limited sense, because we were observing only for a matter of several hours) watch the evolution of a region prior to the event. What I am suggesting is that we may be able to identify particular configurations of coronal structures and magnetic fields that lead to flares. Now, whether that is going to tell us what triggers the flare, I do not know, but we certainly hope that we will be able to describe the circumstances under which flares do take place.

MEMBER OF THE AUDIENCE:

Do you have magnetic field data for this event?

DR. NEUPERT:

Observations of the active region, but not of the flare, were made. We are asking ground-based observers to make magnetic field observations on the groups simultaneously with the OSO observations.

TRANSPORT OF COSMIC RAYS IN THE SOLAR CORONA

Dr. Kenneth H. Schatten

This work was undertaken in collaboration with Len Fisk of Goddard Space Flight Center.

Solar cosmic rays produced by flares, such as Werner Neupert was showing, can gain access to the interplanetary magnetic field near Earth from flares located almost anywhere on the Sun. In fact, there is evidence that at least one flare located near central meridian on the invisible solar hemisphere produced detectable increases in the intensity of picojoule (few-MeV) protons at Earth.

The diffusion of energetic particles in the interplanetary medium cannot account for the observations; therefore, there must exist an efficient mechanism for the transport of cosmic rays in the solar corona.

We are suggesting a method by which these energetic particles can diffuse in solar longitude. The method consists of particle motion occurring along current sheets separating discontinuous field structures in the corona. These sheets can serve as pathways along which energetic particles drift at nearly their propagation speed.

First, let us look at a model of the coronal magnetic field and see how the large-scale field behaves. Figure 1 shows a model for the coronal magnetic field. As you can see, the Sun's magnetic field is much more complicated than the Earth's dipole field. There are all sorts of fields associated with active regions: bipolar magnetic regions and unipolar magnetic regions, which give rise to the coronal magnetic loops and arches seen here.

Energetic particles can travel very easily along the magnetic field but only with great difficulty across the magnetic field. Although the field is very complex, there are some regions that are connected by field lines to others at distant longitudes. Most locations are not connected so that flare particles could travel along the field and arrive at Earth. Hence we require a mechanism by which particles can travel across the coronal magnetic field and arrive at Earth.

Figure 2 shows one such mechanism. The magnetic field in the upper portion of the figure, above the current sheet J, is directed inward; below the current sheet it is directed outward. If current sheets exist in the solar corona such that there are discontinuities in the

117
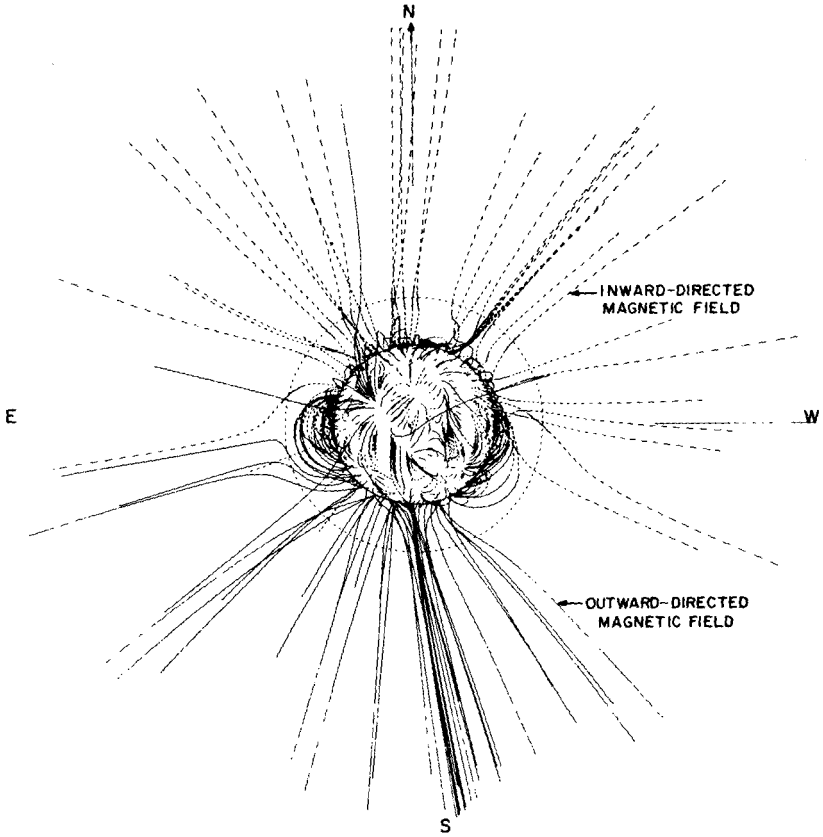
Figure 1 –Model of the coronal magnetic field.

coronal field on a very small scale, a particle can travel along these discontinuities and thus across the field by undergoing a zigzag motion on either side of the current sheet, as shown in the lower portion of the figure. It is a little bit like a sailboat tacking upwind insofar as the particle is making progress it could not make directly by choosing alternate advantageous pathways.

It is important to note that the particle can travel across the field in this way at nearly its propagation speed, thus the particle can diffuse across the Sun in a very short time.
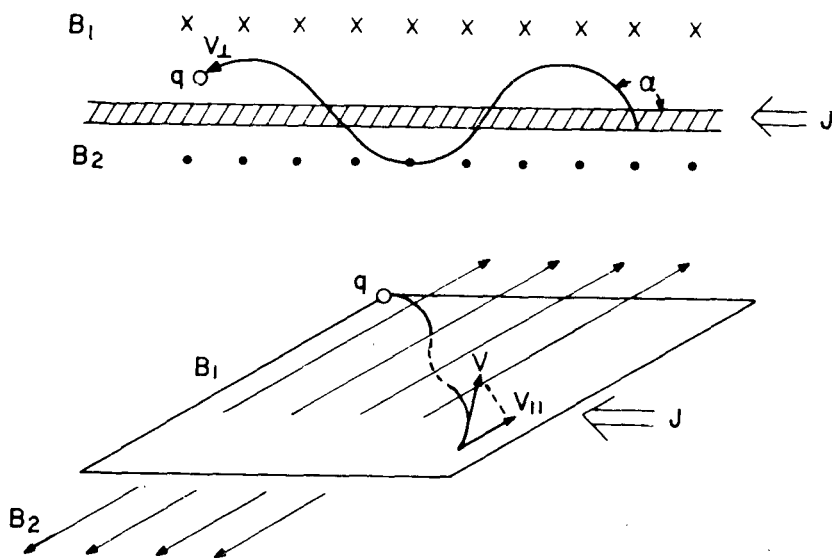
Figure 2—Mechanism by which particles can travel across the coronal magnetic field and arrive at Earth.

Although Figure 2 shows oppositely directed fields on either side of the current sheet, the process occurs nearly as efficiently with alined fields having differing field strengths.

It should be pointed out that this mechanism is not really a new phenomenon but rather an enhanced type of gradient field drift. In addition, Michel and Dessler (Ref. 1) suggested a similar mechanism for particle motion in the Earth's magnetic tail field. Let us take a larger scale look at the diffusion process where many current sheets occur in the coronal field.

Figure 3 shows how an energetic particle would behave in a filamentary coronal field. Each of these cells or filaments might be the extensions of the boundaries of the granules and the supergranules found on the Sun. As one can see, the energetic particle can weave its way along the boundaries of these cells in a sort of random-walk fashion.

We have put this model to a quantitative test by fitting the mechanism to a diffusion equation, choosing reasonable values for the current sheet dimensions. We find that our model can be fit very well to the observations of

CURRENT SHEETS

CORONAL FLUX
TUBE FILAMENTS

CURRENT SHEET
DIFFUSION
OF PARTICLES
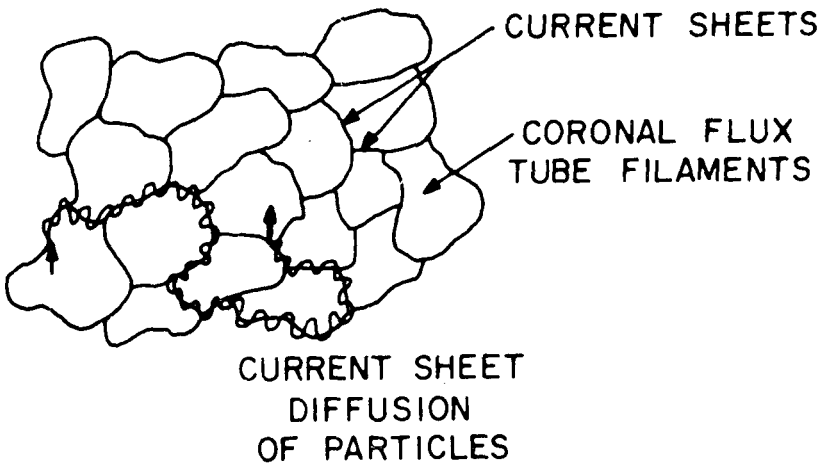
Figure 3—Behavior of an energetic particle in a filamentary coronal field.

McCracken et al. (Ref. 2) that 1.6-pJ (10-MeV) protons decrease in intensity as a function of heliocentric longitude with an *e*-folding angle of 30°. That is, if one is 30° removed from a flare event, one sees only about one-third as many energetic protons. Our model also fits the spectral index variation that McCracken observed.

In conclusion, we are suggesting that the transport of cosmic rays in the solar corona may take place along thin current sheets. In addition, this general type of transport of particles may be important in other astrophysical plasmas.

CHAIRMAN:

Are there any questions on this paper?

MEMBER OF THE AUDIENCE:

Can the mechanism work if the fields on either side of the current sheet are parallel?

DR. SCHATTEN:

Yes, even if the fields are completely parallel as long as the field strengths are different. If the field strengths are the same and they are completely

parallel, then there is no current separating the fields. The particle would just stay there in orbit about a single position. But with different field strengths, the particle would undergo a cycloidal type of motion, and therefore it would still travel along the discontinuity.

REFERENCES

1. Michel, F. C.; and Dessler, A. J.: J. Geophys. Res., vol. 75, 1970, p. 6061.

2. McCracken, K. G.; Rao, U. R.; Bukata, R. P.; and Keath, E. P.: Solar Phys., 1972, in press.

SOLAR PARTICLE COMPOSITION MEASUREMENTS

Dr. Donald V. Reames

For some time now our group at Goddard had been engaged in studying the compositon of solar particle events; that is, the relative abundance of different elements, using nuclear emulsion detectors flown on board sounding rockets. More recently we have been able to extend these observations to elements as heavy as iron.

Figure 1 shows some of the earlier work. Here we are looking at the energy spectra or energy per nucleon spectra (energy per nucleon being related to the particle velocity) for helium nuclei (the open figures), and for carbon, nitrogen, and oxygen combined (the solid figures), here multiplied by a "magic" factor of 58. We see that for the several events and observation times plotted, the spectra of these different nuclei are very similar.

We have been able to understand this phenomenon by the model in which the particles in a flare are stripped of electrons in the high temperature of a flare region, and subsequently are accelerated presumably by magnetic fields. These particles, stripped of electrons, have the same charge-to-mass ratio and therefore are indistinguishable to electric and magnetic fields; therefore, if we compare the abundances of different particles of the same velocity, we would expect to find an abundance that is directly related to that in the source, in this case in the flare region or the Sun itself. So these particle measurements appear to provide a direct measure of solar abundances themselves in these intense events.

Figure 2 shows a more detailed comparison, element by element for the combined result. The solar cosmic ray results (our results — shown in solid figures) are compared with photospheric and coronal abundances for the elements, where comparisons are possible.

In general we see that the agreement is reasonably good with the photospheric abundances, where those are available (all abundances are normalized to oxygen). Note particularly the carbon-to-oxygen ratio and the abundances of neon, magnesium, and silicon.

As we look toward iron, we begin to worry somewhat as to whether the assumptions, the necessary criteria, are met, since iron, even when fully stripped, has a charge-to-mass ratio that differs by about 8 percent from
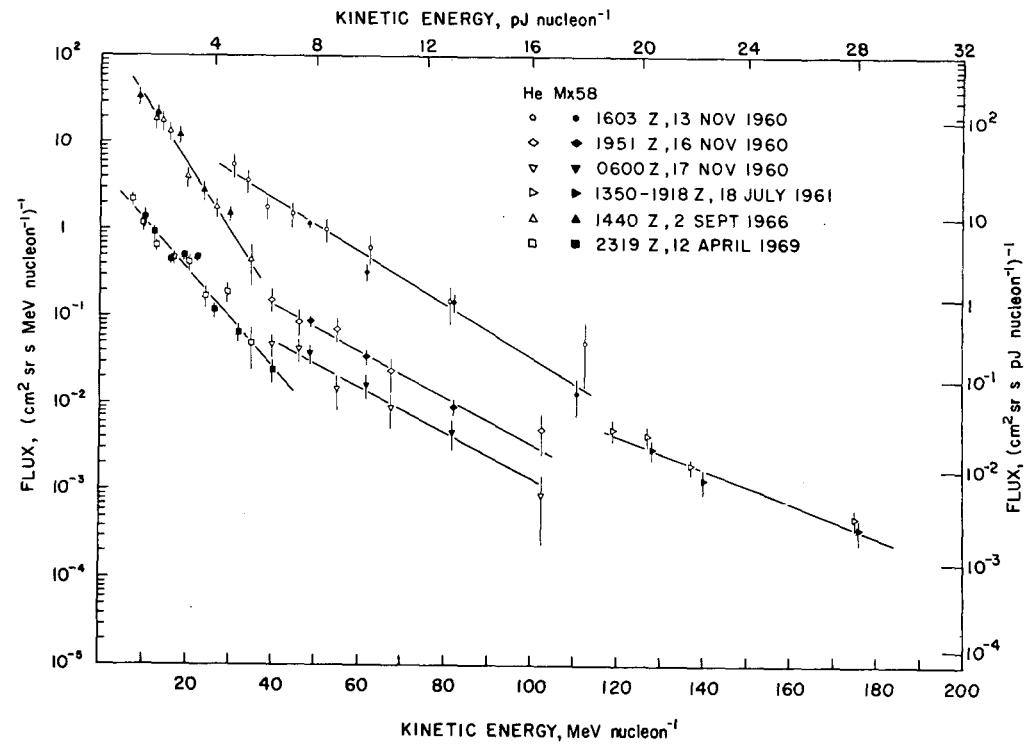
Figure 1—Energy per nucleon spectra.
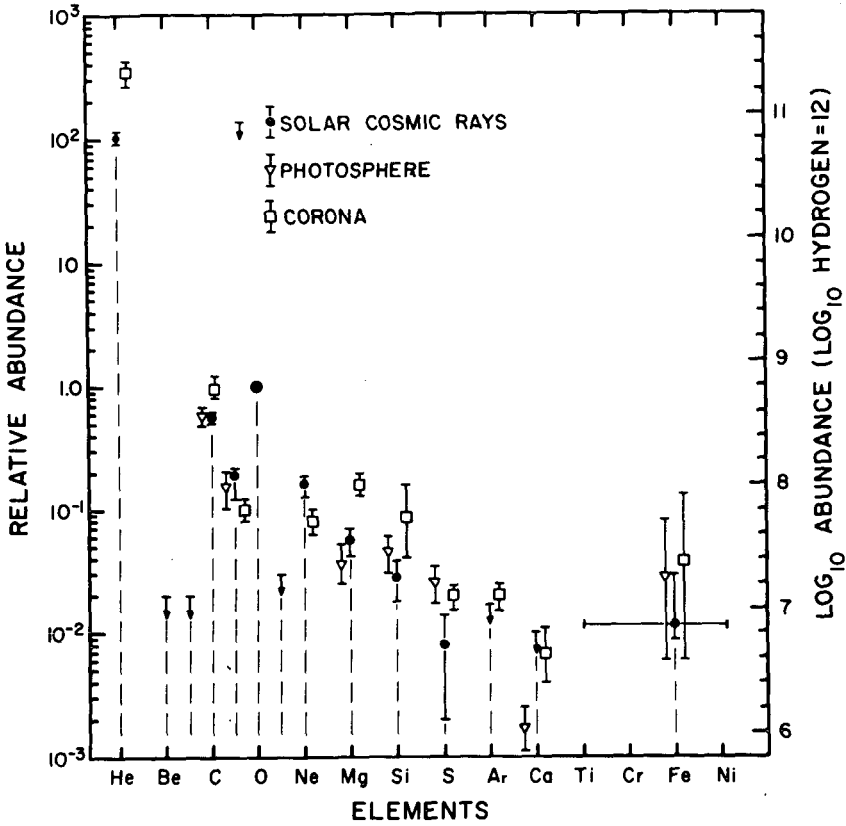
Figure 2–Comparison of solar cosmic ray, photospheric, and coronal
abundances for the elements.

those of the lighter species. We know quite well that in cases where the
charge-to-mass difference is large, in comparing hydrogen and helium, for
instance, we see enormous differences in flux with time and with energy
during the events. So we are somewhat concerned that the abundance of
iron does not fluctuate in a similar manner.

Table I shows the results. Our first measurement, the first observation of
iron in September 1966, was about 1 percent of oxygen. In the event in
January of this year, we were able to obtain a second preliminary measure-
ment which seems to agree quite well statistically with the earlier results.

C

TABLE I. Iron Abundance.

Solar particle events	Percent of oxygen
Nov. 12, 1960	<2
Sept. 2, 1966	1.1±0.3
Apr. 12, 1969	<3
Jan. 24, 1971	1.3±1.2
Solar photosphere (Ref. 1)	2.5±1.2

For comparison, I have shown one of the more recent photospheric abundances. These are somewhat subject to interpretation, and earlier estimates differ by perhaps as much as an order of magnitude.

So it seems that even in the case of iron one can make measurements that relate to the abundance of the element in the Sun.

In these events and a subsequent event in September of this year that has not yet been analyzed, we also flew some plastic detectors for the University of California and hope to make cross comparisons of iron from the two different types of detectors. The plastic detectors observe at somewhat lower energy and can be more directly related then to observations in lunar samples to extend measurements of this kind over large ranges of history.

Also, in the near future we will be increasing our observation area in order to observe the less intense events where some of the conditions for invariant abundances might not be met. By observing changes in composition we might learn something more about the acceleration mechanism. Of course, in addition, we will be able to observe less abundant elements with the increased area.

REFERENCE

1. Aller, L. H.: Paper presented at 12th Int. Conf. Cosmic Rays (Hobart, Tasmania, Australia), 1971.

THE CHARGE SPECTRA OF SOLAR COSMIC RAYS

Dr. Tycho T. Von Rosenvinge

I would like to report on a different approach to measuring charge spectra of solar cosmic rays. These observations were made by a telescope that Frank McDonald, Bonnard Teegarden, and I have on the IMP 6 satellite, and they illustrate very nicely the quantum jump in capability that took place between IMP 6 and the previous IMP satellites.

In particular, we have extended the charge range beyond charge 2 right up to charge 26, and we have also extended the energy range to lower energies. There is a unique innovation in this experiment, which we refer to as our Cancro priority system, after our favorite engineer Jerry Cancro. It preferentially selects rare events above charge 2 and gives them top priority for telemetry readout, thus breaking the monopoly that protons and helium nuclei otherwise would have on the telemetry.

This effectively increases the number of nuclei that we were able to observe above charge 2 by a factor of several hundred. This factor of several hundred is all important for prior to the last few months, there simply have not been any other satellite-borne detectors that could compete with the rocket-borne emulsion technique that Don Reames just described. It must be nice to have 10 yr without competition from anybody else. .

I am referring now to measurements that resolve individual charges above charge 2. With our new capability, we will be able to extend this pioneering work to lower energies and also to smaller flares, and we are hoping to try to measure the charge composition in long-lived solar particle streams as well, which simply can not be done with emulsions.

So far, we have observed two flares since the time IMP 6 was launched in March of this year. I will be reporting today mainly on a small flare that took place in April, since we are just now starting to get our teeth into the larger flare, which took place in September.

Figure 1 illustrates the telescope that we are using. It consists of a thin and a thick solid-state detector surrounded by an active anticoincidence. We analyze particles that enter the front aperture and either stop in the front detector or in the second detector but reject all those particles that intersect the anticoincidence.
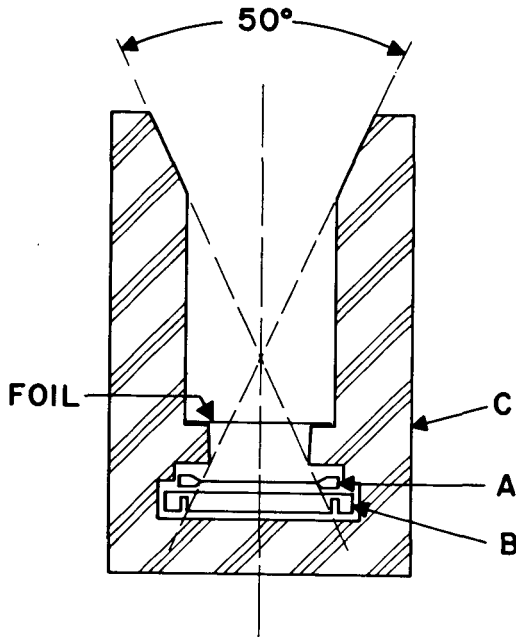
Figure 1—IMP 6 telescope. A is the 150-μm silicon,
300-mm^2 detector; B is the 3-mm silicon, 500-
mm^2 detector; C is the plastic scintillator; and
the foil is 1 mg cm^{-2} titanium.

The response for particles that stop in that front detector is shown in Figure
2. You can see that even though it is only a one-dimensional measurement,
we do have some measure of charge resolution. You can distinguish elec-
trons, protons, helium nuclei, and particles with charge Z greater than 3.
The fantastic thing about these data is that they cover over 9 orders of mag-
nitude in intensity, far more than we have been able to cover before.

Figure 3 illustrates the response of the telescope for particles that penetrate
into that second detector. On the left-hand side you see over a hundred
carbon, nitrogen, and oxygen nuclei from a flare on April 6. We were de-
lighted with these data because without our priority system we would have
had, say, only two of those nuclei, and we could not have done much with
that. But with over a hundred particles and good charge resolution, we
could make a reasonably good measurement.
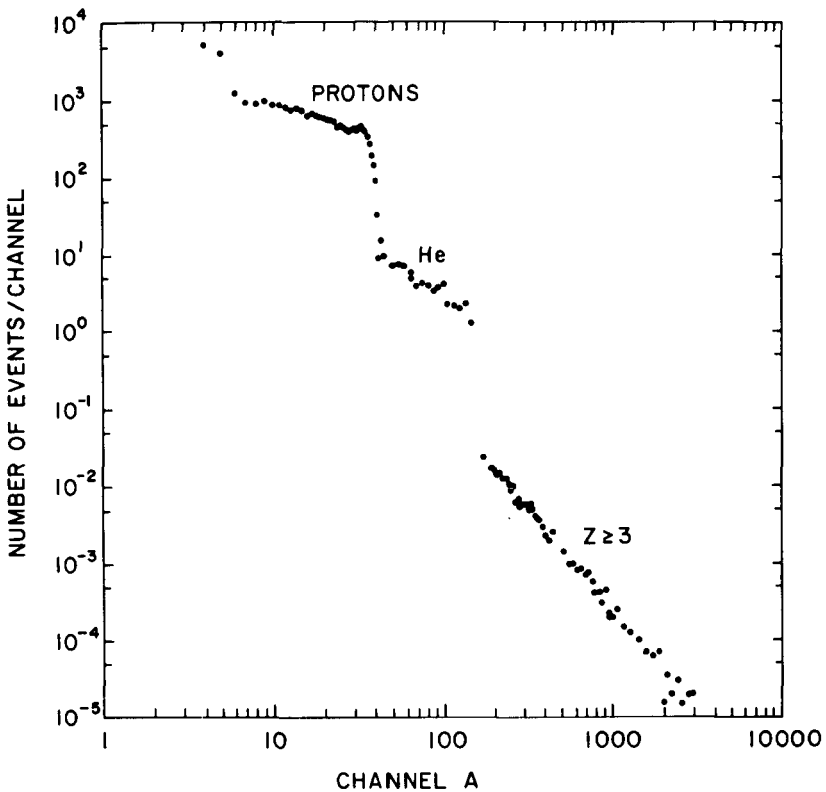
Figure 2—IMP 6 telescope response for particles stopping in detector A.

I might say that the priority system selected these hundred events from over 100000 protons and helium nuclei that were competing for telemetry space, and that is why if we had not had our priority system we would have only seen some two events.

On the right-hand side, you can see the comparable data taken in September and we were ecstatic with this. There are over 4000 particles on that figure, and you can see that nitrogen, which is a low-abundance nucleus, is clearly separated from the neighboring carbon and oxygen, which are much more abundant than the nitrogen.
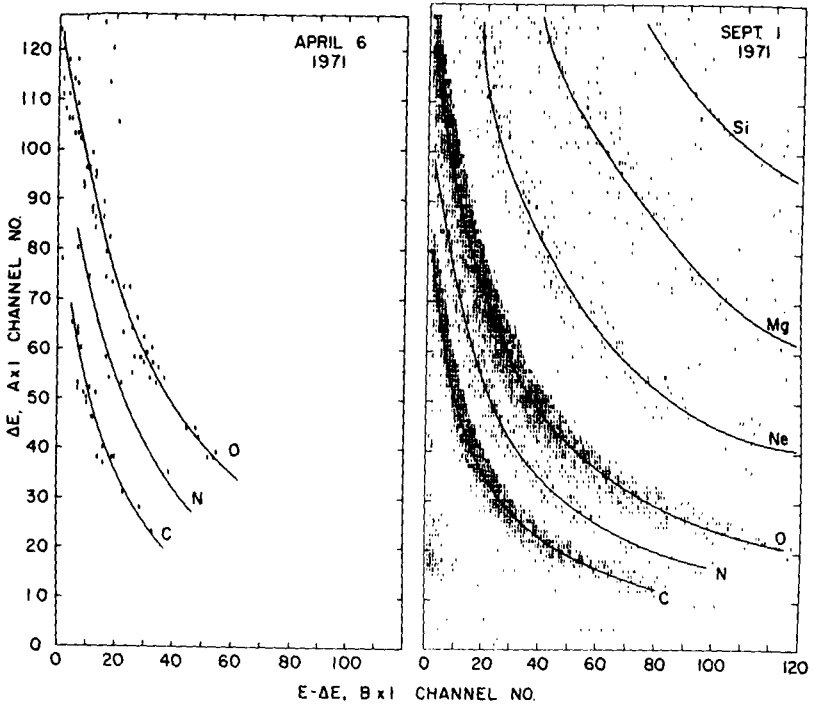
Figure 3—IMP 6 telescope response for particles stopping in detector *B*.

The background-free nature of this telescope is also evident by the fact that there is just no fluorine present here at all and you can see that we have nicely resolved neon, magnesium, and silicon. The data extend beyond those illustrated, and we can see more than 40 iron nuclei in a very nice tight band, indicating that we have good charge resolution right up to charge 26.

Table I shows some of the data that we have obtained from the April flare compared with the results of David Bertsch, Don Reames, and Carl Fichtel (Ref. 1) at higher energies from rocket-borne emulsions. The helium-to-medium ratio (He/M) that we observe is slightly lower than what they have, but it is constant throughout the flare, a point which they have been worried about since some people have recently claimed that it does vary. We saw it to be constant at low energies as well as at the higher energies where the emulsions are measuring.

TABLE I—IMP 6 Measurements Compared With Rocket-Borne
Emulsion Results

Element ratio	IMP 6 measurements at $\sim$1.3 to 3.7 pJ nucleon^{-1} ($\sim$8 to 23 MeV nucleon^{-1})	Emulsion measurements at $\geqslant$3pJ nucleon^{-1} ($\geqslant$20 MeV nucleon^{-1})
He/M	46 ± 9	58 ± 5
C/O	0.42 ± 0.11	0.56 ± 0.06
N/O	0.20 ± 0.08	$0.19 \begin{smallmatrix} +0.03 \\ -0.07 \end{smallmatrix}$
Ne/O	0.11 ± 0.05	0.16 ± 0.03
Mg/O	0.20 ± 0.08	0.056 ± 0.014
Si/O	0.11 ± 0.06	0.028 ± 0.01
Fe/O	0.17 ± 0.08	0.011 ± 0.003

Notice that for the low charges the agreement between the two studies is quite good. As we move to higher charges, the relative abundances are somewhat larger. It has been suggested that this might be characteristic of small flares, but I think it is too early to really say that.

Anyway, we have developed a very fine detector for this sort of observation, and we are very much excited by the data that we are getting. We should be able to come up with more complete results in the near future.

REFERENCE

1. Bertsch, D. L.; Fichtel, C. E.; and Reames, D. V.: Nuclear Composition and Energy Spectra in the April 12, 1969, Solar Particle Event. Astrophys. J., vol. 171, 1972, p. 169.

TYPE III SOLAR RADIO BURSTS

Dr. Larry G. Evans

Rapid drift type III solar radio bursts are caused by streams of high-speed electrons ejected from the Sun that excite radio waves at the local plasma frequency as they move through the corona. Ground-based radio observations can provide information on these electrons only in regions very close to the Sun, within the first one-hundredth of the distance from the Sun to the Earth.

With the detailed low-frequency observations made possible by the RAE and IMP 6 satellites, these electrons can be followed to vastly greater distances, of the order of 1 AU from the Sun. A study of the radio observations, along with the knowledge of how the electrons excite radio waves as they move through the corona can provide information on the structure of the interplanetary media extending from the Sun to the Earth, such as its temperature, density, and magnetic configuration.

In the past 25 yr, since the discovery of these bursts, numerous theories have been proposed to account for this generation process. For the first time, using low-frequency satellite observations, a direct comparison of the different theories is possible, since we have available independent measurements by satellite electron detectors in the same region of the interplanetary media where the radio emission is being generated.

Our results show, on the basis of this comparison, the general inadequacies of current type III burst theories and indicate a needed emphasis on formulating a new theory that is consistent with the low-frequency observations.

Representative observations from the RAE satellite are shown in Figure 1. The brightness temperature, which is a measure of the energy flux, versus frequency is plotted. Shown are two events, a large burst and a large storm, each recorded at frequencies of 2.8 MHz and 700 KHz. Also shown are high-frequency curves obtained from ground-based observations. It can be seen that the RAE observations are consistent with the extrapolation of the ground-based observations.

Each of the different theories of Type III bursts gives a relation between the exciter electron density and the resulting brightness temperature. Since we have these observations of brightness temperature as a function of
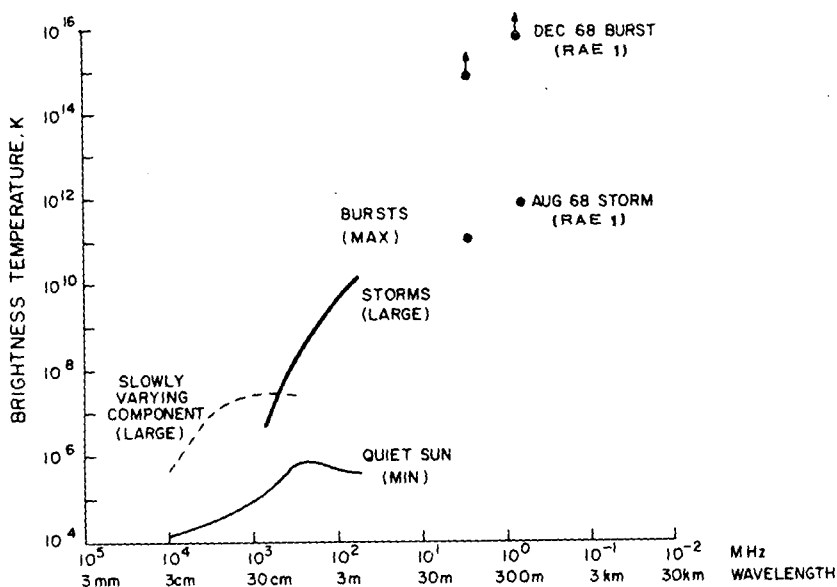
Figure 1—Comparison of RAE and ground-based observations
of brightness temperature.

frequency, we can calculate the required exciter electron density as a function of frequency. With a corona model also obtained from the RAE observations, the plasma frequency scale can be converted into a distance from the Sun scale. Thus we are able to calculate, as shown in Figure 2, the required exciter electron density as a function of coronal distance (in solar radii).

Figure 2 shows some of the most popular and widely used theories of type III bursts. For each of the theories, a curve is plotted using three high-frequency observations indicated by the solid circles and the two low-frequency satellite observations, indicated by open circles. Also shown in this figure are a representative range of 6.4 fJ (400 keV) electron densities measured by satellites in the vicinity of 1 AU. This is the energy range of electrons corresponding to an exciter velocity of 10^{10} cm s^{-1}, calculated from the radio observations.

If we extrapolate the curves to 1 AU, then except for the curve labeled S$_2$, all the theories give an exciter electron density quite different from the measured values; and it has been argued because of other considerations that the S$_2$ curve may not represent a realistic physical solution.
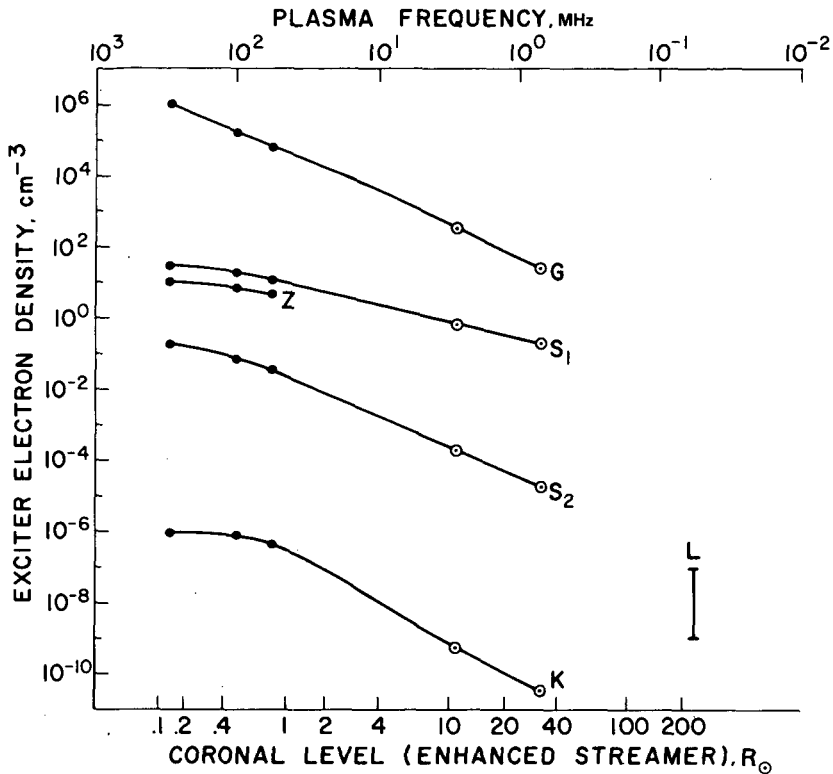
Figure 2—Exciter electron density as a function of coronal distance. The curves are identified as follows: *G* from Ginzburg and Zhelezynakov (Ref. 1); S_1, $\delta \neq 1$, and S_2, $\delta = 1$, from Smith (Ref. 2); *K* from Kaplan and Tsytovich (Ref. 3); *Z* from Zhelezynakov and Zaitsev (Ref. 4); and *L*, the measured energetic density range for a storm, from Lin (Ref. 5).

Thus, we were left with the conclusion that none of the current type III burst theories give an adequate description of the conversion process consistent with these observations. Since the conversion process must be understood before a description of the corona structure and the properties of the interplanetary media can be determined, the low-frequency satellite observations necessitate a renewed emphasis on the theoretical treatment of type III bursts.

In the near future, observations from the IMP 6 satellite at frequencies down to 30 kHz will enable these curves to be extended out to 1 AU. We do not, however, expect that these observations will markedly affect the trends shown in Figure 2 or the resulting necessity for new theoretical work.

REFERENCES

1. Ginzburg, V. L.; and Zhelezynakov, V. V.: Sov. Astron. AJ, vol. 2, 1958, p. 653.

2. Smith, D. F.: Advan. Astron. Astrophys., vol. 7, 1970, p. 147.

3. Kaplan, S. A.; and Tsytovich, V. N.: Sov. Astron., AJ, vol. 11, 1968, p. 956.

4. Zhelezynakov, V. V.; and Zaitsev, V. V.: Sov. Astron., AJ, vol. 14, 1970, pp. 47 and 250.

5. Lin, R. P.: Solar Phys., vol. 12, 1970, p. 266.

QUIETTIME ELECTRON INCREASES

Dr. Lennard A. Fisk

The IMP spacecraft have been monitoring the behavior of cosmic rays in the interplanetary medium almost continuously since the earth 1960's. In particular, the behavior of 0.5- to 1.9-pJ (3- to 12-MeV) interplanetary electrons has been studied. I would like to tell you today about a new cosmic ray phenomenon that has been detected in the behavior of these electrons, and about a possible explanation for this phenomenon, which, if correct, gives us some real clues about interplanetary conditions far beyond the orbit or Earth.

In Figure 1, I have plotted the daily averages of the 0.5- to 1.9-pJ (3- to 12-MeV) electron intensity that was observed from the IMP's by McDonald, Cline, and Simnett (Ref. 1). These data cover the period 1965 through 1968. The abrupt increases in the intensity, which are marked by the dark boxes, are solar flares. The brackets mark the new phenomena that I would like to tell you about. These are known as quiettime electron increases.

There is present throughout this period a relatively steady background flux of galactic electrons. Quiettime increases give every impression of being simply localized increases in this background flux. We suspect this because quiettime increases occur in anticoincidence with increases in the flux of low-energy solar protons. We can be sure of the galactic origin for the electrons in quiettime increases by examining their spectra. Quiettime increases and the galactic background both have the same spectral index of about -2. Quiettime increases occur when there is an enhanced influx of galactic electrons into the inner solar system.

Now clearly, quiettime increases must occur when conditions that normally exclude a large fraction of the 0.5- to 1.9-pJ (3- to 12-MeV) galactic electrons from the inner solar system are altered, permitting more electrons to enter. This exclusion is due presumably to magnetic irregularities that are carried outward with the solar wind. There is no evidence, however, either from gradient measurements or from diffusion coefficients that can be inferred from solar flare time profiles that 0.5- to 1.9-pJ electrons experience much scattering in the inner solar system. In the case of the electrons, the region where the scattering occurs, the modulating region, must lie far beyond the orbit of Earth.
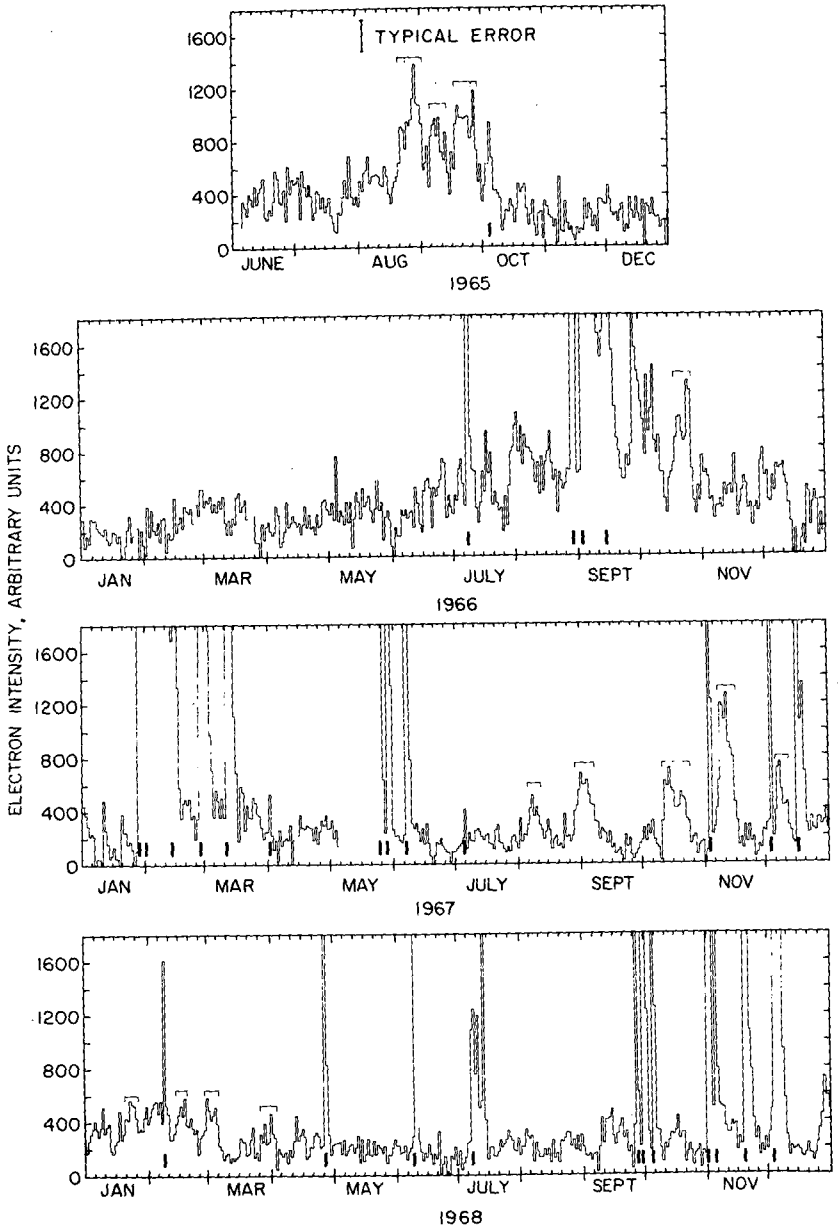
Figure 1—Daily averages of the 0.5- to 1.9-pJ (3- to 12-MeV) electron intensity as obtained from IMP data.

D

We can actually get a measure of the location of this modulating region by considering the sequence of events that might lead to a quiettime increase. The mean field direction in a modulating region far beyond Earth will be essentially azimuthal about the Sun, so particles will pass through this region principally by diffusing perpendicular to the field. Perpendicular diffusion, in turn, is caused principally by field-line random walk; that is, the amount of random walking that individual field lines do about the mean field direction. In the solar system, field-line random walk is caused mainly by photospheric turbulence, the base of the field lines moves randomly with the photospheric turbulence, and then the random walk is executed as the solar wind drags out the field.

We have, then, the following sequence of events leading to a quiettime increase. A group of field lines executes a larger-than-average random walk in the photosphere. The solar wind drags out these field lines past the orbit of Earth to a modulating region lying further out. When they reach this modulating region, more 0.5- to 1.9-pJ (3- to 12-MeV) electrons diffuse through the region and propagate back into the inner solar system, and we have a quiettime increase at Earth. Clearly the delay time between when the field lines with their large random walks pass Earth and when the quiettime increase occurs is a measure of how long the solar wind takes to get to this modulating region, a measure of how far the modulating region is away.

One useful indicator of the random walk is the amplitude of the diurnal anisotropy, as is measured by neutron monitors. Low-amplitude anisotropies occur in coincidence with large random walk. We looked back, then, before each of the quiettime increases to see whether they were preceded by periods of low-amplitude anisotropy. We found that at five solar rotations before each of the well-defined quiettime increases there was a period of low anisotropy, signifying a period of large random walk.

An example of this is shown in Figure 2. This is an enlargement of the electron data shown in the previous figure for a period in February and March of 1968. The brackets mark two quiettime increases. The shading in this diagram denotes interplanetary sector structure, white for sectors that are directed mainly away from the Sun, gray for those directed mainly toward the Sun. The amplitude of the diurnal anisotropy five solar rotations before these events is plotted at the top, in percent. The average anisotropy for the whole year surrounding this period was 0.4 percent. We consider as small any amplitude less than 0.3 percent; that is, below the dashed line. As you can see, if you trace back along the field lines to where these quiettime increases occur, you find that each of these
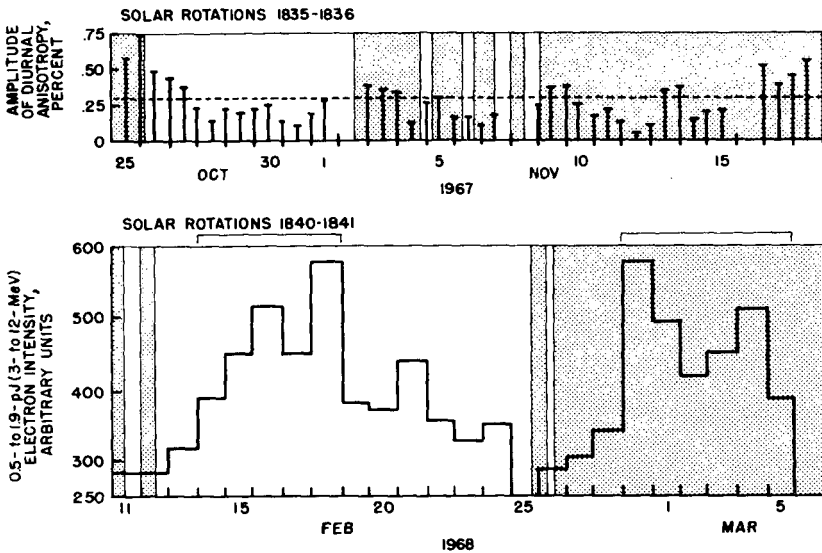
Figure 2—An enlargement of the electron data illustrating how the quiettime increases are preceded by periods of low-amplitude anisotropy.

quiettime increases was preceded five rotations earlier by an extended period of low-amplitude diurnal anisotropy, a period of large random walk.

The solar wind travels roughly 6 AU per solar rotation and in five rotations would carry field lines with their large random walk to a distance of 30 AU. Thus, the delay of five solar rotations between when the random-walking field lines pass Earth and when the quiettime increase occurs, indicates that the modulating region for electrons lies approximately 30 AU from the Sun.

Observations of quiettime increases allow us to make a prediction about interplanetary conditions far beyond Earth. We predict the existence of another modulating region for cosmic rays, 30 AU from the Sun.

REFERENCE

1. McDonald, F. B.; Cline, T. L.; and Simnett, G. M.: The Multifarious Temporal Variations of Low Energy Relativistic Cosmic Ray Electrons. NASA TMX 658-11, Jan. 1972.

COSMIC RAY CHARGE AND ENERGY SPECTRA
ABOVE 10 GeV

Dr. Jonathan F. Ormes

We have been working on a program to study the composition and energy spectra of cosmic rays above 1.6 nJ (10 GeV) on balloons and ultimately on the HEAO satellite.

During the last decade, considerable information on the composition and spectra at low energies has been obtained from balloons and satellite measurements. By extending these measurements to higher energy, we can greatly enhance our understanding of cosmic ray sources and their galactic environment. We have obtained some results from a balloon flight in November of 1970 that I would like to show you today.

The instrument is shown schematically in Figure 1. It is designed to identify cosmic ray electrons, protons, and nuclei up through iron and to measure their energies.

Relativistic particles enter the charge module and pass through four detectors, S_1, Cerenkov, cesium iodide, and S_2, all of which measure the charge through a proportionality to the charge squared. In addition, in this section we have four wire-grid spark chambers (s.c.) which measure the trajectory of the particle through the instrument. Particles then enter a large block of high Z material where their energy is absorbed. The first section is layers of tungsten with scintillators (as indicated by the dash marks on the side) where electromagnetic cascades from electrons rapidly develop. The nuclei pass through some of these layers where they interact and, through π^0 decay and the subsequent electromagnetic cascades, deposit their energy in a series of low-energy particles. The number of these particles is then determined; and through a function which we determine by calibration at high-energy accelerators, we can relate this to the energy of the particles.

The energy is a function of the parameter d which indicates the pathlength of the particle through the spectrometer and the constant, which is a slowly varying function of the energy of the particle.

In Figure 2, we show examples of nuclei identified as iron by the four charge detectors. Let's take the dots as an example of one particle. This particle enters the tungsten stack preserving its identity through the first few layers
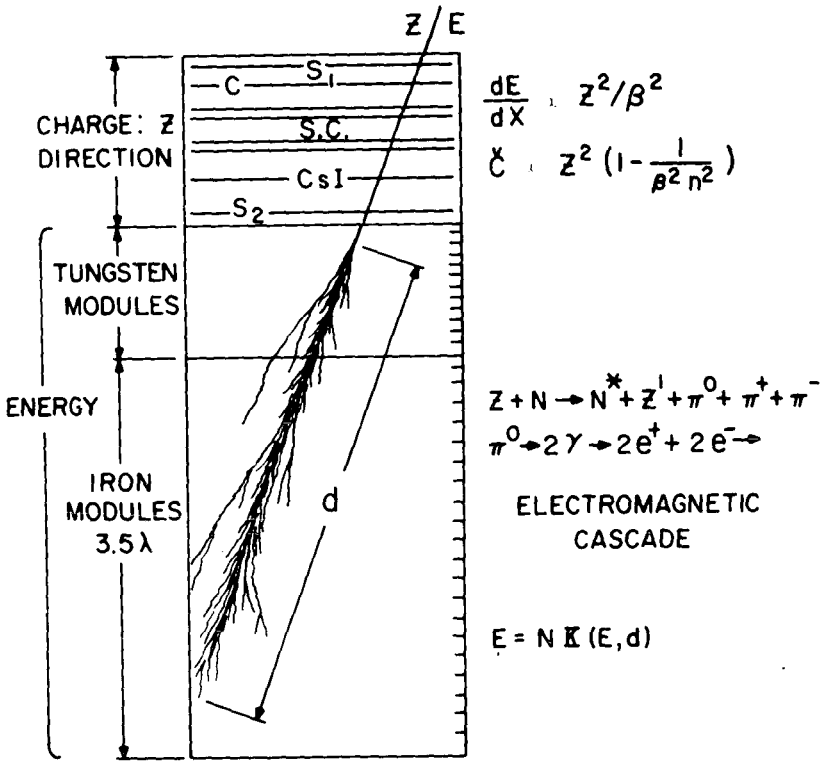
Figure 1—Diagram of instrument designed to identify particles and to measure their energies.

of tungsten, then there is some sort of an interaction, probably a fission-producing interaction. The particle continues to have its identity, then it interacts and produces a cascade shower.

In the case of another iron (represented by the plus marks), the particle comes in, interacts, and has a very large energy deposit. This particle has probably 0.5 μJ (3000 GeV) total energy, and as it passes through one of the layers there is an equivalent number of 1300 singly charged particles going through the detector.

In Figure 3, we show the energy spectra of various groups of nuclei. The nuclei are grouped in the traditional cosmic ray groups in order to obtain statistics that extend to the highest energy. These plots are a function of total energy, which is what our instrument measures.
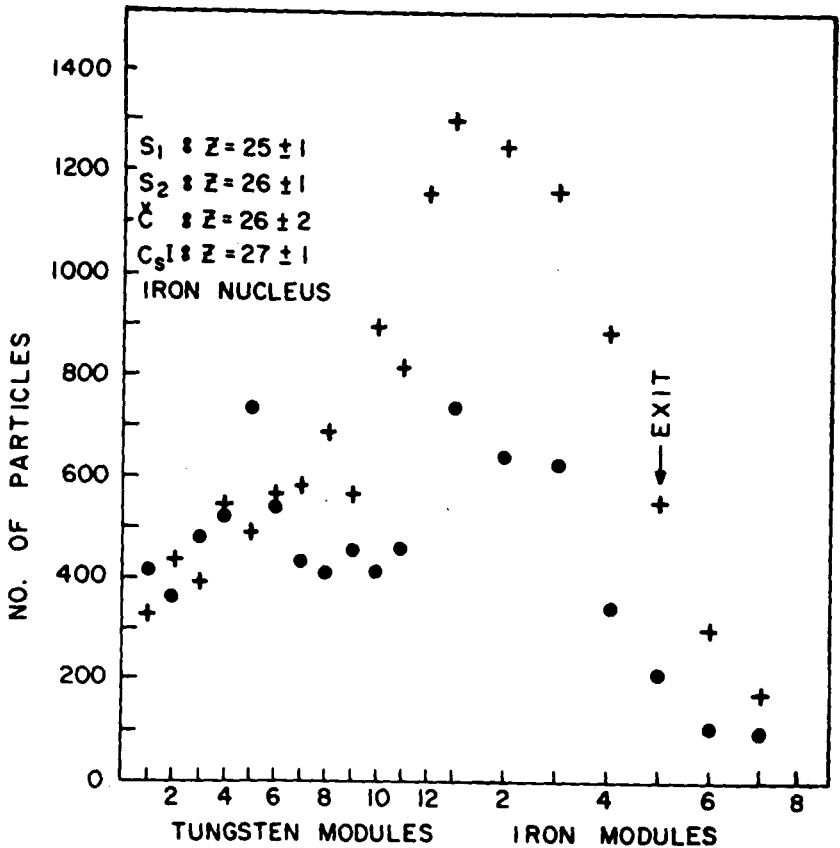
Figure 2—States of two iron nuclei as they pass through the modules. +: 0.5 μJ
(3000 GeV) nucleus; •: 69±11 nJ (430±70 GeV) nucleus.

At the low-energy end, we can see evidence of the geomagnetic cutoff, and that is why this spectrum stops at low energy. This would be sharply cutoff except for the fact that our balloon drifted with respect to the cutoff.

All the nuclei have differential spectra with a power of -2.7±0.1. These data are from the iron group, the L nuclei, the M nuclei, and so on.
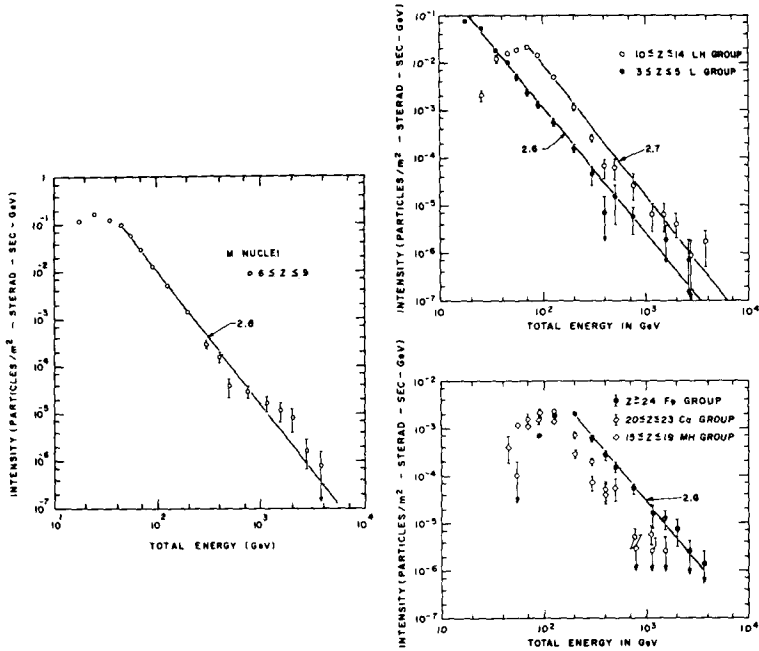
Figure 3—Energy spectra.

There is a suggestion of an interesting structure around 0.2 μJ (1000 GeV), particularly in the M-nuclei spectrum. This structure may be instrumental because we see some evidence for it in the spectra of all the nuclei. However, if it proves to be real, it will be very interesting.

In Figure 4, our proton integral spectrum is compared with that of Grigorov et al., (Ref. 1). The Grigorov data are from the Proton series of satellites. The often-discussed bend in their spectrum at about 10^{-7} J (10^{12} eV) is shown.

We find no evidence for any bend in the proton spectrum up to energies that are two or three times as great as where their bend is. Our helium spectrum agrees quite well with other published data, and the intensity of protons is nearly equal to that reported by the Russians (Ref. 2).
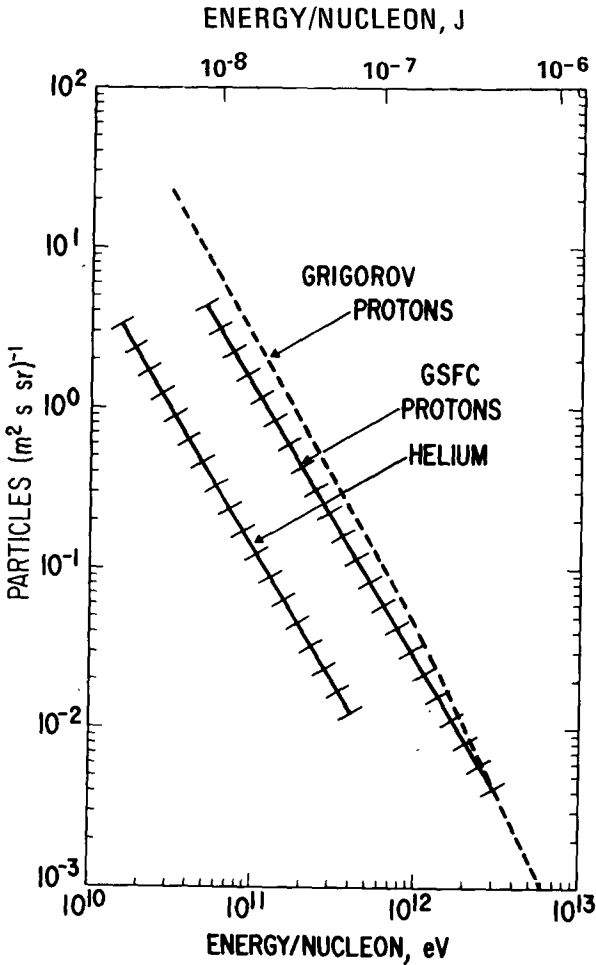
Figure 4—Integral spectra.

Our data give a proton-to-alpha ratio of 26 ± 3 constant from 40 GeV/nuc to 400 GeV/nuc. In addition to the protons, Grigorov measures the total-energy spectrum of all cosmic rays in his calorimeter. At the recent cosmic ray conference at Hobart, he reported evidence for spectral structure at about 0.2 μJ (10^{12} eV) which he attributes to the break that he has in the proton spectrum. However, our results suggest that only a quarter of the particles at a given total energy, which is what he is measuring at the same total energy, are protons. In fact, the energy is roughly equally distributed between protons, helium, the nuclei carbon through silicon, and the heavy nuclei.

So our suggestion is that the all-particle spectrum structure may be related to the structure we see at 0.2 μJ (10^{12} eV) in the medium nuclei spectrum.

In closing, let me just emphasize two points. First, the composition is apparently independent of energy and all the nuclear components have spectral exponents between -2.6 and -2.8, up to several tenths of a microjoule (several thousand gigaelectron volts) total energy; and, second, we find no evidence for any bend in the proton spectrum at 0.2 μJ (10^{12} eV).

CHAIRMAN:

Are there any questions for Dr. Ormes?

MEMBER OF THE AUDIENCE:

How will you decide if the structure in your medium nuclei spectrum is real or experimental?

DR. ORMES:

These results are based on a preliminary analysis. One of the problems we have is to estimate how much energy leaks out the back of the spectrometer and how strong a dependency that has on energy. The first preliminary analysis did not take into account differences in Z and so on. What one has to do now is just go back and do things more carefully. Looking at individual events above a certain energy, we can try and estimate for each event how much fluctuation there is. This will tell us how much error we have in estimating the energy. Once we have done that, we can have a lot more confidence in this kind of spectrum.

MEMBER OF THE AUDIENCE:

How many radiation lengths are there in the calorimeter?

DR. ORMES:

It is 3.5 nuclear interaction mean-free paths thick. The tungsten section on top is 12 radiation lengths thick. That is where we developed the electron cascades. And for the nuclei, the appropriate length is the nuclear mean-free path. The total thickness in radiation lengths is greater than 40.

MEMBER OF THE AUDIENCE:

Where do you calibrate your instrument?

DR. ORMES:

We have calibrated it already in the proton beam at the AGS at Brookhaven, and we have scheduled a calibration at the National Accelerator Laboratory. We are looking forward to that.

MEMBER OF THE AUDIENCE:

Can you measure interaction cross sections at high energy?

DR. ORMES:

We have not looked into that yet, but the problem is that it would be very difficult. The way we would do it with an instrument like this would be to determine the distribution of the first interaction points. We probably do not have enough data. They are not accurate enough and we do not have enough statistics at very high energies to say much about that.

REFERENCES

1. Grigorov, N. L.; et al.: Acta Phys. Suppl. 1, vol. 29, 1970, p. 510.

2. Akimov, V. V.; et al.: Acta Phys. Suppl. 1, vol. 29, 1970, p. 517.

THE SURVIVAL OF HEAVY NUCLEI IN COSMIC RAY SOURCE ENVIRONMENTS

Dr. V. K. Balasubrahmanyan

The study of the composition and energy distribution of high-energy cosmic rays could be used to understand phenomena connected with the acceleration and propagation of cosmic rays near possible source regions. In Figure 1, the results from the Goddard balloon spectrometer and the results reported by Soviet Scientists using the Proton series of satellites are summarized.

The important experimental results related to this discussion which have come from the Goddard balloon spectrometer experiment are as follows:

(1) On a total-energy scale, protons constitute only a minor proportion of the cosmic rays. They account for only 20 percent. The rest of the cosmic rays are complex nuclei.

(2) All the nuclei have the same power low spectrum in total energy and so the composition seems to be independent of energy.

In Figure 1 the continuous curve is the balloon data from Goddard. The points indicate the results of the experiment from Grigorov et al. from the Proton series of satellites. We believe that the agreement between the two measurements is quite good. Thus, the independence of the composition could be extended to much higher energies than has been possible with the balloon results.

Pulsars have been considered as possible sources of cosmic rays. The evidence for particle acceleration has been demonstrated from the radiation detected from them. They have also been associated with large magnetic fields. Also, large energy releases from pulsars have been detected.

Julian and Goldreich and Gunn and Ostriker have developed theories regarding the electromagnetic environment of pulsars and acceleration of cosmic rays.

In Figure 2, a schematic representation of the pulsar environment relevent to the acceleration of cosmic rays is shown. The period of rotation of the pulsar is approximately 30 ms. The velocity-of-light circle is shown with the dashed line, and the outer circle is a schematic representation of the supernova surface material blown off. In one form of Gunn and Ostriker's theory,

146
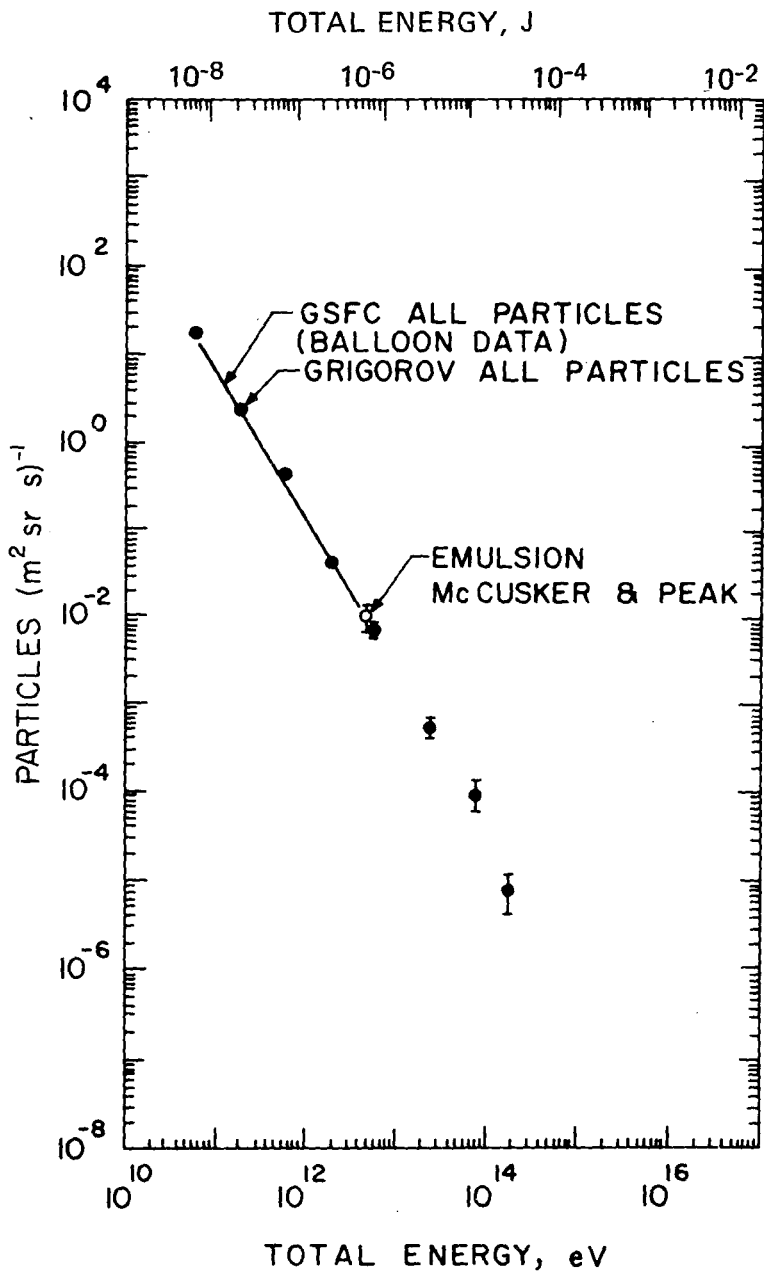
Figure 1—Balloon spectrometer results.
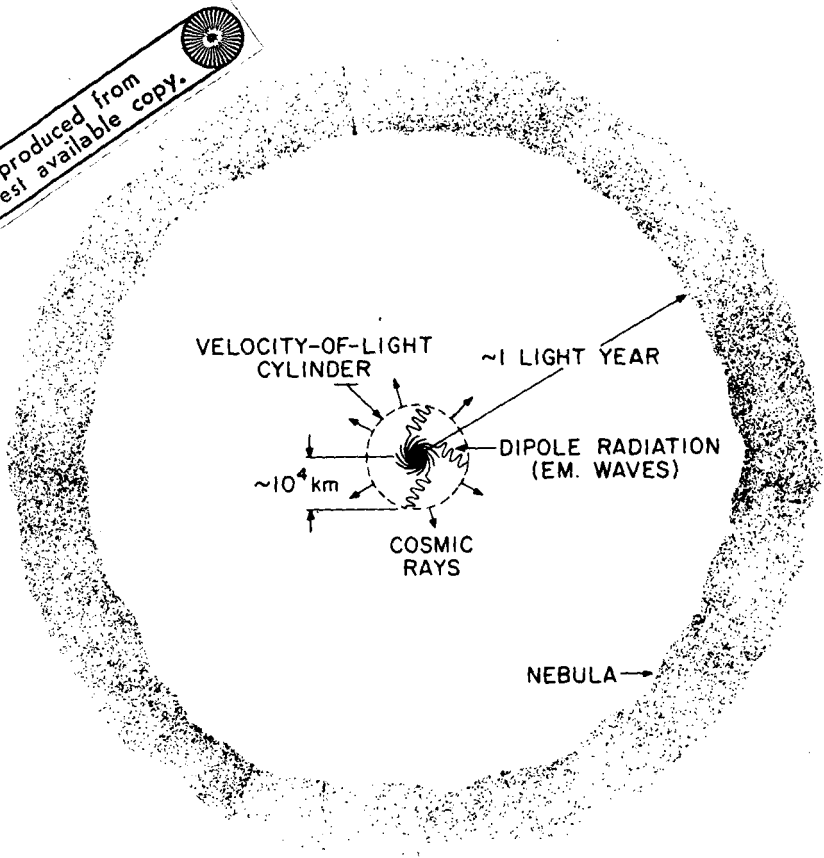
Figure 2—Pulsar environment.

the dipole radiation from the rotating pulsar produces low-frequency electromagnetic rays which accelerate cosmic rays near the velocity-of-light circle.

Another experimental observation, which has come from X-ray experiments on the study of NP0532 is the enormous density of X-ray photons around the pulsar. It will be interesting to see whether all these physical facts we know about the pulsar are consistent with the acceleration of heavy cosmic rays of high energy near the pulsar.

In the case of X-rays, a 100-kV X-ray, for example, appears to be a gamma ray of 1.6 pJ (10 MeV) when seen from the frame of reference of a nucleus with a velocity of 16 nJ (100 GeV) nucleon^{-1}. A gamma ray of 1.6 pJ energy can photodisintegrate the heavy nucleus through the giant dipole resonance with a cross-section that is quite large, namely 10^{-25} cm^2.

Photonuclear interactions remove neutrons preferentially from nuclei. In the region of iron nuclei, if you remove three neutrons from any nucleus, the nucleus becomes unstable and quickly breaks down to lighter nuclei. So the composition would become drastically altered if photonuclear reactions were to take place in any preferential manner.

Using the observed X-ray fluxes, the number of interactions suffered by an iron nucleus and a carbon nucleus have been calculated and are shown in Table I. We see that right up to 200 yr, it is very difficult to accelerate complex nuclei. They will all be broken down by the photonuclear reactions.

TABLE I. Number of Photodisintegrations of a Nucleus of Energy
16 nJ (100 GeV) Nucleon^{-1}

Time after supernova explosion, yr	Iron	Carbon
10	16798	2154
100	183	24
200	46	6
500	7.4	1.0
700	3.7	0.5
1000	2	—

So our conclusion from our experimental observations that composition is independent of energy up to a few-tens of nanojoules (a few hundred giga-electron volts) per nucleon, and also that it is strictly similar to the observed composition at nonrelativistic energies, is that it is very difficult to accelerate heavy cosmic rays, using the Gunn and Ostriker model near the velocity-of-light circle.

I would conclude with the following observation: If acceleration takes place through low-frequency electromagnetic waves, it takes place much farther from the velocity-of-light circle — probably in the nebula.

CHAIRMAN:

Are there any questions?

MEMBER OF THE AUDIENCE:

What effect would the plasma around the pulsar have on the acceleration?

DR. BALASUBHRAHMANYAN:

The Gunn and Ostriker calculations are done for a vacuum. Basically, the
arguments for the existence of a plasma around the pulsar come from
Goldreich and Julain and they are fairly general. The electrostatic field
is so large compared to the gravitational field that there is bound to be a
plasma environment. There has been a recent paper published in Astronomy
and Astrophysics in which corrections for the existence of the plasma have
been made. The mechanism essentially holds but it slightly affects the
upper limit to which you can accelerate the particles.

THE NEUTRON STAR AS A QUANTUM CRYSTAL

Dr. Vittorio M. Canuto

During the last 8 months I have been studying the structure of the interior of neutron stars in collaboration with Dr. S. M. Chitre, an NAS-NRC Research Associate at the Institute for Space Studies in New York.

This is one of the current concerns in astrophysics for the following reason: Few regions in astronomy have profound and general significance because they have a direct bearing on the validity of the basic physical laws that govern the universe as we know them.

The explanation of these specific areas in astronomy stretches the existing scientific knowledge to its limits and indicates a direction in which we may want to modify the basic laws of nature.

One such area is quasars, seyfert galaxies, and exploding galaxies, with energy releases that are very difficult to explain with any known mechanics or any known kind of forces.

A second area can be defined as the complexity of general relativity, gravitation, and cosmology. A third area is the role of neutrinos in stellar evolution with impact on theories of weak interactions.

The fourth area, which is especially close to me as a former nuclear physicist, is the existence of super-dense states of matter, such as neutron stars, where matter is being squeezed down to such densities (about a billion tons per cubic centimeter) that the particles are less than 10^{-13} cm apart. This is not much more than the size of the particles themselves, and new information about the structure of the elementary particles may result from the computation of the properties of such highly compressed objects and their comparison with the observational data.

Our work has gone into calculating the equation of state for the interior of neutron stars. Now, the interior of neutron stars involves known forces, i.e., nuclear forces, and almost completely unknown forces, such as hyperonic forces. By hyperons I mean the collection of strange particles — lambda, sigma, etc.

The physical principles behind our work are the following. Since the density is so high, the particles are so close together that they only feel a strong repulsion. They repel each other; therefore, it makes sense to think that to minimize the energy the particles would arrange themselves in a very orderly system (as a crystal) instead of being randomly distributed (as in a gas). We therefore computed the energy considering that the system was really a crystal and that the system was a gas. To do that we had to build up the hyperonic nuclear forces. That took at least 50 percent of our work. Now we have a very reliable, good potential. The set of equations that we had to employ was not available at the time because this work was absolutely new in the field of solid state.

Putting the two things together, we arrived at the first conclusion: The lower state of energy is really achieved by arranging these heavy particles in a crystal array.

Figure 1 shows what we have found for densities of 10^{15} g cm^{-3}. The minimum energy is achieved when you arrange neutrons in this way, which is centered cubic lattice. I just want you to recall that cesium chloride crystallizes with this structure.

You see we have neutrons in the corners and the proton in the middle. The arrows indicate the spin. One has to try all the possibilities by moving all of these particles and spin configurations until one finds the minimum energy. This combination appears to minimize the energy up to 10^{15} g cm^{-3}. After that, the body-centered cubic structure switches to face-centered cubic structure (Fig. 2) until 10^{16} g cm^{-3}. We therefore come to the conclusion that a system of strong-interacting particles achieves its minimum energy by arranging the particles in a very orderly crystal.

The conclusion is that the previous computations of the neutron star mass based on a gaseous arrangement of particles are off; there appears to be a new configuration.

CHAIRMAN:

Are there any questions for Dr. Canuto?

MEMBER OF THE AUDIENCE:
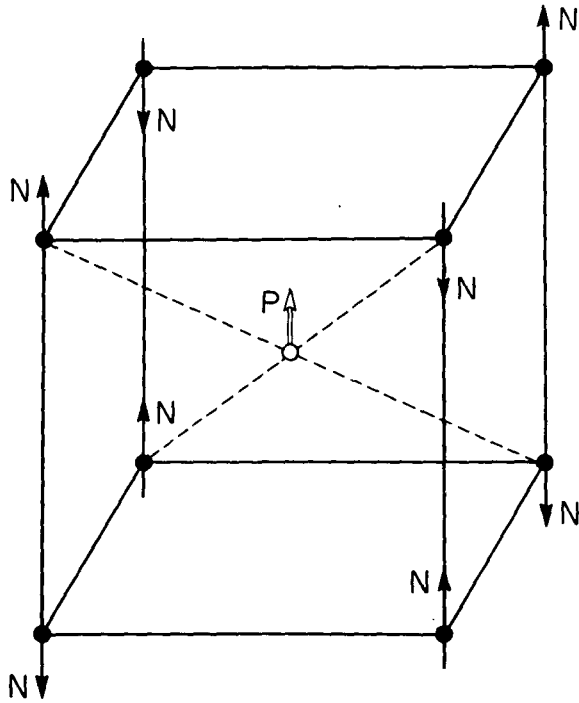
Does the crust remain crystallike?

Figure 1–The body-centered cubic crystalline arrangement
of protons P and neutrons N.
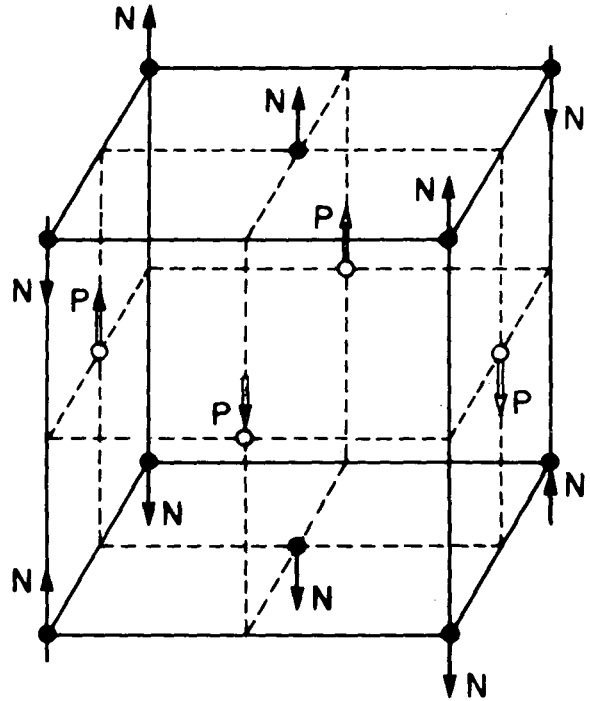
Figure 2–The face-centered cubic crystalline arrangement.

DR. CANUTO:

Sure.

MEMBER OF THE AUDIENCE:

What is in between?

DR. CANUTO:

In between there is probably a layer of superfluid neutrons; at least the density is such that neutrons can become superfluid. This computation refers only to the interior of the star. What goes on when the density is far behind the one we computed, far behind the density of 10^{16} cm^{-3}, is really a mystery since there is no theoretical model on which you can rely to compute anything.

MEMBER OF THE AUDIENCE:

Does the magnetic field affect your computation?

DR. CANUTO:

No. The point is that a magnetic field of the order of 10^{10} T (10^{14} G) in the interior is not affecting the structure because the mass of the protons and the mass of the neutrons are too high to have any effect.

The critical magnetic field is of the order of 10^{9} T (10^{13} G) for electrons, and it should be of the order of 10^{16} T (10^{20} G) in order to affect anything. We feel that such a tremendous magnetic field, if it is there, will not change the structure of the solid in any significant way, since the nuclear forces will be dominant.

MEMBER OF THE AUDIENCE:

Have you seen a recent paper on the influence of a magnetic field on neutron stars by M. Ruderman?

DR. CANUTO:

Yes. The magnetic field surely affects many phenomena of a neutron star, mostly the cooling of it, because it affects the energy flowrate out of the star. The magnetic field only affects electrons; it does not affect protons because they are too heavy to be affected by any reasonable value of the magnetic field.

SUPRATHERMAL PROTON BREMSSTRAHLUNG

Dr. Frank C. Jones

With the advent of X-ray and gamma ray astronomy, there has been a revival of theoretical interest and study of those physical processes capable of producing energetic photons.

One such process that has been studied recently is suprathermal proton bremsstrahlung. In this process, a suprathermal proton, or if you prefer, simply an energetic proton, strikes a relatively motionless electron in a background plasma and causes the electron to radiate.

We are interested in knowing for this process the differential cross section as a function of energy of the emitted photon. This cross section has been calculated by several authors using a method that I will discuss very briefly in just a moment. I have calculated this cross section by a method that I believe is considerably superior to the conventional one in the case of relativistic collisions, and in doing this I believe I have been able to correct a rather serious error regarding the relativistic cross section only, that existed in the literature.

To understand the conventional method of calculating this cross-section, it is convenient to view this collision process from the point of view of the incoming fast proton. If you sit on this proton, in this frame of reference, what you see is that a fast electron comes whizzing by, is deflected in the proton's coulomb field, and in so doing radiates photons. Viewed from this frame, the process is just plain old bremsstrahlung, a simple process which has been known for a long time; the cross section of this process is described quite well by the Bethe-Heitler formula. The conventional approach, therefore, is to first view the process in the proton's rest frame, using the Bethe-Heitler formula, or a generalization of it, to obtain a resulting photon spectrum.

This result is then transformed, using the Lorentz transformation, back into the laboratory frame, in which it is the electron rather than the proton that is at rest. When the velocity of the incoming proton is much less than the velocity of light, the effect of the Lorentz transformation in this procedure on the photon's energy, in other words, the Doppler shift, is quite small. In fact, you can neglect it.

In this case, the cross section in the laboratory frame is really quite simple and, as Boldt and Serlemitsos (Ref. 1) here at Goddard have shown, it is simply the Bethe-Heitler formula, the same one you started with for bremsstrahlung in the first place, only with the provison that you must understand that the kinetic energy in this formula must refer to the kinetic energy of the electron as viewed in the proton's rest frame.

However, now, when the proton's velocity approaches that of light, the doppler shift actually becomes quite important in this transformation, and one must in fact keep track of the emission angles as well as the energy of the emitted photons in order to correctly transform the spectrum back into the laboratory frame.

This is in fact a very complicated and tricky procedure, and one that really requires a computer. The procedure has been attempted by Brown (Refs. 2 and 3), who obtained rather surprising result. He found that the total cross section for the process exhibited a rather sharp peak at a proton energy of 3.2 nJ (20 GeV), and then fell off rather rapidly above that energy. From this he deduced that the process could be responsible for a significant amount of the cosmic gamma rays seen above 0.2 pJ (1 MeV) or so by Vette et al. (Ref. 4) on the ERS 18 satellite.

This result actually was rather surprising because there is no characteristic energy of 3.2 nJ (20 GeV) in the quantum electrodynamics of electrons or protons. It is rather difficult to see how one could get a resonance of this kind in this type of a process.

It occurred to me that there was really a very much simpler way of calculating this cross section. The basic method one can use is called the Weizsäcker-Williams method, but as you might have guessed was actually first used by Fermi (Ref. 5).

In this approach, one begins by noticing the fact that in the rest frame of the electron, the coulomb field of the incoming proton is distorted, if you wish by the Lorentz transformation, such that it strongly resembles a plane pulse of radiation. Figure 1 shows what the fields, the electric and magnetic fields of either a stationary charge or a rapidly moving charge, would look like to someone watching them go by.

Actually one can exploit the similarity of this field for the moving charge to a radiation pulse by Fourier analyzing this pulse and considering the results obtained to represent the spectrum of simply an incoming burst of photons. You just pretend they are real photons. The radiation process is then considered to be nothing more than the Compton scattering of these photons off the stationary electron.
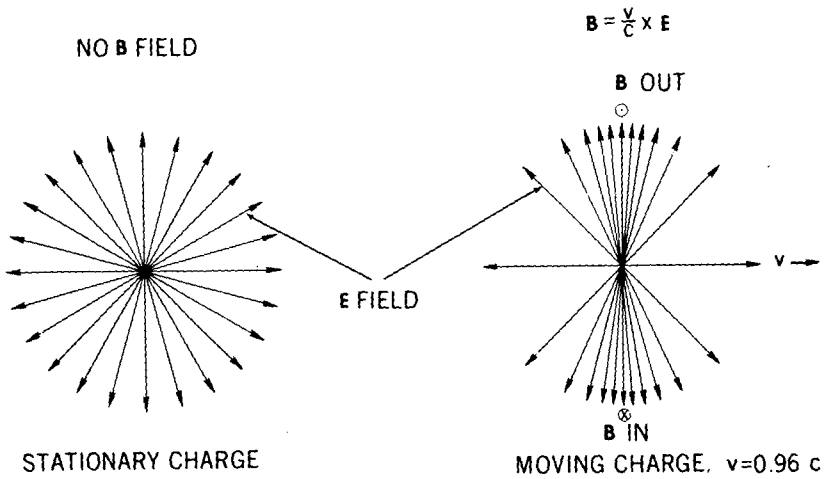
Figure 1 —Electromagnetic field of stationary and moving charges.

Now, at this point you are essentially through with the calculation. There is no Lorentz transformation to perform, and there is no angle to consider. The only thing to do is to integrate the well-known cross sections for Compton scattering over the spectrum of these incoming photons.

The expression obtained from this is a single integral, and the expression for this incoming photon spectrum can be found in Jackson's book on classical electrodynamics (Ref. 6), among other places. The integral can be done analytically in fact, and the result can be obtained in a closed form. The results of the calculation are shown in Figure 2 as simple curves.

The cross sections are plotted as functions of the photons energy on the lower axis; the number labeling each curve is the proton's kinetic energy in nanojoules (gigaelectron volts).

One thing we should note is that these curves go smoothly right through 3 nJ (20 GeV) without a ripple. So I believe that the resonance that appeared in the earlier work does not exist. I think it was an artifact of the extremely complicated computation procedure that was needed in that method. This actually is the most pronounced difference between my result and those of Brown's, but it is by no means the only difference.

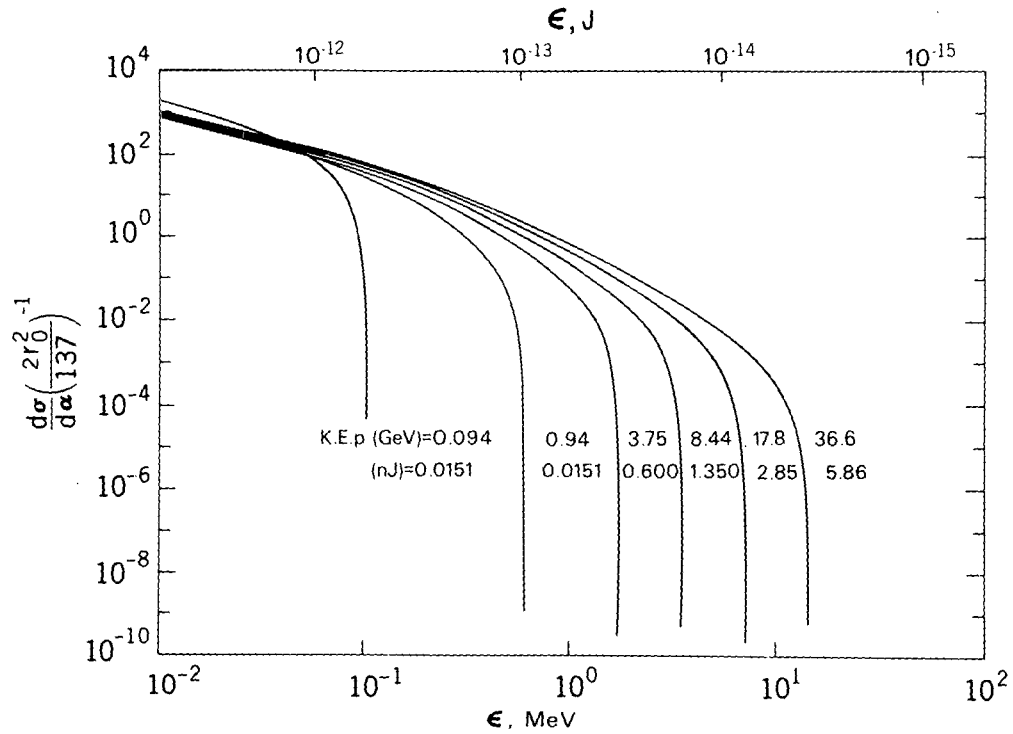Figure 2—Results of calculations.

As I said, the expressions for these curves are a bit complicated, but for photons energies above about 0.2 pJ (1 MeV), the various curves obey an approximate scaling law rather well. Those with a practiced eye might actually be able to see that these curves essentially just displace along a diagonal line, as you go to high-energy protons.

But from the scaling law it is possible to deduce the photon spectrum that would arise from an inverse power law spectrum of protons. This actually can be done very quickly, using a method that I discussed about 4 yr ago at the cosmic ray conference in Calgary, and the result is that one would obtain an inverse power law spectrum of photons that is one power steeper than that of the incoming protons.

Since you would not expect a proton spectrum to be much flatter than E^{-2} you would not expect the photons spectrum resulting from this process to be much flatter than E^{-3}, which is in fact rather steeper than I believe is seen in gamma ray spectra around this energy. Therefore, you would not expect this process to contribute too significantly, at least not over any reasonable band of photon energies.

REFERENCES

1. Boldt, E.; and Serlemitsos, P.: Astrophys. J., vol. 157, 1969, p. 557.

2. Brown, R. L.: Astrophys. J. Lett., vol. 159, 1970, p. L187.

3. Brown, R. L.: Lett. Nuovo Cimento, vol. 4, 1970, p. 941.

4. Vette, J. I.; Gruber, D.: Matteson, J. L.; and Peterson, L. E.: Astrophys. J. Lett., vol. 160, 1970, p. L161.

5. Fermi, E.: Z. Phys., vol. 29, 1924, p. 315.

6. Jackson, J. D.: Classical Electrodynamics. John Wiley & Sons, Inc., 1962, secs. 15.5 and 15.6.

SUPERNOVAE STUDIED WITH A GROUND-LEVEL
ATMOSPHERIC FLUORESCENCE

Dr. David L. Bertsch

Current theoretical models on supernova explosions predict that super-
novae are important sources of cosmic ray particles. Colgate's theory
(Ref. 1) predicts that during the explosion phase, when the outer mantle
of the star is accelerated by the hydromagnetic shockwave, an intense
gamma ray burst will be produced that will contain energies up to 5×10^{40} J (5×10^{47} ergs). Because of the importance of the supernova theory
and the possibility that other, as yet unknown exceptional phenomena might
exist to produce similar bursts, we undertook a monitoring experiment in
late 1968 to search for photon bursts of extraterrestrial origin. I would like
to briefly describe our experiment and summarize the results of the observa-
tions to date.

Our method of detection employs ground-based photomultiplier tubes which
are sensitive to the secondary fluorescence light that would be produced
when the primary pulse is absorbed in the atmosphere.

Figure 1 shows a simplified picture of incident photons being absorbed at
some depth h in the atmosphere and producing isotropic, secondary photon
emission.

INCIDENT PULSE OF SUPERNOVA PHOTONS

SUPERNOVA PHOTONS ARE ABSORBED AND PRODUCE FLUORESCENCE
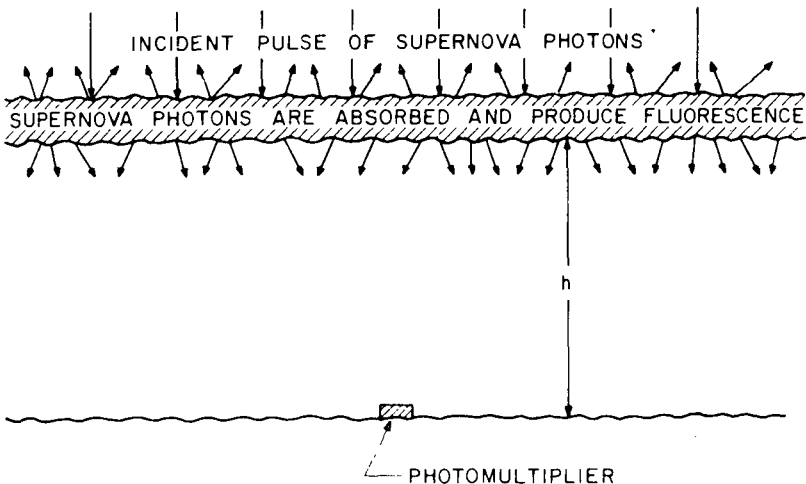
h

PHOTOMULTIPLIER

Figure 1—Absorption of incident photons in the atmosphere and resultant photon
emission. The photomultiplier observes all of the fluorescence photons emitted in
the proper solid angle.

From the work of Greisen and collaborators at Cornell (Refs. 2 and 3), it is known that the absorption occurs from 30 to 100 km in altitude, and that for a ground-based detector at least, the important emission is due to nitrogen molecular stimulation producing emission lines near 391.4 nm.

The whole process is fast. The primary pulse itself is expected to be sub-microsecond in duration and its absorption in the atmosphere requires about 1 μs. For a wide-angle detector system at ground level, the observed pulse is broadened by the propagation time from different parts of the sky and has a total width of the order of 300 μs.

To observe fluorescence bursts, we operate ground-based detectors consisting of large photomultiplier tubes with optical filters whose response is keyed to the 391.4 nm emission that we expect. The output of each photomultiplier tube is displayed on an oscilloscope. When the incoming light exceeds a preset threshold level, the oscilloscope is triggered. An open-shutter camera views the trace and produces a data frame such as shown in Figure 2. The time scale is 1 ms across, and the amplitude is proportional to the amount of light incident on the tubes.

Three traces are shown in Figure 2, one for each tube. The upper one is inverted simply to distinguish it from the other two.

After a short amount of running time, we learned that there was a wide variety of background light from airplanes, lightning, distant city lights, and so forth, and as a result it was difficult to distinguish real, extraterrestrial events from the background light. To help resolve that question, we built a second station and located it several hundred miles from the first site. Accurate timing was installed in both stations so that we can determine whether events are in coincidence over a long baseline. In this manner, local background can be distinguished from signals of extraterrestrial origin. The timing given across the center of Figure 2 is simply the output of a time code generator and it is accurate to about 10 ms.

To date, we have looked at some 70 000 frames of data like the one in Figure 2. Table I summarizes the results from the two stations which have been operated at four different locations since late 1968. Each location has its own background peculiarities and this dictates the threshold levels to which the system can be set. Goddard, as you see, is a rather poor location because of the proximity of Washington and Baltimore. Here it is necessary to have pulses above 200 photons cm^{-2} in the 50-μs sampling time of the apparatus because of the level of the random background light. The best station is in Arizona, with a background of 50 photons cm^{-2}.

TIME
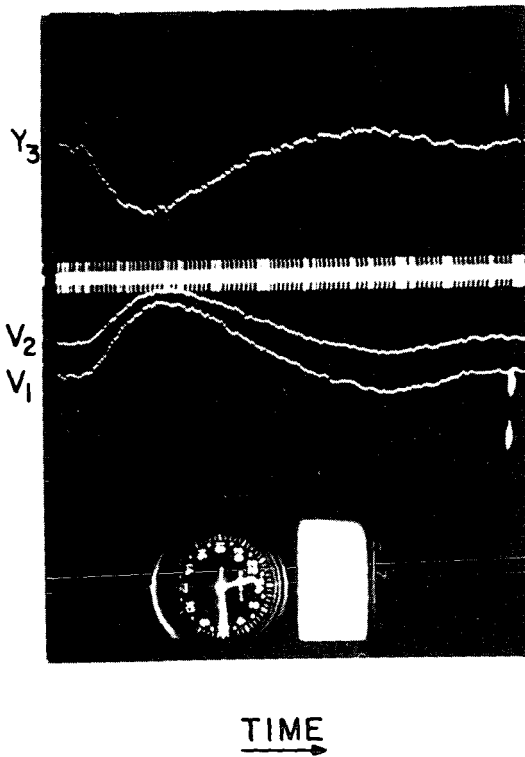
Figure 2—Data frame showing photomultiplier output.

Having established the threshold levels, the sensitive radius within which the apparatus can record a supernova is determined. Using this sensitive volume one can estimate the rate of occurrence of supernova. Taking Colgate's values for the photon emission, expect to observe supernova at the rate of one every 96 hr at Goddard and one every 13 hr in Arizona, for example, as shown in Table I.

During the time periods indicated in the table, we have accumulated a total of over 1200 hr of Moon-free, clear-sky running time. By operating in co-incidence between Goddard and Fan Mountain, 170 hr of data have been collected. This period of time and the predicted rates given in the table indicate that we should have seen 1.7 supernova events. Likewise, coincidence operation between Virginia and Arizona produced 60 hr of running time. During this time, we should have found 2.7 supernova events.

TABLE I.–Summary of Supernova Running Times

Station location	Operation interval	Threshold, photons cm^{-2} in 50 μs	Expected supernova rate	Running time, hr	2-Station coincidence time, hr	Expected number coincident
Goddard, Maryland	Sept. 1968 to Sept. 1969	200	1/96	450		
Fan Mountain, Virginia	June 1969 to Dec. 1969	70	1/21	350	170	1.7
Mount Hopkins, Arizona	Nov. 1969	50	1/13	60	60	2.7
Middle East Tech. Univ., Turkey	June 1970 to Jan. 1971	100	1/36	376		

Number of events expected in single station runs, $\sim$36; possible number observed, $\sim$10

Number of events expected in coincidence, $\sim$4.4; observed number, 0.

Altogether, we expected to observe 4.4 events, but have found none. From the single station data, we should have seen on the order of 36. There have been a possible number of 10 events that could be due to supernova. However, this must be regarded as an upper limit because of the noise ambiguity. Assuming that the parameters involved in estimating the rates are correct (e.g., the density of galaxies, the rate of supernovae per galaxy, etc.), we can place an upper limit on Colgate's photon energy of about one-half of what he said, namely 3×10^{40} J (3×10^{47} ergs).

However, many of the necessary parameters are uncertain so that this limit is still not very significant. We are continuing to observe and will either see supernovae or will be able to significantly improve that limit.

CHAIRMAN:

Are there questions?

MEMBER OF THE AUDIENCE:

What is the energy region of the primary photons?

DR. BERTSCH:

Colgate predicts energies up to 0.3 nJ (2 GeV), and probably down to 10^{-14} J (a few kiloelectron volts), so we expect a very wide band of energy emission from the supernova.

MEMBER OF THE AUDIENCE:

At what altitude in the atmosphere does the absorption of the primary pulse occur?

DR. BERTSCH:

You can excite fluorescence up to several hundred kilometers. The efficiency is dependent on the pressure; at 1.6 fJ (10 KeV), for example, photons are absorbed at about 100 km primarily by the photoelectric process, and for more energetic photons, say 16 fJ (100 KeV), the absorption is strongest at about 20 km, where the Compton process and pair production are the dominating processes.

MEMBER OF THE AUDIENCE:

What is the spectral response of your system?

DR. BERTSCH:

We have two wavelength regions that we monitor. One is in the fluorescence band near 391.4 nm and the other one begins at about 600 nm. Both of these observing bands are about 30 nm wide so it is a rather wideband system. Consequently, we record emission over most of the optical region. For a time we did monitor radio signals at ~100 MHz in Arizona, but we did not see any correlation between radio and optical emission.

REFERENCES

1. Colgate, S. A.: Can. J. Phys., vol. 46, 1968, p. S476.

2. Greisen, K.: Proc. 9th Int. Conf. Cosmic Rays (London), 1965, p. 609.

3. Bummer, A. M.: Cosmic Ray Detection by Atmospheric Fluorescence. Ph. D. thesis, Cornell Univ., 1966.

DIFFUSE X-RAYS FROM THE GALACTIC DISK

Dr. Peter J. Serlemitsos

We wish to report on an anisotropic feature of the diffuse hard X-ray background that tracks the concentration of interstellar hydrogen in the plane of the galaxy. This feature supports a model of galactic X-ray emission by subrelativistic cosmic rays via a bremsstrahlung process. The measurement was carried out on August 9, 1971, using two multianode multilayer gas proportional counters onboard Aerobee 170 flight 13.08. A schematic diagram of the detectors used is shown in Figure 1. This type of construction and the appropriate utilization of the signals from the many anodes result in a low detector background, a prerequisite before undertaking a measurement of possible small variations in the brightness of the X-ray sky.

The measurement of possible galactic effects on the generally isotropic X-ray sky is a long-term objective of our group. As such, it has greatly influenced the inception and design of experiments proposed by us and approved for flight on board future satellites. The same objective but on a much limited scale underlied the planning of Aerobee flight 13.08. Consequently, the detectors and their collimators as well as the flight plan were carefully chosen for optimum utilization of the available time. The segment of the galactic plane near $l^{II} \sim 62°$ was specifically chosen because during our previous Aerobee flight we found that region to be free of discrete X-ray sources down to a limiting strength of less than 1 percent of the Crab Nebula. Shown in Figure 1 is the orientation of the collimators relative to the galactic plane and the limits of the scan that took place. During the flight, the plane was crossed a total of four times.

Detectable galactic disk effects will be the net result of absorption and emission processes involving energetic charged particles and interstellar matter. Assuming extragalactic origin for the diffuse X-radiation, the galactic medium causes varying amount of absorption depending on the amount and composition of matter in the line of sight. The dominant absorption mechanism is the photoelectric effect which proceeds discontinuously as the incident photon energy exceeds the K-shell absorption edges of the abundant elements. If a given K-shell absorption edge could be resolved we would obtain a direct measure of the columnar density of the corresponding atomic species. At energies above 0.3 fJ (2 keV) it is the heavy elements beyond silicon that come into play.
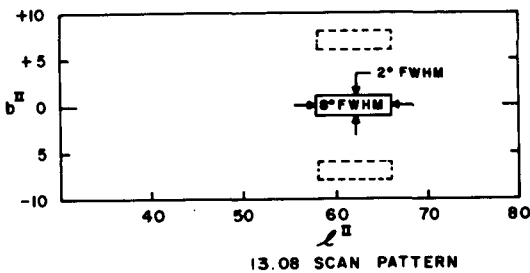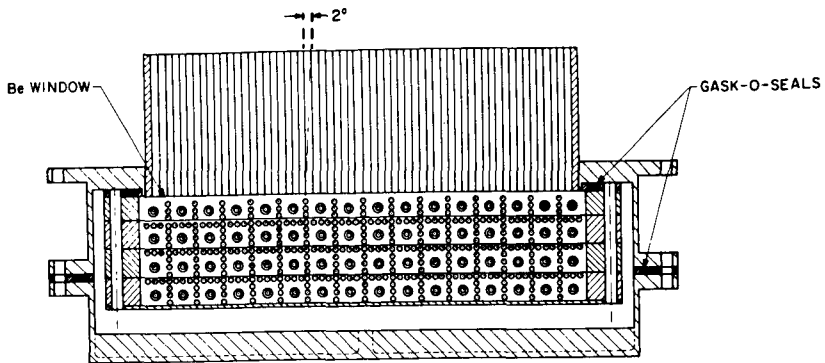
Figure 1—Schematic diagram of detectors.

An enhanced diffuse X-ray flux at low galactic latitudes likely signifies some interaction involving energetic charged particles, be it bremsstrahlung, inverse Compton, synchrotron, or recombination radiation. The profile of the radiation as it relates to the hydrogen concentration, as well as the spectrum, may be used as bases for identifying the particles involved and the nature of the process. In addition, because the same charged particles will necessarily ionize the interstellar gas, we have at our disposal an additional constraint; i.e., the ionization rate of this gas.

In Figure 2 we show the counting rate in selected energy channels from both detectors as a function of galactic latitude. The excess within $3.5°$ of the galactic plane is at least 6σ. A two-parameter least-squares fit rejects a single-point source contribution with 90 percent confidence. The best fit to a diffuse source is obtained with a $2°$ extended source centered near the galactic plane. This is in close accord with the hydrogen profile.
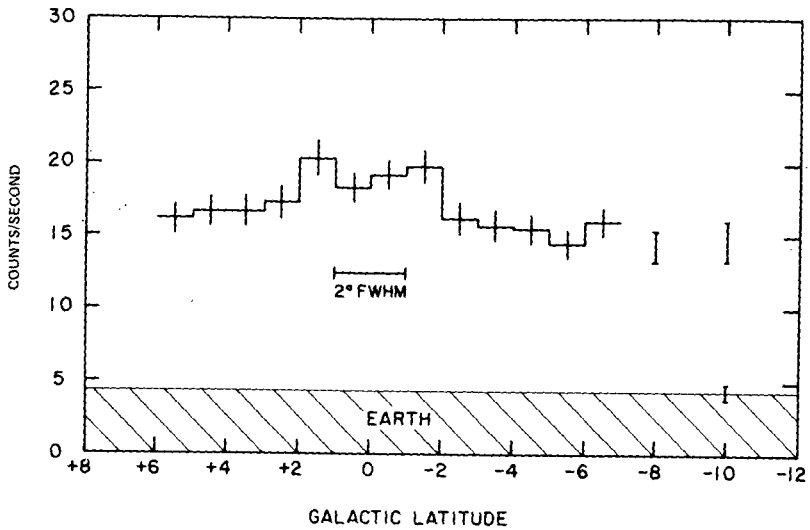
Figure 2–Counting rate as a function of galactic latitude.

To obtain a spectrum for the observed excess, we have broken the data into two groups separated by the latitudes $b^{II} = \pm3.5°$. The combined spectrum from both detectors is shown in Figure 3. The two most significant data points give a flux of about 9.6 aJ $(cm^2 \ s \ aJ \ rad)^{-1}$ (or about 0.06 keV $(cm^2 \ s \ keV \ rad)^{-1}$) which is about half as much as previous estimates of a galactic flux. Of special interest is the energy bin 0.94 to 1.5 fJ (5.9 to 9.1 keV) where the data point lies some 2.5σ below the average of the two neighboring points. This is where iron K edge effects would be expected. Observations of 21 cm at this longitude give a hydrogen columnar density through the plane of 2×10^{22} H atoms cm^{-2}. A universal abundance of iron relative to hydrogen would result in only a 2 percent absorption jump, whereas the effect in our data is at least five times that amount. Thus, if the low point is indeed caused by absorption, we would require at least a five-fold increase in the iron abundance relative to the hydrogen density as given by 21-cm measurements.

In general, however, this spectrum allows us to draw only limited conclusions about the mechanism of emission. Based on the profile of the radiation as well as existing upper limits at higher energies and radio data, we favor a bremsstrahlung process. If that is the case, we would expect about 2×10^4
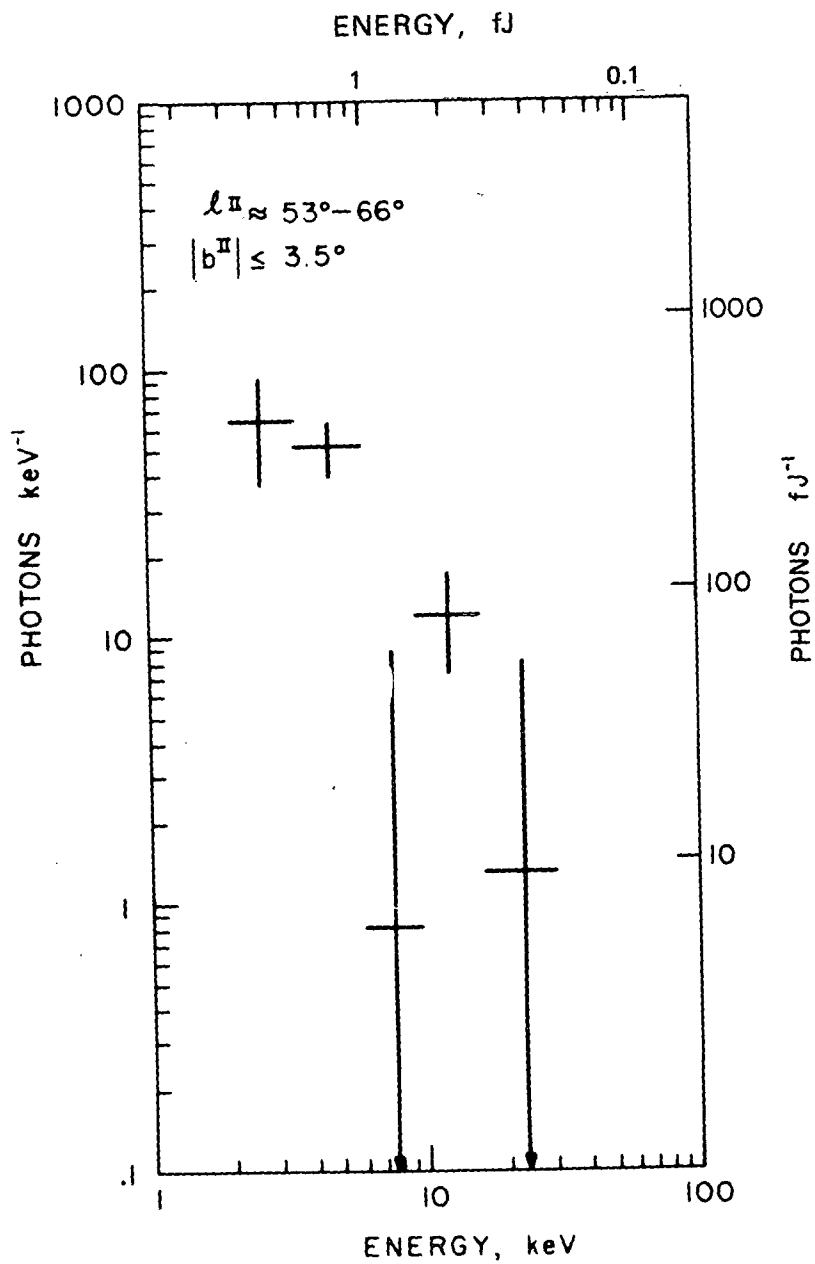
Figure 3—Galactic disk net X-ray flux.

as much energy to go into ionizing the interstellar medium as the amount that goes into producing the observed X-rays. Using this efficiency, we estimate a hydrogen ionization rate of 3×10^{-15} (s H atom)$^{-1}$. This value is well in agreement with estimates based on pulsar dispersion measures and current models of the interstellar gas.

STELLAR X-RAY TEMPORAL VARIATIONS

Dr. Stephen S. Holt

At the lowest level of what we mean by the understanding of an X-ray
source is the qualitative nature of the emission process (whether synchrotron
or thermal bremsstrahlung, for example), and we can usually get a handle
on this from the shape of the X-ray spectrum. If we want to dig a little
deeper into the problem and determine from where the energy comes, we
find that the shape of the spectrum is no help at all. But the temporal
behavior of the source may give us a hint.

For example, consider the Crab Nebula, the archtype synchrotron source.
It has a featureless power law spectrum, and we know that the magnetic
field must be there from the Crab's radio emission. But if we construct
a synchrotron model from the observational parameters, we find that it
has only enough energy for 1 yr of operation. As you know, we found
out where the energy to keep the Crab going came from when we found
pulsed emission from the source. The pulsed power itself is very small,
but the interpretation of the periodicity in terms of a rapidly rotating
central object which can transfer rotational kinetic energy to relativistic
electrons in the far reaches of the nebula completely satisfies the overall
energy requirements. That's a 2-yr-old story, I would like to tell you now
about some temporal studies we have performed this year.

The first is on Sco X-1, where the spectral shape indicates thermal emission.
But the observational parameters in this case indicate a lifetime much
smaller than 1 yr; in fact, smaller than 100 ms. So we looked for a pulsar
in our rocket data for Sco X-1, and we could not find one. We also looked
for nonperiodic fluctuations and we could not find them, either. In
Figure 1 we present 5σ upper limits to the pulsed fraction for those condi-
tions under which fluctuations would be the most difficult to detect; that
is, when each pulse is smeared out over half the interval between pulses.
Thus these are very conservative upper limits.

We get about 1 percent for periodic fluctuations (independent of period)
in the range 3 to 300 ms, and let me remind you that the Crab would be
at 33 ms and it would have about 15 percent pulsed fraction in this energy
band. We get somewhat larger limits for fluctuations that are not periodic
but which have the average time scale of the abscissa between bursts. In
the 2 full minutes we spent looking Sco X-1 straight in the eye, we could
not find any variations in excess of Poisson statistics whatsoever. And this,
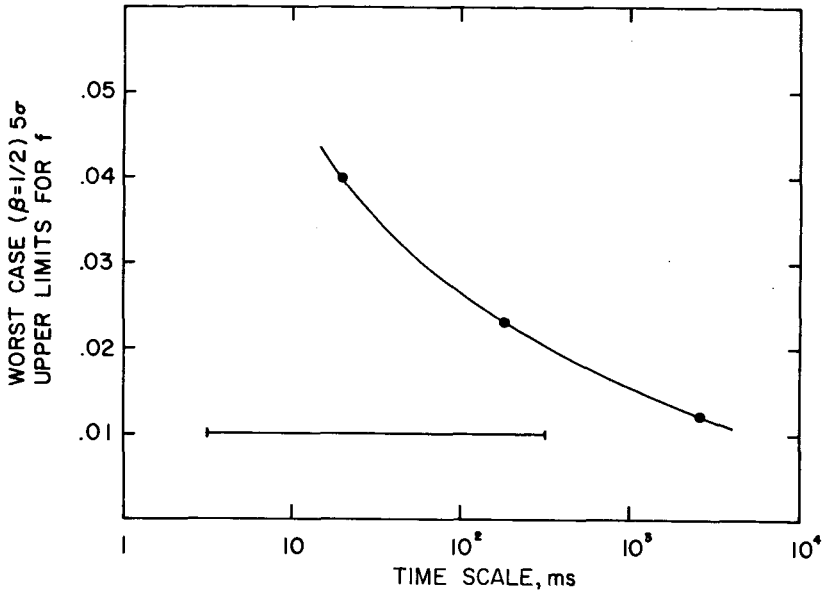
Figure 1—Upper limits to the pulsed fraction for those conditions causing the
most difficult detection of fluctuations.

remember, when we calculated a lifetime for Sco X-1 of less than 100 ms.
The conclusion we are forced to is that the energy input must be
essentially continuous on this time scale.

At least two separate detailed theoretical models of X-ray sources have been
proposed this year based on the premise that a pulsar can be hidden under-
neath a thick plasma cloud (so that you cannot see the pulsed component
of the radiation), and the X-ray emission would come secondarily from the
pulsar energy incident from the cloud from underneath. It is important to
remember that the loss of rotational kinetic energy from a pulsar is con-
tinuous, not pulsed. In the Crab, the pulsed component is a minuscule
fraction of the energy, and is important only because it tells us where to
find all the continuous energy input. In this case we cannot find the pulsed
part so we cannot make a positive identification of the pulsar origin for the
Sco X-1 energy input. However, the lack of nonperiodic variations demands
a continuous energy source, and that in itself rules out lots of other possi-
bilities. So a pulsar in Sco X-1 is not only consistent with our data, it is
also, I think, the most reasonable explanation for it, even if a pulsed com-
ponent is never detected.

Are all X-ray sources driven by pulsars, then? Some direct evidence
for another X-ray pulsar was offered by the experimenters on Ex-
plorer 42 (SAS A) this year who reported a 73-ms period for Cyg X-1, which
could also have been 4 times 73 or 292 ms owing to their 96-ms sampling
time. We looked at a 5-s exposure to Cyg X-1 in our rocket data for con-
formation and we found some very surprising results. We found nothing at
73 ms but lots of variations in excess of Poisson statistics. Figure 2 is our
power density spectrum for Cyg X-1, with a whole multitude of seemingly
unrelated peaks of high statistical significance; this means either that there
is no real periodicity (just aperiodic bursts), or a combination of separate
harmonic components. Alpha and beta are two components that, if modu-
lating each other, explain most of our peaks and are also consistent with
the original Explorer 42 results, as alpha is about 290 ms.
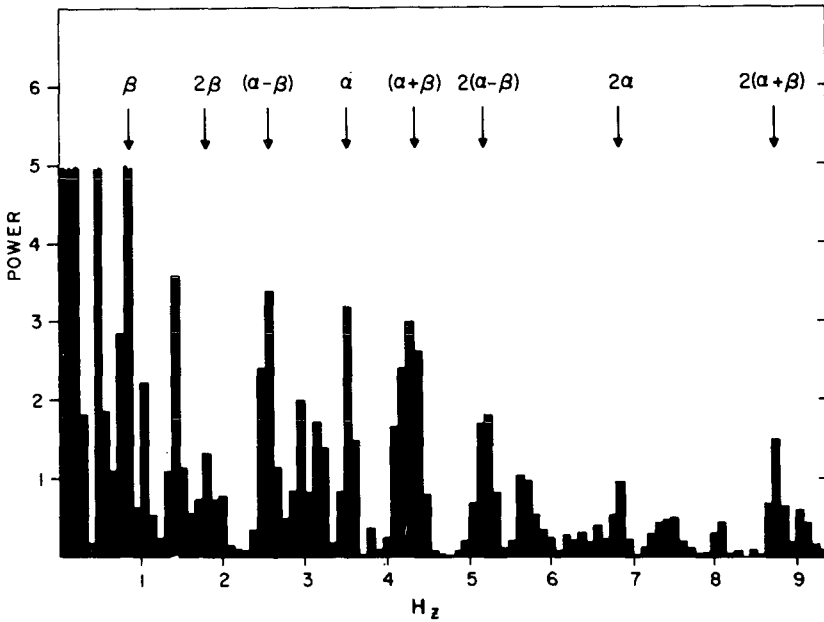
Figure 2—Power density spectrum for Cyg X-1.

In Figure 3 you can see the source of the power spectrum. The overall
triangular pattern is the collimator response as the source moves across our
field of view, and it does not take too much imagination to see an ampli-
tude modulation of the basic 290-ms periodicity, at least during the first
half of the exposure. During the second half we seem to lose phase, al-
though the average separation between these minima is still about 290 ms.
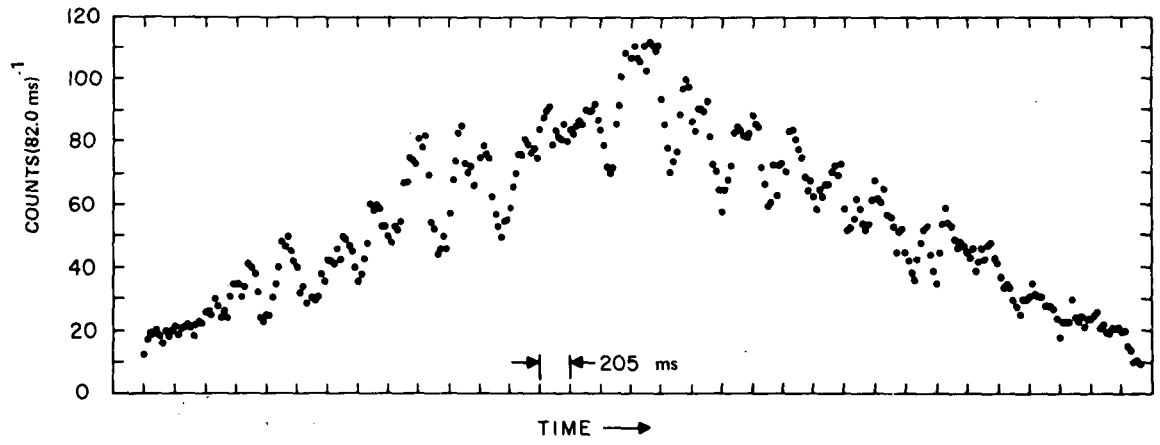
Figure 3–Source of power spectrum.

Subsequent investigations from Explorer 42 and from rockets indicate that this sort of pseudoperiodic behavior, where harmonic components seem to come and go with characteristic times of less than 10 s, seems to be the rule for Cyg X-1. This is definitely not what you would expect from a pulsar, and I wish I could tell you what it is.

So you might say that we win one and we lose one, in the sense that of the two temporal studies that I have discussed, we can at least reconcile one with a respectable model on an energetics basis now in addition to just identifying the emission mechanism. As far as Cyg X-1 is concerned, however, it appears that our analysis has raised more questions than it has answered. Perhaps someone on next year's program can come up with a believable explanation for what we have found.

INTERSTELLAR MEDIUM MODEL

James C. Novaco

Miss Nancy Vandenberg of the University of Maryland and I developed a model of the ionized part of the interstellar medium based on the low-frequency observations by the Radio Astronomy Explorer (RAE) Satellite with a background of nonthermal radiation. This nonthermal background radiation is caused by synchrotron emission from cosmic ray electrons, and at low frequencies this emission is heavily absorbed by free-free absorption from the residual thermal electrons in the interstellar medium. Hence, by an appropriate model, one can get a handle on parameters relevant to both the thermal and nonthermal components of the interstellar medium.

The observations were taken with the 100° dipole antenna and separated into galactic and extragalactic components by Clark, Brown, and Alexander (Ref. 1). This model was developed using only the separated galactic component.

Our model has a two-dimensional geometry, the plane of the model being perpendicular to the galactic disk and passing through the center and anti-center. Figure 1 is a schematic diagram of the geometry of this model. The directions anticenter (AC), galactic center (GC), and north and south galactic poles (NGP and SGP) are as marked. Cross sections of the three spiral arms in the Sun's local region are shown with the Sun imbedded in the middle spiral arm. The spiral arms are assumed to consist of two components, a warm intercloud region and randomly distributed cold denser clouds. The interarm region is assumed to be similar to the intercloud region with the exception that it is cloud free.
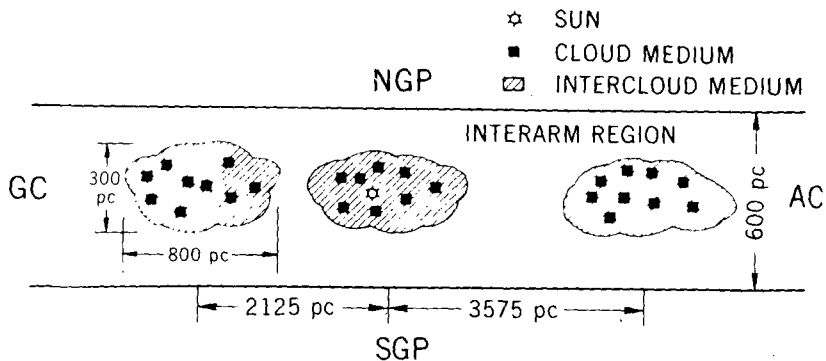

Figure 1—Geometry of the model of the interstellar medium.

At each frequency the model integrated the equation of transfer along lines of sight in a radial grid centered about the Sun. The flux contributions for each frequency were then averaged together to produce the spectra. Integration and averaging were done over a $100°$ cone comparable to the RAE antenna pattern. The $100°$ cone was centered on two directions, the north galactic pole and the anticenter.

The best results are shown in Figure 2. Brightness is plotted as a function of frequency, the solid line is the model, the dashed line is the RAE disk component; the error bar is applicable for the entire range shown on the graph. As we can see the two agree pretty closely.

In Table I, our parameters are broken down for the various regions. The first two columns are for the spiral arm, the third for the interarm region.

The volume emissivity for the intercloud and cloud regions was set at 1.0×10^{-39} W m^{-3} Hz^{-1} Sr^{-1} which was determined by Alexander et al. (Ref. 2) from RAE observations. We found that the interarm emissivity had to be 0.16×10^{-39} to fit the observations. This gave an average emissivity of 0.3, which agrees well with the average values extrapolated from higher frequency radio data. The radio of the two emissivities is supported by both theory and observation; and it is quite reasonable to expect a higher emissivity in the spiral arms, where the magnetic field has been compressed.

The intercloud temperatures were found to be 1500 and 2500 K in the two directions. This supports the concept of a thermal gradient away from the plane of the galaxy. The best results were obtained for cloud temperatures between 50 and 150 K. For temperatures less than 50 K the spectrum was flattened too much as the clouds became virtually opaque. For the sake of simplicity we chose the median value of 100 K. The interarm temperatures are not well defined. We can place only the lower limits shown.

The densities shown were fixed throughout the development of the model, and these values were taken from the Hjellming et al. interpretation of observations of the Crab Nebula pulsar (Ref. 3). To get a good fit with the observations we had to have a filling factor of less than 1 percent, which meant there is less than 1 pc of cloud for every 100 pc of intercloud medium.

In conclusion we can state that we have constructed a model using low frequency observations of the heavily absorbed non-thermal background emission that supports the theory of Hjellming et al. of the interstellar medium with an intercloud temperature of approximately 1000 K.
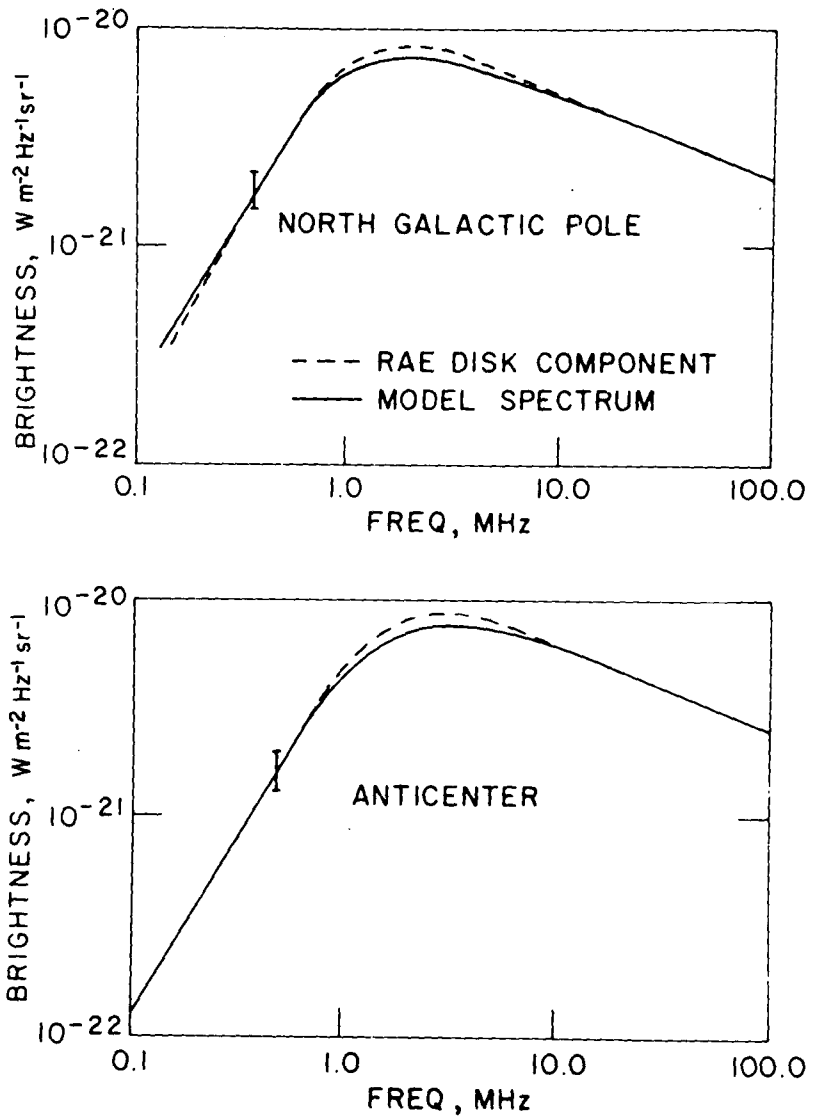
Figure 2—Brightness as a function of frequency for the model (solid line) and the RAE disk component (dashed line).

TABLE I—Summary of the Results

Parameter	Intercloud	Cloud	Interarm
Emissivity, W m^{-3} Hz^{-1} sr^{-1}	1.0×10^{-39}	1.0×10^{-39}	0.16×10^{-39}
Temperature, K			
Anticenter	1500	100	>2500
North Galactic pole	2500	100	>3000
Electron density, cm^{-3}	.028	.044	.028
Filling factor		<1 percent	

While the densities were taken from Hjellming's observations, they are in agreement with densities required by Field et al. (Ref. 4) for their theory of the interstellar medium; but we cannot say that the model can lend support to their theory.

The model also supports the concept of a thermal gradient away from the galactic plane.

CHAIRMAN:

Any questions?

MEMBER OF THE AUDIENCE:

Is this filling factor a linear filling factor or a cubic?

MR. NOVACO:

It is linear.

MEMBER OF THE AUDIENCE:

When the intercloud and the interarm emissivities differ by a factor of 10, why do you get the same densities with the higher temperature in the interarm region?

MR. NOVACO:

The only region in which there is any appreciable absorption from the interarm region is from about 1 to 9 MHz, and by the time we can integrate out

to the interarm region, the gas is already essentially transparent and hence we can get no real values for the temperatures. At those frequencies the gas is already essentially transparent. All we can do is place that lower limit. It has to be greater than those values in order to agree with the observations.

MEMBER OF THE AUDIENCE:

What was worrying me is that the density is as great between the arms as in the arms and yet the emissivity is way down.

MR. NOVACO:

Yes, we chose the values of electron densities rather than trying to determine them. Mainly because we have no idea of what value it should be or even what ratio it should be. The emissivity was down in order to agree with the higher frequency data from say 10 to 1000 MHz. If we raised it beyond that, the spectrum was much too bright in those frequencies.

REFERENCES

1. Clark, T. A.; Brown, L. W.; and Alexander, J. K.: Nature, vol. 228, 1970, p. 648.

2. Alexander, J. K.; Brown, L. W.; Clark, T. A.; and Stone, R. G.: Astron. Astrophys., vol. 6, 1970, p. 476.

3. Hjellming, R. M.; Gordon, C. P.; and Gordon, K. J.: Astron. Astrophys., vol. 2, 1969, p. 202.

4. Field, G. B.; Goldsmith, D. W.; and Habing, H. J.: Astrophys. J. Lett., vol. 158, 1969, L73.

THE SHAPE OF THE INTERSTELLAR REDDENING LAW

Dr. Michel Laget

A simple way to deduce the interstellar reddening law is to compare the spectral distribution of pairs of stars within the same spectral type and luminosity class, one of which is reddened and the other unreddened. Then, the observational problem can be summarized as two questions:

(1) What is the wavelength dependence of the reddening law?

(2) Is this law the same for all the stars?

Making this assumption that the observed difference between two stars is only attributed to the interstellar medium, the answers to these questions help us in the identification of the components responsible for such a reddening (molecules and grains), as well as their physical properties, size distribution of particles, geometrical shape, and their location in space.

Twelve stars of spectral type B0 have been observed by OAO 2 with the set of broadband photometers at 10 effective wavelengths and gave us the opportunity to derive the interstellar reddening and to consider a statistical approach.

Figure 1 represents four color-color diagrams at four representative effective wavelengths. As shown here we have used a least-squares fit of the observed values to a straight line for each effective wavelength to define the mean reddening line, the standard deviation, the slope of the reddening line and its probable error.

The standard deviation, which represents the scatter of the points increases from 0.03 mag at 332.0 nm to 0.28 mag at 155.0 nm and can be attributed to—

(1) Possible errors in V and $B - V$ values
(2) Instrumental fluctuations
(3) Differences in the interstellar reddening law
(4) Differences in the intrinsic flux distribution among the stars themselves

V and $B - V$ have been chosen from recent values given by Lesh (Ref. 1) and Hiltner et al. (Ref. 2) and we can expect to have a homogeneous system.
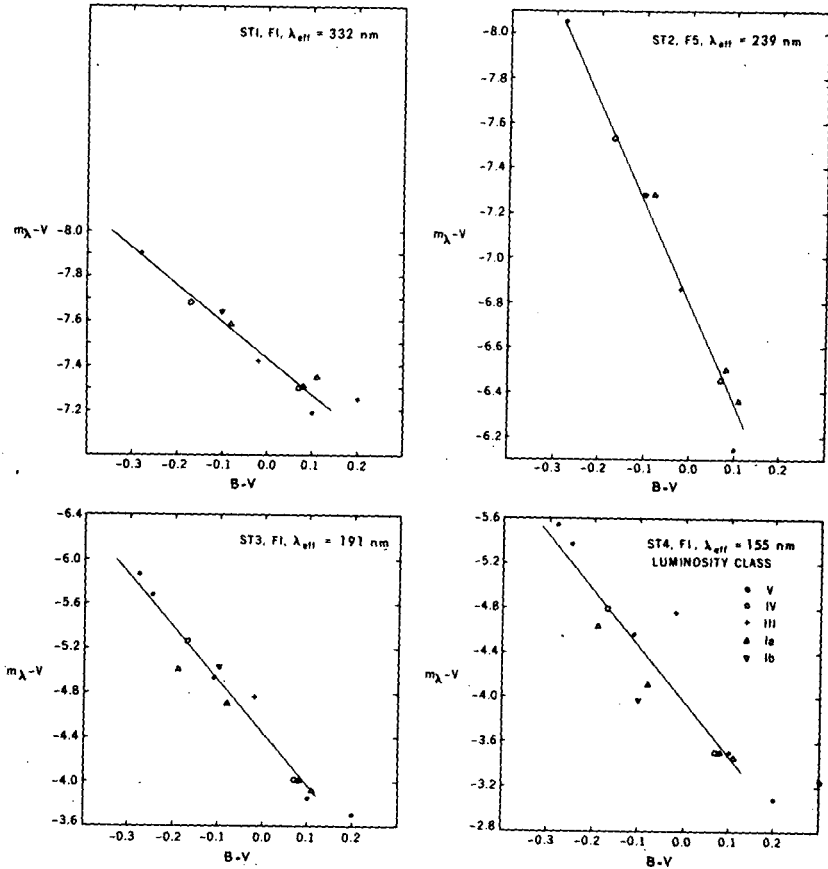
Figure 1–Color-color diagrams at four representative effective wavelengths.

Figure 2 illustrates by the pair of stars (ϵ, v) Orionis the intrinsic difference that may appear by comparing within the same spectral type the relative flux distribution of a supergiant and a main sequence star. A similar deficiency in the far ultraviolet flux of the supergiant ϵ Orionis was found by Carruthers (Ref. 3) at 111.5-nm.

It is also interesting to point out that this effect appears to be more important than the one due to a misclassification of a star as B0 or B0.5, which is illustrated by the pair (λ Leporis, v Orionis).
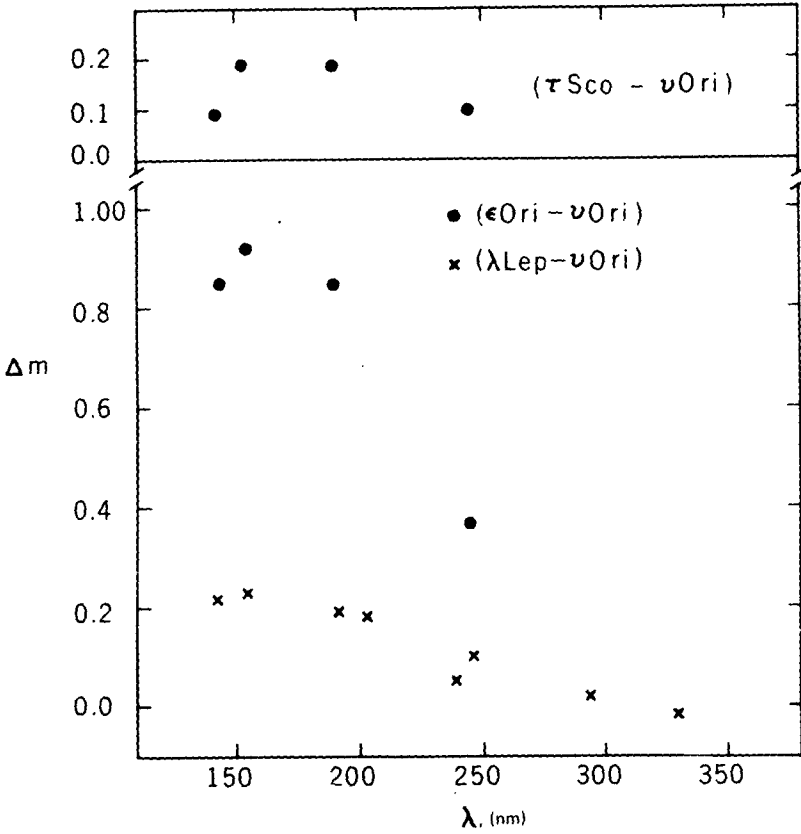
Figure 2–Comparison of the relative flux distribution of a supergiant
and a main sequence star.

Although the preceding remarks cannot be representative of a general effect,
we can expect to minimize the influence of such intrinsic differences for
the reddening determination by comparing stars within the same spectral
type and similar luminosity class.

Figure 3 shows the mean reddening law and its probable error and repre-
sentative individual reddening features obtained by comparing pairs of
stars. Separate calculations for main sequence stars and supergiants indicate
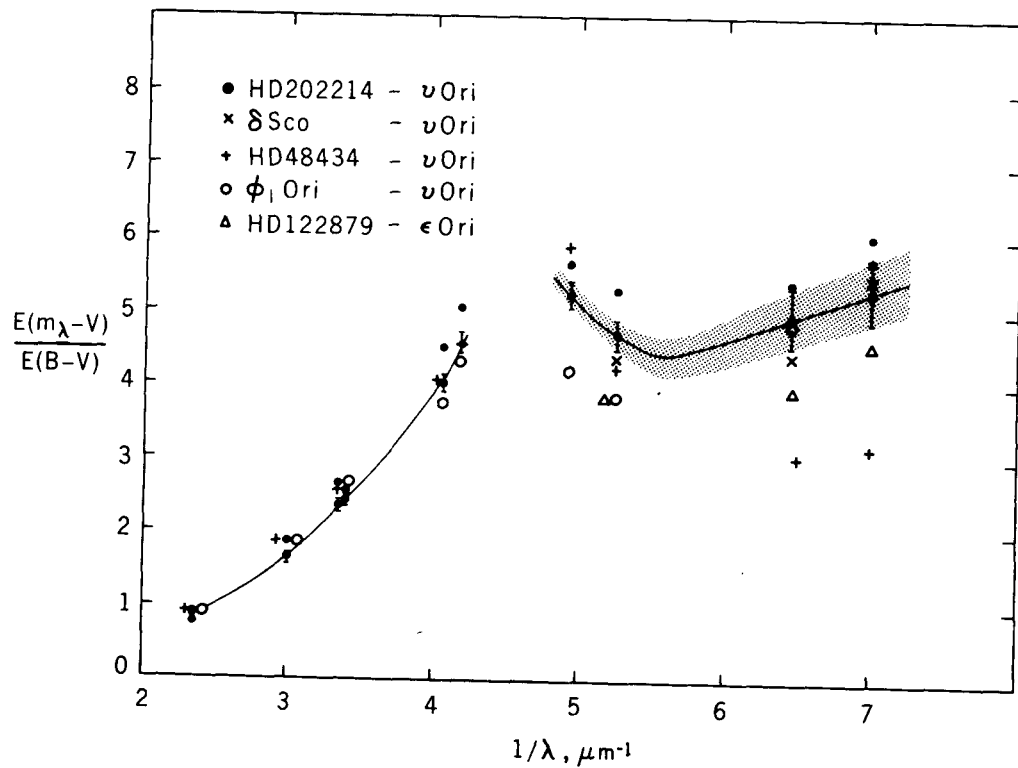that the probable error is independent of the luminosity class.

Figure 3–The mean reddening law and its probable error and representative reddening features obtained by comparing pairs of stars.

The general feature is the same as reported by Stecher (Ref. 4) and by Bless and Savage (Ref. 5) with the existence of a maximum attributed to small graphite particles and a minimum in the range 5.24 to 6.45 μ m^{-1}.

In addition, we note the constant increase of the probable error toward the far ultraviolet, being relatively small in the near ultraviolet.

An estimate of the statistical mean instrumental fluctuations for the sample case at 155.0 nm indicates that a real scattering in the far ultraviolet part of the reddening law exists.

Of the two questions posed at the beginning, the answer to the first is illustrated in Figure 3 by the average reddening law; these data give a negative answer to the second question which can be theoretically interpreted in terms of a different component responsible for the far and near ultraviolet extinction as well as possible change in the nature or in physical properties of components from star to star.

REFERENCES

1. Lesh, J. R.: Astrophys. J. Suppl., vol. 17, 1968, p. 371.

2. Hiltner, W. A.; Garrison, R. F.; and Schild, R. E.: Astrophys, J., vol. 157, 1969, p. 313.

3. Carruthers, G. R.: Astrophys. Space Sci., vol. 5, 1969, p. 387.

4. Stecher, T. P.: Astrophys. J. Lett., vol. 157, 1969, L125.

5. Bless, R. C.; and Savage, B. D.: Int. Astron. Union Symp. 36, 1970, p. 28.

INTERSTELLAR CO IN THE ULTRAVIOLET SPECTRUM
OF ζ OPHIUCHI

Dr. Andrew M. Smith

One of the most important characteristics of interstellar molecules is the sensitivity of their internal energy to the ambient gas and radiation field. Consequently, the molecules make good monitors of such physical parameters as particle density, gas temperature, radiation field energy density, and radiation field spectrum. Until recently, all observations of interstellar molecules have been made by radioastronomical techniques, which because of the large volumes of space sampled afford great sensitivity. This sensitivity, however, is accomplished at the expense of spatial resolution and, where the signal is saturated, spectral sensitivity.

Within the past year using optical methods in the vacuum ultraviolet, Carruthers at NRL (Ref. 1) has detected interstellar H_2 in the spectrum of ϵ Persei and we at Goddard have observed CO in the spectrum of ζ Ophiuchi. By contrast with radio results the regions sampled are small, being one or a few clouds in the line of sight, and, in addition, isotopic effects may be detected in the spectrum.

Let me now discuss the second of these observations further.

Figure 1 shows portions of the ζ-Ophiuchi spectrum in which the spectral resolution is about 0.05 nm and the linear dispersion is 0.4 f nm mm^{-1}. Wavelengths are plotted on the abscissa where each division is 1 nm; the stellar flux in relative units is plotted on the ordinate. Vibrational transitions in the fourth positive system $(A^1 \pi - X^1 \Sigma^+)$ of $^{12}C^{16}O$ are indicated by the vertical solid lines and in the case of $^{13}C^{16}O$ by the vertical dashed lines. The vibrational quantum numbers are shown in parentheses. It is noteworthy that this system of bands is very strong when observed in the laboratory. Although there are easily identified stellar features, e.g., the lines of C-IV (154.82, 155.08 nm) Si-IV (139.37 nm), and O-I (130.22 nm) that blend with the CO lines, we feel that the correlation of observed features with laboratory-measured lines in the CO spectrum is good and that the presence of this molecule in some interstellar cloud or clouds between us and ζ Ophiuchi may be observed.

Figure 2 illustrates the curve-of-growth analysis by which column densities of the $^{12}C^{16}O$ and $^{13}C^{16}O$ molecules were estimated. On the abscissa is plotted the log of the optical depth in the center of the line; and on the
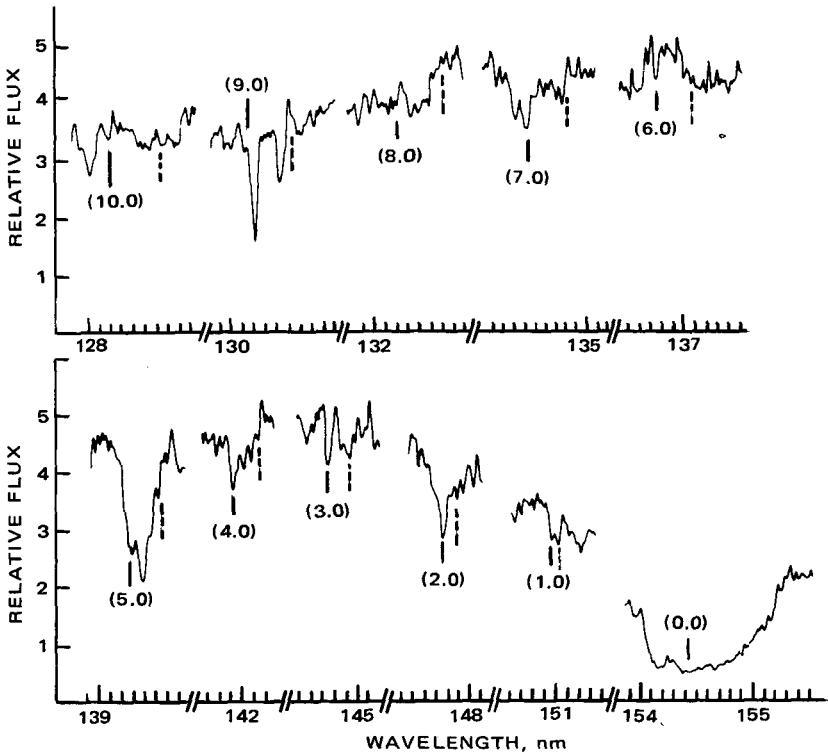
Figure 1—Portions of the ζ-Ophiuchi spectrum.

ordinate, the log of the equivalent width in units of the doppler width. The solid curve is computed assuming that the molecules are in thermodynamic equilibrium with a fossil 2.7 K blackbody radiation field. Thus, three rotational levels in the ground state molecules are excited giving rise to six lines in each vibrational transition. Equivalent widths of eight lines in the $^{12}C^{16}O$ spectrum were measured and were plotted against their corresponding oscillator strengths. This array, indicated by the black dots, was then fitted to the computed curve-of-growth at the "knee," and a turbulence parameter b, related to the Doppler width b_λ by the relation $b = c/\lambda \, b_\lambda$, and the column density n, which is proportional to τ_0, were derived. The values of these parameters are 1.5 km s^{-1} and 1.8 × 10^{15} cm^{-2}, respectively. These results are consistent with the results obtained by both rocket and ground-based observations of interstellar lines arising in different atoms and ions. Such
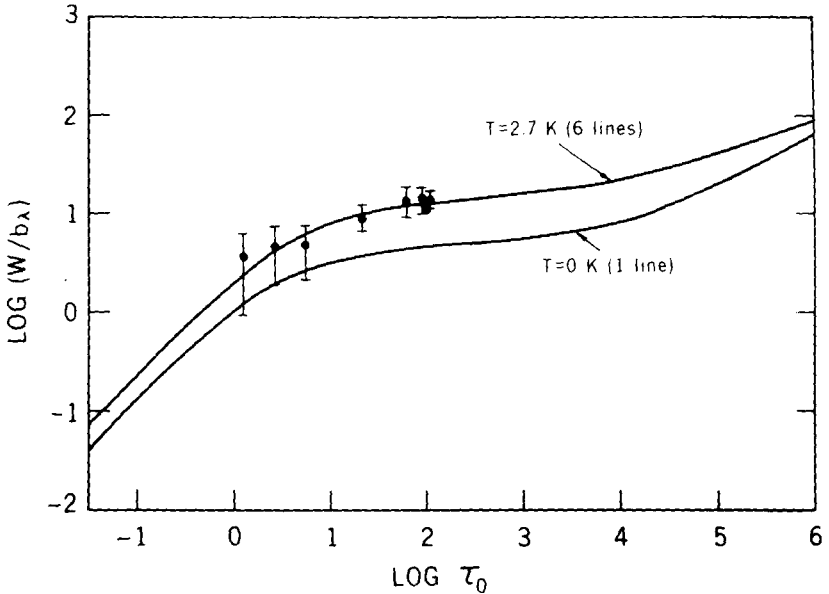
Figure 2–Fit of equivalent widths of $^{12}C^{16}O$ lines to computed curve of growth. The parameters are $b = \sqrt{2KT/Am_0} = 1.5$ km s^{-1} and $n = 1.8 \times 10^{15}$ cm^{-2}

plausible results cannot be obtained if only the lowest rotational level ($J = 0$) of the ground state is populated; but on the other hand, the higher rotational levels may be excited by collisions with ambient gas particles as well as by the ambient radiation field.

A similar analysis of four lines in $^{13}C^{16}O$ in the interstellar cloud or clouds between here and ζ Ophiuchi is 79, which is close to the terrestrial value of 89.

In summary four points may be made:

(1)   Interstellar CO has been observed optically in the ultraviolet spectrum of ζ Ophiuchi, and is probably located in one or a small number of clouds intercepted by the line of sight.

(2)   The column density and turbulence parameters are 1.8×10^{15} cm^{-2} and 1.5 km s^{-1}, respectively, and are consistent with observations of other interstellar lines.

(3)   The abundance ratio of interstellar ^{12}C to ^{13}C is 79; i.e., nearly terrestrial.

(4)   These results are consistent with viewing the interstellar CO molecules as being in thermodynamic equilibrium with a 2.7 K fossil blackbody radiation field.

CHAIRMAN:

Are there any questions?

MEMBER OF THE AUDIENCE:

It seems that you tried to obtain a vertical and horizontal fit of the data points to the computed curve of growth.

DR. SMITH:

Yes.

MEMBER OF THE AUDIENCE:

However, it seems to me that really you can only get one parameter because your data points do not define the shape of your computed curve accurately enough to permit a bit both vertically and horizontally. In other words, if you move the data points up and, say, over to the right, you still fit the computed curve you have drawn there. Thus, it seems that the fit parameters are not independent, and that there is a functional relationship between them.

DR. SMITH:

That's a problem. If you shift the data up and to the right the essential problem that arises is with the turbulence parameter and in this case it becomes quite small. I tried essentially the same thing by seeing what would happen if I assumed the molecules were in thermodynamic equilibrium with a 30° gas. When the data were fitted to this new curve of growth the turbulence parameter came out to be 0.46 km s^{-1}. Why is this not possible? I cannot say exactly that it is not possible. Maybe in the interior of the cloud that is what the case is. But that is not what is observed by Herbig (Ref. 2). Herbig has derived turbulence parameters from roughly 0.8 to 2.4 km s^{-1}, but he has used the value 1.5. What I have tried to do here is to find a fit that produces a value of the turbulence parameter consistent with that found by Herbig.

REFERENCES

1. Carruthers, G. R.: Astrophys. J. Lett., vol. 161, 1970, p. L81.

2. Herbig, G. H.: Z. Astrophys., vol. 68, 1968, p. 243.

LOW-INTENSITY H-BETA EMISSION FROM THE INTERSTELLAR MEDIUM

Dr. Ronald J. Reynolds

Pulsar pulse dispersions and low-frequency absorption of galactic and extra-galactic radio sources strongly suggest that the interstellar medium is much more ionized than previously assumed.

It used to be assumed that the interstellar medium consisted mostly of large regions of neutral hydrogen gas and that any free electrons within this neutral hydrogen medium would be the result of the ionization of carbon, silicon, and iron atoms by ultraviolet starlight with photon energies less than 2.18 aJ (13.6 eV).

But this model falls short of producing the observed number of interstellar electrons by nearly a factor of 100. Therefore, one is forced to conclude that the interstellar hydrogen is also being ionized by some process, and there are now many people working on various possible ionization and heating mechanisms for the interstellar hydrogen.

Experimentally a great deal of information can possibly be learned about the ionization and heating processes acting upon the interstellar hydrogen by studying the very faint hydrogen recombination radiations that would result. A search for the resulting H-beta line was recently made using a spectrometer at the Coude focus of Goddard's 36-in. telescope. This work was done in collaboration with Fred Roesler and Frank Scherb at the University of Wisconsin and Elihu Boldt at Goddard.

The search was confined to directions near pulsars because of the additional information provided by the dispersion measure which gives the total number of electrons along the line of sight to the pulsar. Of the four directions in which observations were made, an emission line appears to be present in at least two and possibly three directions.

Figure 1 shows the data obtained from a low galactic latitude direction near the Crab Nebula pulsar. The observing direction was about 9 arcmin off the Crab with the field of view of about 1.5 arcmin. The number of counts has been plotted versus the local standard of rest velocity and local standard wavelength of H-beta.
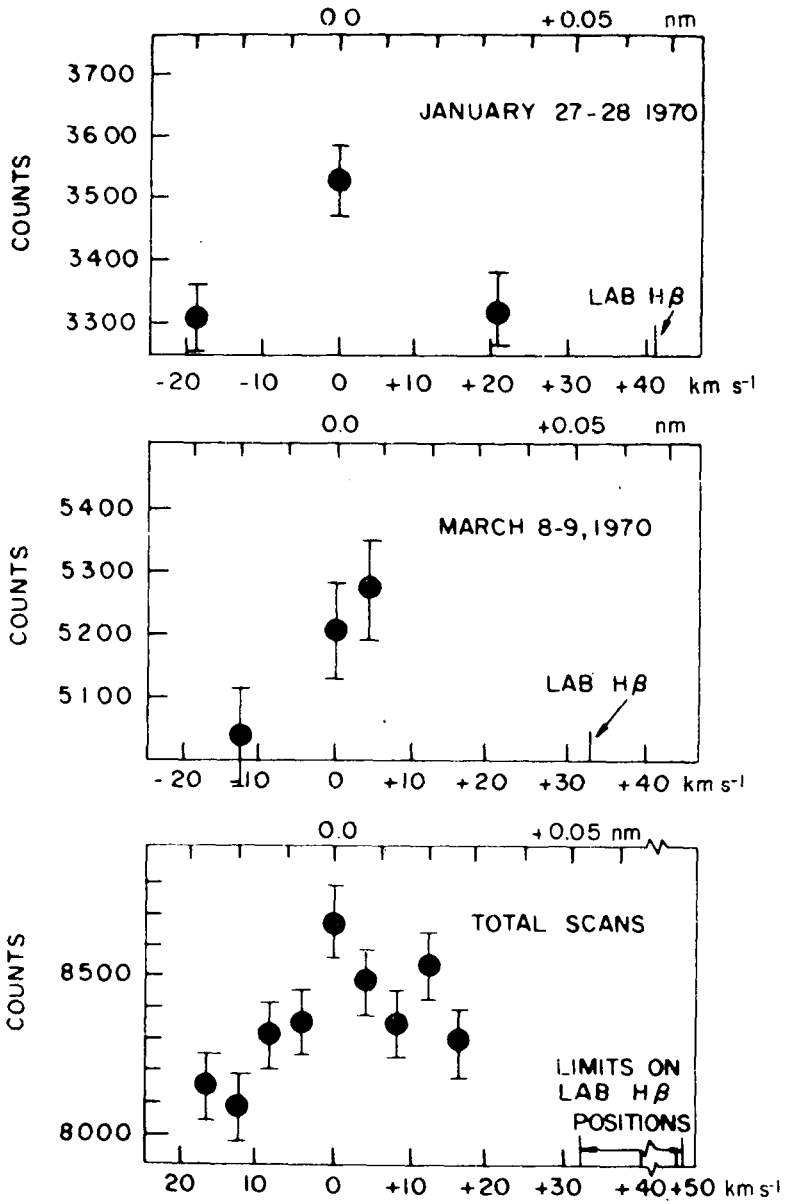
Figure 1—Data from a low galactic latitude direction near the Crab Nebula pulsar, PSR 0532 direction.

The resolving width of the spectrometer is about 8 km s^{-1} or 0.014 nm. The top two graphs consist of just the three data points, each to confirm the presence of an emission feature; the bottom graph shows an attempt to measure the line profile and represents the total accumulating time of 1 hr per data point. This feature coincides in position and approximate width with the velocity distribution of the neutral hydrogen in this direction as determined from 21-cm data.

The data from a high galactic latitude direction is shown in Figure 2; the galactic latitude is +50° for this pulsar. The neutral hydrogen in this direction is also peaked at 0 km s^{-1}, as this emission feature appears to be.

If these features are galactic H-beta, then there are two main conclusions that can be deduced from the data. First, the data can be combined with galactic radio absorption measurements and pulsar dispersion measures to set a lower limit of 1000 K for the electron temperatures of the emitting regions and upper limit of 1 electron cm^{-3} for the densities.

Secondly, the average recombination rate of hydrogen along the line of sight must be greater than or about equal to 10^{-14} per hydrogen atom per second. Assuming steady-state conditions, this would also be the value of the average ionization rate for hydrogen and is a factor of 3 to 10 times higher than what people working on steady-state ionization models had been assuming.

These observations are continuing with a spectrometer of much larger area, and preliminary results of the data obtained last month (October 1971) at 13 additional directions seem to confirm these general conclusions.
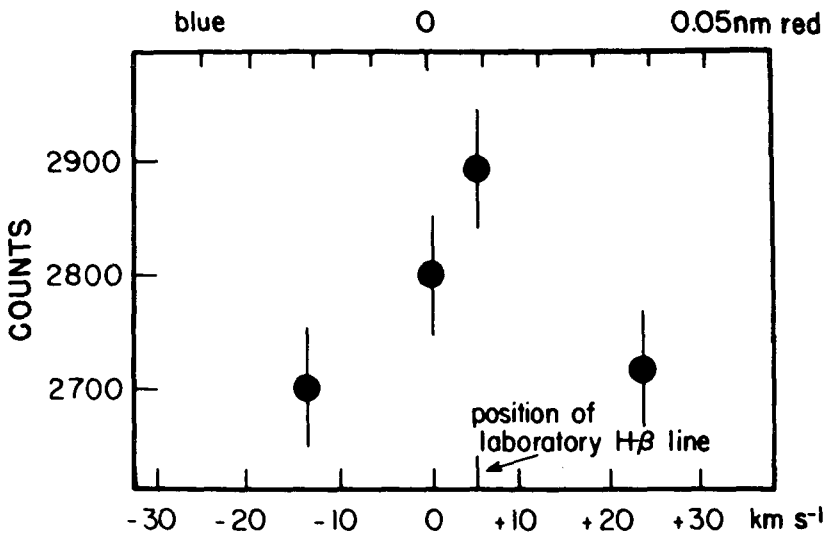

Figure 2—Data from a high galactic latitude direction, PSR 1508.

C-IV 155-nm LINE IN β CEPHEI

Dr. David Fischel

The class of early B variable stars known as β Cephei stars are characterized by short-period radial velocity and light variations. The coolest stars of this group have an effective temperature of about 20,000 K and the hottest, about 28,000 K; the surface gravities are of the order of 10^4 cm s^{-2}. These stars are not related to the classical Cepheids whose temperatures are of the order of 6000 K.

The amplitude of the radial velocity variation β Cephei stars is in the tens of kilometers per second and the light variation is less than 0.2 mag, that is, less than 10 percent. The fastest pulsation is 3 hr and the shortest is 6 hr. The prototype β Cephei has a period of 4 hr 34 min. Ultraviolet observations were taken using OAO 2 to investigate the relationship between the visual and the ultraviolet variations.

The lower curve in Figure 1 shows data taken on April 5, 1971, with the resonance lines of hydrogen at 121.5 nm, 3 times ionized silicon at 139.9 nm, and 3 times ionized carbon at 154.8 nm. The ordinate in this figure is the decadic logarithm of the instrumental counts and the abscissa is wavelength in nanometers.

Data taken 14 days later on April 19 are shown in the upper curve, which has been arbitrarily shifted upward for visibility. One can clearly see that the C-IV line is in emission. The slight bump that exists at a slightly shorter wavelength is persistent through all the observations that we have; it is not part of C-IV line.

Additional data were taken because of this mysterious disappearance to investigate the cause. We obtained considerable data in June for a total of 64 scans covering 76 days, including the April data.

If we connect the left-hand side of the line at 153 nm to the right-hand side at 157 nm and measure the area lost to the line and follow this measurement with time, we have then a measure of the strength of this line with time.
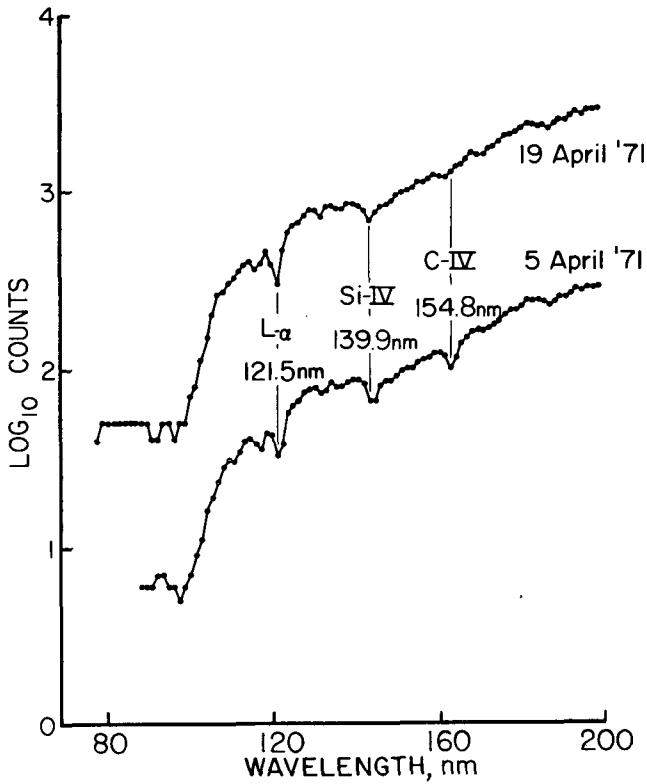
Figure 1 – Results of ultraviolet observations of β Cephei.

Figure 2 shows this measurement of the equivalent width in counts in the C-IV line as a function of phase over a 6-day period. These are data taken and folded back on themselves every 6 days, showing a reasonable light curve.

No other feature shows any variation with a period of 6 days and we are unable to detect any other periodic variation except the 4 hr 34 min fundamental period characteristic of β Cephei. If this 6-day variation is due to the beating of another pulsation against the 4 hr 34 min one, then that pulsation would have to have a period of either 4 hr 43 min or 4 hr 26 min. Neither have been observed, either in the visual or in the ultraviolet spectra.
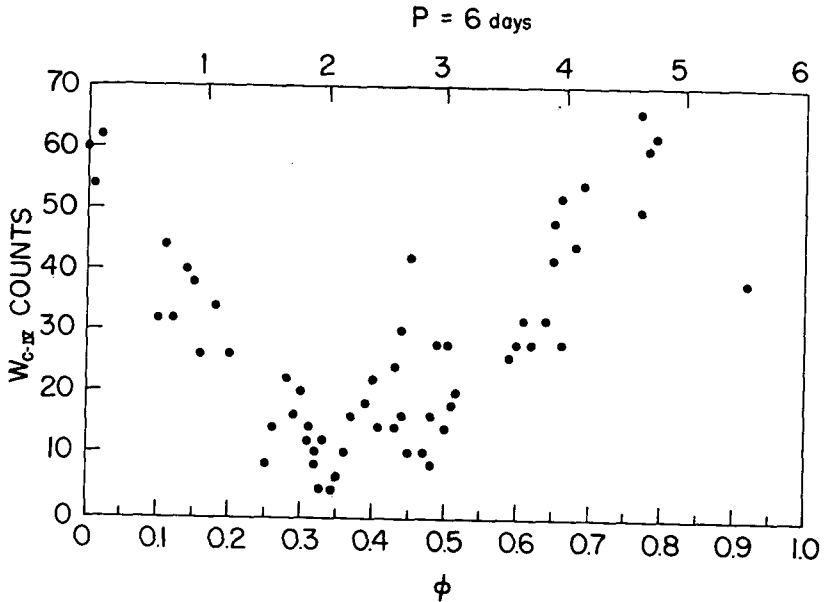
Figure 2—Measurement of the equivalent width in the C-IV line.

Alternatively there is evidence from the visual spectrum that β Cephei is a single-line spectroscopic binary. The estimated period from those data is 11 days, but it has a very highly eccentric orbit. There is also some difficulty in interpreting the data. In any event, if β Cephei is a binary, then the tidal distortions caused by the unseen companion would give rise to the variation in the C-IV line because C-IV is very sensitive to pressure.

Figure 3 illustrates two possible models of β Cephei. One model has a nearly circular orbit with a period of 12 days such that the front and back tidal bulges are seen alternately by the observer, one every 6 days. The other model has a very elliptical orbit whose period is of the order of 6 days; the tidal bulge comes and goes so that one sees the bulge every 6 days.

At this point in time we are rather partial to the first model, but we need more proof of that. In any event, we believe that the variation in the C-IV line at 155 nm in β Cephei is a very dramatic effect of tidal distortion.
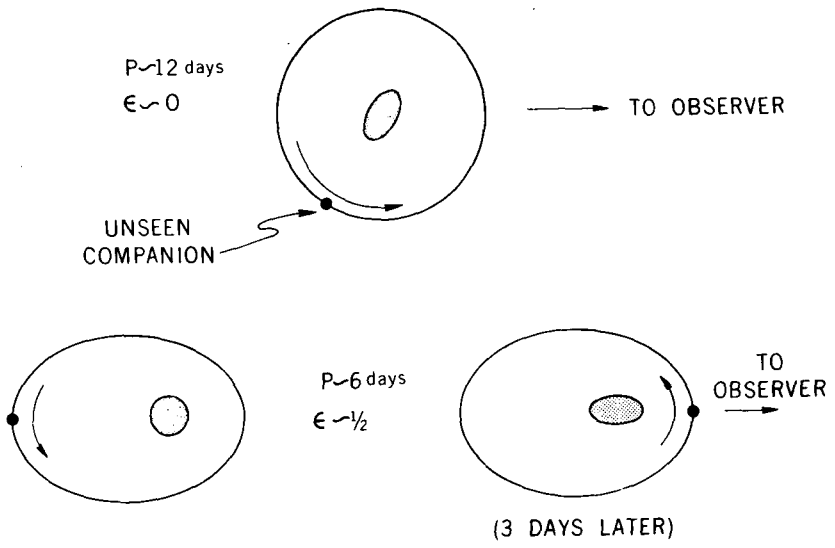
P

Figure 3—Two possible models of β Cephei.

GIANT LOOPS — A NEW KIND OF NEBULA

Dr. Stephen P. Maran

Four enormous, loop-shaped features were found in ground-based surveys of the low-frequency galactic radio emission (Ref. 1) (Fig. 1). With diameters of $40°$ to $116°$, they include the Cetus Arc and the North Polar Spur and were formerly called the radio spurs. More recently, the tendency in the literature has been to call them "loops," and two leading theories for these objects have emerged.
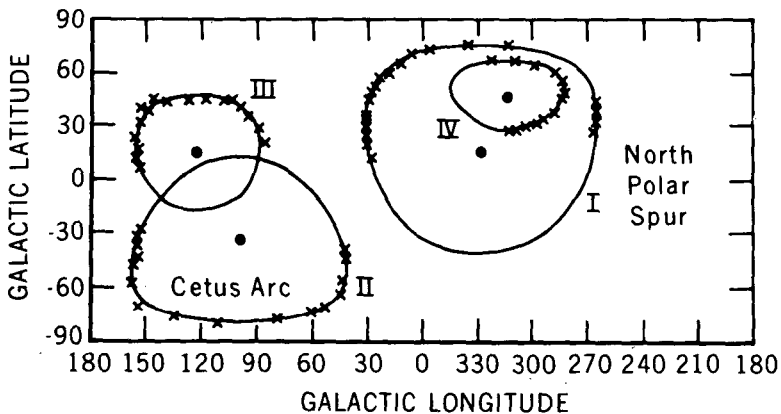

Figure 1—Map showing the distribution of the giant loops in new galactic coordinates, according to Haslam, Kahn, and Meaburn (Ref. 1).

One theory, by Mathewson in Australia (Ref. 2), ascribes the loops to synchrotron radiation by cosmic ray electrons that are spiraling in the helical pattern of the galactic magnetic field near the Sun. This idea is based on an apparent correspondence between the local field pattern that is derived from optical polarization measurements of stars and the pattern of the loops as obtained from the radio surveys. However, the model cannot explain the observation of H-alpha and H-beta emission filaments that are associated with the loops. In addition, the fit of the polarization pattern is poor in the case of Loop II (Cetus Arc), and it appears that the loops do not connect in the manner expected for the helix model of the galactic field.

197

The other theory, widely discussed but most notably advanced by the group at Manchester (Ref. 1), which has made almost all of the loop observations, suggests that they are very large, old, supernova remnants. Here are three of the many objections to this view:

(1)   There is no evidence for expansion.

(2)   The large angular size and relatively high galactic latitudes leave the supernova remnant theory with the problem of explaining why there are four remnants within an estimated 250 pc of the Sun.

(3)   Whether you look at the few accepted supernova remnants for which diameters are accurately known, or at the roughly 100 known remnants in the galaxy for which estimated diameters are available, you find that the diameters are all less than 40 pc or less than 70 pc, depending on who did the estimates. The supernova remnant theory of the giant loops leads to lower limits on their diameters of about 170 pc, or even twice as much. Therefore, we are compelled to ask, "Where are all the supernova remnants with diameters between 70 and 170 pc?"

Now I wish to remind you of the Gum Nebula (Fig. 2, taken from Ref. 3), which we last year suggested was a new class of object, the fossil Strömgren sphere, that was created when the interstellar gas was ionized by ultraviolet light from a supernova explosion. The group at the Harvard College Observatory (Ref. 4), has calculated the evolution of fossil Strömgren spheres, as shown in Figure 3. Although the center of the sphere starts out about 10 times hotter than the exterior region, it cools much more rapidly. This occurs because a fully ionized plasma radiates more efficiently than does a partially ionized gas. Thus, it was predicted that after a million years have elapsed, the fossil Strömgren sphere will have the form of a large hot shell.

John C. Brandt and I now propose an alternative theory for the giant loops, which we believe is compelling although not conclusive: the loops are ancient fossil Strömgren spheres. On our model, there has been a slow expansion of the hot shell, due to the pressure difference between the hot gas and its cool surroundings. In fact, the velocities that have been observed in the optical filaments are of the order of the speed of sound at 10^4 K. This expansion produces an outward-directed hydromagnetic shock wave that compresses the ambient galactic magnetic field and thus generates

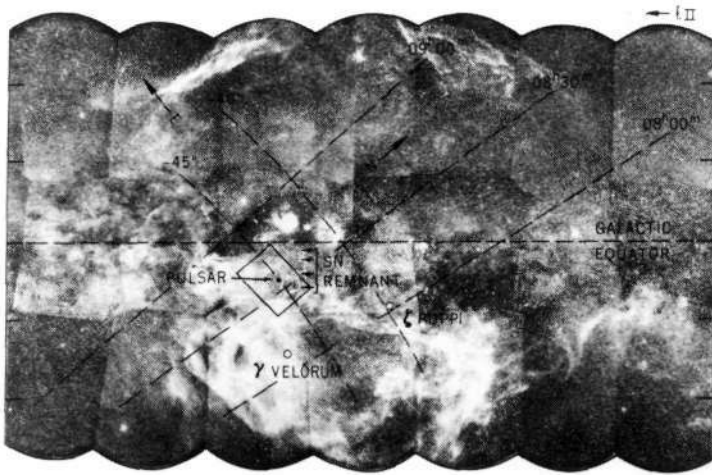Figure 2—The Gum Nebula in H-alpha, a mosaic from Reference 3, prepared at the Australian National University. The box shows the region of Vela X that appears in the familiar ultraviolet-light photograph of B. J. Bok.
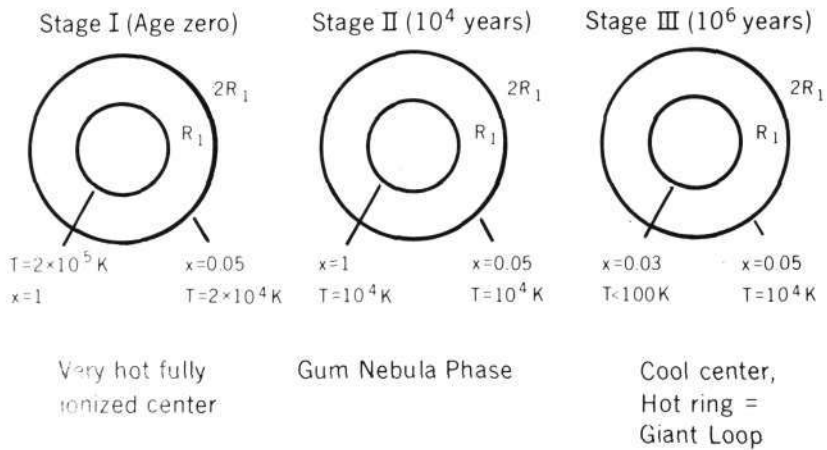

Figure 3—The evolution of a fossil Strömgren sphere, according to the computations of Richard McCray and Joseph Schwarz. At all stages, $x < 10^{-3}$ and $T < 100$ K at $3R_1$.

synchrotron radiation by the van der Laan mechanism. The emission is produced by the ambient cosmic ray electrons and not only by electrons from the supernova. This provides at least a qualitative explanation for the observed spectrum and polarization of the continuous radio emission from the loops. The optical radiation comes from the still partially ionized denser filaments of the fossil Strömgren sphere.

In our theory, the giant loops, so called to distinguish them from the Cygnus Loop and Vela X (which are much smaller and which are known to be supernova remnants), are much older than the remnants. Thus, there is a higher probability of finding several of them near the Sun than is given by the supernova remnant theory. Also, in our theory the size of the loops depends on the interstellar gas density, averaged over large regions, and on the ultraviolet luminosities of the supernovae. We have no problem with the deduced linear sizes and expansion speed limits and indeed could let them be more severe without compromising our theory.

In conclusion, we believe that the giant loops were created by radiation from supernovae and that they do not consist of matter ejected by the explosions.

REFERENCES

1. Haslam, C. G. T.; Kahn, F. D.; and Meaburn, J.: Astron. Astrophys., vol. 12, 1971, p. 388.

2. Mathewson, D. S.: Astrophys. J. Lett., vol. 151, 1968, p. L47.

3. Atlas of H-alpha Emission in the Southern Milky Way, Australian National University, 1960.

4. McCray, R.; and Schwarz, J.: The Gum Nebula and Related Problems, S. P. Maran, J. C. Brandt, and T. P. Stecher, eds. TMX 657-49, 1971, p. 60.

INTERPLANETARY DUST AND COMET ORBITS

Dr. Robert G. Roosen

In the early days of space flight a large number of experiments were launched that consisted of sounding boards and piezoelectric crystal detectors, or microphones. Clicks heard by the microphones were interpreted as being caused by micrometeoritic particles hitting the sounding boards. This interpretation suffered from two difficulties. First, it led to a cumulative spatial distribution almost a factor of a million higher than that derived from measurements by other techniques. Second, a number of the microphone experiments experienced "dust storms" — periods in which their count rates increased by as much as a factor of 1000 over their average background rate.

Last year at this meeting Otto Berg described the results from his extremely sensitive micrometeoroid detectors flown on Pioneers 8 and 9. He described a low-flux model for the interplanetary dust distribution that is in good agreement with other recent measurements and hence casts serious doubt on the validity of the microphone results.

The only comprehensive explanation of the dust storms was attempted by Eric Silverberg in his Ph. D. thesis at the University of Maryland. He suggested that the orbital planes of short-period, low-inclination comets are filled with micrometeroroids because of the effect of solar radiation pressure on their orbits. He further pointed out that "in general there appears to be no dust event seen by the satellites carrying microphone detectors which was not near the plane of a periodic comet. Furthermore no orbiting satellite passed through the plane of a low-inclination comet without registering a flux increase."

Several years of observational results are now available from the Pioneer 8 and 9 interplanetary dust detectors. This makes it possible to test the validity of Silverberg's hypothesis.

Table I summarizes the characteristics of the five largest dust showers discussed by Silverberg. The last column of the table lists the number of counts that would be expected to be observed by the Pioneer 8 and 9 detectors in the same showers. As you can see we would expect with the Pioneer detectors to see as many as 600 counts in a day. For some of the other showers we would expect to see tens of counts per day.

201

TABLE I—Characteristics of Five Largest Dust Showers

Satellite	Date of storm	Associated comet	Count rate, $m^{-2} s^{-1}$	Duration of storm, hr	Predicted counts per day for a Pioneer-type detector
Vanguard 3	Nov. 16 to 18, 1959	Honda-Mrkos-Pajdusákova	0.2	70	250
Explorer 1	Feb. 3, 1958	Ororsen-Metcalf	.2	15	55
Electron 2	Jan. 30 to 31, 1964	Brorsen-Metcalf	.11	15	30
Sputnik 3	May 15, 1958	Halley	7	5	630
Electron 2	Feb. 23 to 25, 1964	Encke	.0058	44.4	5

Figure 1 shows all counts registered on the front films of the Pioneer 8 and 9 detectors during the periods when complete telemetry was available. Since solar interference was believed to be present, the count rates were shown separately depending on whether the Sun was within the 120° field of view of the detectors. Each vertical line represents one event. Tick marks are added if more than one event occurred during the same day. The date scale should be interpreted as satellite longitude. The times at which cometary enhancements are predicted are shown at the bottom of the figure. It is apparent that no dust showers are seen then, indeed no detectable showers appear anywhere in the data.
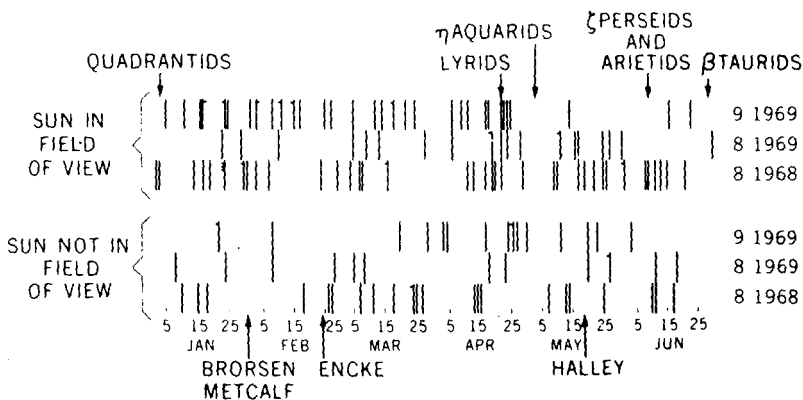

Figure 1—Pioneer 8 and 9 interplanetary dust detector counts.

This makes the Pioneer observations completely at odds with early micro-phone observations. In particular we can make the following points:

First, no comet-associated dust storms were detected to a limit of at least the factor of 100 more sensitive than previously reported highest rates.

Second, the reported microphone events were for particles in the mass range of 10^{-8} to 10^{-9} g, whereas the events shown in this figure are due to particles smaller than 10^{-11} g. Indeed the largest particle observed by the Pioneer detectors in more than 3 yr of operation is 10^{-10} g. Hence the particles presumed to cause these dust storms are much too rare to even have been observed.

Third, it is no good to suppose that these storms occur only occasionally since Silverberg's claim that they are invariably observed whenever a satellite-borne detector passed through the orbital plane of any short-period, low-inclination comet with perihelion distance less than 1 AU.

The arrows at the top of the figure show the dates of some of the most active meteor showers. The lack of any observed concentration of small particles on these dates is not surprising since it is well known that meteor streams are deficient in small particles.

In conclusion, the dust storms observed by the microphone detectors re-main unconfirmed and unexplained. This, combined with their unreasonably high measured particle flux casts serious doubt on any results from this type of detector.

EVIDENCE ON THE COMPOSITION AND MINERALOGY OF
THE LUNAR HIGHLANDS

Dr. Charles C. Schnetzler

Today I would like to show some lines of evidence that give us some indication of the composition and mineralogy of the lunar highlands, a region not directly sampled by Apollo landings.

Figure 1 shows our analyses of rare Earth elements in various lunar samples. The elements are listed in order of increasing atomic number and the abundances are relative to primordial abundances as determined from stony meteorites.

We show here our analyses of soils from Apollo 11, 12, and 14 and Luna 16 missions. Note that the abundances of the rare Earth elements are in general smooth functions of atomic number. This is the reason we study these elements — they show small regular differences in chemical and physical properties with atomic number.
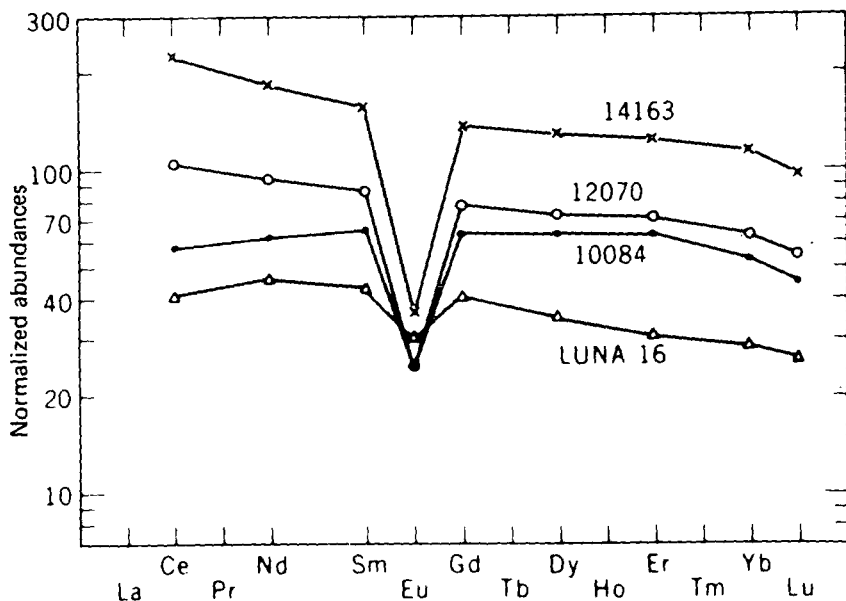

Figure 1—Abundances of rare Earth elements in lunar samples.

Exception to this smooth function is europium, which is depleted relative to the abundances expected from the extrapolation of the other rare Earth elements. This europium depletion is observed in every whole-rock sample, with one exception, returned by lunar missions to date, whether the samples be soil, breccia, or igneous rock. This is known in the lunar business as the europium anomaly.

Now why is this? Figure 2 shows our measurements of the partitioning of rare Earth elements between liquid magma and minerals crystallizing in the magma. We have studied the common rock-forming minerals including the minerals that make up the bulk of the lunar rocks. The main point to be seen here is that for most of these minerals, the partitioning of the rare Earth elements including europium, is a smooth function of atomic number. For any particular mineral, even though there is a wide range in absolute abundances, the patterns are roughly the same. The only exception is the common mineral feldspar. Every feldspar-melt pair measured to date (approximately 25) have positive europium anomalies.

Europium is the only rare Earth element that can be reduced in nature from the normal +3 valance state to the +2 state and, for some reason not completely understood, feldspar prefers the +2 state. It is the only mineral known to have this preference. Thus since the mare basalts and soils are depleted in europium, there is reason to think that feldspar with the europium occurs somewhere else on the Moon, somewhere that is older than the
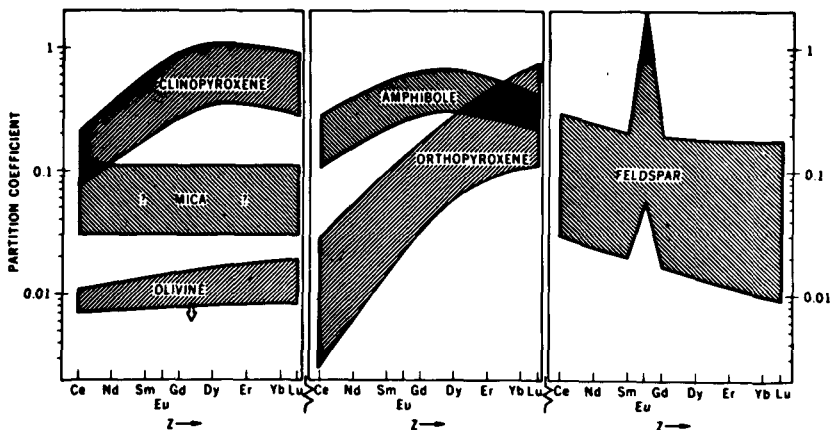

Figure 2—Mineral/liquid partition coefficients for rare Earth elements.

mare basalts. Large amounts of feldspar cannot be at depth as it would convert with high pressure to a high-density form that is not compatible with a bulk density of the Moon. As feldspar is light it is reasonable to suggest that it floated upward to the surface of the Moon and concentrated in the highlands.

Figure 3 shows a rather representative sampling of small particles found in the Apollo 11 soil. The scale represents 1 mm. The sample contains small pieces of fine- and medium-grained basalt and some glasses that have representatives in the large bulk igneous rocks that were brought back. However, there is one piece which is exotic, the white, translucent piece, which has no representative in the larger samples brought back from the Apollo 11 mission. This piece is composed almost entirely of feldspar. Terrestrial rocks composed mainly of feldspar are called anorthosites and are rather rare. They are all very ancient (over about 1.7 billions yr old) and their origin has been a subject of much debate. Approximately 5 percent of the less than 1-mm size particles in Apollo 11 and 12 soils are anorthositic; that is, they are very high in feldspar. Interestingly, cratering studies indicate that approximately 5 percent of the particles of this size should come from greater than 100 km away.

A third line of evidence on the composition of the highlands comes from the alpha back-scattering chemical determinations by Surveyor 7 on the rim of Tycho in the highlands. Calcium and aluminum are high, compatible with a high feldspar content. This brings us to the Apollo 15 mission. The indirect evidence preceding Apollo 15 (discussed in this paper), indicated the highlands should be high in feldspar. One large fist-size anorthositic rock was returned on Apollo 15, the famous "Genesis" rock. In this rock europium is approximately 50 times the relative abundances of the other rate Earth elements. The rock is also very old, about 4.2 billion yr old.

The second line of evidence that came from Apollo 15 is a subject of the next talk. Dr. Adler will discuss the X-ray fluorescence experiment flown in lunar orbit.
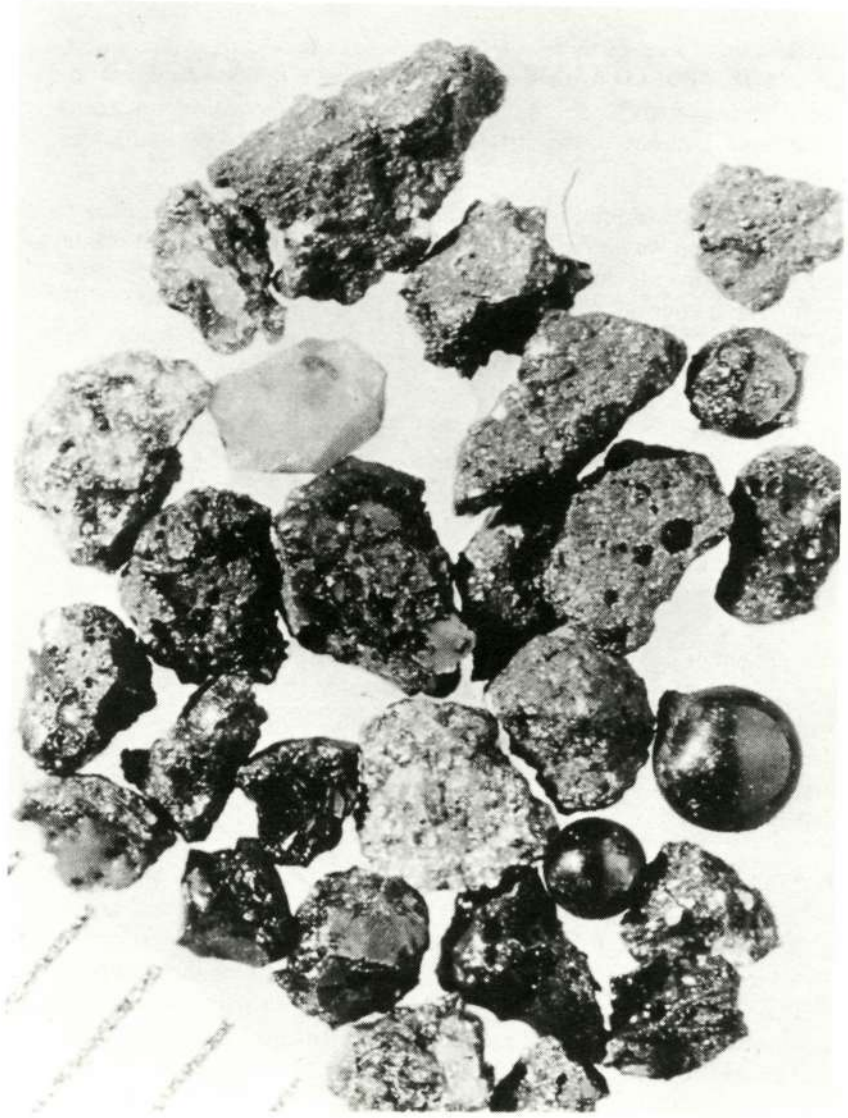
Figure 3—Apollo 11 lunar soil sampling.

THE APOLLO 15 X-RAY FLUORESCENCE EXPERIMENT

Dr. Isidore Adler

I want to give you a brief report of the results of an X-ray fluorescence experiment that we flew as one of the components of a number of orbital science experiments carried in the service module of the Apollo 15 spacecraft. The framework for what I am going to say has been very neatly laid by Charlie Schnetzler because it is in light of his presentation that we want to examine the results.

The objectives of our experiment were to obtain a partial chemical map of a large portion of the Moon. As Dr. Schnetzler has pointed out, what we know about the Moon was learned by sampling given selected sites, but what is really needed is a large global survey. This was the objective of our experiment as well as some other component experiments of this Apollo 15 mission, such as the gamma ray and alpha particle experiments.

Our present estimate is in fact that we did succeed in mapping a fairly large portion of the lunar surface; approximately 10 percent. This represents the part of the surface that was illuminated during the course of the Apollo 15 mission and includes the area over which the spacecraft flew. We actually succeeded in getting mapping information from approximately $150°$ east on the Moon to about $50°$ west.

Just to briefly describe the experiment, we know that the Sun bombards the lunar surface with high fluxes of very soft X-rays and that these X-rays are sufficiently energetic to produce secondary X-rays by photoelectric processes. These secondary X-rays are characteristic of silicon, aluminum, and magnesium. I talk about these three elements because the nature of the spectral distribution is such that these and the lighter elements are the only ones that are excited.

We flew in the SIM Bay of the service module three large-area proportional counters; two of these had selected filters, one for aluminum, and one for silicon, in order to give us both information about the X-ray intensities and the spectral distribution of the X-rays from which we were then able to deduce something about the composition.

We actually succeeded in determining aluminum/silicon ratios and magnesium/ silicon ratios for large portions of the Moon. As we see in Figure 1, the
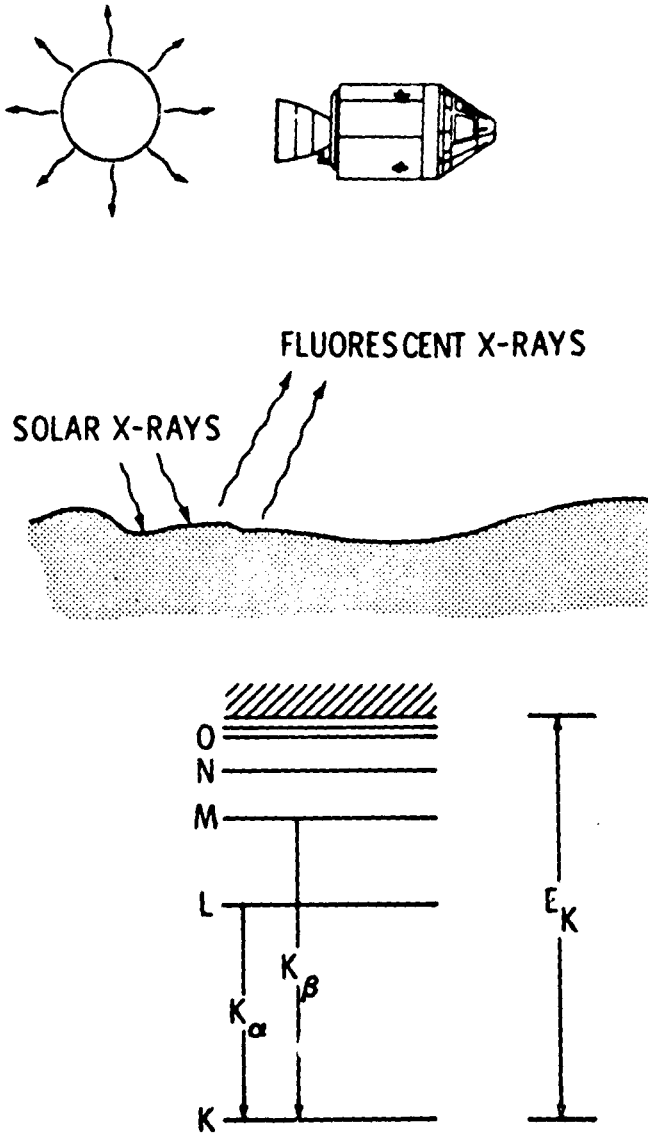
Figure 1—X-ray fluorescence at lunar surface. Lower diagram shows the electron transitions giving rise to characteristic K X-ray spectra.

spacecraft flew around the lunar surface. Some of the energies necessary for exciting these characteristic X-rays are given in Table I. We can see that the energies are relatively low, of the order of 0.2 to 0.3 fJ (1 to 2 keV). The kinds of transitions involved in the production of these characteristic X-rays are also shown in Figure 1.

TABLE I—Energies of Absorption Edges and Characteristic Lines

Element	$E(K_\alpha)$, keV	Absorption edges E_k, keV
O	0.54	
Na	1.04	
Mg	1.25	1.37
Al	1.49	1.57
Si	1.74	1.85
K	3.35	
Ca	3.70	

I should say a little bit about the resolution of our experiment. The collimators permitted a 60° field of view which at orbital altitudes represented a sector on the lunar surface of about 110 km (60 n. mi.) on edge. However, to talk about the spatial resolution, one has to be concerned with the spacecraft motion.

The preliminary data which I will discuss resulted from the upgrading of our spectra at 1-min intervals, and at 1-min intervals then we were looking at a portion of the surface which was approximately 110 by 220 km (60 to 120 n. m.).

Our prime data have now begun to come in. These data were taken at 8-s intervals, so we are going to do another iteration on the data processing at a much better spatial resolution, something on the order of 110 by 150 km (60 by 80 n. m.).

Let me show you the sorts of games we have been playing with the data. In Figure 2 we have actually been able to make a plot of aluminum/silicon intensity ratios versus longitude and have identified some of the features over which we have flown. These values are intensity ratios. We have now reduced them actually to concentration ratios and so if you look at this plot of the aluminum/silicon ratio versus longitude, you can see what aluminum/silicon ratios correspond to the various features on the Moon. These numbers can in fact be compared with numbers of known sites and known analyzed lunar materials (as shown to the right in Figure 2).
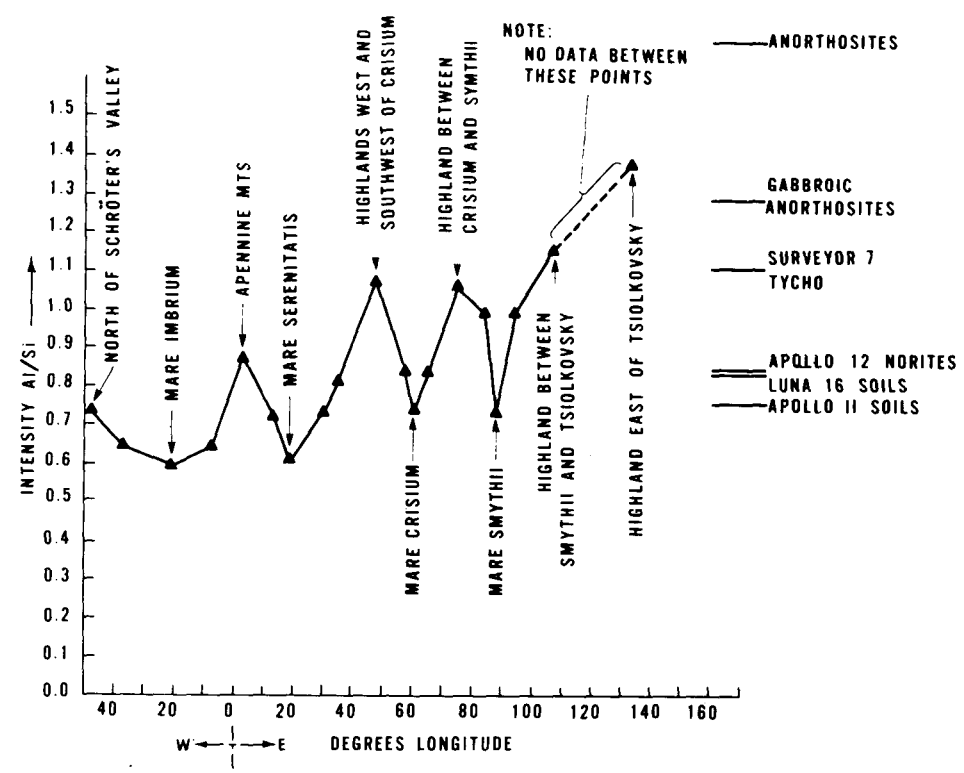
Figure 2–Plot of Al/Si intensity ratios along a northerly ground track.

We see as one goes from west to east that there are gradually increasing con-
centrations of aluminum. The mare areas tend to be low, which is in fact
characteristic of the basalts as we have come to know them.

The interesting thing is that in the highland areas we find rather high
aluminum/silicon ratios; this fact has considerable bearing on the subject
that Dr. Schnetzler talked about, the fact that the highlands are probably
very rich in these feldspars which have been found at the various sites.
The fact that they are rich in these feldspars is of great significance in trying
to understand the origin of the highlands.

We had one problem, I hope when we see our prime data we will be able to
do something about it. When we flew over this very strange crater, Tsiolkovsky,
we were able to get data on both sides of the crater, but in the middle of the
crater the instrument decided to calibrate itself, which is one of the frustra-
tions you sometimes have to put up with.

We have also made a plot of aluminum/silicon intensity ratios against optical
albedo to see if there is a correlation (Fig. 3). We find that for large-scale
features there is excellent correlation; where the albedo is high, as for ex-
ample in the highlands, the aluminum/silicon ratios are high. In the mare
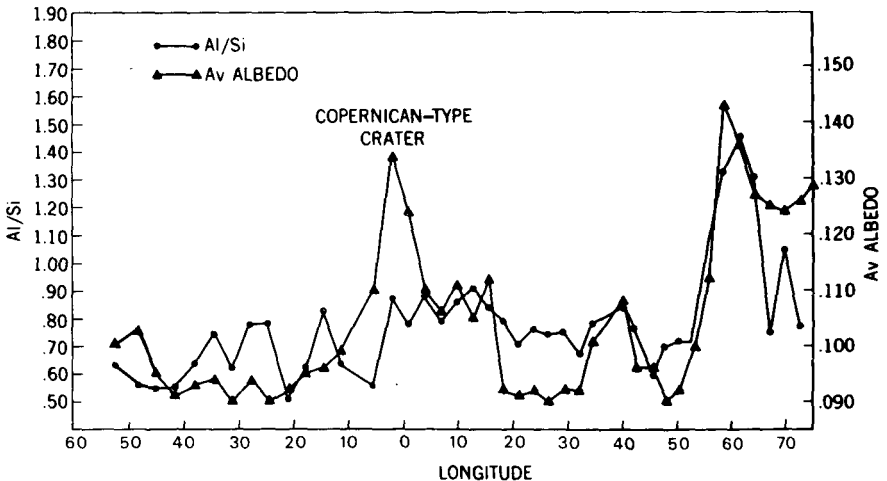areas we find that they are low.

Figure 3–Comparison of average albedos and Al/Si intensity ratios for revolution 72.

Every now and then you find some anomaly such as a high value in albedo which is not reflected in the chemistry. Herb Blodget has pointed out that from the actual albedo maps, the high albedo in this case is clearly identifiable as a Copernican-type crater. I think this is a very good way of actually relating albedo to chemistry. We can in fact distinguish whether the albedo actually represents chemical differences or perhaps some sort of cratering event. The result of the high albedo is sometimes due to mechanical factors rather than chemistry.

Let me sum this up by telling you some of our conclusions today. The most important one I think is that we seem to bear out that the plagioclase rocks that have been found at the Apollo sites actually have as their source or point of origin the highlands. This is very important.

We also have this information on the albedos, which is very, very nice.

An interesting implication of these experiments is that we are looking at very soft X-rays which is essentially a surficial type of analysis. In fact if it were not for the gardening which occurs on the Moon, we would perhaps have trouble because the sampling would not be representative. But the soil is nicely turned over, so even though we are looking at the surface, we are getting information from below the surface.

But because it is a surficial analysis, we now think we have an upper limit on the effectiveness of horizontal transport which is supposed to be a highly active mechanism on the Moon for transporting material. The fact is that if this horizontal transport were very effective, then we would have great difficulty seeing chemical differences between the highlands and the mares. The fact of the matter is that we do see detailed differences. So there is I think a very distinct limit to the effectiveness of the transport.

The data which I presented here have been essentially for aluminum and silicon. We are now working on the magnesium/silicon ratio which is again a very important diagnostic element if one is concerned with magmatic differentiation. We hope to be able to publish something about that.

As an additional bonus on this experiment, we were actually able to do some X-ray astronomy. The results are being reduced. Actually the astronauts were very obliging and agreed to point the spacecraft at some of these newly exciting X-ray objects such as Cygnus X-1 and Sco X-1. We have begun to reduce the data, but before we can publish the results, we must determine what the spacecraft was doing at the time. They fixed on these objects, but we want to be sure that there was no spacecraft rotation, which would then be responsible for some of the variations that we have seen.